Non-linear electrophoresis of metal-dielectric Janus particles in nematic liquid crystals

A Thesis submitted for the award of the degree of

Doctor of Philosophy in Physics

by

Dinesh Kumar Sahu

16PHPH02

Supervisor: Prof. Surajit Dhara

School of Physics

University of Hyderabad

Hyderabad, India

June 2022

To

My Family

Declaration

I, **Dinesh Kumar Sahu**, hereby declare that this thesis entitled **"Non-linear electrophoresis of metal-dielectric Janus particles in nematic liquid crystals"** has been carried out by me under the supervision of Prof. Surajit Dhara, School of Physics, University of Hyderabad, as per the Ph.D. ordinances of the University. I declare to the best of my knowledge that this is a bonafide work and no part of this thesis has been submitted for the award of a research degree by any other University. A report on plagiarism statistics from the University Librarian is enclosed.

Dinesh Kumar sahu
(Dinesh Kumar Sahu)
Reg. No: 16PHPH02

Date: 24.06.2022
Place: Hyderabad,

Certificate

This is to certify that the thesis entitled **"Non-linear electrophoresis of metal-dielectric Janus particles in nematic liquid crystals"** submitted by Dinesh Kumar Sahu bearing Reg. No. 16PHPH02 in fulfillment of the requirements for the award of Doctor of Philosophy in Physics is a bonafide work carried out by his under my supervision and guidance.

This thesis is free from plagiarism and has not been submitted previously in part or in full to this University or any other University or Institution for the award of any degree or diploma. Further, the student has the following publications before the submission of the thesis for adjudication.

1. **Dinesh Kumar Sahu**, Swapnil Kole, Sriram Ramaswamy, and Surajit Dhara, Omnidirectional transport and navigation of Janus particles through a nematic liquid crystal film, *Phys. Rev. Res.* **2**, 032009(R) (2020). Chapter-3.
2. **Dinesh Kumar Sahu** and Surajit Dhara, Electric field driven controllable motility of metal-dielectric Janus particles with boojum defects in thin films of a nematic liquid crystal, *Phys. Fluids* **33**, 087106 (2021). Chapter-4.
3. **Dinesh Kumar Sahu** and Surajit Dhara, Enhanced electrophoretic mobility of nematic dipolar Janus colloids, *Soft Matter* **18**, 1819 (2022). Chapter-5.
4. **Dinesh Kumar Sahu** and Surajit Dhara, Measuring electric-field-induced dipole moments of metal-dielectric Janus particles in a nematic liquid crystal, *Phys.*

Rev. Appl. **14**, 034004 (2020). Chapter-6.

5. **Dinesh Kumar Sahu**, Thriveni G. Anjali, Madivala G. Basavaraj, Jure Aplinc, Simon Čopar and Surajit Dhara, Orientation, elastic interaction and magnetic response of asymmetric colloids in a nematic liquid crystal, *Sci. Rep.* **9**, 81 (2019). Chapter-7.

Further, the student has passed the following course towards the fulfilment of coursework required for Ph.D.

SN	Course Code	Name	Credits	Pass/Fail
1)	PY601	Research Methodology	4	Pass
2)	PY602	Advanced Quantum mechanics	4	Pass
3)	PY60305	Advanced Experimental Techniques	4	Pass
4)	PY60309	Advanced Mathematical Methods	4	Pass

24/6/2022

Dean,
School of Physics,
University of Hyderabad

संकाय अध्यक्ष / Dean
भौतिकी संकाय / School of Physics
हैदराबाद विश्वविद्यालय
UNIVERSITY OF HYDERABAD
हैदराबाद / HYDERABAD-500 046. भारत / INDIA.

Sdhara

Prof. Surajit Dhara
Thesis Supervisor
School Of Physics,
University of Hyderabad.

Dr. Surajit Dhara
Professor
School of Physics
University of Hyderabad
Hyderabad-500 046. INDIA.

Acknowledgement

It gives me immense pleasure to express my sincere gratitude to all the people who supported me during the course of my doctoral thesis.

Firstly, I would like to express my deep gratitude to my thesis supervisor, Prof. Surajit Dhara, for his constant guidance and support. His dedication and enthusiasm towards research is highly appreciable. I highly value his timely constructive criticisms. I could not thank him enough for providing the freedom to carry out my research work. I would like to extend my thanks to the Doctoral Committee members: Prof. BVR Tata, Prof. S. Srinath and Dr. G. Venkataiah for their valuable suggestions throughout my research work.

I am very much grateful to Prof. Sriram Ramaswamy for many stimulating discussions and providing theoretical support to our work. It was indeed a great learning experience working with him. I also thank one of his students, Swapnil Kole for his contributions. I thank our collaborators, Prof. M. G. Basavaraj and T.G. Anjali for providing samples. I am also grateful to Prof. Simon Čopar and Jure Aplinc for conducting the simulation studies of my experiments.

I take this opportunity to thank the former Deans, Prof. R. Singh,Prof. Bindu A. Bambah, Prof. Ashok Chatterjee and the present Dean Prof. K C James Raju, for providing all the facilities and also all the other faculty members of School of Physics for their valuable suggestions at appropriate times. I am thankful to all the non-teaching staffs in the department for their help and support.

I specially acknowledge Department of Science and Technology (DST) and University of Hyderabad for the financial support through INSPIRE fellowship scheme.

I specially admire my senior Dr. Sathyanarayana Paladugu for his encouragement and guidance during the experimental studies. My sincere gratitude to other seniors, Rasna M. V., Rasmita Sahoo, Zuhail K. P. and Junaid Ahmed Sofi for their motivations. I specially thank Muhammed Rasi M for his help at the beginning of the study. I thank my lab-mate M. Praveen Kumar for his help and support. I highly appreciate my colleague Devika V. S. for all the fruitful discussions we had. My best wishes to Abinash, Archana, Ashish, Saikat, Kamakhya and Anashwara.

Heartiest thanks to my friends Vinod, Atasi, Pooja, Sharif, Rudra, Mitesh, Lipu and others who made my stay in the University enjoyable. Also, special thanks to Sambit, Nila, Srinivas, Rajesh, Indrajeet and Dukhishyam for always being there for me. I highly appreciate my roommate Akshay for his help and cooperation during the stay in hostel. A special mention to my senior Chakradhar Sahoo for his constant support and encouragement.

I feel blessed to have my family for their unconditional love and support throughout my life. I am indebted to my mother for providing everything to fulfill my desires. I could not wish for anything more than to have my twin-brother Deepak, who never left my side throughout the journey. I am eternally grateful to my sisters Sunita and Sasmita for their constant love and care.

Preface

Liquid crystal (LC) is an intermediate state of matter between completely ordered crystals and completely disordered liquids. LCs possess long range orientational order with no positional order and exhibit different phases depending on the orderliness. The most common phase, Nematic (N), forms when the LC molecules get aligned locally (over a few micrometer) along a certain direction, the average of which is called the director, $\hat{n}$. Like crystals, LCs also exhibit topological defects in the form of points or lines, known as disclination lines which are formed due to the symmetry breaking phase transition from the isotropic phase to the nematic phase. The defects are the discontinuities in the director field where the orientation of the molecules can not be defined uniquely. These topological defects can also be induced in a uniformly aligned LC medium by introducing foreign particles with certain surface anchoring conditions. For example, particles with normal anchoring to LC molecules could nucleate either a hyperbolic hedgehog (dipolar) or a Saturn-ring defect (quadrupolar) depending on the anchoring strength and the cell confinement while particles with degenerate planar anchoring stabilise boojum defects. Here the dipolar and quadrupolar terms represent the type of director profile (transverse components) around the particles in analogy with electrostatics. The elastic distortion around the particles facilitates anisotropic long range interaction among them, instigating spontaneous self-assembly which is in general of high interest in the context of colloidal crystals for photonic band gap materials and tunable devices.

The LC medium acts as a fascinating dielectric medium for the study of electrophoresis. Under external electric field, the conductivity anisotropy and the director structure play an important role in separation of free charges over a length scale of particle's dimension. Symmetric director profiles around the particles make them immobile. If the director profile around the particle breaks the fore-aft symmetry of the surrounding fluid flows, then the particle starts propelling, a phenomenon known as liquid crystal-enabled electrophoresis (LCEEP). Such an ability of LC medium to bring out activeness to the dispersed particles is important for both fundamental and technological perspectives.

Designing self-propelled or externally powered particles is a topic of immense interest in the area of soft and active matter physics. The control over the dynamics of particles is a very important for developing new technologies. Propulsion of particles in fluids at low Reynolds number resembles the swimming mechanism of many living micro-organisms like bacteria, algae, etc. These particles are usually transported by electrophoresis, diffusiophoresis, thermophoresis and light. Recently, electrophoresis of symmetric particles in LCs have been studied. The direction of motion of the particles is guided by the nematic director field pattern and consequently, it lacks the tunability of the particle trajectories. We focus on the electrophoretic mobility of surface asymmetric particles, namely Janus (metal-dielectric) particles, accompanied with different types of defects, dispersed in LC medium. This thesis mainly aims at studying and manoeuvring the direction of transport of the particles. In addition, we present a novel method of measuring induced dipole moment of metal-dielectric Janus particles. Finally, we investigate the orientation dependent elastic interactions of hematite peanut-shaped particles and estimate magnetic moment of the particles from the competing effect between the elastic and magnetic torques.

The **first chapter** gives a brief introduction to different liquid crystal phases, physical properties and topological defects. We also discuss about the induced defects by dispersing microparticles with different surface anchoring conditions in uniformly aligned LC medium. We also present an introduction to the non-linear electrophoresis of particles in LCs.

The **second chapter** consists of all the relevant experimental techniques needed for studying colloidal interactions, effect of electric and magnetic fields in the nematic liquid crystals. Experiments including sample preparation, cell preparation (both in-plane and out-of-plane cells), polarizing optical microscopy and particle manipulation using optical tweezer etc. are explained in detail. Finally, we discuss about the experimental procedure for observing the electro-osmotic flows and the required software and mathematical programmes used for tracking trajectory of the particles.

In the **third chapter**, we focus on electrophoresis of metal-dielectric Janus particles nucleating Saturn-ring defect encircling the particle by creating symmetric director profile in the nematic LC. We create controllable active Janus particles which acquire motility through a nematic liquid crystal film by transducing the energy of an imposed perpendicular AC electric field. We show that the direction of transport of Janus particles is purely dictated by the orientation of the metal-dielectric interface i.e angle between the Janus vector $\hat{\mathbf{s}}$ and the far field director. The underlying mechanism exploits the sensitivity of electro-osmotic flow to the asymmetries of the particle surface and the quadrupolar defect structure. We present a calculation of the dipolar force density produced by the interplay of the electric field with director anchoring and the contrasting electrostatic boundary conditions on the two hemispheres, which accounts for the dielectric-forward (metal-forward) motion of the colloids due to induced puller (pusher) force dipoles. We achieve complete command over the particle trajectories by varying field amplitude and frequency of the applied field. We demonstrate the navigational capabilities of particles. These results open unexplored directions for the use of colloids and liquid crystals in controlled transport, assembly, and collective dynamics.

In the **fourth chapter** we study the electrophoresis of Janus particles with degenerate planar anchoring condition on the particle surface which induces two antipodal surface defects, known as boojums in a thin film of liquid crystal. Even though boojum Janus particles have quadrupolar symmetric director structure, the electro-kinetics of the particles is significantly different. In a sharp contrast to the propulsion of Saturn-ring Janus particles, we show that the boojum Janus particles self-propel along all possible directions on a plane perpendicular to the electric field but always facing the metal hemisphere. We control the direction of motion of boojum Janus particles by changing the amplitude and frequency of the field and show that the navigational capability of boojum Janus particles is markedly different than that of the Saturn-ring Janus particles. We show that the electro-osmotic flow of fluids around a static boojum Janus particle is always pusher type.

In the **fifth chapter**, we study electrophoresis of metal-dielectric Janus particles with dipolar director symmetry in two nematic liquid crystals (LCs) having same sign of conductivity anisotropy but opposite sign of dielectric anisotropy. The applied ac electric field is parallel and perpendicular to the director for positive and negative dielectric anisotropy LCs, respectively. We show that the Janus dipolar particles propel faster than the non-Janus dipolar particles in both LCs. The propelling speed of Janus dipolar particles is also significantly higher compared to the quadrupolar Janus particles studied previously. We map the electro-osmotic flows surrounding a fixed particle using micro-particle image velocimetry (μ-PIV) technique and show that the flows on the metal hemisphere is stronger than that of the dielectric hemisphere and pumping of LC along the direction of motion of Janus particles is more compared to that of the non-Janus particle. Altogether, Janus dipolar particles demonstrate efficient electrophoresis compared to both Janus and non-Janus quadrupolar particles. These findings may be useful for active matter, microrobotic and microfluidic devices.

In the **sixth chapter**, we demonstrate a novel method for estimating the induced dipole moment of individual Janus particle dispersed in a nematic host. Here, we focus on a pair of metal-dielectric Janus quadrupolar colloids assembled as a result of attractive elastic forces between them. Upon application of the electric field, the particles get polarized and a net electric dipole moment is induced along the direction of the field as a result of which the particles experience electrostatic repulsion. From the competing effect between the attractive elastic and repulsive electrostatic forces, we estimate the induced dipole moment of the Janus particles. Here the electric field is low enough so that the effect of electrokinetic flow is negligible. We theoretically calculate electric polarizability using Clausisus-Mossotti factor and show that the experimental results agree well with the theory. Although, our study focuses on spherical particles in nematic liquid crystals, this method is applicable to all microscopic Janus particles irrespective of their shape in a variety of liquid crystals.

In the **seventh chapter**, we report experimental studies on spontaneous orientation, mutual interaction, laser assisted self-assembly and the effect of external magnetic fields on the hematite peanut-shaped particles dispersed in a nematic LC. Majority of the particles spontaneously orient either parallel or perpendicular to the nematic director. Particles oriented parallel to the director nucleate dipolar director distortions while the particles oriented perpendicularly exhibit two types of quadrupolar textures due to the out of plane tilting, which is corroborated by the Landau-de Gennes Q-tensor modelling. The transverse magnetic moment (1.7×10^{-11} emu) of the peanut-shaped colloids is estimated by using a simple analysis based on the competing effects of magnetic and elastic torques.

Contents

List of Abbreviations and Symbols

LC	Liquid crystal
N	Nematic Phase
SmA	Smectic-A phase
ITO	Indium-Tin Oxide
$\hat{\mathbf{n}}$	Director
K_{11},K_{22},K_{33}	Splay, twist and bend elastic constant
$n_{\parallel}$	Refractive index parallel to $\hat{n}$
$n_{\perp}$	Refractive index perpendicular to $\hat{n}$
$\epsilon_{\parallel}$	Dielectric permittivity parallel to $\hat{n}$
$\epsilon_{\perp}$	Dielectric permittivity perpendicular to $\hat{n}$
Δn	Birefringence
$\Delta\epsilon = \epsilon_{\parallel} - \epsilon_{\perp}$	Dielectric anisotropy
$\sigma_{\parallel}$	Conductivity parallel to $\hat{n}$
$\sigma_{\perp}$	Conductivity perpendicular to $\hat{n}$
$\Delta\sigma = \sigma_{\parallel} - \sigma_{\perp}$	Conductivity anisotropy
V_{th}	Freedericksz threshold voltage
$\hat{\mathbf{s}}$	Janus vector
α	Polarizability
ICEP	Induced charge electrophoresis
ICEO	Induced charge electro-osmosis
LCEEP	Liquid crystal enabled electrophoresis
LCEO	Liquid crystal enabled electro-osmosis
μ-PIV	Micro-particle image velocimetry

1

Introduction

1.1 Liquid Crystals

Liquid crystal (LC) phase usually appears between the completely ordered solid crystals (Fig.1.1(a)) and the disordered isotropic liquids (Fig.1.1(c)). Although LCs show flow properties at macroscale, on the molecular scale, it possess an orientational order (Fig.1.1(b)). They are consist of shape anisotropic organic molecules and the interaction between them leads to orientational ordering. As the name suggests,

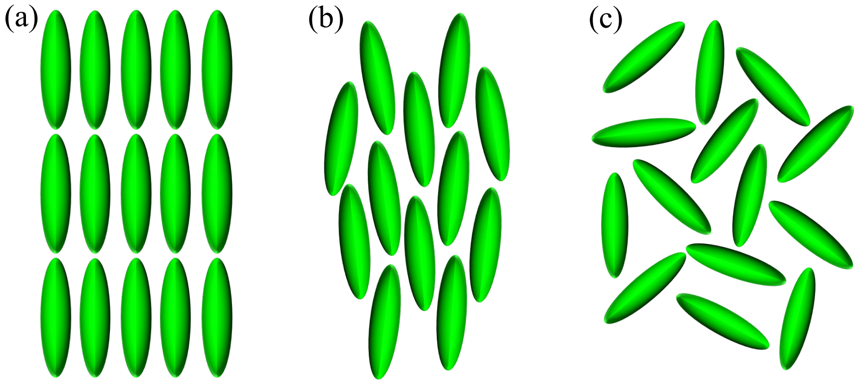

Figure 1.1: Schematic representation of the molecular arrangement in a (a) solid crystal exhibiting both orientational and positional order, (b) LC with only orientational order and an (c) isotropic fluid with neither positional nor orientatinal order.

LCs exhibit both liquid-like properties like viscosity, surface tension as well as solid-like properties like anisotropy in optical (birefringence) and electrical (dielectric permittivity and conductivity) properties [1, 2]. LCs are broadly classified into two categories namely, thermotropic and lyotropic. Thermotropic LCs possess different phases as a function of temperature whereas lyotropic LCs show phase transitions as a function of both temperature and concentration of LC molecules in a solvent. Thermotropic LCs are further classified into calamitic, discotic and bent-core LCs if the constituent molecules are rod-shaped, disc-shaped and bent-shaped, respectively. Thermotropic calamitic LCs exhibit several phases such as nematic, smectic, cholesteric etc. In the next section, we briefly introduce these phases.

1.1.1 Nematic phase (N)

Nematic phase is the most common LC phase which has the least order and the highest symmetry. The word nematic comes from a Greek word *nema* which means thread and the name was justified due to the presence of thread like defects. In nematic phase, the molecules have long range orientational order with no positional order. The elongated molecules tend to align locally (over a few micrometer range) along a certain direction called the director and is denoted by n̂ as shown in Fig.1.2(a). A Schlieren texture is shown in Fig.1.2(b). Nematic phase is apolar in nature i.e, n̂ and -n̂ are equivalent. Most of the nematics have rotational symmetry along the director, consequently they are uniaxial.

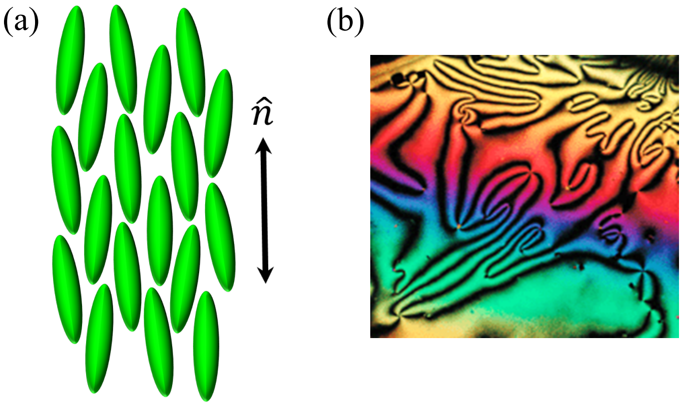

Figure 1.2: (a) Schematic representation of a nematic phase. The average orientation of molecules is represented by a double headed arrow known as director, n̂. (b) Schlieren texture of a nematic (adapted from ref. [3]).

1.1.1.1 Nematic order parameter

An order parameter is a measure of degree of order of a system which changes across the phase transitions. In nematic phase, the scalar order parameter S is the ensemble average of the second Legendre polynomial which describes the degree of orientational ordering of the molecules. In order to express S, let us consider the director is along Z-axis and orientation of the molecules is characterized by the azimuthal angles, θ and ϕ as shown in Fig.1.3(a). The state of molecular alignment can be described by a distribution function $f(\theta,\phi)$ which provides the probability of finding a molecule oriented within a solid angle $d\Omega$ as $dp = \frac{1}{4\pi} f(\theta,\phi) d\Omega = \frac{1}{4\pi} f(\theta,\phi)\sin\theta d\theta d\phi$. For uniaxial nematic, $f(\theta,\phi)$ is independent of ϕ (Fig.1.3(b)), hence can be expressed as

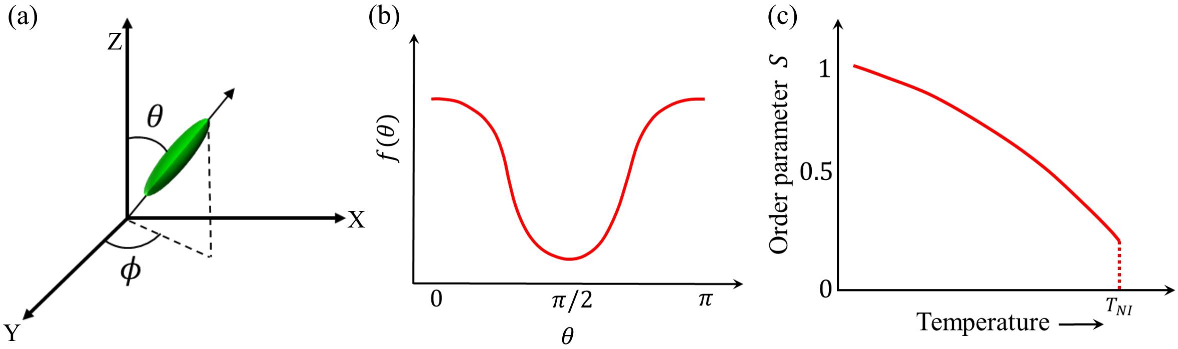

Figure 1.3: (a) Characterization of orientation of a molecule in spherical polar coordinate. Director $\hat{\mathbf{n}}$ is along z-axis. (b) Distribution function $f(\theta)$ versus θ for molecular alignment. $f(\theta)$ is small for constituents normal to $\hat{\mathbf{n}}$, i.e $\theta = \pi/2$ and it is large for $\theta = 0$ or π. (c) Typical behavior of scalar order parameter of a NLC with temperature. T$_{NI}$ denotes the isotropic to nematic phase transition temperature.

$$f(\theta,\phi) = f(\theta) = \Sigma_{n=0}^{\text{inf}} f_n P_n(cos\theta) \tag{1.1}$$

where $P_n(cos\theta)$ is the nth Legendre polynomial and $f_n = \frac{2n+1}{2}\int_{-1}^{+1} f(\theta) P_n(cos\theta) d(cos\theta)$ is the corresponding coefficient. The first term, $f_0 = 1$ and all the odd order terms vanish as $\hat{\mathbf{n}}$ and $-\hat{\mathbf{n}}$ are equivalent. Thus, the first non-zero contribution comes from the quadrupolar term f_2 which defines the order parameter as

$$S = \langle P_2(cos\theta)\rangle = \frac{1}{2}\langle 3cos^2\theta - 1\rangle \tag{1.2}$$

where $\langle ...\rangle$ denotes the ensemble average of the molecules. Due to the apolar nature of the nematic phase, the order parameter is a second rank tensor and for a uniaxial nematic it can be expressed as [1]

$$S_{\alpha\beta}(\vec{r}) = S(n_\alpha(\vec{r}) n_\beta(\vec{r})) - \frac{1}{3}\delta_{\alpha\beta} \tag{1.3}$$

where the term $n_\alpha(\vec{r})n_\beta(\vec{r})$ represents the spatial variation of $n(\vec{r})$. Theoretically, S can vary from 0 (isotropic phase) to 1 (completely ordered phase), as shown in Fig.1.3(c). The sharp discontinuity in S at the nematic to isotropic phase transition (T_{NI}) denotes the first order phase transition. However, experimentally S varies approximately from 0.3 at N-I transition to 0.8 at lower temperature.

1.1.2 Cholesteric phase (N*)

The chiral nematic phase, broadly known as cholesteric phase exists when either chiral dopants are added to the nematic phase or the molecules are inherently chiral. The chirality of molecules causes a twist in the director structure, which rotates in a helical manner (Fig.1.4(a)). The director completes a full rotation along the helical axis over a distance, called pitch p and the repetition occurs at a distance p/2 as n̂ and -n̂ are equivalent. Typically pitch varies in the range of 200-1000 nm depending on the chirality and it is temperature dependent. A schlieren texture is shown in Fig.1.4(b).

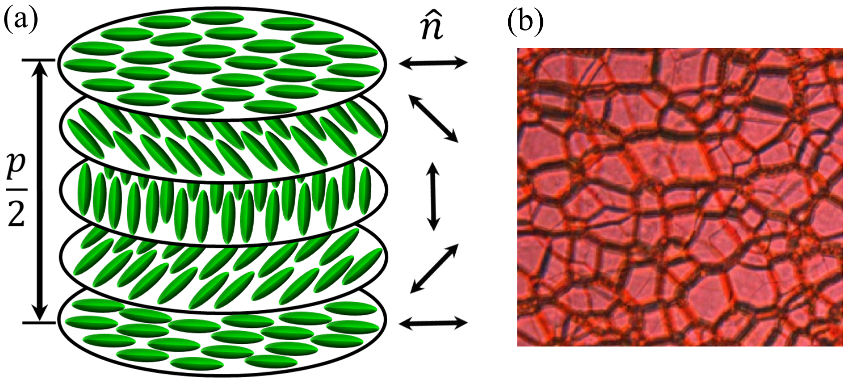

Figure 1.4: (a) Schematic representation of molecular arrangement in cholesteric phase. (b) Polarizing optical micrograph (POM) of a cholesteric phase showing oily streaks (adapted from ref. [4]).

1.1.3 Smectic phases

In smectic phases, the molecules possess one dimensional positional order in addition to the long-range orientational order. That's why smectic liquid crystals are known as 1-dimensional crystals. The positional ordering gives rise to layer structure where the molecules in each layer possess orientational order. Depending on the type of molecular arrangement within a layer, there are several subcategories of smectic phases like smectic-A, smectic-C, smectic-C*, etc.

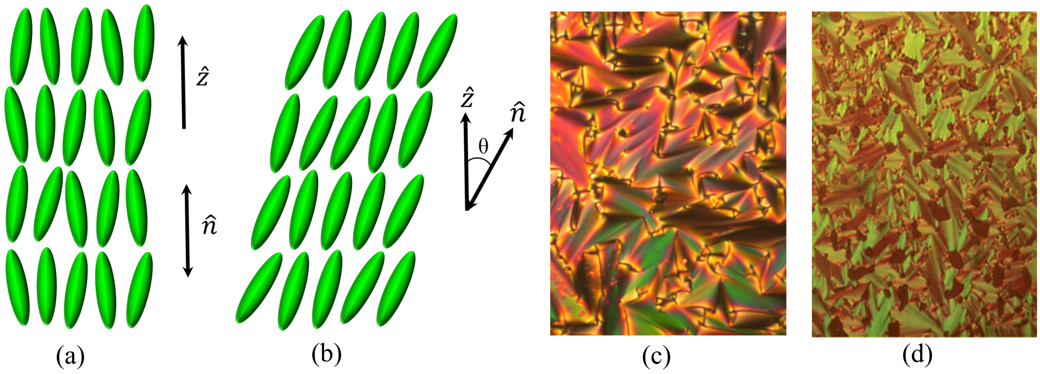

Figure 1.5: Schematic representation of alignment of rod shaped molecules in (a) SmA and (b) SmC phases. $\hat{n}$ is the director and $\hat{z}$ is the layer normal. Focal conic texture of a (c) SmA and (d) SmC phase (adapted from ref. [5,6]).

Smectic-A (SmA) phase is the least ordered smectic phase where the average orientation of the molecules in each layer is parallel to the layer normal. Each layer behaves as a two dimensional fluid as there is no long range correlation among the center of mass of the molecules. Hence, the layers can slide over each other and the molecules can diffuse into the consecutive layers. A schematic representation of the arrangement of rod-shaped molecules in the SmA phase is shown in Fig.1.5(a). The density of molecular distribution along the layer normal can be written as [2]

$$\rho(z) \simeq \rho_0 + \psi e^{iq_A \cdot z} \tag{1.4}$$

where ρ_0 is the average density and $\hat{z}$ is a unit vector along the layer normal and ψ, the complex order parameter known as smectic density wave which is given by

$$\psi(z) =\mid \psi \mid e^{iq_A z \phi} \tag{1.5}$$

where $\mid \psi \mid$ is the complex amplitude of density wave, $q_A = 2\pi\hat{z}/d$, where d is the layer thickness and ϕ an arbitrary phase. ψ is non-zero in smectic phase while $\psi = 0$ in the nematic phase.

In smectic-C (SmC) phase, the long axis of the molecules make an angle θ with the layer normal $\hat{z}$ as shown schematically in Fig.1.5(b). The tilt angle of the molecules is temperature dependent. Usually it decreases as the temperature is increased and varies at SmA-SmC transition.

1.2 Alignment of liquid crystals

A uniform defect free alignment of LC molecules with a preferred orientation on the substrates is the primary requirement for both physical studies and their application in displays. This can be achieved by an appropriate chemical treatment on the substrate which provides the desired boundary condition. In case of anisotropic surface of the substrate, the LC molecules prefer to orient in such a direction that costs less energy, which is denoted as easy axis (Fig.1.6(a)). The mismatch between the director and the easy axis gives rise to anchoring energy function $f_s = f_s(\theta, \phi)$, where θ and ϕ are polar and azimuthal angle assigned to the director. Defining polar angle θ_0 and the azimuthal angle ϕ_0 for easy axis (Fig.1.6(a)), the anchoring energy can be expressed as [7]

$$f_s = \frac{1}{2} W_p \sin^2{(\theta - \theta_0)} + \frac{1}{2} W_a \sin^2\theta_0 \sin^2{(\phi - \phi_0)} \tag{1.6}$$

where W_p and W_a are the polar and azimuthal anchoring strengths. For isotropic surface, usually two types of alignment of LC, namely homogeneous (planar) and homeotropic (perpendicular) are used.

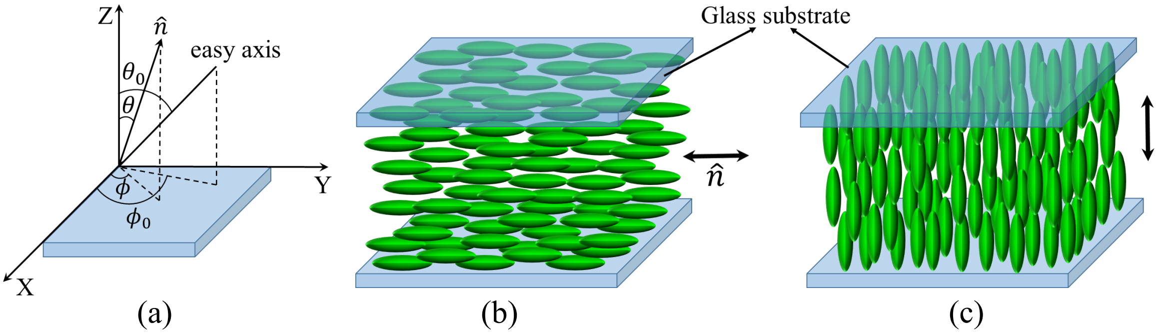

(a) (b) (c)

Figure 1.6: (a) Easy axis and the director on the substrate. Schematic diagrams of (b) homogeneous and (c) homeotropic alignments of LC molecules.

1.2.1 Homogeneous alignment

The homogeneous or planar alignment of the director can be achieved by treating the glass substrates with an appropriate polyimide. A list of polyimides used in our studies is given in chapter-2. The unidirectional rubbing on the coated glass surface creates micro-grooves along which the LC molecules get align. A schematic representation of homogeneous alignment is shown in Fig.1.6(b).

1.2.2 Homeotropic alignment

The homeotropic alignment of the director can be obtained by coating the glass substrates with an appropriate polyimide. In this case, the molecules have amphiphilic polar groups and long aliphatic alkyl chains, where the polar groups stick to the surface and the alkyl chains stand freely. The LC molecules get aligned along the long alkyl chain providing normal anchoring to the surface. A schematic diagram of homeotropic alignment is shown in Fig.1.6(c).

1.3 Physical properties of liquid crystals

The order parameter of nematic LCs is a second rank tensor. Consequently most of the physical properties are anisotropic. The anisotropy vanishes as the LC goes to isotropic phase. This property together with the fluidity makes LCs suitable for designing optically or electrically tunable devices. In this section, we discuss some physical properties of conventional nematic LCs which are relevant to our studies. For uniaxial LCs, the anisotrpy is evaluated by measuring the physical properties parallel and perpendicular to the director.

1.3.1 Birefringence

The interaction of light with a material depends on the preferred molecular orientation of the constituent molecules in LCs. If the material possesses rotational symmetry, light passes through it at a certain velocity without any polarization. If the molecules have orientational order, light gets polarized and travels at different speeds depending on it's direction of propagation with respect to the symmetry axis (optic axis) of the material.

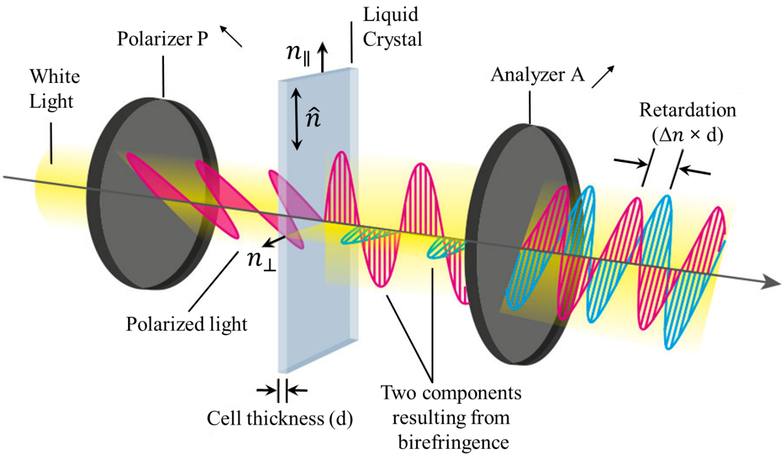

Figure 1.7: Schematic presentation of retardation of light due to birefringence of LC.

Specifically, in LCs, light with polarization parallel to the director moves with a different speed than that with polarization perpendicular to the director $\hat{\mathbf{n}}$. This suggests that LCs possess two refractive indexes corresponding to the polarization of light parallel ($n_{\parallel}$) and normal ($n_{\perp}$) to the director. The interaction of light passing through a LC medium is shown schematically in Fig.1.7. The polarized light splits into two components due to the anisotropy in refractive index known as, birefringence and is defined as

$$\Delta n = n_{\parallel} - n_{\perp} \tag{1.7}$$

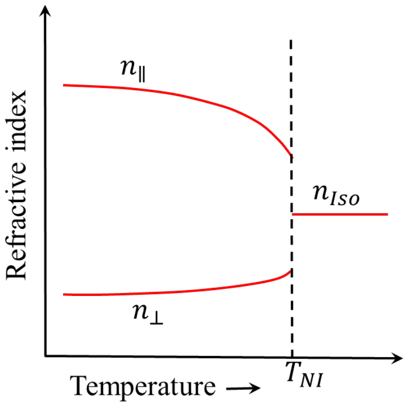

Figure 1.8: Temperature dependence of refractive indices of uniaxial nematic LCs.

The resulting path difference or retardation can be calculated as $\Delta n \times d$, where d is thickness of the LC film . Δn is usually positive for uniaxial calamatic liquid crystals (Fig.1.8) and it varies from 0 to 0.4 [11, 12]. Since LC director is tunable by external electric and magnetic fields, LCs act as a controllable birefringent medium.

1.3.2 Dielectric anisotropy

Dielectric permittivity is a measure of the response of the LCs to an external applied electric field. The dielectric constant depends on the molecular charge distribution, polarity of the molecules and intermolecular interactions. For LCs consisting of apolar molecules, dielectric permittivity arises due to the induced polarization whereas in case of LCs consisting of polar molecules, the dielectric permittivity arises due to both the induced and the permanent polarizations. The dielectric permittivity of a nematic can be written in the form of a second rank tensor with two components of permittivities, $\epsilon_{\|}$ (parallel to $\hat{\mathbf{n}}$) and $\epsilon_{\perp}$ (perpendicular to $\hat{\mathbf{n}}$) as

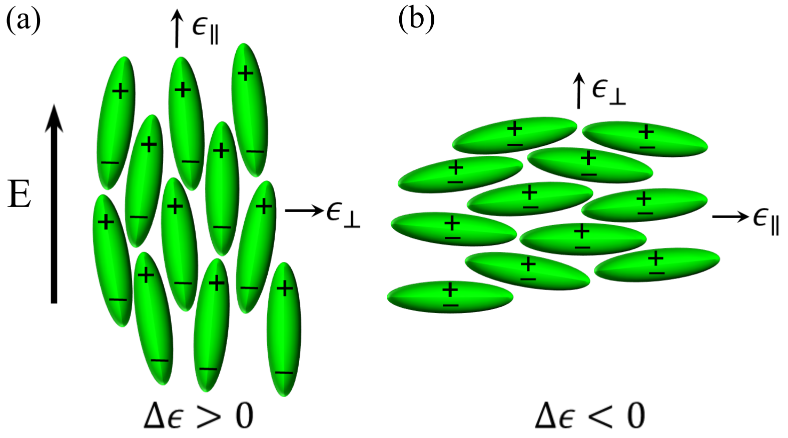

Figure 1.9: Schematic presentation of electrical polarization of LC molecules (a) parallel ($\Delta\epsilon > 0$) and (b) perpendicular ($\Delta\epsilon < 0$) to the director.

$$\epsilon_{ij} = \epsilon_{\perp}\delta_{ij} + \Delta\epsilon n_i n_j \tag{1.8}$$

where the dielectric anisotropy ($\Delta\epsilon$) is defined as [13]

$$\Delta\epsilon = \epsilon_{\|} - \epsilon_{\perp} \tag{1.9}$$

$\Delta\epsilon$ can be positive or negative depending on the directional polarity and position of the polar group of the constituent molecules. In case of $\Delta\epsilon > 0$ ($\Delta\epsilon < 0$), the molecules get polarized parallel (perpendicular) to the director as schematically shown in Fig.1.9. The dielectric constant varies with the temperature and frequency of the applied field.

1.3.3 Electrical Conductivity

The presence of residual impurity ions are responsible for the conductivity of LCs. The magnitude of conductivity depends on the mobility of ions in response to the applied electric field and is, in general of the order of 10^{-11} Sm^{-1}. The anisotropy in conductivity arises due to the difference in the mobility of ions parallel and perpendicular to the director and can be written in the form of second rank tensor

$$\sigma_{ij} = \sigma_{\perp}\delta_{ij} + \Delta\sigma n_i n_j \tag{1.10}$$

where $\Delta\sigma = \sigma_{\parallel} - \sigma_{\perp}$, $\sigma_{\parallel}$ and $\sigma_{\perp}$ are conductivities parallel and perpendicular to the director $\hat{\mathbf{n}}$, respectively. Usually, $\Delta\sigma$ is positive in most calamitic nematic LCs, but negative in smectics as the ions move easily in the layer than along the layer normal.

1.3.4 Curvature elastic constants

External force can create director distortions in a uniformly aligned LC medium which eventually leads to the gradient in the director field. The medium tries to restore the undistorted state which gives rise to elastic properties. Commonly observed elastic deformations in NLCs are called splay, twist and bend. Schematic representations of three deformations are shown in Fig.1.10. The elastic free energy density in Frank-Oseen form is defined as [8–10]:

$$f = \frac{1}{2}\left[K_{11}(\nabla.\hat{n})^2 + K_{22}(\hat{n}.\nabla\times\hat{n})^2 + K_{33}(\hat{n}\times\nabla\times\hat{n})^2\right] \tag{1.11}$$

where K_{11}, K_{22} and K_{33} are splay, twist and bend elastic constants, respectively. Usually, in case of rod-shaped molecules, $K_{33} > K_{11} > K_{22}$. The Frank-Oseen free energy can be further expanded by the divergence energy density terms as

$$\begin{aligned} f_{13} =& K_{13}\nabla.\left(n\left(\nabla.n\right)\right) \\ f_{24} =& -K_{24}\nabla.\left(n\left(\nabla.n\right) + n\times\left(\nabla\times n\right)\right) \end{aligned}$$

where K_{13} and K_{24} are called splay-bend and saddle-splay elastic constants, respectively whose contributions are however limited to the surface of liquid crystals and

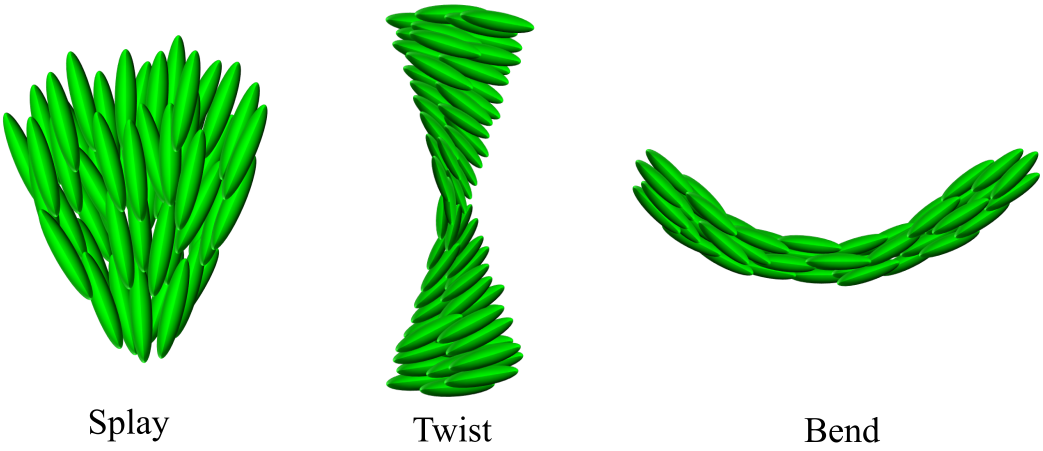

Figure 1.10: Schematic representations of splay, twist and bend elastic deformations of the director field.

roughly affect the bulk behavior. A simple and common approach to simplify all the functional is to adapt one-constant approximation which implies $K_{11} = K_{22} = K_{33} = K$ and the corresponding free energy density can be written as

$$f = \frac{1}{2}K\left[(\nabla.n)^2 + (\nabla\times n)^2\right] \tag{1.12}$$

These constants are positive and their typical magnitude is of the order of 10^{-12}N.

1.3.5 Flow Viscosity

LCs exhibit liquid-like flow properties as it can flow under the application of small amount of shear. The flow viscosity depends on the director orientation relative to the direction of applied shear or flow of LCs called Miesowicz viscosity. There are three principal viscosity coefficients; η_1, where the director is parallel to the velocity gradient, η_2, where director is parallel to the flow direction (normal to velocity gradient) and η_3, where the director is perpendicular to both the velocity gradient and the flow direction as depicted in Fig.1.11. Typical value of these viscosity coefficients of low molecular weight nematic LCs are of the order of 10-200 mPas which is 10-100 times larger than the viscosity of water.

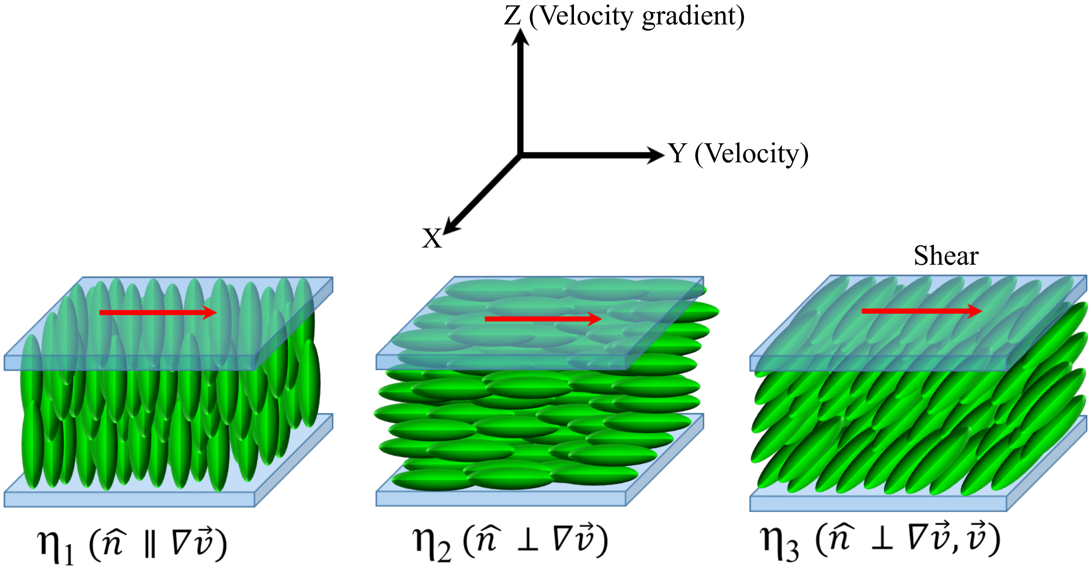

Figure 1.11: Schematic representation of three fundamental director orientations of nematic liquid crystals with respect to the shear direction. Miesowicz viscosities corresponding to each orientations are designated by η_1, η_2 and η_3, respectively.

1.3.6 Diamagnetic anisotropy

An external magnetic field can also cause reorientation of LC molecules analogous to the application of electric field. As mostly organic molecules are diamagnetic, the aromatic ring present in the LC molecules contribute to the diamagnetism of LCs. On application of magnetic field, the plane of the aromatic rings tend to align with the field.

Diamagnetic susceptibility (χ) of LCs is also anisotropic. The susceptibilities parallel ($\chi_{\parallel}$) and perpendicular ($\chi_{\perp}$) to the director are negative and small (10^{-7} to 10^{-6} cm^3/g). The difference between $\chi_{\parallel}$ and $\chi_{\perp}$ defines the diamagnetic anisotropy ($\Delta\chi$). Usually in calamitic nematics, $\Delta\chi > 0$. Typical value of external magnetic field needed to align LC molecules is of the order of 0.5 to 1T.

1.4 Freedericksz transition

The response of LCs to an external applied electric field depends on the dielectric anisotropy ($\Delta\epsilon$) and director orientation with respect to the direction of the applied field. The LC molecules can reorient themselves either parallel or perpendicular to the direction of applied field depending on the sign of dielectric anisotropy ($\Delta\epsilon$). In case of electric field applied across a homogeneous cell filled with a positive LC ($\Delta\epsilon > 0$), the molecules in bulk reorient along the field direction as shown in Fig.1.12. Similar reorientation of LC molecules takes place perpendicular to the field direction in case of field applied across a homeotropic cell filled with a negative LC ($\Delta\epsilon < 0$). This phenomenon is known as Freedericksz transition [12] and it occurs beyond a certain threshold electric field known as the Freedericksz threshold field.

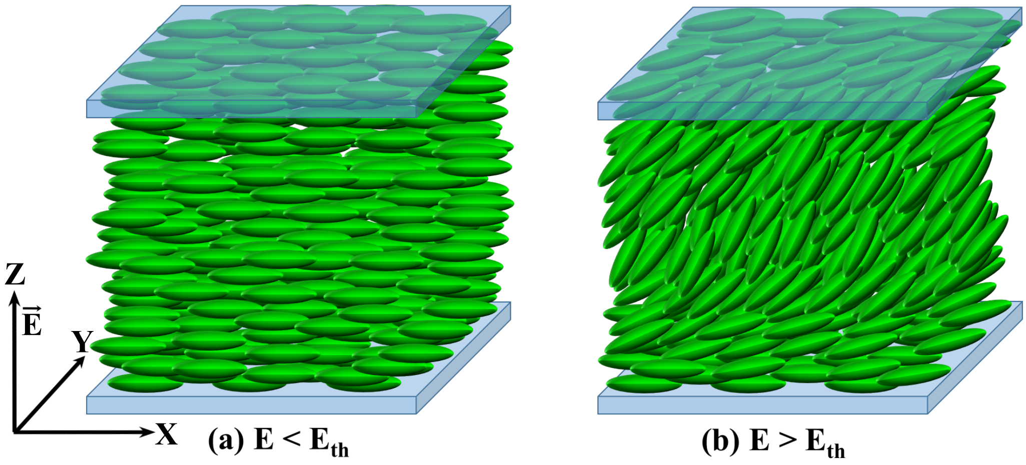

Figure 1.12: (a) Schematic presentation of bulk orientation of positive LC ($\Delta\epsilon > 0$) in a homogeneous cell (a) below and (b) above the Freedericksz threshold field.

Let's consider a homogeneously aligned nematic with the director along x-axis in equilibrium. An external electric field is applied along z-axis which creates elastic distortions in the director field. But the director distribution is limited to one-dimension only. In this geometry, the elastic deformation has contribution from splay and bend and the corresponding free energy can be written as [1]

$$f_{elastic} = f_0 + \frac{1}{2}\left(K_{11}\cos^2\theta + K_{33}\sin^2\theta\right)\left(\frac{d\theta}{dz}\right)^2 \tag{1.13}$$

where θ is the tilt of the bulk nematic director with respect to the far field director.

For undistorted nematic, $\frac{d\theta}{dz} = 0$ and hence f_0 gives the minimum energy. The elastic torque density originating from any deformation in the nematic in terms of elastic energy is given by

$$\tau_{elastic} = -\frac{\partial}{\partial\theta}\Delta f_{elastic} + \frac{d}{dz}\frac{\partial}{\left(\frac{d\theta}{dz}\right)}\Delta f_{elastic} \tag{1.14}$$

The resulting elastic torque density is then given by

$$\tau_{elastic} = (K_{33} - K_{11})\sin\theta\cos\theta\left(\frac{d\theta}{dz}\right)^2 + \left(K_{11}\cos^2\theta + K_{33}\sin^2\theta\right)\frac{d^2\theta}{dz^2} \tag{1.15}$$

On the other hand, the molecules try to align with their long axis parallel to the field in order to minimize the elastic free energy density. Similarly, the corresponding electrostatic torque acting on the LC molecules is given by

$$\tau_{elec} = -\frac{\partial}{\partial\theta}\Delta f_{elec} + \frac{d}{dz}\frac{\partial}{\left(\frac{d\theta}{dz}\right)}\Delta f_{elec} \tag{1.16}$$

where the change in the electric field energy (Δf_{elec}) is given by [1]

$$\Delta f_{elec} = \frac{1}{2}\frac{D_z^2}{\epsilon_\parallel\sin^2\theta + \epsilon_\perp\cos^2\theta} - \frac{1}{2}\frac{D_z^2}{\epsilon_\perp} \tag{1.17}$$

where D is the displacement vector. Since the uniform alignment is in the xy-plane of the cell, the dielectric tensor reduces to a function of z only. As the electric field directly correlates with the local distribution of ϵ, it also becomes a function of z. Hence, D_z is constant and the second term becomes independent of the director orientation $\theta(z)$. Therefore,

$$\tau_{elec} = \frac{D_z^2\left(\epsilon_\parallel - \epsilon_\perp\right)}{\left(\epsilon_\parallel\sin^2\theta + \epsilon_\perp\cos^2\theta\right)^2}\sin\theta\cos\theta \tag{1.18}$$

which can be further simplified to

$$\tau_{elec} = \left(\epsilon_\parallel - \epsilon_\perp\right)E^2\sin\theta\cos\theta \tag{1.19}$$

The equilibrium condition demands

$$\tau_{elastic} + \tau_{elec} = 0 \tag{1.20}$$

Assuming only very small distortion of director field ($\theta << 1$) leads to a pure splay deformation and the corresponding linear differential equation for $\theta(z)$ can be written as

$$K_{11}\frac{d^2\theta\left(z\right)}{dz^2} + \epsilon_0\Delta\epsilon E^2\theta = 0 \tag{1.21}$$

One of the solutions of the above equation is given by

$$\theta(z) = \theta_0 \sin\left(\frac{\pi z}{d}\right) \tag{1.22}$$

where θ_0 is a constant and d is the cell gap. Substituting this solution in the eq.(1.21) for equilibrium condition and considering the first order terms, we get

$$\epsilon_0 \Delta E^2 \sin\theta \cos\theta - K_{11}\left(\frac{\pi}{d}\right)^2 \theta = 0 \tag{1.23}$$

For sufficiently small distortions, $sin\theta cos\theta < \theta$, the nontrivial solution requires

$$E^2 = \frac{\pi^2 K_{11}}{d^2 \epsilon_0 \Delta\epsilon} \approx E_{th}^2 \tag{1.24}$$

The corresponding voltage known as Freedericksz threshold voltage is given by,

$$V_{th} = \pi\sqrt{\frac{K_{11}}{\epsilon_o \Delta\epsilon}} \tag{1.25}$$

The typical value of Freedericksz threshold voltage is in the range of 0.5 - 5 V.

1.5 Topological defects in nematic LCs

Topological defects are the singularities where the order parameter of a system goes to zero. They are spontaneously formed as a consequence of symmetry breaking phase transitions. In liquid crystals, defects are the discontinuities in the director field i.e the regions where the molecular orientations can not be defined uniquely. In NLCs, we see disclinations which are either line or point defects. In smectic phase, defects are observed in the form of edge or screw dislocations. These defects are topologically stable as they can not be transformed to a uniform director state through any continuous deformation of the order parameter field. In NLCs, disclinations appear as lines or points with the defect core (∼10 nm). A schlieren texture of an unaligned NLC and the corresponding molecular arrangement around a point defect (under cross polarizers) is shown in Fig.1.13(a) and (b), respectively. These defects are characterised by strength or winding number s which indicates the number of times the director rotates around the singularity when one surrounds the defect core by 2π angle [2]. So mathematically s can be calculated as the degree of rotation of the director around the defect core or line divided by 2π in one full rotation. In other words, the strength s of

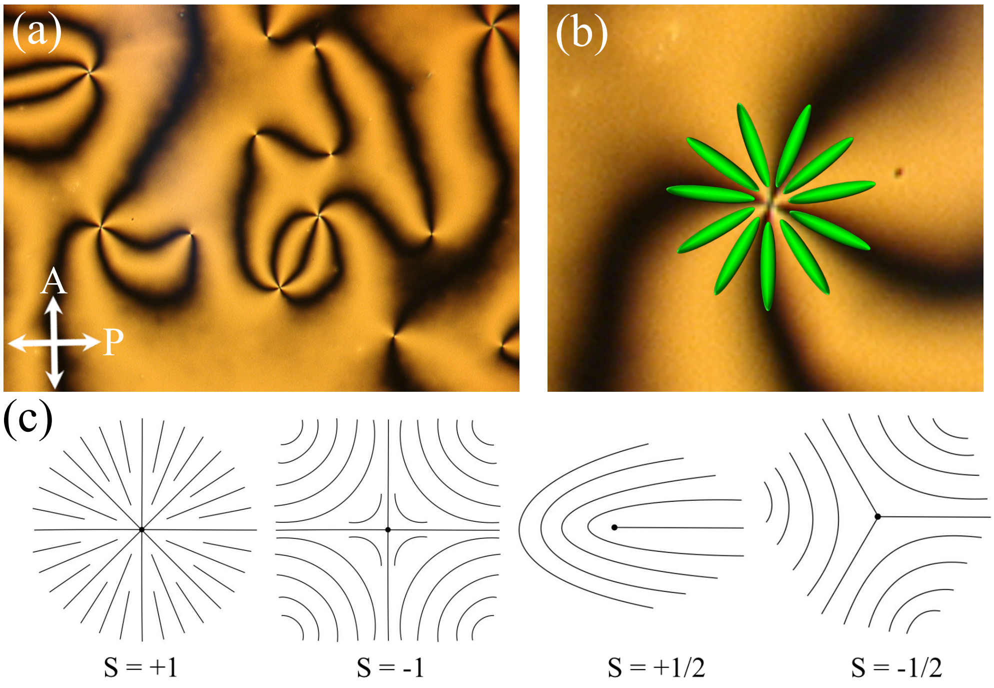

Figure 1.13: (a) The schlieren textures of a nematic liquid crystal under cross polarizers. (b) Molecular arrangement around a point defect of strength +1. (c) Director field lines representing point and line defects of strengths $s = +1, -1, +1/2, -1/2$

a disclination is the angle by which the director rotates along a closed loop enclosing the disclination by 2π (1.13(b)),

$$\oint \frac{d\varphi}{dl} dl = 2\pi s \tag{1.26}$$

where φ denotes the orientation of the director field in a plane. The integral is taken in a counter-clock-wise direction. The Frank elastic energy with one elastic constant approximation can be expressed as [10]

$$f_{el} = \frac{1}{2} K (\bigtriangledown \varphi)^2 \tag{1.27}$$

The Euler-Lagrange minimisation condition corresponding to Eq. 1.27 is given by

$$\bigtriangledown^2 \varphi = 0 \tag{1.28}$$

The orientation of the director field φ can be defined as:

$$\varphi = s \, tan^{-1}(\frac{y}{x}) + \beta = s\alpha + \beta \tag{1.29}$$

where β is a constant. The defect strength s depends on the symmetry of the medium. s can be any integral multiple of $\pm 1/2$ where positive or negative sign indicates the rotation direction of the director with respect to the sense of rotation. Fig.1.13(c) shows schematic representation of some frequently occurring defects with different strength with $\beta = 0$ in NLCs.

1.6 Topological defects induced by microparticles in NLCs

Dispersion of foreign particles in a uniformly aligned nematic medium creates elastic distortion and nucleate topological defects around them. The elastic distortion created by the presence of colloids increases the elastic energy which scales as KR, where K is the typical elastic constant and R denotes the size of the particles [18]. The elastic distortion also depends on the anchoring of LC molecules on the surface of particles. The anchoring energy varies as WR^2, where W is anchoring coefficient describing the amount of energy spent to align the molecules on the particle's surface per unit area. The comparison between these two energy gives rise to a characteristic length, $\lambda = K/W$, known as de Gennes-Kleman length. Typically, value of K ($k_B T/a$, where a is molecular length) is 10 pN and anchoring coefficient W ranges from 10^{-6} to 10^{-3} Jm^{-2}. Consequently, λ ranges from 10 nm to 10 µm and lies between the molecular dimension and micrometer sized particles. Thus, there exist two situations based on the comparison of λ and the size of the particles.

1.6.1 Case-I ($R << \lambda$)

In case of $R << \lambda$, i.e when the size of particles is smaller or compared to the de Gennes-Kleman length λ, they are mostly nano particles and they do not create any elastic distortion as the LC molecules can not pin at small surface area (Fig.1.14). Instead, liquid crystal provide a platform to achieve assembly of these nanoparticles. In case of elongated nano particles, the long axes of the particles usually gets aligned along the director and generate one dimensional array. Although these particles do not perturb the director field, but they significantly affect the anisotropic physical

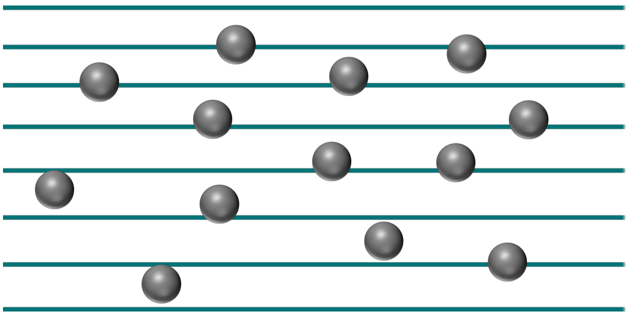

Figure 1.14: Schematic representation of nano-particle dispersion in a uniformly aligned liquid crystal in dilute regime. Small particles ($R << \lambda$) do not create director distortion.

properties of LCs [17, 19–23]. In fact, ferromagnetic NLC was prepared by dispersing ferromagnet nanoparticles in conventional NLCs [24].

1.6.2 Case-II ($R >> \lambda$)

In case of $R >> \lambda$, i.e when the size of the particles is larger than the de Gennes-Kleman length λ, the LC molecules tend to follow the anchoring condition on the particle's surface and create elastic distortions in the surrounding LC medium. The size of the particles, type and strength of the anchoring condition decides the nature of distortions. The distortions generally nucleate topological defects as a result of competition between the anchoring energy and the bulk elastic property, ensuring the conservation of topological charge and stability of the system [25, 26, 38, 39]. Here the particles act as a source of defect and another defect of opposite strength is nucleated so that topological charge is conserved.

1.6.2.1 Spherically symmetric particles in nematic LCs

To study the LC colloidal systems, it is important to understand the defects associated with individual particle and the effective interaction among the colloids. The defect formation depends not only on the surface anchoring of the particles but also the anchoring of the molecules on the substrate and confinement.

For simplicity, let us consider spherical particles with diameter of a few micrometer in a homogeneously aligned (planar) nematic LC (Fig.1.15(a)). If the particles provide homeotropic anchoring to the LC molecules, they act as a source of virtual point defect of strength +1 (radial hedgehog where the director field lines diverges from a single point). The elastic distortion created surrounding the particles nucleates a point defect of strength -1 (hyperbolic hedgehog, Fig.1.15(b)) without disturbing the far field director in order to fulfil the demand of conservation of topological charge [27,28]. If the particles are weakly anchored, then the hyperbolic hedgehog open up to a ring defect of strength $-1/2$ encircling the sphere, which is known as Saturn ring defect [27,38,39]. The ring defect appears as two black spots on the top and bottom of the particle as shown in Fig.1.15(c). This can be achieved experimentally by confining the cell such that the gap between the two plates is comparable to the size of the particles. Both point and ring defects are topologically equivalent as one can be transformed to the

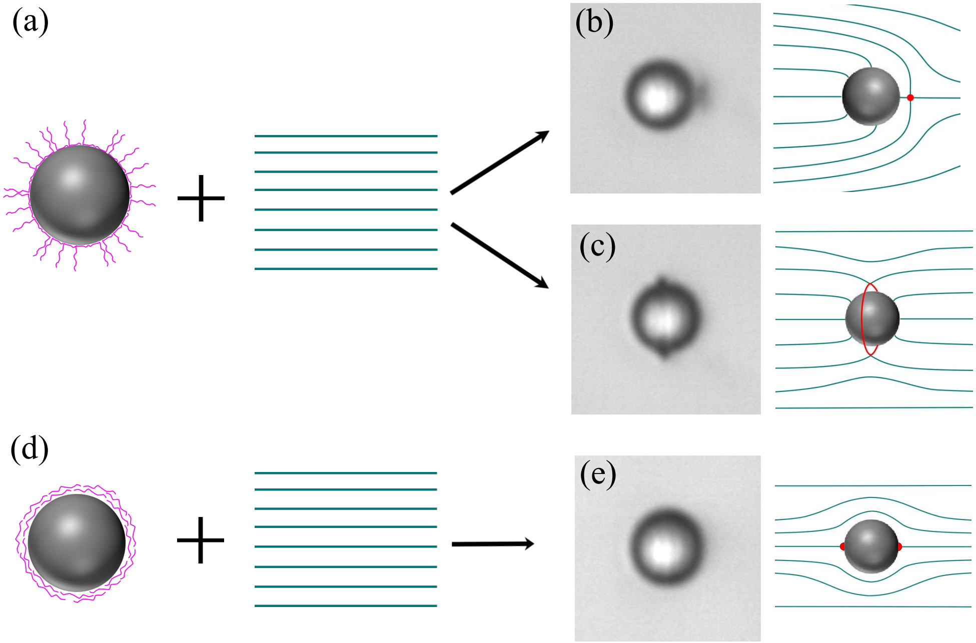

Figure 1.15: (a) A spherical microparticle with a strong homeotropic surface anchoring dispersed into a uniformly aligned nematic liquid crystal exhibits two possible director configurations: (b) the dipolar, where the particle induces a hyperbolic hedgehog of strength -1 and (c) a quadrupolar defect where the particle is encircled by a -1/2 disclination ring. (d) A spherical particle with planr anchoring dispersed in a uniformly aligned liquid crystal. (e) Particle induces a pair of antipodal surface defects.

other without any discontinuous deformation. When the surface of particles provide planar anchoring to the surrounding LC molecules in a homogeneously aligned nematic cell (Fig.1.15(d)), the elastic distortion nucleates a pair of antipodal surface defects of strength $-1/2$ on the equator of the particle (Fig.1.15(e)). The particle-defect pair is known as boojum-particle [40]. The corresponding director pattern is shown in Fig.1.15(e).

Due to the pronounced nonlinearity of nematic elasticity near the particle's surface, director profiles can not be found analytically. Considering the far-field behavior of the nematic, where director gradients are small, Euler-Lagrange's equation can be linearized. Using Frank's one elastic constant approximation, the elastic free energy of the LC colloidal system is given by [27]

$$U_{el} = \frac{K}{2}\int d^3r(\nabla.n)^2 \tag{1.30}$$

where n is unit nematic director, chosen along x-axis to give the lowest order $n \approx n(1, n_y, n_z)$. The minimisation of free electric energy reduces to Laplace equation for n as

$$\nabla^2 n^i = 0, i = y, z \tag{1.31}$$

At a large distance r, the solution of Eq.(1.31) is given by a multipole expansion in n^i as [27]

$$n^i = \frac{A^i}{r} + \frac{P^i_j r_j}{r^3} + \frac{Q^i_{jk} r_j r_k}{r^5} + ... \tag{1.32}$$

where A is the elastic monopole moment of the particle-defect combination. Summation over j and $k = x, y, z$ is implied. The director field around the spherical particle should be invariant with respect to rotations about the far-field director, which sets the monopole coefficient $A = 0$. P and Q are dipole and quadruple moments, respectively. Using dimensional analysis, $P \propto a^2$ and $Q \propto a^3$, where a is the radius of the particle. Finally, for $n \approx n(1, n_y, n_z)$, the director component in terms of multipoles can be written as [27]

$$n^i = P\frac{r^i}{r^3} + 2Q\frac{xr^i}{r^5}, \quad i = y, z \tag{1.33}$$

The far-field solutions of director field around a particle are found to resemble with the solution for electric field far from a conducting sphere of radius a_c with a reduced charge p. Electric field at a distance r along the symmetric axis along x is given by [27]

$$\vec{E} = \hat{e}_x + pa_c^2 \frac{\vec{r}}{r^3} - a_c^3 \frac{r^2 \hat{e}_x - 3x\vec{r}}{r^5} \tag{1.34}$$

where e_x is unit vector along coordinate axis x. The electrostatic analog assigns the dipole moment pa_c^2 and the quadrupole moment $\frac{3}{2}a_c^3$ to the particle. The charge p is considered as the variational parameter of the director field which determines the distance form the point defect to the center of the particle as $1.17a$. If $P > 0$, the far field Eq.(1.33) resembles with the dipolar term of Eq.(1.34) and the director configuration is of dipolar type with the defect on the right side of the particle (Fig.1.15(b)). Hence, the particle with the pair of virtual $(+1)$ and induced (-1) defects is called an elastic dipole as the director field lines are reminiscent of that of an electric dipole. Saturn-ring and surface defect configurations possess symmetry about an axis perpendicular to the director. Therefore, the dipole term vanishes ($P = 0$), and the far field Eq.(1.33) resembles quadruplar term of Eq.(1.34) which belong to a quadrupolar configuration. Hence, the particles nucleating Saturn ring and surface defects are called elastic quadrupoles as the transverse component of director field lines around it are reminiscent of that of an electric quadrupole. The particles can also induce many complex defect structures if they possess hybrid surface anchoring condition. For example, conically degenerate boundary condition on the particle's surface gives rise to elastic hexadecapolar distortion [41]. Complex size and shape of the particles could also induce complicated and higher order elastic distortions and defetcs [43–45, 49].

1.6.2.2 Shape asymmetric particles in LCs

In contrast to spherically symmetric particles, shape asymmetric particles create complex elastic distortion and defects in LCs which plays a key role in complex colloidal assembly. There are many studies on nonspherical particles in LCs as shown in Fig.1.16(a-h). Some examples are: rod-shaped [43, 46], star-shaped [44], rectangular [47, 48], ring [51], square [49], cube [50], bullet [52], doughnut-shaped [51] and snowman-shaped particles. Such particles are useful in designing heterostructures.

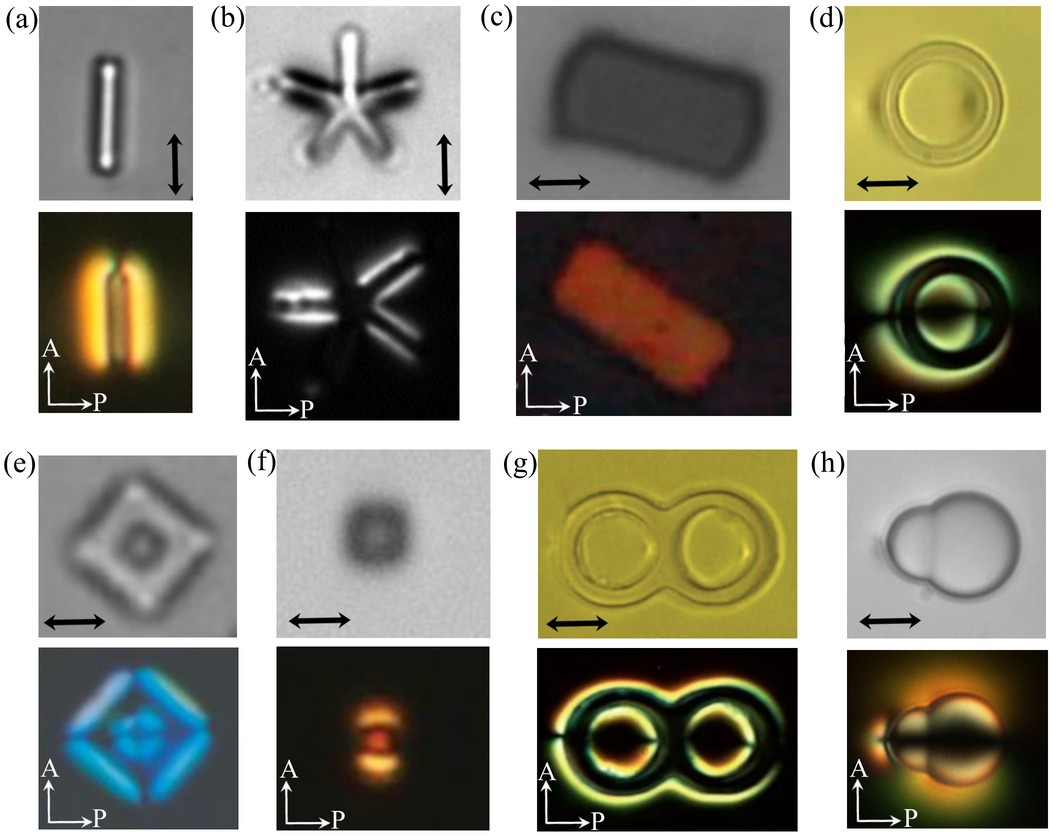

Figure 1.16: Bright and polarizing optical micrograph of (a) rod-shaped, (b) star-shaped, (c) rectangular-shaped, (d) ring-shaped, (e) square-shaped, (f) cube-shaped, (g) doughnut-shaped, (h) Snowman-shaped particles in LCs. Double headed arrows indicate the director.

1.6.3 Elastic levitation of microparticles in LCs

If the density of dispersed particles (ρ_p) is higher than that of surrounding fluid medium (ρ_m), i.e $\Delta\rho = \rho_p - \rho_m > 0$, the gravity causes sedimentation of particles and the particles tend to accumulate near the bottom plate. Sedimentation of such particle is usually countered by thermal (Brownian) motion as the thermal noise can raise a sphere of radius r up to a height of $z_s = 3k_BT/4\pi r^3 g\Delta\rho$ from the bottom plate, where $g = 9.8$ ms^{-2} is the acceleration due to gravity. For typical glass or silica particles, $\Delta\rho \sim 10^{-2}$ Kgm^{-3} and thus, z_s =1 μm [53].

In case of liquid crystal as a host, sedimentation of particles is mainly opposed by the elastic repulsion from the bounding walls as the contribution from the thermal noise is negligible. Consider a homeotropically anchored sphere of radius $r = 1$ μm inducing a point defect in a uniformly aligned planar cell of height (cell gap) h with bottom plate at $z = 0$ (Fig.1.17(a)). Clearly, the mismatch in the anchoring condition between the particle's surface and the substrate creates elastic repulsion which prevent sedimentation. In the dipole approximation, the elastic potential of repulsion can be written as [54]

$$F_{repulsion} \approx A^2 \pi K \frac{r^4}{z^3} \tag{1.35}$$

where the dimensionless coefficient A depends on anchoring strength, anisotropy in elasticity, etc. The competition between the gravity and the elastic repulsion levitate the particles upto a certain height which is given by [54]

$$z_{elastic} = \left(\frac{3}{2}A\right)^{1/2} \left(\frac{Kr}{\Delta\rho g}\right)^{1/4} \tag{1.36}$$

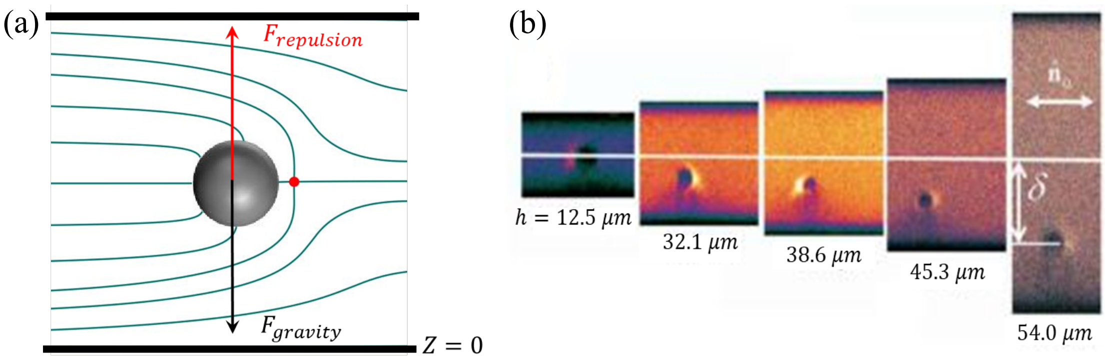

Figure 1.17: (a) Schematic presentation of competing effect between elastic and gravitational force in NLCs. (b) Fluorescence Confocal Polarizing Microscopy (FCPM) images of cross sections of a particle nucleating point defect levitated in planar cells of different thickness (h). The shift δ from the center of the cell increases with cell thickness (adapted from ref. [54]).

For $A = 1$, $K = 10pN$, $\Delta\rho \sim 10^{-2}$ Kgm^{-3}, $z_{elastic} = 10$ μm, which is higher than the sedimentation distance z_s in isotropic fluids by one order of magnitude. This was confirmed in experiments which was carried for a dipolar particle dispersed in different cell thickness and observing the shift $\delta = h/2 - z_{elastic}$ from the middle of the cell through fluorescence confocal polarizing microscopy as shown in Fig.1.17(b).

1.6.4 Brownian motion of particles in LCs

The random displacement of particles in a fluid caused by thermal fluctuations is known as Brownian motion. The average displacement of particles is zero, but the average mean square displacement (MSD) varies linearly with time, $\langle \Delta r^2(\tau) \rangle = 6D\tau$, where D is the translational diffusion coefficient of the particles. Using Stoke-Einstein relation for a sphere of radius a in a fluid of viscosity η, D can be expressed as $D = k_B T / 6\pi\eta a$.

In case of complex fluids, Brownian motion can become anomalous allowing MSD to follow power law as $\langle \Delta r^2(\tau) \rangle \propto \tau^{\alpha}$. $\alpha > 1$ corresponds to superdiffusive behavior while subdiffusive motion is characterized by $\alpha < 1$. Especially, in case of LCs, dispersed particles possess both anomalous as well as anisotropic diffusive behavior. At relatively large time scales, particles experience anisotrpic diffusion as a consequence of viscous anisotropy with diffusion coefficients $D_{\parallel}$ and $D_{\perp}$ along and normal to the director, respectively (Fig.1.18(b)). The corresponding Stoke-Einstein relation can be written as [55]

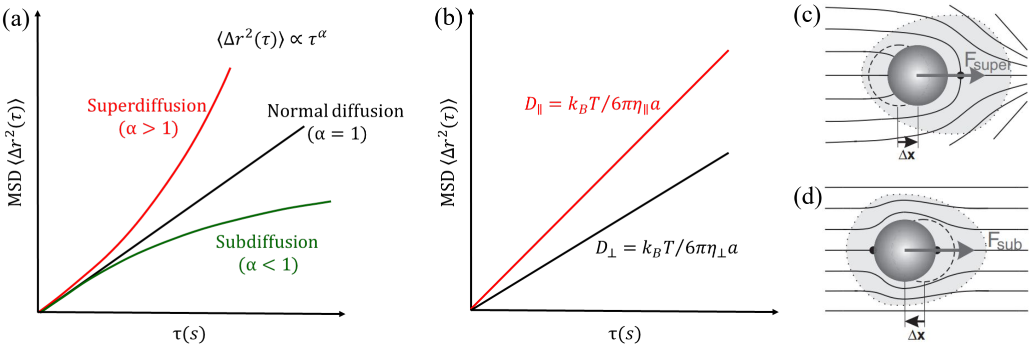

Figure 1.18: (a) MSD ($\langle \Delta r^2 \rangle$) versus τ for normal and anomalous Brownian behaavior. (b) Typical anisotopic diffusion of particles in LCs. (c) Elastic forces pushes the particle towards the splay gaining superdiffusive behavior. (d) Restoring elastic force opposite to particle displacement leads to subdiffusive behavior (adapted from ref. [55]).

$$D_{\parallel,\perp} = k_B T / 6\pi\eta_{\parallel,\perp} a \tag{1.37}$$

where $\eta_{\parallel}$ and $\eta_{\perp}$ are the viscosities parallel and perpendicular to the director, respectively. On the other hand, at time scales equal to the relaxation time of the director

(0-20 s), molecular orientation, director fluctuations and type of anchoring play crucial role in determining the diffusive behavior. Particles with planar anchoring show subdiffusive behavior whereas particles with homeotropic anchoring feature a superdiffusive character which can be explained by the interplay between the fore-aft elastic forces acting on the particle's displacement [55]. In case of planar anchoring (subdiffusive regime), fluctuations in displacement increases elastic energy in the direction of displacement which generates a restoring elastic force that slows down the diffusive motion (Fig.1.18(d)). Opposite effect is observed in case of superdiffusive regime, where particles experience elastic force in the direction of displacement towards the distorted region (Fig.1.18(c)).

1.7 Interaction and assembly of LC colloids

Unlike the short-ranged colloidal interactions in isotropic solvent, the nematic LC colloids experience a long-range elastic interaction which enables them to form an efficient assembly. The interactions among LC colloids are mediated by minimizing the local structural or elastic forces acting between them through sharing the induced topological defects. The orientational order of nematic medium further offers an additional feature of anisotropy in the interaction which guides the directional assembly of particles. As long as the particles are isolated form each other, they display Brownian motion as a random displacement controlled by kinetic energy dissipation. In LCs, Brownian motion becomes anisotropic and the corresponding anisotropic drag coefficient is given by [18]

$$\zeta_{\parallel,\perp} = k_B T / D_{\parallel,\perp} \tag{1.38}$$

Here we present a semi-classical approach to understand the interaction between a pair of colloids. Each particle associated with topological defect possesses it's own region of elastic distortion around it. When two such particles come closer, the distortion region starts overlapping and the system try to minimize the local elastic energy either by attracting or repelling the colloids. When two particles approach towards each other, they experience two forces, namely elastic ($\vec{F}_{el}$) and drag ($\vec{F}_d$) forces while the inertial forces are negligible. The drag force is given by $\vec{F}_d = -\zeta \frac{d\vec{R}(t)}{dt}$, where ζ is the drag coefficient and $R(t)$ represents the time dependent separation between two colloids. As both the forces act opposite to each other, the equation of motion is given by

$$\vec{F}_{el} + \vec{F}_d = 0 \tag{1.39}$$

or

$$\vec{F}_{el} + \zeta \frac{d\vec{R}(t)}{dt} = 0 \tag{1.40}$$

If the particles are elastic dipoles, the force acting between them is given by $F_{el} = -k/R^4$, where k is a constant. Therefore Eq.(1.40) becomes

$$-k/R^4 = \zeta \frac{dR(t)}{dt} \tag{1.41}$$

On solving $R(t)$ we get

$$R(t) = (R_0^5 - 5\alpha t)^{(1/5)} \tag{1.42}$$

where $\alpha = k/\zeta$ and R_0 is the initial separation between two particles at time $t = 0$. Similarly, if the two interacting colloids are elastic quadrupoles, then the elastic force would be $F_{el} = -k/R^6$ and the corresponding $R(t)$ can be written as

$$R(t) = (R_0^7 - 7\alpha t)^{(1/7)} \tag{1.43}$$

As an example, the time dependent separation between two interacting elastic dipolar and quadrupolar particles are shown in Fig.1.19(a) and Fig.1.19(b), respectively. The experimental data is well fitted to Eq.(1.42) and Eq.(1.43).

The interparticle potentials can be analytically calculated using the multipole expansion approach. It is assumed that particles are far away from each other for the director around the particles to retain the dipolar or quadrupolar multipole structure. Thus, particles interact due to the over-lapping region of elastic deformations and the change in elastic energy drives the interaction. As discussed in ref [27], the long-range elastic pair interaction between two elastic dipoles is

$$U_{d-d} = C_1 \frac{P}{R^3} \left(1 - 3\cos^3\theta\right) \tag{1.44}$$

where C_1 is proportionality constant, R is the distance between the centres of mass of interacting particles and θ is the angle between the line connecting centres of the

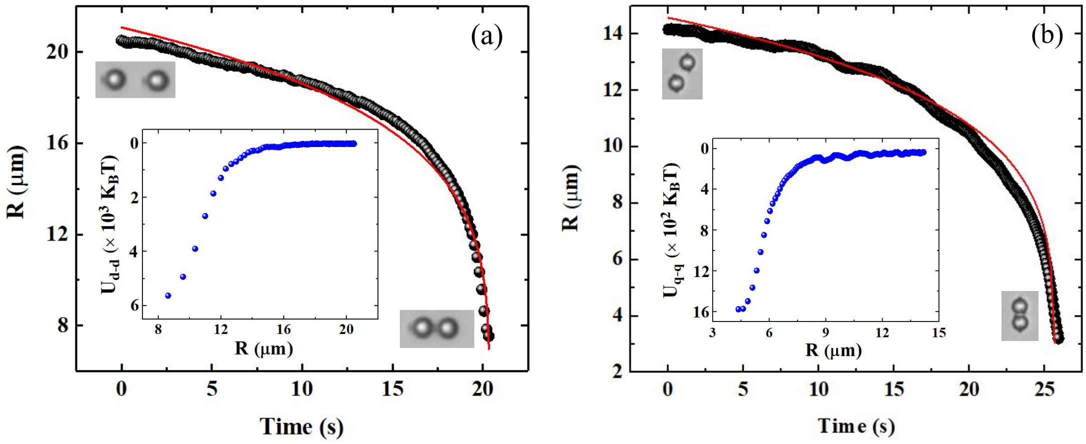

Figure 1.19: (a) Equilibrium separation with time between two elastic dipolar particles. Red line is the best fit to the equation, $R(t) = (R_0^5 - 5\alpha t)^{(1/5)}$ with $\alpha = 2.8 \times 10^4$ μm^5 s^{-1}. (b) Equilibrium separation with time between two elastic quadrupolar particles. Red line is the best fit to the equation, $R(t) = (R_0^7 - 7\alpha t)^{(1/7)}$ with $\alpha = 1.2 \times 10^4$ μm^7 s^{-1}. Inset shows the corresponding interaction energies.

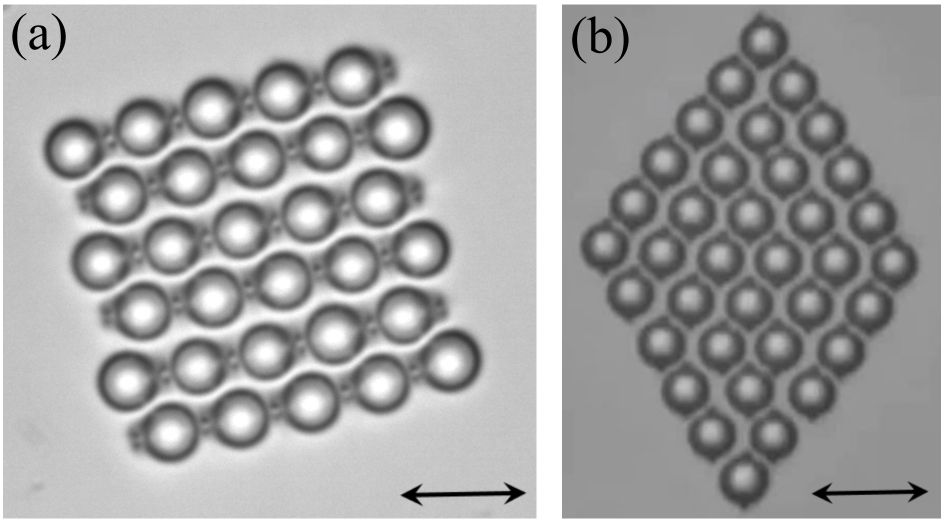

Figure 1.20: Laser assisted 2D assembly of (a) dipolar and (b) quadrupolar particles. Double headed arrows denote the director.

particles and the far field director. Similarly, the interacting potential between two elastic quadrupoles is derived as [28]

$$U_{q-q} = C_2 \frac{Q}{R^5} \left(9 - 90\cos^2\theta + 105\cos^4\theta\right) \tag{1.45}$$

where C_2 is a proportionally constant. For example, the interacting potential between two dipolar and quadrupolar particles are shown in the inset of Fig.1.19(a) and (b), respectively. The value of potential energy is of the order of few thousands of k_BT. Since the interaction is defect mediated, the value of potential depends on the type of defects induced on the particles. For example, the interaction energy between two dipolar particles is higher than that between two quadrupolar particles. This potential energy makes the colloidal pairs in LCs more stable than it's isotropic counterpart. With the help of laser tweezers, these particles can also be assembled to regular crystalline structures. For example, 2D-crystals made out of dipolar and quadrupolar particles are shown in Fig.1.20(a) and (b), respectively.

1.8 Active particles

The term 'active' represents self-propelled systems which are able to extract energy from the surrounding medium and convert to mechanical energy for steady motion. At large scale, active natural agents like human crowd, flock of birds, swarm of fishes show collective behavior as a result of interaction with neighborhood. At small length scales, of the order of micrometer, living organisms like bacteria, algae show self-propulsion. Propulsion of such organism broadly can be classified in two types; (i) pusher type, where the surrounding fluid is pushed away by the swimmer and (ii) puller type, where the fluid is pulled towards the swimmer with respect to the direction of motion. For example, E.coli bacteria is a pusher [29, 30] whereas chlamydomonas algae is a puller type microswimmer [31, 32] as shown in Fig.1.21.

In order to establish efficient and controlled propulsion at microscale, artificial microswimmers have been developed in the laboratories. These microswimmers are passive until unless they are powered by either internal or external forces. Internal phoretic-based propulsion involves interaction of particles with a gradient field like chemical concentration or temperature gradient in the medium. These are known as diffusiophoresis or thermophoresis, respectively.

For example, silica or polystyrene spherical particles with one hemisphere coated with Pd or Pt starts propelling in a solution of hydrogen peroxide due to the con-

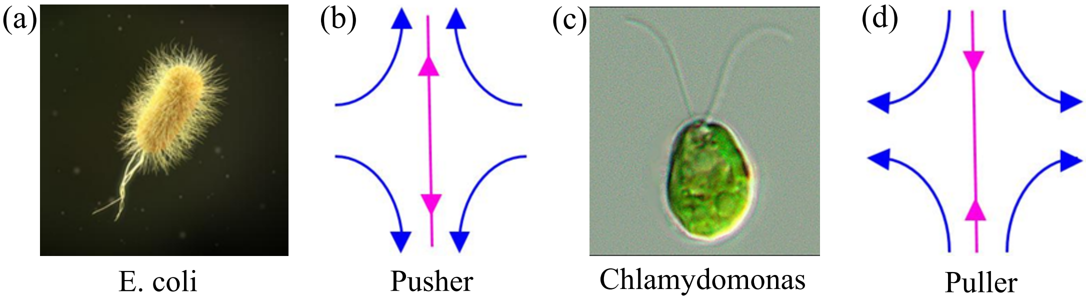

Figure 1.21: Bright-field image of (a) Escherichia coli bacteria and (c) Chlamydomonas algae. (b) Pusher and (d) puller type flow patterns with respect to the direction of motion.

centration gradient created by the decopmposition of H_2O_2 into water and oxygen by the metal catalyst as shown in Fig.1.22(a) [33]. Similarly, a hemispherical metal (Au) coating on silica particles can create an asymmetric temperature profile around themselves by absorbing the radiation when exposed by defocused laser beam [34]. This leads to propulsion of such particles in a fixed direction as shown in Fig.1.22(b).

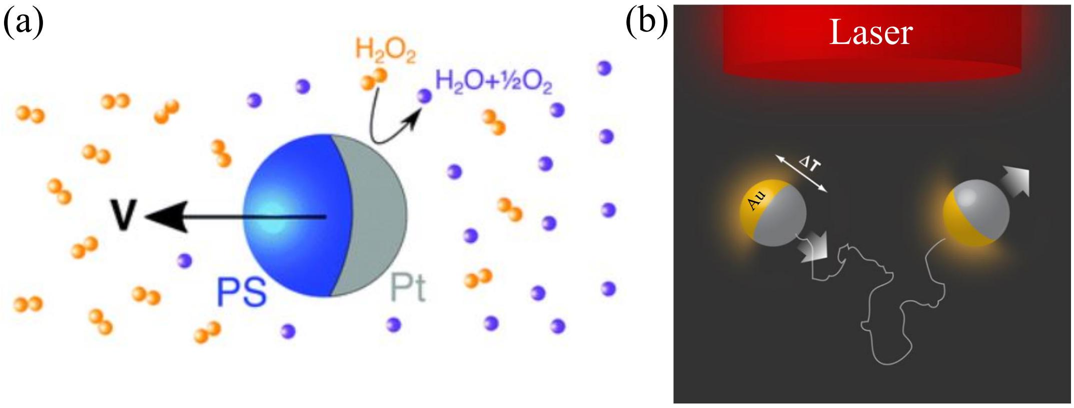

Figure 1.22: (a) Diffusiophoresis of hemispherical Pt coated polystyrene particles by decomposing hydrogen peroxide. Orange dimers present H_2O_2 molecules (adapted from ref. [33]). (b) Thermophoresis of Au coated Janus particles (adapted from ref. [34]).

On the other hand, external forces like magnetic or electric fields can be used to generate phoretic forces in order to make the functional particles motile. For example, silica with helical nanostructured tail can be navigated along a pre-defined direction

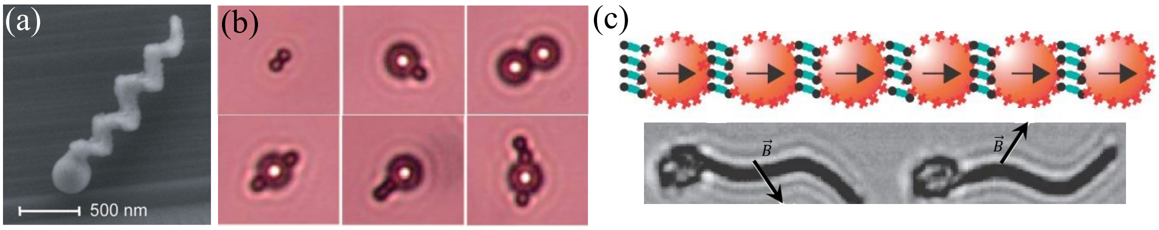

Figure 1.23: (a) SEM image of a silica screw wuth hielical tail structure. Adapted from ref. [35]. (b) Colloidal assemblies achieved by paramagnetic colloids. Adapted from ref. [36]. (c) streptavidin (red cross symbols) coated magnetic particles linked with Dna shoing beatin behaviour under magnetic field. Adapted from ref. [37].

by applying homogeneous magnetic field (Fig.1.23(a)) [35]. Paramagnetic colloids linked with biotin-terminated cDNA strand can stabilize doublets of different sizes. These doublet can rotate and achieve controlled propulsion under magnetic field and form different assemblies (Fig.1.23(b)) [36]. Similarly magnetic particles coated with streptavidin and linked by double stranded DNA with biotin at each end show beating pattern when subjected to magnetic field (Fig.1.23(c)) [37]. While propulsion due to electric field, a phenomena known as electrophoresis is discussed in more details in the following sections.

While considering the swimming mechanism at micrometer length scale, two parameters namely Reynolds (R_e) and Ericksen (E_r) number becomes important. $R_e = \rho v L/\mu$ presents the ratio of the inertial to viscous forces where as $E_r = \mu v L/K$ is a dimensionless number that describes the ratio of elastic to viscous forces, where ρ is the density, v is swimming velocity, L is characteristic length, μ is the dynamic viscosity of the fluid and K is elastic constant. In the regime of small R_e, viscous force dominates and effect due to inertia is negligible.

1.9 Electrophoresis and Electroosmosis

Electrophoresis is the motion of charged particles in an electrolyte under the application of an external uniform electric field. Historically, fundamental research and industrial applications mainly aim at electrophoresis as the most efficient approach for transporting particles in isotropic solvents like water [56–58]. The separation of charges which eventually forms the space charge over the particles is essential for particle propulsion. The force experienced by the space charge leads to ion flows around the particles known as electroosmosis, and consequently the particles propel. The linear and non-linear nature of electrophoresis depends on several factors which are discussed below in both isotropic (water) and in anisotropic (LC) solvents.

1.9.1 Electrophoresis in isotropic electrolytes

In case of aqueous electrolytes, the applied external electric field creates separation of charges over the charged particles and forms an electric double layer (EDL) of thickness, so called Debye screening length $\lambda_D = \frac{1}{e}(\epsilon\epsilon_0 k_B T / \sum_i c_i z_i^2)$ around the particles, where e is the electron charge, ϵ is the dielectric constant of the electrolyte, z_i and c_i are the valency and concentration of ions in the electrolyte. Even though, the electrolyte near the electrodes or the particle itself remains neutral, the spatial separation of charges is sufficient enough to induce electrokinetics. The applied electric field ex-

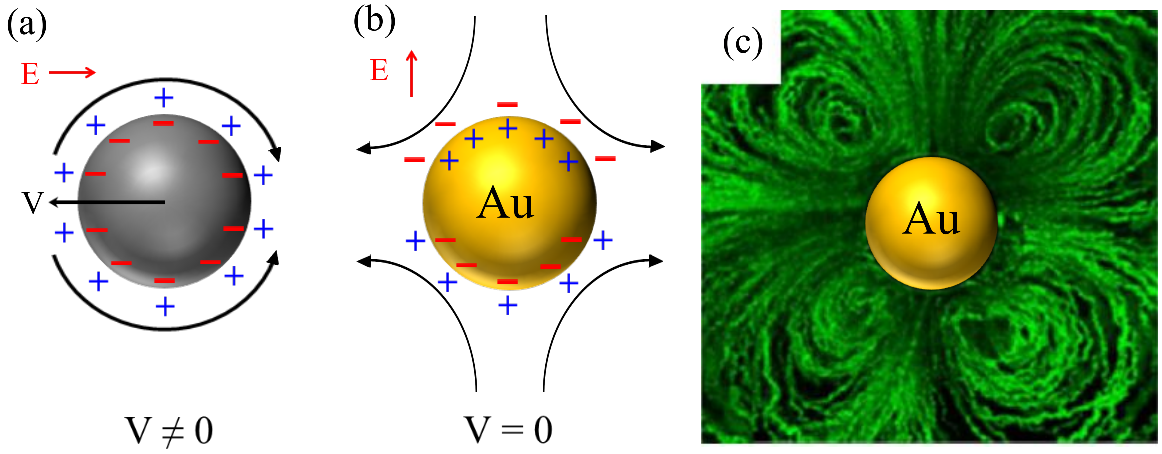

Figure 1.24: (a) Linear electrophoresis of a charged dielectric particle in the isotropic electrolytes. Curved arrows indicate the electro-osmotic flows around the particle. (b) Induction of an electric double layer over a polarizable (metallic) particle and generation of a flow pattern having symmetry with respect to both horizontal and vertical planes, resulting no propulsion. (c) Symmetric quadrupolar ICEO flow pattern around a metallic (Au) particle (adapted from ref. [66]).

erts a torque on the EDL, resulting in acceleration of the counter ions relative to the charge on the electrode. As a result, the ion slips on the particle's surface with a slip velocity (Fig.1.24(a)), subsequently the electrophoretic velocity of the particles is given by Helmholtz–Smoluchowski formula [59]

$$v = \mu E = \frac{\epsilon\epsilon_0\zeta}{\eta} E \tag{1.46}$$

where $\mu = \epsilon\epsilon_0\zeta/\eta$ is the mobility of ions in the electrolyte and ζ is the zeta (surface) potential of the particles. This suggests that the particle velocity depends only on it's zeta potential and not on it's size or other properties. It was further shown that when the electric double layer is negligible (low Dukhin number regime, $Du = \sigma_p/\sigma_m r <<$ 1, r is particle's radius, σ_p and σ_m are conductivity of the particle and electrolyte, respectively), the velocity does not depend even on the shape of the particles and is completely predetermined by ζ [60]. For $Du >> 1$, the electrophoretic velocity becomes nonlinear function of particle's size and electric field, and is given by

$$v = \epsilon\epsilon_0\zeta \left(E + \beta(r)E^n\right)/\eta \tag{1.47}$$

where index n depends on the Peclet number ($P_e = rv/d$, D is diffusion coefficient of ions and v is particle velocity relative to fluid) [60]. Both the linear and non-linear relationship between the velocity and electric field implies that the flow of particles and fluid are only possible under the application of DC electric field. A symmetric AC electric filed with zero time average would give rise to no propulsion. DC driving does not produce steady flow longer than the time for screening of the electric field and invites undesirable electrochemical reactions at the electrodes. Due to these limitations, there is a growing interest towards the nonlinear phenomena, especially where electrokinetics flows are quadratic to the field, which can be achieved by AC electric field.

In case of nonlinear electrokinetics, separation of charges is induced by the applied electric field where charges of opposite polarity accumulate in different regions to form the 'space charge' [61]. In the first approximation, the space charge density is proportional to the field strength E, i.e $\rho \propto E$. Therefore, the force determined by the product of the charge and field strength, acting on the charge cloud is proportional to E^2, i.e $F \sim \rho E \sim E^2$ [61–64]. It implies that the polarity of driving force does not change by the reversal of field polarity. This is known as induced charge electrophoresis (ICEP). Hence AC driving produces persistent flow of steady directionality. Since in the first approximation, the viscous resistance is independent of the applied electric field, the velocities of electrokinetic flows should be proportional to E^2. For example, let us consider a metallic spherical particle in an isotropic electrolyte under the application of a uniform field. The field polarizes the particle and induces a electric double layer by driving the ions through the electrolyte. The double layer expels the field lines and drives the induced charges. This generates an electroosmotic flow around the particle. The flows have fore-aft symmetry due as the homogeneity of the particle and consequently, there is no propulsion as schematically illustrated in Fig.1.24(b). The ICEO flow pattern obtained by illuminating Q-dots as tracers around such particles is symmetric as shown in Fig.1.24(c). Propulsion is possible when the particle becomes asymmetric either by its physical or chemical or surface functionalization.

For example, in case of metal-dielectric Janus particles, the fore-aft symmetry of the surrounding flow is broken as the density of induced charge and the electro-osmotic flows are stronger on the metallic side than on the dielectric side as shown in Fig.1.25(a) [65]. This induced-charge electrophoresis was first experimentally reported by Velev et al. [65]. Using the standard low-voltage model for thin double layers, Squires and Bazant predicted that a metallic sphere with a hemispherical dielectric coating will

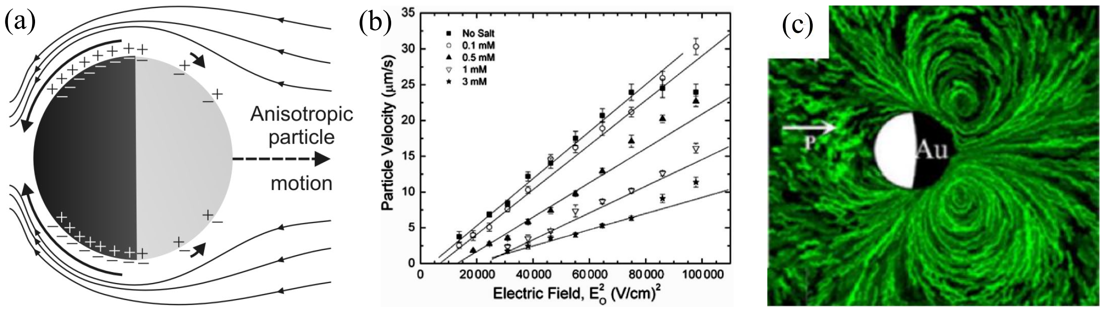

Figure 1.25: (a) Symmetry breaking of charge cloud around a Metal-dielectric Janus particle resulting propulsion facing the dielectric hemisphere. (b) Quadratic field dependence of velocity of Janus particles at different ion concentration in the electrolyte, adapted from ref. [65]. (c) Asymmetric quadrupolar ICEO flow pattern around a immobile Janus particle, adapted from ref. [66].

move due to ICEP in the direction of its dielectric end at a velocity [65]

$$v_{ICEP} = \frac{9}{64}\frac{\epsilon a E^2}{\eta(1+\delta)} \tag{1.48}$$

where ϵ is the permittivity and η the viscosity of the bulk electrolyte, a is the radius of the particle, E is the field amplitude, and δ is the ratio of the differential capacitance of the compact and diffuse layers. For highly polarizable particles, the induced space charge density is proportional to the applied field strength, thus the ICEP velocities vary quadratically with the field (Fig.1.25(b)). The asymmetric ICEO flow pattern around Janus particle can be seen in Fig.1.25(c).

The electrophoretic velocity is also frequency dependent and there exist two important characteristic time scales; (i) particle charging time $\tau_p = \epsilon\lambda_D^2/\epsilon_p D$ for a dielelctric sphere or $\tau_p = \lambda_D a/D$ for a conductive sphere and (ii) electrode charging time $\tau_e = \lambda_D L/2D$. For $\lambda_D << a << L$, the bulk AC field is controlled by τ_e and given by [67]

$$E_0(t) = \frac{V_0}{L} cos(\omega t) Re\left[\frac{i\omega\tau_e}{1+i\omega\tau_e}e^{-i\omega t}\right] \tag{1.49}$$

The time-dependent polarization of the sphere is proportional to Re$\left(\frac{e^{i\omega t}}{1+\omega\tau_p}\right)$. The resulting frequency dependence of the velocity is given by [67]

$$v(\omega) = v_0\frac{1+\omega^2\tau_e^2}{(1+\omega^2\tau_e^2)(1+\omega^2\tau_p^2)} \tag{1.50}$$

with a single peak at the characteristic charging frequency $\omega_c = \tau_p^{-1}$ of electric double layer. v increases as ω^2 when ω is low. At higher frequency, velocity decreases as ions can not follow the rapidly changing field. The reciprocal of these time scales, τ_p^{-1} and τ_e^{-1} stand for the higher and lower cut off frequency of the electrophoresis.

1.9.2 Electrophoresis in LCs

Electrophoresis in isotropic solvents requires certain conditions i.e either the particles must be charged or highly polarizable, where the solvents play a supportive role by supplying counter ions. When LC replaces the isotropic electrolyte, the anisotropy of LCs bring new mechanism for separation of charges and the consequent electrophoresis and electroosmosis is called liquid crystal-enabled electrokinetics (LCEK) [67, 69]. This phenomenon is rooted in anisotropy of physical properties, director distribution and resulting topological defects and lifts many impositions on the properties of the particles as discussed below [54, 70, 71].

1.9.2.1 Liquid crystal-enabled electroosmosis (LCEO)

Electrically powered transport of particles in an anisotropic fluid, especially in liquid crystal is rich in dynamics than it's isotropic counterparts. Replacement with LCs as an electrolyte brings anisotropy in dielectric permittivity and conductivity of the host medium which plays crucial role in transporting particles. The dielectric anisotropy causes the director realignment, especially in the distorted region while conductivity anisotropy give rise to anisotropy in ionic mobility around the particles. This phenomena is primarily caused by the asymmetric director distribution around the particles and known as liquid crystal-enabled electrophoresis (LCEEP). So, particles inducing symmetric director structure (Saturn ring and boojum defects) do not propel due to LCEEP. The electrophoretic velocity could be both linear and non-linear with electric field depending on the charge, size and strength of the applied field, thus allowing a high degree of freedom for moving the particles in LCs.

Let us consider a spherical particle with normal anchoring disperse in a uniformly aligned LCs ($\Delta\epsilon \sim 0$) placed between two planr anchored electrodes. Suppose the particle induce a disclination ring (Saturn ring) defect due to the confinement of the cell. The electric field is applied along the far field director $\hat{n} = (1, 0, 0)$, i.e $E = (E_x, 0, 0)$ (Fig.1.26). The applied field does not perturb the far field director as the dielectric anisotropy is zero. LCs have some free ions and they have higher mobility along the director as the conductivity anisotropy, $\Delta\sigma > 0$. For the shown polarity $E_x > 0$ in Fig.1.26(a), negative ions accumulate on the right side of the sphere and positive ions deposit on the left side. The charge density induced by the electric field in a distorted LC can be calculated under the approximation of weak anisotropies of conductivity and permittivity ($\Delta\epsilon << \overline{\epsilon}$, where $\overline{\epsilon} = (\epsilon_{\parallel} + \epsilon_{\perp})/2, \Delta\sigma << \overline{\sigma}$, where $\overline{\sigma} = (\sigma_{\parallel} + \sigma_{\perp})/2$) and weak director gradients as: [69]

$$\rho(x, y) = \epsilon_0 \overline{\epsilon} \left(\frac{\Delta\epsilon}{\overline{\epsilon}} - \frac{\Delta\sigma}{\overline{\sigma}} \right) \frac{\partial \phi}{\partial y} E_x \tag{1.51}$$

The charge density is directly dependent on properties of LCs, namely (i) the director gradients $\frac{\partial \phi}{\partial y}$, where ϕ is the angle between the unperturbed $\hat{n_0}$ and the far field director $\hat{n}$ (Fig.1.26(a)) and (ii) anisotropies $\Delta\epsilon, \Delta\sigma$ and the field strength. The electric field drives the separated charges by imposing a Coulomb force of density $f \propto \rho E_x$, which yields an electroosmotic flow of the nematic around the sphere (Fig.1.26(a)). Reversing the field polarity alters the sign of the induced charge $\rho \propto E_x$, but the product $f \propto \rho E_x \propto E_x^2$ remains insensitive to the field polarity. It implies that the flows and forces are also independent of polarity. The polarities of space charge is dependent on the type of anchoring on the particle's surface. For example, tangentially anchored particle acquires positive and negative ions on the right and left side of the particle, respectively (Fig.1.26(b)) which is exactly opposite to the case of homeotropically anchored particles. This depicts the sensitiveness of induced space charge to the sign of director gradient $\frac{\partial\phi}{\partial y}$. The electro-osmotic flow is of "puller" type around the homeotropically anchored particle and of "pusher" type around the planar anchored

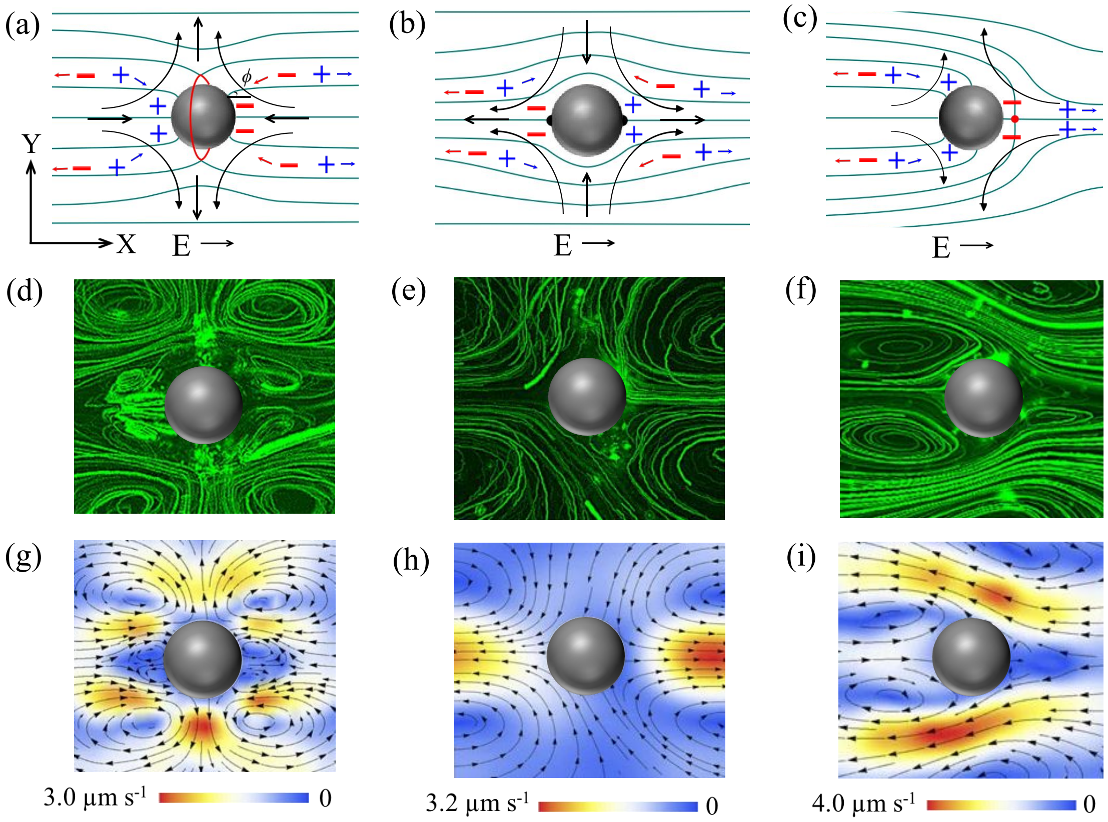

Figure 1.26: Schematic diagram showing charge separation across the particles with (a) Saturn-ring, (b) boojum and (c) hyperbolic point defect in a NLC. (d-f) LCEO flows around the respective particles. (g-i) Velocity field mapping of LCEO flows around the particles (adapted from ref. [69]).

particle as shown in Fig.1.26(a) and (b), respectively. These particles show no propulsion as the flows have fore-aft symmetry in both the cases which can be clearly seen from the fomation of four vertices in the streamline flow pattern around the particles (1.26(d,e,g,h)). But the fore-aft symmetry of the flow is broken when the normally anchored particle induce a point defect and possesses dipolar director structure (1.26(c). If the dipolar particle is made immobile, the induced electro-osmotic flow pump the LCs from right to left of it as shown in Fig.1.26(f,i). If the particle is free, it moves with a electrophoretic velocity proportional to E_x^2. The amplitude of electro-osmotic flow around the particle or equivalently the electrophoretic velocity of the free dipolar particle can be obtained by balancing the driving Coulomb force $f \propto \rho E_x$ and viscous resistance $\eta v/a^2$ and given by [69]

$$v = \frac{\alpha \epsilon_0 \bar{\epsilon} a}{\eta} \mid \frac{\Delta\epsilon}{\bar{\epsilon}} - \frac{\Delta\sigma}{\bar{\sigma}} \mid E^2 \tag{1.52}$$

where $\alpha \sim 1$ is a dimensionless quantity introduced to account for the director gradients.

1.9.3 Electrophoresis of charged particles in NLCs

Let's consider a positively charged particle with homeotropic surface anchoring dispersed in a uniformly aligned liquid crystal having positive dielectric anisotropy with the director along x-axis, i.e $\hat{n} \sim n(1,0,0)$ (Fig.1.27(a)). As $\Delta\epsilon > 0$, electric field is applied along the director $\hat{n}$, i.e $E = (E_x, 0, 0)$ so that it does not influence the far field director. In the isotropic phase, the charged particle shows a classical linear electrophoresis similar to the discussed above with a linear mobility coefficient. Once the medium is cooled down to the nematic phase, the particle induce radial director configuration in it's vicinity and nucleate a point defect (hyperbolic hedgehog). The particle-defect represents an elastic dipole, $p \sim (p_x, 0, 0)$ as already discussed. Due to mismatch in anchoring conditions between the electrodes and the particle surface, the particles levitate in the bulk, resisting sedimentation.

Under DC field, the particle has two velocity along the same direction i.e along the director; (i) $v \propto E$ due to it's charge and (ii) $v \propto E^2$ due to asymmetric director

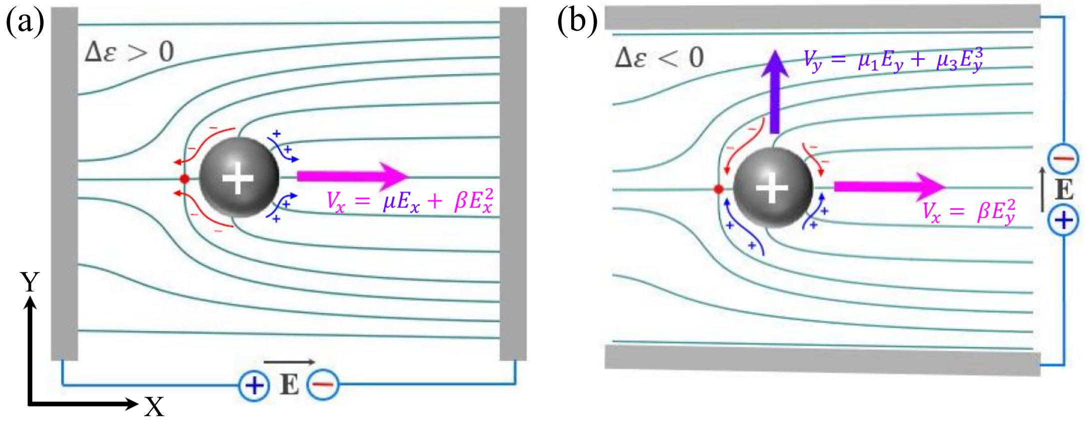

Figure 1.27: Schematic diagrams of two types of electrophoretic motion of a spherical charged particle nucleating dipolar director profile in a uniformly aligned nematic liquid crystal having (a) $\Delta\epsilon > 0$ and (b) $\Delta\epsilon < 0$.

profile around it (LCEEP). So, the electrophoretic velocity of the particle is given by

$$v_x = \mu E_x + \beta E_x^2 \tag{1.53}$$

where β is the field-dependent coefficient. The sign of β changes with the reversal of elastic dipole, p.

In case of LC with negative dielectric anisotropy, the field is applied perpendicular to the director,i.e $E = (0, E_y, 0)$ as shown schematically in Fig.1.27(b). Here, the particle possesses two velocity components, one along the field due to classical electrophoresis and the other along the director due to LCEEP. The velocity component along the field shows a linear dependence on field, when field strength is weak. The direction of transport of particle changes as one reverses the field polarity. For stronger field, the cubic term becomes more apparent [68],

$$v_y = \mu_1 E_y + \mu_3 E_y^3 \tag{1.54}$$

where μ_3 is a mobility coefficient and is more effective for larger particles. The velocity component along the director (perpendicular to field) due to LCEEP as discussed previously is

$$v_x = \beta E_y^2 \tag{1.55}$$

In general, the electrophoretic velocity in the tensorial form can be written as

$$v_i = \mu_{1ij} E_j + \beta_{ijk} E_j E_k + \mu_{3ijkl} E_j E_k E_l \tag{1.56}$$

with linear (μ_{1ij}), quadratic (β_{ijk}) and cubic (μ_{3ijkl}) tensorial coefficients ($i, j = x, y, z$).

References

[1] P. G. de Gennes and J. Prost. *The physics of liquid crystals*. International series of monographs on physics, Clarendon Press, 1993.

[2] S. Chandrasekhar. *Liquid Crystals*. Cambridge University Press, 1992.

[3] D. Andrienko, *Introduction to liquid crystals*, Jour of Molecular Liquids, vol. 267, pp. 520-541, 2018.

[4] E. M. Therézio, S. F.C. da Silva, G. G. Dalkiranis, P. A. Filho, G. C.Santos, F. Ely, I. H. Bechtold and A. Marletta, *Light polarization states of a cholesteric liquid crystal probed with optical ellipsometry*, vol. 48, pp. 7-11, 2015.

[5] A. G.Cook, J. L. Wardell, N. J. Brooks, J. M. Seddon, A. Martínez-Felipe and C. T. Imrie, *Non-symmetric liquid crystal dimer containing a carbohydrate-based moiety*, vol. 360, pp. 78-83, 2012.

[6] P. Subhapriya, V. N. Vijayakumar, M. L. N. Madhu Mohan and P. S. Vijayanand, *Study and characterization of double hydrogen-bonded liquid crystals comprising p-n alkoxy benzoic acids with azelaic and dodecane dicarboxlic acids*, vol. 537, pp. 36-50, 2011.

[7] Shin-Tson Wu and Deng-Ke Yang, *Fundamentals of Liquid Crystals Devices*, John Wiley & Sons Ltd, Chichester, 2006.

[8] M. Kleman and O. D. Lavrentovich, *Soft Matter Physics: An Introduction*. Springer-Verlag Berlin, 2003.

[9] P. M. Chaikin and T. C. Lubensky, *Principles of Condensed Matter Physics*. Cambridge University Press, Cambridge, 2000.

[10] F. C. Frank. *I. liquid crystals. on the theory of liquid crystals.* Discussions of the Faraday Society, vol. 25, pp. 19–28, 1958.

[11] W. H. de Jeu. *Physical properties of liquid crystalline materials.* Liquid Crystal Monographs, Gordon and Breach, 1980.

[12] L. M. Blinov and V. G. Chigrinov. *Electrooptic effects in liquid crystals.* Springer-Verlag, New York, 1996.

[13] W. Maier and G. Meier. Z. *Naturforsch*, vol.16a, 1961.

[14] H. J. Deuling. *Deformation of nematic liquid crystals in an electric field.* Mol. Cryst. Liq. Cryst., vol. 19, pp. 123-131, 1972.

[15] H. Gruler and G. Meier. *Electric field-induced deformations in oriented liquid crystals of the nematic type.* Mol. Cryst. Liq. Cryst., vol. 16, pp. 299-310, 1972.

[16] Y. Garbovskiy. *Electrical properties of liquid crystal nano-colloids analysed from perspectives of the ionic purity of nano-dopants.* Liq. Cryst., vol. 43, no. 5, pp. 648-653, 2016.

[17] R. Basu, A. Garvey. *Effects of ferroelectric nanoparticles on ion transport in a liquid crystal.* Appl. Phys. Lett., vol. 105, no. 151905, 2014.

[18] P. Poulin, V. Cabuil and D. A. Weitz, *Direct measurement of colloidal forces in an anisotropic solvent.* Phys. Rev. Lett., vol. 79, pp. 4862-4865, 1997.

[19] M. Rahmaan and W. Lee. *Scientific duo of carbon nanotubes and nematic liquid crystals.* J. Phys. D: Appl. Phys., vol. 42, no. 063001, 2009.

[20] R. Basu and G.S. Iannacchione. *Orientational coupling enhancement in a carbon nanotube dispersed liquid crystal.* Phys. Rev. E., vol. 81, no. 051705, 2010.

[21] R. Basu and G.S. Iannacchione. *Evidence for directed self-assembly of quantum dots in a nematic liquid crystal.* Phys. Rev. E., vol. 80, no. 010701R, 2009.

[22] R. Manda, V. Dasari, P. Sathyanarayana, M. V. Rasna, P. Paik and S. Dhara. *Possible enhancement of physical properties of nematic liquid crystals by doping*

of conducting polymer nanofibres. Appl. Phys. Lett., vol. 103, pp. 141910-141914, 2013.

[23] M. D. Lynch and D. L. Patrick. *Organising carbon nanotubes with liquid crystals.* Nano Lett., vol. 2, pp. 1197-1201, 2002.

[24] A. Mertelj, D. Lisjak, M. Drofenik and M Čopič, *Ferromagnetism in suspensions of magnetic platelets in liquid crystal*, Nature, vol. 504, pp. 237-241, 2013.

[25] A. Nych, U. Ognysta, M. Skarabot, M. Ravnik, S. Zumer and I. Musevic. *Assembly and control of 3D nematic dipolar colloidal crystals.* Nat. Commun., vol. 4, no. 1489, 2013.

[26] O. Guzman, E. B. Kim, S. N. Grollau, L. Abbott and J. J. Pablo. *Defect Structure around Two Colloids in a Liquid Crystal.* Phys. Rev. Lett., vol. 91, no. 235507, 2003.

[27] H. Stark. *Physics of colloidal dispersion in liquid crystals.* Phys. Rep., vol. 351, pp. 387-474, 2001.

[28] T. C. Lubensky, D. Petty, N. Currier and H. Stark. *Topological defects and interactions in nematic emulsions.* Phys. Rev. E., vol. 57, pp. 610-625, 1998.

[29] N. Darnton, L. Turner, K. Breuer and H. C. Berg, *Moving fluid with bacterial carpets*, Biophys. J., vol. 86, pp. 1863-1870, 2004.

[30] A. V. Singh, M. Sitti, *Patterned and Specific Attachment of Bacteria on Biohybrid Bacteria-Driven Microswimmers.* Adv. Healthcare Mater., vol. 5, 2325-2331, 2016.

[31] O. Yasa, P. Erkoc, Y. Alapan, M. Sitti, *Microalga-Powered Microswimmers toward Active Cargo Delivery*, Adv. Mater., vol. 30, no. 1804130, 2018.

[32] G. Santomauro, A. V. Singh, B. W. Park, M. Mohammadrahimi, P. Erkoc, E. Goering, G. Schütz, M. Sitti and J. Bill, *Incorporation of Terbium into a Microalga Leads to Magnetotactic Swimmers.* Advanced Biosystems, vol. 2, pp. 1800039, 2018.

[33] P. Illien, R. Golestanian and A. Sen, *'Fuelled' motion: Phoretic motility and collective behaviour of active colloids.* Chem. Soc. Rev., vol. 46, pp. 5508-5518, 2017.

[34] H. Jiang, N.Yoshinaga and M. Sano, *Active motion of a Janus particle by self-thermophoresis in a defocused laser beam*, Phy. rev. Lett., vol. 105, pp. 268302 (1-4), 2010.

[35] A. Ghosh and P. Fischer, *Controlled propulsion of artificial magnetic nanostructured propellers*, Nano Lett. vol. 9, pp. 2243-2245, 2009.

[36] P. Tierno, R. Golestanian, I. Pagonabarraga and F. Sagués, *Magnetically actuated colloidal microswimmers*, J. Phys. Chem. B, vol. 112, pp. 16525–16528, 2008.

[37] R. Dreyfus, J.Baudry, M. L. Roper, M. Fermigier, H. A. Stone and J. Bibette, *Microscopic artificial swimmers*, Nature, vol. 437, pp. 862–865, 2005.

[38] P. Poulin, H. Stark, T. C. Lubensky, and D. A. Weitz. *Novel Colloidal Interactions in Anisotropic Fluids.* Science, vol. 275, pp. 1770-1773, 1997.

[39] I. Muševič, M. Škarabot, U. Tkalec, M. Ravnik, and S. Zumer. *Two-dimensional nematic colloidal crystals self-assembled by topological defects.* Science, vol. 313, pp. 954-958, 2006.

[40] Q. Liu, B. Senyuk, M. Tasinkevych and I. I. Smalyukh.*Nematic liquid crystal boojums with handles on colloidal handlebodies.* Proc. Natl. Acad. Sci. U. S. A., vol. 110, pp. 9231-9236, 2013.

[41] B. Senyuk, O. Puls, O. M. Tovkach, S. B. Chernyshuk and I. I. Smalyukh, *Hexadecapolar colloids.* Nat. Commun., vol. 7, no. 10659, 2016.

[42] C. P. Lapointe, T. G. Mason and I. I. Smalyukh. *Shape-controlled colloidal interactions in nematic liquid crystals.* Science, vol. 326, pp. 1083-1086, 2009.

[43] U. Tkalec, M. Škarabot and I. Muševič. *Interactions of micro-rods in a thin layer of a nematic liquid crystal.* Soft Matter, vol. 4, pp. 2402-2409, 2008.

[44] C. P. Lapointe, K. Mayoral and T. G. Mason. *Star colloids in nematic liquid crystals*. Soft Matter, vol. 9, pp. 7843-7854, 2013.

[45] D. A. Beller, M. A. Gharbi and I. B. Liu. *Shape-controlled orientation and assembly of colloids with sharp edges in nematic liquid crystals*. Soft Matter, vol. 11, pp. 1078-1086, 2015.

[46] D. Andrienko, M. P. Allen, G. Skačej and S. Žumer, *Defect structures and torque on an elongated colloidal particle immersed in a liquid crystal host*. Phys. Rev. E, vol. 65, no. 041702, 2002.

[47] M. V. Rasna, K. P. Zuhail, U. V. Ramudu, R. Chandrasekar and S. Dhara, *Dynamics of electro-orientation of birefringent microsheets in isotropic and nematic liquid crystals*. Phy. Rev. E, vol. 94, no. 032701, 2016.

[48] M. V. Rasna, K. P. Zuhail, U. V. Ramudu, R. Chandrasekar, J. Dontabhaktuni and S. Dhara, *Orientation, interaction and laser assisted self-assembly of organic single-crystal micro-sheets in a nematic liquid crystal*. Soft Matter, vol. 11, pp. 7674-7679, 2015.

[49] C. P. Lapointe, T. G. Masonand, I. I. Smalyukh, *Shape-controlled colloidal interactions in nematic liquid crystals*, Science, vol. 326, pp. 1083-1086, 2009.

[50] D. V. Sudhakaran, R. K. Pujala and S. Dhara, *Orientation dependent interaction and self-assembly of cubic magnetic colloids in a nematic liquid crystal*, Adv. Optical. Mater., vol. 8, pp. 1901585(1-9), 2020.

[51] B. Senyuk, Q. Liu, S. He, R. D. Kamien, R. B. Kusner, T. C. Lubensky, and I. I. Smalyukh, *Topological colloids*, Nature, vol.493, pp. 200-205, (2013).

[52] M. A. Gharbi ,M. C. Jr., G. Wu, D. A. Beller, R. D. Kamien, S. Yang and K. J. Stebe, *Microbullet assembly: interactions of oriented dipoles in confined nematic liquid crystal*, Liquid Crystals, vol. 40, pp. 1619-1627, 2013.

[53] H. N. W. Lekkerkerker and R. Tuinier, *Colloids and the Depletion Interactions*, Springer, Dordrecht, 2011.

[54] O. D. Lavrentovich, *Transport of particles in liquid crystals.* Soft Matter, vol. 10, pp. 1264-1283, 2014.

[55] T. Turiv, I. Lazo, A. Brodin, B.I. Lev, V. Reiffenrath, V. Nazarenko and O. D. Lavrentovich, *Effect of collective molecular reorientations on Brownian motion of colloids in nematic liquid crystal*, Science, vol. 342, pp. 1351-1354, 2013.

[56] H. Morgan and N. G. Green, *AC Electrokinetics: colloids and nanoparticles*, Research Studies Press, Baldock, UK, p.324, 2003.

[57] R. C. Hayward, D. A. Saville and I. A. Aksay, *Electrophoretic assembly of colloidal crystals with optically tunable micropatterns.* Nature, vol. 404, pp. 56-59, (2000).

[58] M. Z. Bazant, M. S. Kilic, B. D. Storey and A. Ajdari, *Nonlinear electrokinetics at large voltages.* New J. Phys., vol. 11, no. 075016, 2009.

[59] W. B. Russel, D. A. Saville and W. R. Schowalter, *Colloidal Dispersions.* Cambridge University Press, 1989.

[60] F. V. Podgornov, A. V. Ryzhkova and W. Haase, *Dynamics of nonlinear electrophoretic motion of dielectric microparticles in nematic liquid crystal.* J. Mol. Liq., vol. 267, pp. 345–352, 2018.

[61] M. Z. Bazant, M. S. Kilic, B. D. Storey and A. Ajdari, *Towards an understanding of induced-charge electrokinetics at large applied voltages in concentrated solutions.* Adv. Colloid Interface Sci., vol. 152, pp. 48–88, 2009.

[62] T. M. Squires and M. Z. Bazant, *Induced-charge electro-osmosis.* J. Fluid Mech., vol. 509, pp. 217-252, 2004.

[63] M. Z. Bazant and T. M. Squires, *Induced-charge electrokinetic phenomena: Theory and microfluidic applications.* Phys. Rev. Lett., vol. 92, no. 066101, 2004.

[64] T. M. Squires and M. Bazant, *Breaking symmetries in induced-charge electroosmosis and electrophoresis.* J. Fluid Mech., vol. 560, pp. 65-101, 2006.

[65] S. Gangwal, O. J. Cayre, M. Z. Bazant, and O. D. Velev, *Induced-charge electrophoresis of metallodielectric particles.* Phys. Rev. Lett., vol. 100, no. 058302, 2008.

[66] C. Peng, I. Lazo, S. V. Shiyanovskii and O. D. Lavrentovich, *Induced-charge electro-osmosis around metal and Janus spheres in water: Patterns of flow and breaking symmetries*, Pyh. Rev. E, vol. 90, pp. 051002 (1-5), 2014.

[67] O. D. Lavrentovich, I. Lazo, and O. P. Pishnyak,*Nonlinear electrophoresis of dielectric and metal spheres in a nematic liquid crystal.* Nature, vol. 467, pp. 947-950, 2010.

[68] A. V. Ryzhkova, F. V. Podgornov, and W. Haase, *Nonlinear electrophoretic motion of dielectric microparticles in nematic liquid crystals.* Appl. Phys. Lett. vol. 96, pp. 151901, 2010.

[69] I. Lazo, C. Peng, J. Xiang, S. V. Shiyanovskii, and O. D. Lavrentovich, *Liquid crystal-enabled electro-osmosis through spatial charge separation in distorted regions as a novel mechanism of electrokinetics.* Nat. Commun., vol. 5, no. 5033, 2014.

[70] I. Lazo and O. D. Lavrentovich, *Liquid-crystal-enabled electrophoresis of spheres in a nematic medium with negative dielectric anisotropy.* Phil. Trans. Soc. A. vol.371, no. 2012255, 2013.

[71] O. D. Lavrentovich, *Active colloids in liquid crystals* Curr. Opin. Colloid Interface Sci. vol. 21, pp. 97-109, 2016.

2

Experimental Setup

2.1 Introduction

In this chapter we briefly discuss about different experimental techniques and setup used in the experiments. First, we describe the preparation of LC cells. Then, we discuss fabrication of Janus particles and chemicals desired for surface alignment of liquid crystals on the particle's surface. Further, we explain the setup and working principle of optical tweezers which was used to manipulate the particles. An imaging technique with λ-plate is discussed in order to construct the director field and identify the defects surrounding the particles. Finally, we present the video-microscopy technique for tracking the position of the particles.

2.2 Preparation of LC cells

LC cells are made by arranging two glass plates (1.6×1.1 cm^2) of thickness 0.5 mm. The glass plates are washed thoroughly with soap water and then, rinsed with distilled water for several times. They are further cleaned through sonication using an ultrasonic water bath in both acetone and water. Then the glass plates are dried in the oven at 100°C for 20 minutes and also by blowing Nitrogen gas. After drying, the glass plates are spin coated with a polymer (AL-1254, JSR Corporation, Japan) using a spincoater (Holmarc) which is programmed to rotate at a speed of 4000 rpm for first 20 s and 6000 rpm for the next 20 s. The coated glass plates are cured at 180° in the furnace for 1 hour. The surface of the cured glass plates are rubbed unidirectionally using a bench-top rubbing machine (HO-IAD-BTR-01). Finally, two such plates are attached with the help of an optical adhesive mixed with spacer (silica microspheres) in antiparallel fashion with respect to their rubbing direction in order to provide uniform planar alignment of the LC director. For applying electric field, we used ITO (Indium-Tin Oxide) coated glass plates. In order to apply electric field parallel to the LC director, we make in-plane cells where a region of the bottom ITO is etched using conc. HCl and Zinc powder while the top glass is a non-ITO (Fig.2.1(a)). For applying electric field perpendicular to the director, we used two ITO glass plates and made cells as discussed above (Fig.2.1(b)). Electrical contacts are made by soldering copper wires using ultrasonic soldering (Sunbonder USM-IV). Alternating current electrical signals to the cells in the sinusoidal form are applied by a function generator (AFG 3102, Tektronix) which was further magnified by a voltage amplifier (TEGAM 2350).

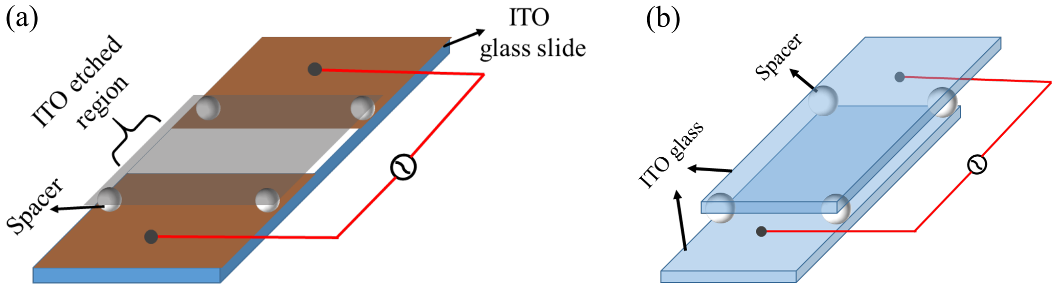

Figure 2.1: (a) Schematic diagram of a cell for applying in-plane electric field. The ITO etched portion is the region of interest. (b) Schematic diagram of a a cell for applying out-of-plane electric field. Red lines represent the electrical wires.

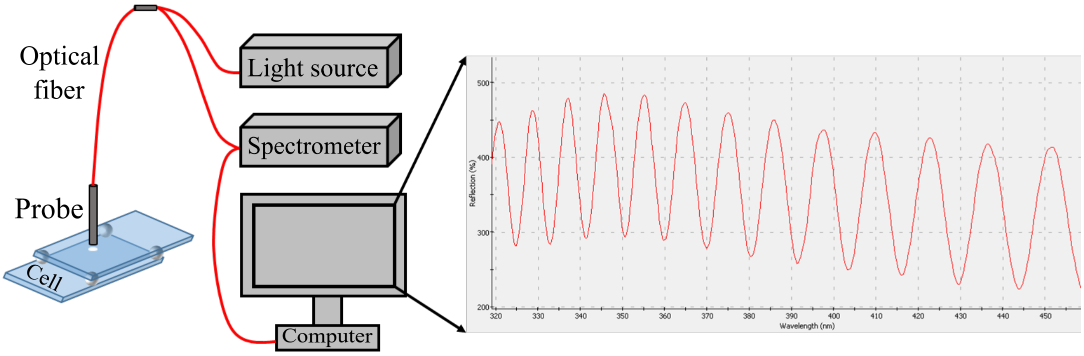

Figure 2.2: Experimental setup for measuring cell thickness.

The empty cell gap is measured by using a standard interference technique with the help of a high resolution spectrometer (Ocean Optics HR4000CG-UV-NIR). The cell is illuminated with light through an optical fiber as shown in the Fig.2.2. The light reflected from the top and bottom plates is collected by the probe and the resulting interference pattern can be analyzed through a software (SpectraSuite) interfaced with a computer. The spectrum consists of maxima and minima as shown in Fig.2.2. The thickness of the cell is calculated using the formula

$$d = \frac{\lambda_m \lambda_n}{\lambda_m - \lambda_n} \times \frac{m-n}{2} \tag{2.1}$$

where λ_m and λ_n are the corresponding wavelengths of $\mathrm{m^{th}}$ and $\mathrm{n^{th}}$ maxima or minima.

2.3 Liquid crystals and colloids

In all experiments, we used calamitic liquid crystals (consist of rod shaped molecules) such as 5CB (4-cyano-4'-pentylbiphenyl) and MLC-6608 obtained from Sigma Aldrich and Merck, respectively. 5CB is a room temperature nematic liquid crystal exhibiting the following phase transitions : Cr 22°C N 35°C Iso. At room temperature, the birefringence of 5CB, Δn = 0.18 and the dielectric anisotropy, $\Delta\epsilon$=13. On the other hand, MLC-6608 is a mixture of liquid crystals exhibiting a large temperature range of nematic phase: SmA -30° N 90° Iso. The dielectric anisotropy of MLC-6608 is negative ($\Delta\epsilon$= -4.2) and it possesses low birefringence (Δn = 0.08). The values of some physical properties of both LCs are presented in Table 2.1.

Liquid crystals	$n_{\parallel}$	$n_{\perp}$	$\epsilon_{\parallel}$	$\epsilon_{\perp}$	$\sigma_{\parallel}$ ($\times10^{-9}$) Sm^{-1}	$\sigma_{\perp}$ ($\times10^{-9}$) Sm^{-1}
5CB	1.77	1.59	19.7	6.7	7.18	5.18
MLC-6608	1.55	1.47	7.8	3.6	0.5	0.2

Table 2.1: Values of refractive index, dielectric permittivity and electrical conductivity of 5CB and MLC-6608 LCs at room temperature.

2.3.1 Fabrication of Janus particles

We prepared metal-dielectric Janus particles using directional deposition (Fig.2.3(a)) of metal onto dry silica particles (SiO_2) of diameter $2a = 3.0 \pm 0.2$ µm (Bangs Laboratories, USA) in vacuum [1–3]. Approximately 2% suspension (25 µl) of silica particles is spread on a half glass side (40 mm×25 mm), whose surface is made hydrophilic by treating with Piranha solution and dried to form monolayer as shown in Fig.2.3(b,c). A enlarged view of monolayer shows a hexagonal closed packed structure of particles (Fig.2.3(d)). Next, a thin Titanium (Ti) layer of thickness 35 nm is deposited vertically using electron-beam deposition at a pressure of 3×10^{-6} torr, and deposition rate of 0.5 Ås^{-1}. On top of this, a thin layer of SiO_2 film (10-15 nm) is deposited in order to make the particle surface chemically isotropic as shown in Fig.2.3(e)). Ti coating on the silica particles appear dark when observed through transmitted light (Fig.2.3(f)).

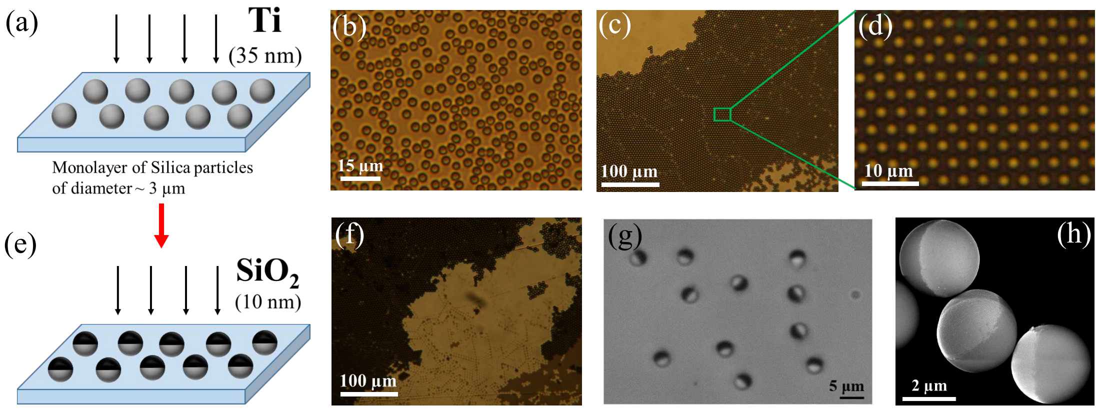

Figure 2.3: (a) Schematic presentation of directional deposition of Ti on a monolayer of silica microspheres. (b) SiO_2 microspheres on a glass substrate. (c) Dried silica particles forming crystalline structure. (d) Closed hexagonal pattern of monolayer of silica particles. (e) Coating SiO_2 above Ti-coating. (f) Optical micrograph of coated particles through transmitted light. (g) Bright field image of a few Janus particles. (h) Scanning electron microscopic (SEM) image of a few Janus particles.

Then the slides with silica monolayer are washed thoroughly with deionized water (DI) and isopropyl alcohol. The particles are detached from the slides by ultrasonication in deionized water of volume 20 ml for 100 s. The bright region in Fig.2.3(f) indicates that the particles are removed, leaving their mark on the sustrate. Further, the collected particles are sonicated for 30 minutes to breakup any agglomeration of the particles. After sedimentation of the particles at the bottom of the centrifuge tube, the concentrated suspension is used for the experiments. A bright field image of a few Janus particles is shown in Fig.2.3(g) where the metal-dielectric interface is easlily distinguishable. The darker part represents metal while the brighter part represents silica. The thin layer of SiO_2 coating on Ti does not make much difference in appearance due to the transparency of silica. Scanning electron microscope (SEM) image of a few Janus particles is shown in Fig.2.3(h).

2.3.2 Surface treatment of particles

The particles are treated with appropriate polymer to get the desired anchoring of the LC molecules on their surface. N,N-dimethyl-Noctadecyl-3-aminopropyl-trimethoxy-silyl chloride (DMOAP) is functionalized on the surface of particles to obtain normal or homeotropic alignment of LC molecules [4,5]. Schematic diagram of surface coupling of DMOAP is shown in Fig.2.4(a).

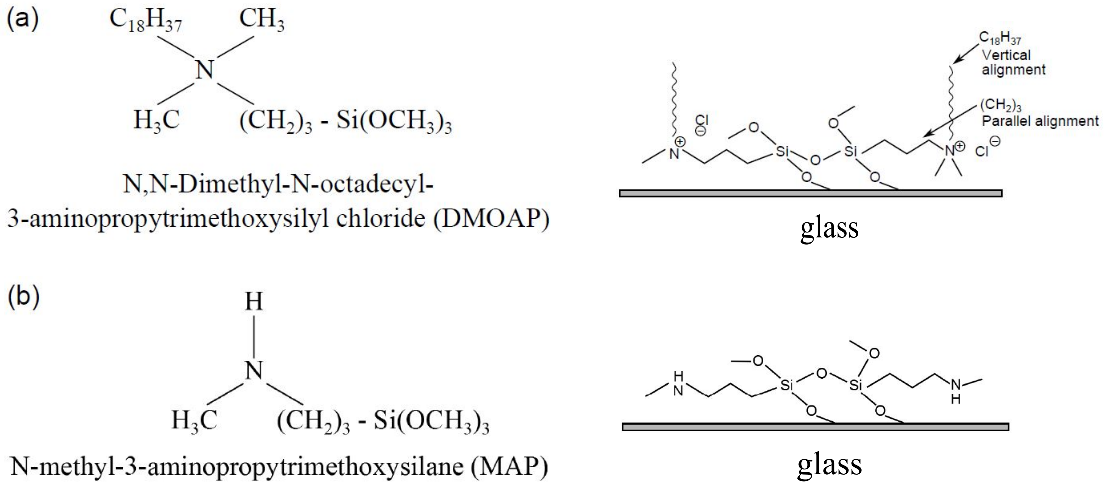

Figure 2.4: Schematic diagram showing coupling of (a) DMOAP and (b) MAP on the surface.

The procedure for surface functionalisation is as follows: about 2wt% of DMOAP was added to a diluted solution of Janus particles. Next, it was mixed for 10 minutes using a vertex mixture (SPINIX) to get uniform coating of octadecyl chains on the particle surface. Then the excess DMOAP was removed by centrifuging the mixture using Mini Spin centrifuge (Eppendorf) and by rinsing in deionized water several times. The solution is then cured at 100°C in the oven to make permanent bonding which provides normal anchoring to LC molecules. The particles are treated with N-methyl-3-aminopropyltrimethoxysilane (MAP) to induce planar anchoring of LC molecules on the surface. The MAP was coated on the microsphere following the same procedure discussed above. Schematic diagram of surface coupling of particle surface with MAP is shown in Fig.2.4(b).

2.4 Optical Setup

We have used optical tweezers in order to manipulate the micro-particles in LCs. The laser tweezers setup is built on an inverted optical polarizing microscope (Nikon, Eclipse Ti-U) installed on a vibration free optical bench. The optical setup is presented schematically in Fig.2.5 and the actual setup in the laboratory is shown in Fig.2.6. A sample stage (PRIOR) is fixed with the microscope and a halogen lamp is used to illuminate the sample. The movement of the sample stage is controlled with the help of a joystick (PRIOR optiscan II). Polarizer, analyzer and required filters are kept along the optical path. Objectives used in our experiments are 20X air (WD = 2.6 - 1.8 mm) and 60X water immersion (WD = 2.8 mm). 60X water objective with NA=1.0 was used for creating laser traps. Water as immersion medium is used to reduce spherical aberrations of light for better trapping. The microscope has multiple ports for connection to the cameras. Right side port is connected to a CCD camera (IDS UI-3370CP, 2048-2048 pixels, resolution 4.19 MPix, black/white) camera which is interfaced with a computer through Tweez software. A colour camera (Nikon DS-Ri2) is attached to the left side of the microscope for capturing colour images and movies. All the optical devices are interfaced with the system through various computer programs.

We used an infrared laser (1064 nm) with maximum power 5W for creating laser traps. A single mode output, typically gaissian mode TEM_{00} is delivered by the laser. The beam passes through an acusto-optic deflector (AOD) which helps in creating multiple traps simultaneously by time sharing. AOD consists of a piezo-electric crystal (TeO_2) which produces a travelling sound wave and the wavelength of the sound wave act as diffraction pattern for the laser beam. The first order diffracted light of wavelength λ is deflected through an angle $\Delta\theta = \lambda f/v$, where f and v are the frequency and velocity of the acoustic wave, respectively. AOD has four output slots which are connected to the followings: (i) a safety switch in order to abort the operation in case of emergency, (ii) a photodiode for checking laser power, (iii) a CCD camera and (iv)

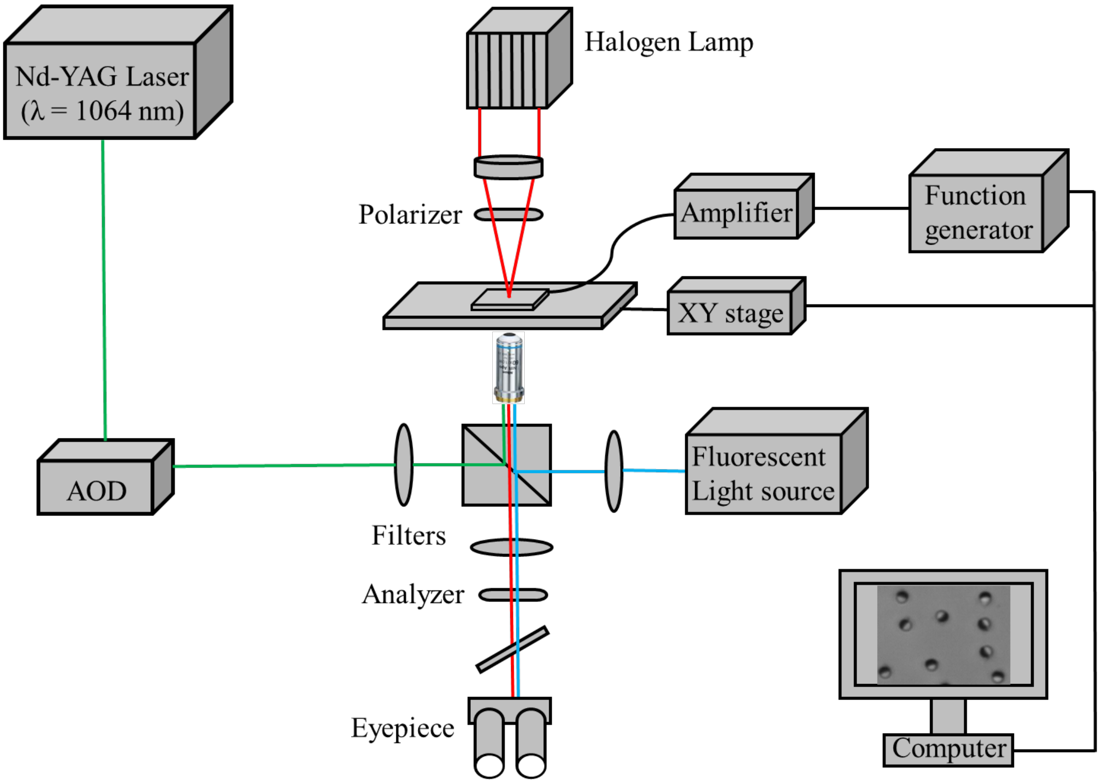

Figure 2.5: Schematic diagram of the experimental setup.

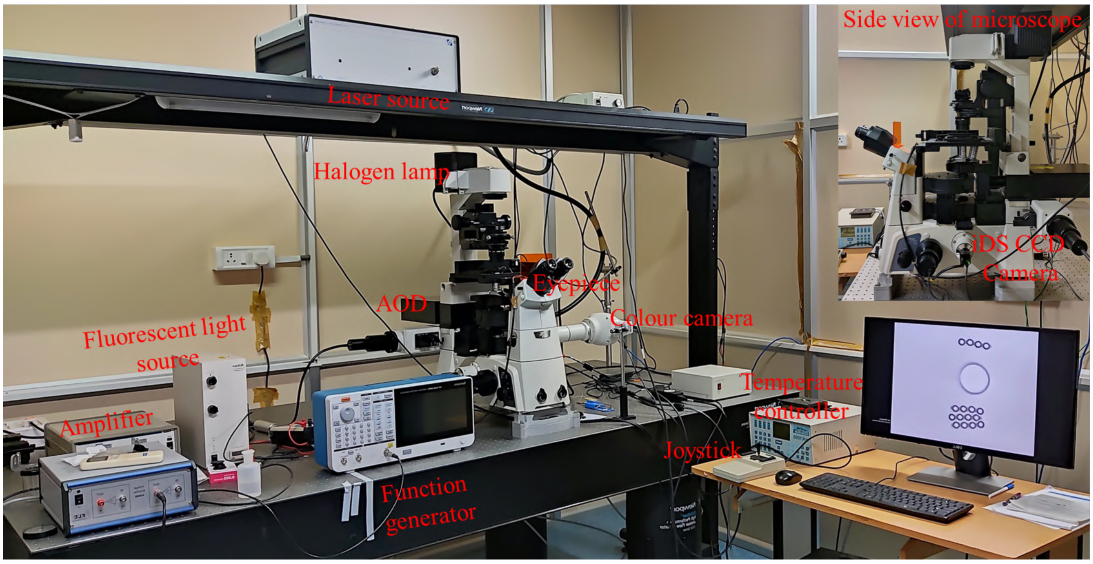

Figure 2.6: Photograph of the actual experimental setup. Side view of the microscope is given in the inset. Equipments are marked with red colour text.

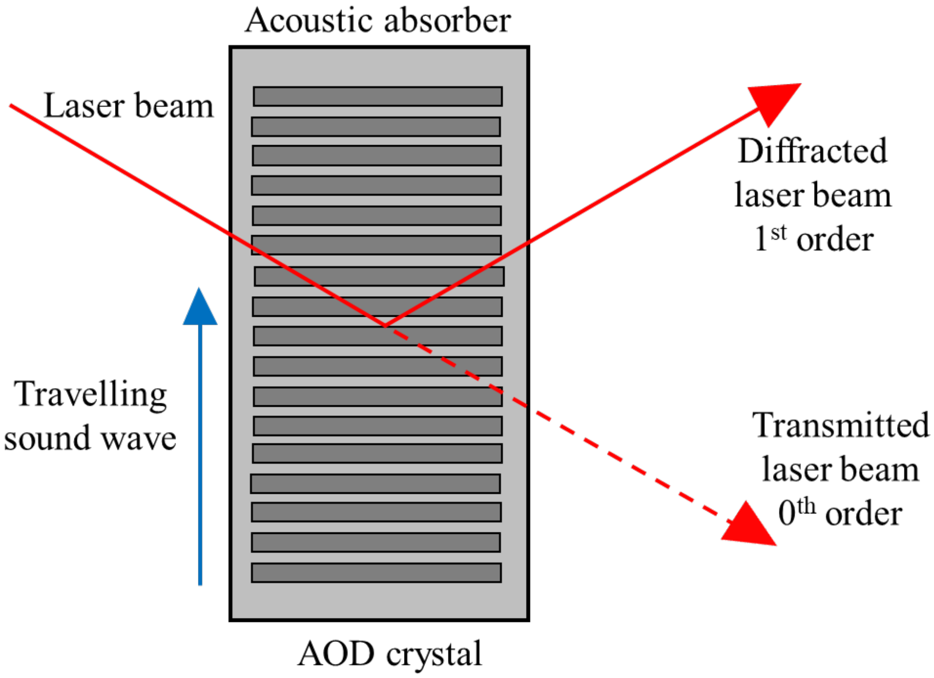

Figure 2.7: Schematic diagram of acusto-optic deflector (AOD).

interlock to the microscope.

2.5 Optical trapping

Here we discuss basic principles of optical trapping of particles. Laser light exerts a force on the particles through momentum transfer when it undergoes reflection or refraction [6–8,10]. The force exerted by the light has two components such as gradient forces (F_{grad}) and scattering forces (F_{scat}). Based on the relative wavelength (λ) of the light and size of the particles (r), it is broadly classified in to two regimes such as Rayleigh regime ($r << \lambda$) and Mie regime ($r >> \lambda$). In Rayleigh regime, particles can be considered as dipoles polarized by the component of light field and creates a electrostatic potential with interaction of electric field of light. So, the gradient force can be given as [8]

$$F_{grad} = -\nabla U = \frac{n_m^3 r^3}{2} \left(\frac{n_r^2 - 1}{n_r^2 + 2} \right) \nabla \vec{E}^2 \tag{2.2}$$

where n_p and n_m are refractive indexes of the particle and the medium, respectively and $n_r = n_p/n_m$, the relative index of the particle to the the surrounding medium.

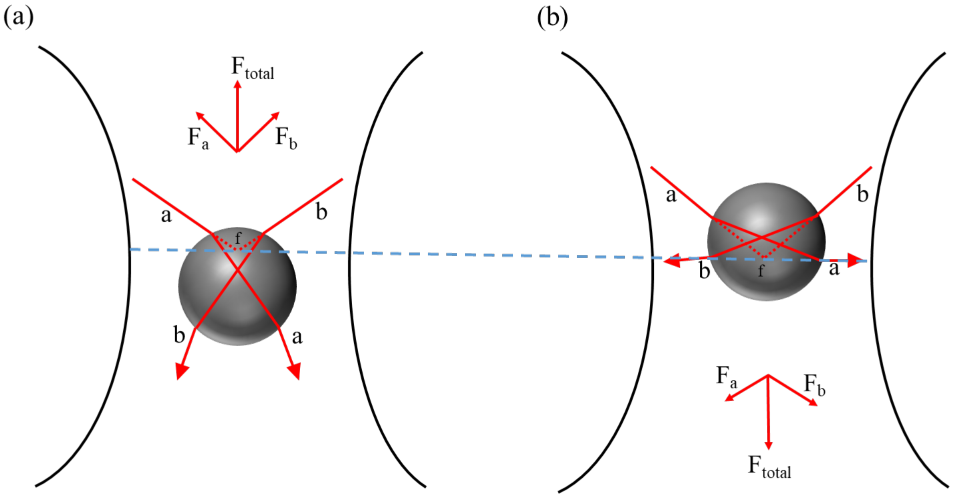

Figure 2.8: Schematic representation of axial trapping forces. In the absence of the particle, two rays (a and b) are focused through the objective at the true laser focus, f. (a) Particle placed above the focus leads to the refraction of light rays resulting the new focus to lie below f. The two rays become more convergent upon exiting the particle; F_a and F_b are the forces exerted on the particle by rays 'a' and 'b', respectively. F_{total} is the sum of these two vectors and points upwards. (b) Displacement of particle above the focus makes the rays 'a' and 'b' are more divergent, and the resulting force points downward [11].

The scattering force along the direction of propagation of light of intensity I_0 arises due to the transfer of momentum carried by the photons and can be expressed as [8]

$$F_{scat} = \frac{128\pi^5 r^6}{3\lambda^4}\left(\frac{n_c^2-1}{n_c^2+2}\right)\frac{n_m}{c}I_0 \tag{2.3}$$

A stable trap is possible when F_{grad} is greater than the F_{scat} and n_p is greater than n_m. On the other hand, when the size of particle larger than the wavelength of the light, we are in the Mie regime and the scenario can be understood with the help of ray optics where the particle can be treated as a lens. When light interacts with the particle, it bends away due to refraction and the change in field momentum leads to create equal and opposite forces on the particle. The resultant force acting on the particle is the vector sum of the forces resulting from ensemble of rays of light refracted through the particle. Fig.2.8 shows the trapping mechanism of an axially displaced particle. F_a and F_b are the forces experienced by the particle due to rays a and b, respectively and

F_{total} is the sum of these two vectors. When the particle is displaced down the focal point, F_{total} is upward (Fig.2.8(a)) and when the particle is displaced above the focal point, F_{total} is downward (Fig.2.8(b)). In practical applications, neither Rayleigh nor the ray optics is considered as the particle size is almost comparable to the wavelength of the light. In both the cases, trapping is possible only if the refractive index of the particles is higher than that of the host medium. However, the trapping mechanism of particles in liquid crystals is very different than in water. Here, we present a brief description of the laser trapping of particles in nematic liquid crystals.

2.5.1 Force Calibration

For all practical applications of optical tweezers, it is desired to have information about the optical force acting on a trapped object. Moreover, for effective use, the tweezers need to be calibrated. One of the easiest way to calibrate tweezers is to analyze the Brownian motion of a trapped particle. For example, we consider spherical particles of diameter 2 μm dispersed in water. A tightly focused laser beam was used to trap a particle and the position fluctuations were recorded. Figure 2.9(a) shows the position of a trapped particle with time. The inset of Fig.2.9(a) shows a bright field image of a trapped particle. The position distribution of the trapped particle well fits with Gaussian distribution as shown in Fig.2.9(b). We present two simple methods of trap calibration [9].

2.5.1.1 Calibration using equipartition theorem

An optical trap can be calibrated using the equipartition theorem assuming the trapping potential is harmonic. Equipartition theorem states that each degree of freedom contributes $k_BT/2$ to the average energy, where k_B is the Boltzmann constant. From the recorded position of the trapped particle, the averaged square of the displacement from the trap center is given by

$$\sigma_x^2 = \langle (x - \langle x \rangle)^2 \rangle \quad \text{and} \quad \sigma_y^2 = \langle (y - \langle y \rangle)^2 \rangle \tag{2.4}$$

where $< x >$ and $< y >$ are the mean displacements along x and y -axis, respectively and the trap stiffness $k_{x,y}$ can estimated as

$$k_{x,y} = k_BT/\sigma_{x,y}^2 \tag{2.5}$$

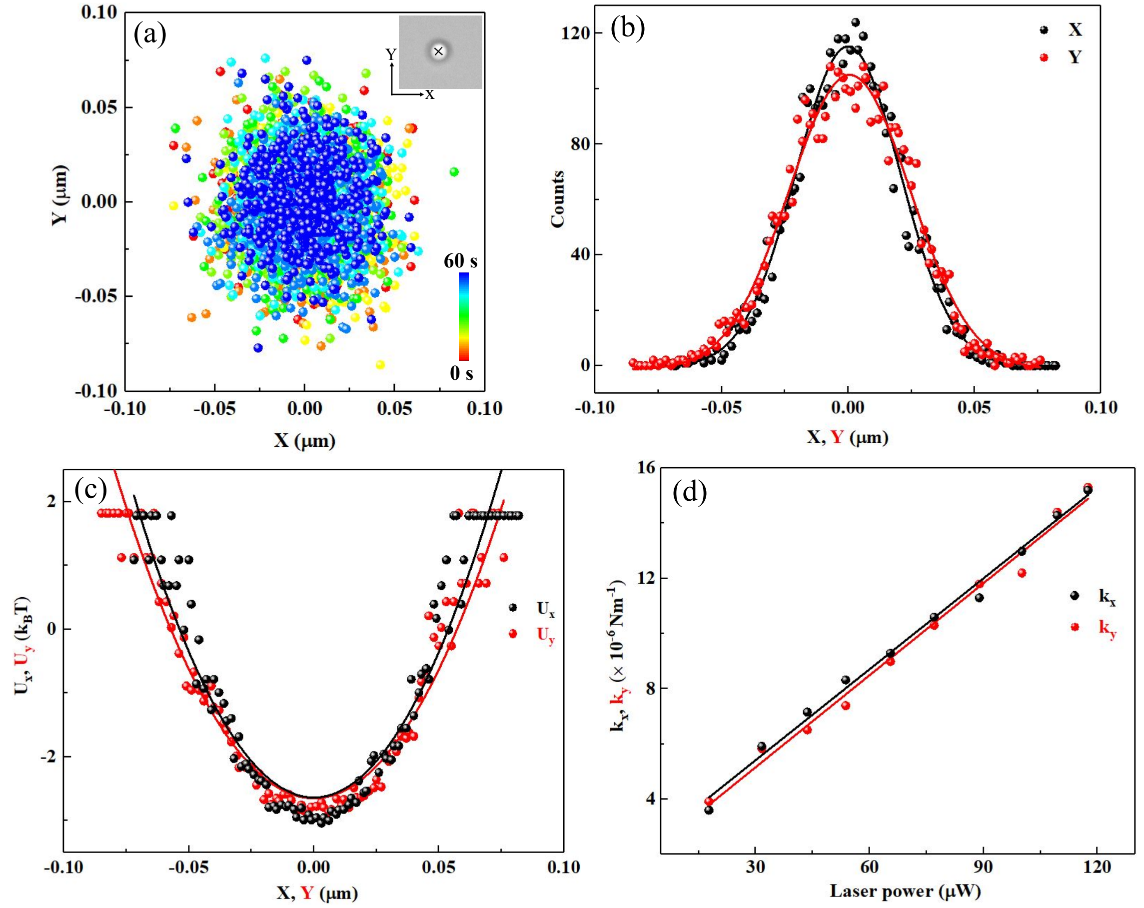

Figure 2.9: (a) Positions of a trapped spherical particle of diameter 2 μm with time in water. (b) Position distribution along both x and y-axis. Solid lines represent Gaussian fits. (c) Trapping potential in x and y directions. Solid lines represent fittings to harmonic potentials. (d) Linear variation of stiffness coefficients with laser the power. (Objective used 60X)

This method however is not accurate for particle position far from the center of the trap where the potential is not harmonic.

2.5.1.2 Calibration using Boltzmann statistics

According to Boltzmann statistics, the probability density $\rho(x, y)$ of particle position is given by

$$\rho(x, y) = Cexp\left(-U\left(x, y\right)/k_B T\right) \tag{2.6}$$

where C is a constant and $U(x,y)$ is the trapping potential. The potential can be estimated from the normalized histogram of particle position as

$$U\left(x,y\right)=-ln\left(\rho\left(x,y\right)\right) \tag{2.7}$$

The harmonic potential can be fitted with a parabola $y=ax^2+b$ in the central region. The stiffness coefficient can be calculated as $k=2ak_BT$ and is more accurate than Eq.(2.5). For example, the harmonic potential of the trapped particle is shown in Fig.2.9(c) and the corresponding fitting parameter gives the value of stiffness coefficients as $k_x=9.18\times10^{-6}$ and $k_y=8.5\times10^{-6}$ Nm^{-1}. The stiffness coefficients are found to be linear with laser power as shown in Fig.2.9(d). The corresponding force experienced by the particle for displacement at length scales of micrometer is in the range of 1-10 pN.

2.5.2 Optical trapping and manipulation of microparticles in nematic liquid crystals

As discussed earlier, for an effective trapping the refractive index of the particle should be larger than that of the medium. When the host medium is a nematic LC, the trapping mechanism is very different as the refractive of the LC is greater that the particles. There are different mechanisms of trapping. One of the techniques involves creation of an elastic distortion of low refractive index using laser tweezers and it’s interaction with the real colloid [12–15]. For demonstration purpose, we have used dielectric silica microspheres (diameter = 5.2 μm) of low refractive index (n = 1.4) as compared to the host medium liquid crystal ($\overline{n}=1.65$) which is contrary to the basic requirement for optical trapping.

An isotropic bubble is created due to the local heating of LC medium which can be seen as grey circular line in Fig.2.10. The distorted region acts as a trapping site for the particle and attracts the real colloid over several micrometers. Figure.2.10(a-d) show the sequence of a trapping event. The point defect shows a long range attractive interaction with the distorted region.

Optical tweezers can be used to manipulate the defects around the particles. Isotropic bubble created by local quenching converges to different types of defects. Fig.2.11

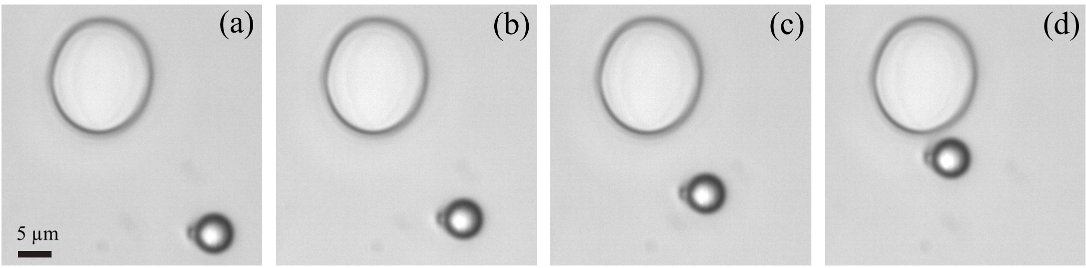

Figure 2.10: Sequence of snapshots (a-d) showing the motion of a particle towards the ghost colloid. The circular region is the melted region of nematic due to the laser heating. Cell thickness is 10μm.

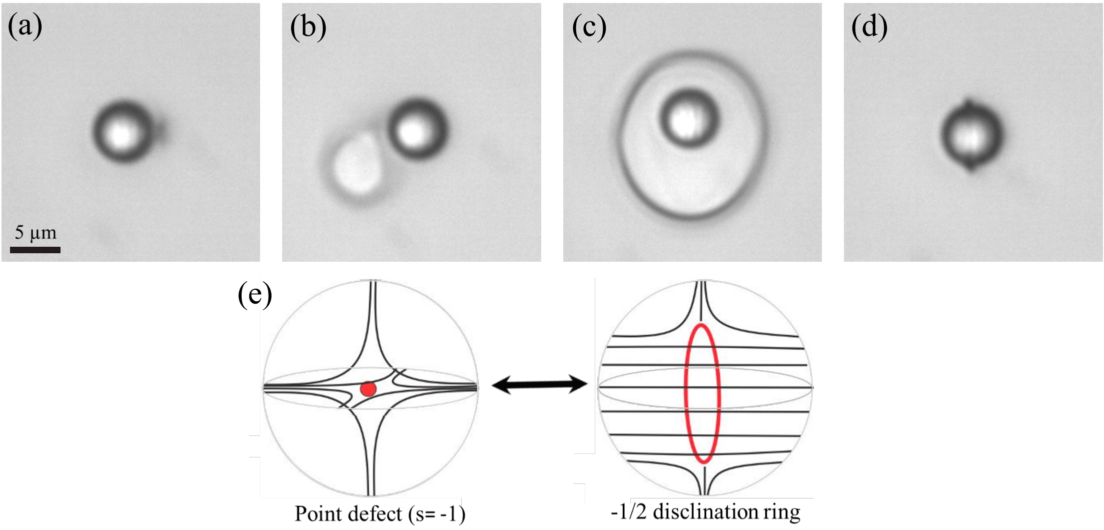

Figure 2.11: Sequence of snapshots (a-d) showing the manipulation of a particle from Saturn ring defect to a hyperbolic hedgehog defect. (e) Topological transformation from hyperbolic hedgehog to a disclination ring.

shows the conversion of a point defect in to a ring defect using an optical trap. Figure.2.11(e) shows the schematic of transformation from hyperbolic hedgehog ($s = -1$) to a disclination ring of strength $s = -1/2$. The reverse transformation is also possible. The optical trap is also used to change the position of point defects which is an important factor in assembling colloidal particles.

Optical tweezers are used to direct assemble of many particles nucleated with defects to form linear chains as shown in Figs.2.12(a-b). Many such chains can also be brought

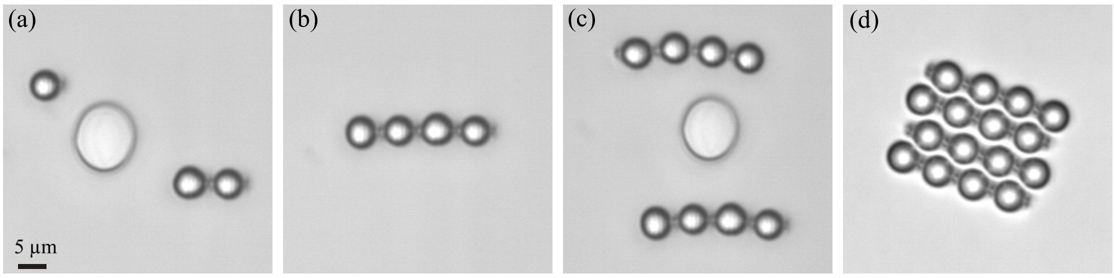

Figure 2.12: Sequence of snapshots (a-d) showing the laser assisted 2D assembly of dipolar particles.

together in an anti-parallel fashion to make 2D crystal [16, 17].

2.6 Determination of director orientation using full waveplate (λ-plate)

In order to study the defects around the particles and resulting elastic distortions in a uniformly aligned LC, it is important to know about the orientation of the LC molecules. The particles create elastic distortions in the medium. The images of the particles are seen with an additional full wave retardation plate (λ-plate) kept in between the sample and the polarizer. The λ-plate introduces an exact retardation of one wavelength (530 nm) between the ordinary and extraordinary wavefronts. The consequence of a λ-plate in linearly polarized white light as a combination blue, green and red wavefronts is schematically shown in Fig.2.13. Without the sample, the λ-plate induces elliptically polarized blue and red wavefronts, but linear polarized green wavefront which gets blocked by the analyzer as it is placed cross to the polarizer. The combination of red and blue give rise to bright magenta colour (visible light without the green component) as shown in Fig.2.13(a). When a birefringent sample with wavefront ellipsoid parallel to the slow axis of the λ-plate, the relative retardation is increased so that the linearly polarization character is shifted to higher wavelength (red). The blue and green wavelengths interfere to form a hue similar to second order blue color as shown in Fig.2.13(b). If the birefringent sample is rotated by 90°,

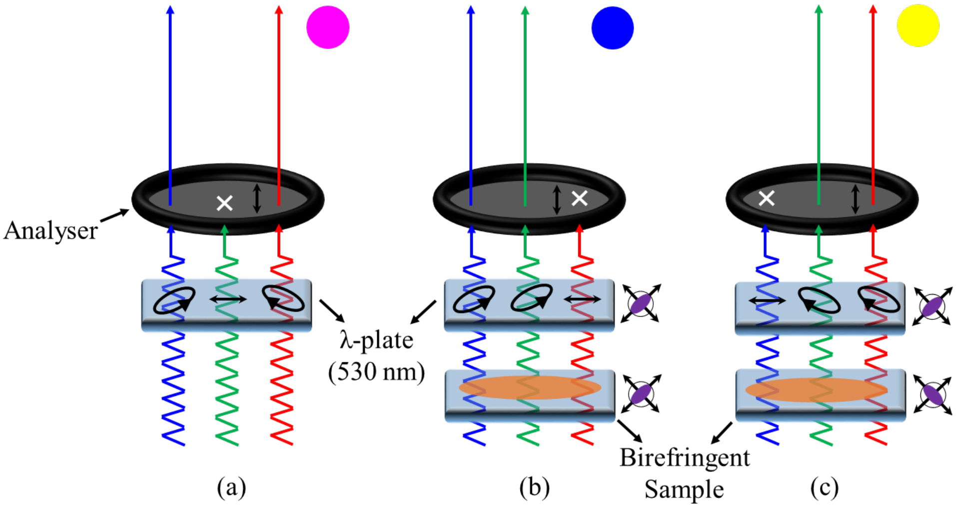

Figure 2.13: The effect of λ-plate on the white polarised light. (a) Without any sample in the optical pathway. A birefringent sample with ellipsoidal wavefront with (b)parallel and (c) perpendicular to λ-plate.

the resultant retardation will decrease and the shorter wavelengths (blue) get linear polarized. Elliptically polarized green and red wavelengths ultimately recombine to form a first order yellow (subtraction) interference color. Consequently, elliptically polarized red and green wavelengths combine to form a first order yellow interference color (Fig.2.13(c)).

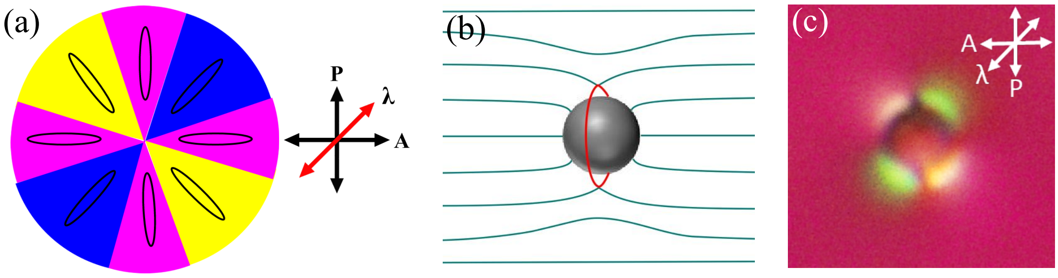

Figure 2.14: Display of the color pattern according to the orientation of LC molecules with respect to the λ-plate. Red arrow shows the slow axis of the λ-plate. (b) Director profile around a particle nucleating Saturn-ring defect. (c) The corresponding POM image with the λ-plate inserted at 45° in between the sample and the polarizer.

In our experiments, the emerging color depends on the orientation of the director field. The effect of λ-plate on the orientation of director filed is shown schematically in Fig.2.14(a). If the director field is parallel to the polarizer, it will display magenta color. If the LC molecules are oriented parallel (perpendicular) to the slow axis of the retardation plate, the retardation will be towards higher (lower) wavelength and consequently display blue (yellow) color. For example, consider a particle with homeotropic anchoring nucleate a Saturn-ring defect as discussed in the previous chapter. Figure.2.14(b) shows the director pattern around the particle. Figure.2.14(c) shows the corresponding POM image with λ-plate where the color pattern matches with the director orientation as expected from Fig.2.14(a).

2.7 Particle tracking

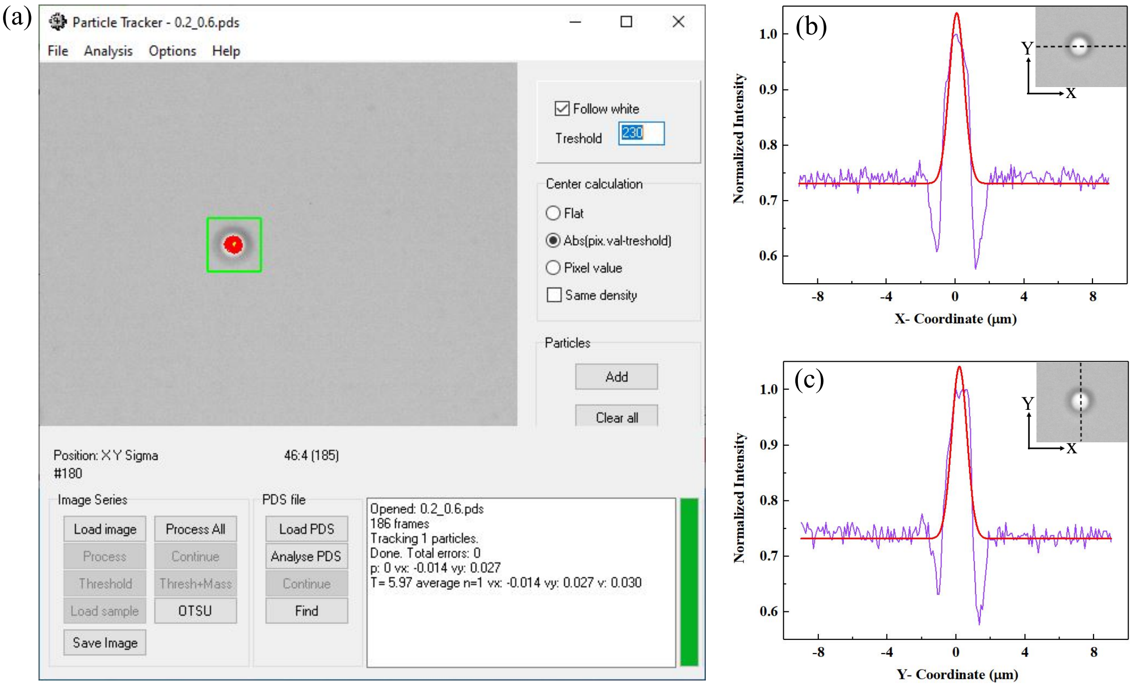

☑ Follow white
Treshold 230

○ Flat
● Abs(pix.val-treshold)
○ Pixel value
☐ Same density

Position: X Y Sigma 46:4 (185)
#180

```
Opened: 0.2_0.6.pds
186 frames
Tracking 1 particles.
Done. Total errors: 0
p: 0 vx: -0.014 vy: 0.027
T= 5.97 average n=1 vx: -0.014 vy: 0.027 v: 0.030
```

Figure 2.15: (a) Screenshot of the PartTrack software. The green square presents the region containing the particle. The red color presents the tracked region and the yellow color shows the particle's trajectory. Intensity profile of the tracked particle along (b) x and (c) y-axis.

We have traced the position of the particles using the video-microscopy technique.The movies with 30-100 frames per second were captured by an iDS CCD camera attached to the microscope. A particle tracking software (PartTrack4) was used for particle tracking. Figure.2.15 shows a screenshot of the software interface tracking a spherical particle of diameter 2 µm. The software treat the video as an array of images. We manually choose a region containing the desired particle and fix the highest or lowest (depending upon the contrast of the particle with respect to the background) intensity of the particle on the basis of grey scale as shown by green box around the particle in Fig.2.15. The intensity profiles along both x and y-axis with the origin passing through the center of the particle are shown in Fig.2.15(b) and (c), respectively. Both intensity profile well fit to Gaussian distribution with FWHM (full width half maximum) 1.03 ± 0.06 and 1.04 ± 0.05 µm along x and y-axis, respectively. The same intensity with deviation (same as FWHM), set as threshold is followed for the consecutive images in that selected region and eventually the software provides the pixel coordinate (center of the tracked region shown in red color) of the particle. It is then converted to real time coordinate by calibrating the image using a microscope scale bar (1 px = 0.08 µm). This enables us in getting the time coded trajectory as well as the velocity of the particles. The accuracy of determining the position of the particle is about 20 nm.

References

[1] J. Yan, M. Han, J. Zhang, C. Xu, E. Luijten, and S. Granick, *Reconfiguring active particles by electrostatic imbalance.* Nat. Mater., vol. 15, pp. 1095-1099, 2016.

[2] L. Hong, S. Jiang, and S. Granick, *Simple Method to Produce Janus Colloidal Particles in Large Quantity.* Langmuir, vol. 23, pp. 9495–9499, 2006.

[3] J. Zhang, B. A. Grzybowski and Steve Granick, *Janus Particle Synthesis, Assembly and Applications.* Langmuir, vol. 33, pp. 6964-6977, 2017.

[4] F. J. Kahn, *Orientation of liquid crystals by surface coupling agents.* Appl. Phys. Lett., vol. 22, pp. 386-388, 1973.

[5] K. Kočevar and I. Muševič, *Surface-induced nematic and smectic order at a liquid-crystal-silanated-glass interface observed by atomic force spectroscopy and brewster angle ellipsometry.* Phys. Rev. E, vol. 65, pp. 021703, 2002.

[6] A. Ashkin, *Acceleration and trapping of particles by radiation pressure.* Phys. Rev. Lett., vol. 24, pp. 156, 1970.

[7] A. Ashkin and J. M. Dziedzic, *Observation of resonances in the radiation pressure on dielectric spheres.* Phys. Rev. Lett., vol. 38, pp. 1351, 1977.

[8] A. Ashkin, J. M. Dziedzic, J. E. Bjorkholm, and S. Chu, *Observation of a single-beam gradient force optical trap for dielectric particles.* Opt. Lett., vol. 11, pp. 288-290, 1986.

[9] N. Osterman, *TweezPal - Optical tweezers analysis and calibration software*, Comp. Phys. Commun., vol. 181, pp. 1911-1916, 2010.

[10] A. Ashkin, *Forces of a single-beam gradient laser trap on a dielectric sphere in the ray optics regime.* Biophysical journal, vol. 61, pp. 569-582, 1992.

[11] J. W. Shaevitz, *A practical guide to optical trapping.* University of Washington, 2006.

[12] I. Muševič, M. Škarabot, D. Babič, N. Osterman, I. Poberaj, V. Nazarenko and A. Nych, *Laser trapping of small colloidal particles in a nematic liquid crystal: clouds and ghosts.* Phys. Rev. Lett., vol. 93, pp. 187801, 2004.

[13] M. Škarabot, M. Ravnik, D. Babič, N. Osterman, I. Poberaj, S. Žumer, I. Muševič, A. Nych, U. Ognysta and V. Nazarenko, *Laser trapping of low refractive index colloids in a nematic liquid crystal.* Phys. Rev. E, vol. 73, pp. 021705, 2006.

[14] I. I. Smalyukh, A. V. Kachynski, A. N. Kuzmin, and P. N. Prasad, *Laser trapping in anisotropic fluids and polarization-controlled particle dynamics.* Proc. Nat. Acad. Sci., vol. 103, pp. 18048-18053, 2006.

[15] R. P. Trivedi, D. Engstrom and I. I. Smalyukh, *Optical manipulation of colloids and defect structures in anisotropic liquid crystal fluids.* J. Opt., vol. 13, pp. 044001, 2011.

[16] I. Muševič, M. Škarabot, U. Tkalec, M. Ravnik and S. Žumer, *Two dimensional nematic colloidal crystals self-assembled by topological defects.* Science, vol. 313, pp. 954-958, 2006.

[17] U. Ognysta, A. Nych, V. Nazarenko, M. Škarabot and I. Muševič, *Design of 2D Binary Colloidal Crystals in a Nematic Liquid Crystal.* Langmuir, vol. 25, pp. 12092-12100, 2009.

3

Electrophoresis of metal-dielectric Janus particles with quadrupolar director field: Particles with equatorial ring defects

3.1 Introduction

Electrophoresis, the use of electric fields to transport tiny particles through fluids, is an important technology for macro-molecular sorting, colloidal assembly and display devices and a challenging area of soft-matter research [1–8]. As discussed in chapter-1, classic electrophoresis is linear where ions in the electrical double layer drag the fluid, and hence the particle propels with a velocity proportional to and along the applied field direction. However, induced-charge electroosmosis (ICEO) of particles is nonlinear where the applied field itself creates the double layer. Polarity in the shape or surface properties of the particle results in a flow pattern that picks out a direction of motion, with velocity quadratic in and normal to the field as discused in chapter-2 [9–13]. Neither effect offers the option of continously tuning the direction of transport and hence the desired motility of the microscopic particles. Thus, the controlled motility and navigational ability of the microscopic particles is still challenging [14,15].

When the ambient fluid is a nematic liquid crystal (NLC), the anchoring of the mean molecular orientation or director $\hat{\mathbf{n}}$ normal to the surface of a suspended homogeneous spherical particle mandates Saturn-ring [16, 17] or asymmetric [18, 19] defect structures, resulting, respectively, in quadrupolar or dipolar elastic distortions in the NLC (see chapter-1). The nonlinear electro-osmotic flow resulting from an imposed electric field yields transport of dipolar particles parallel to the local director, thanks to their broken fore-aft symmetry, an effect termed liquid crystal-enabled electrophoresis (LCEEP) [20–24] as dicussed in chapter-1. The Saturn-ring particles, by contrast, maintain the quadrupolar symmetry of the flow as shown in Fig.3.1 and hence display no motility [23, 24].

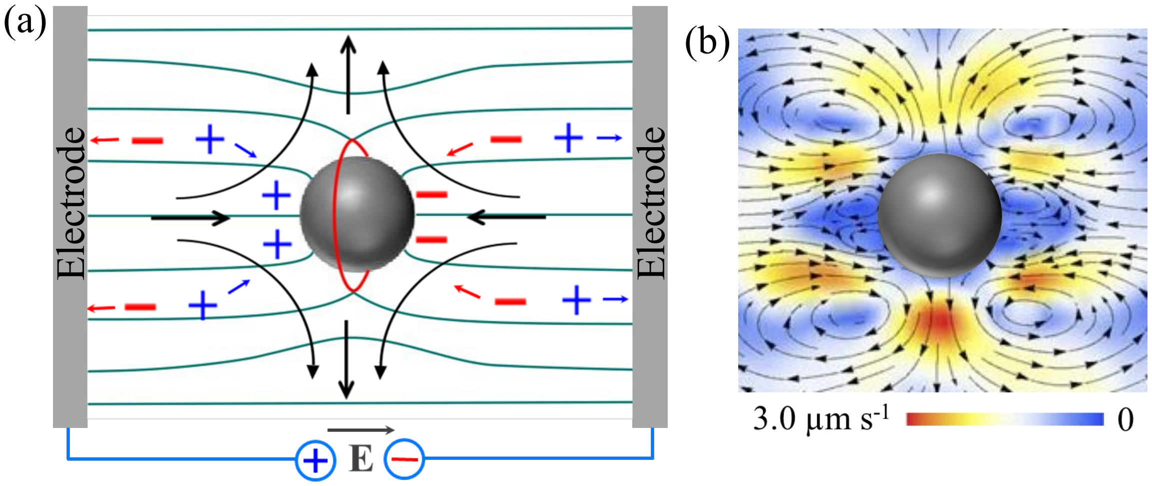

Figure 3.1: (a) A quadrupolar particle (with Saturn ring) under in-plane electric field. (b) Directional streamlines of electroosmotic flows around the same particle (adapted from ref. [24]).

In this chapter, we focus on spherical particles with two hemispherical faces, one metal, the other dielectric. Their “Janus” character is sensed only by the electrostatics of the medium; as far as the mechanics of the ambient NLC is concerned they are elastic quadrupoles. Our central result is that purely by tuning the amplitude and frequency of an imposed electric field, and not its direction, we can achieve guided transport of quadrupolar Janus colloids in the direction of our choosing perpendicular to the field, amounting to a realization of controllable active particles [25].

3.2 Experimental

We prepared metal-dielectric Janus particles using directional deposition of metal (Ti) onto dry silica (SiO_2) particles as discussed in the chapter-2. The surface of Janus particles was coated with N, N-dimetyl-N-octadecyl-3 aminopropyl-trimethoxysilyl chloride (DMOAP) in order to induce perpendicular (homeotropic) orientation of the liquid crystal director. A schematic diagram showing successive coatings is presented in Fig3.2(a). A small quantity (0.5 wt%) of DMOAP coated Janus particles was dispersed in nematic liquid crystal, MLC-6608 (SmA -30° N 90° Iso). The liquid crystal obtained from Merck wass used directly without any further purification. The dielectric anisotropy of MLC-6608 is negative ($\Delta\epsilon = \epsilon_{\parallel} - \epsilon_{\perp} = -4.2 \pm 0.1$, where $\epsilon_{\parallel}$ and $\epsilon_{\perp}$ are the dielectric permittivities for electric field E, parallel and perpendicular to $\hat{n}$, respectively) whereas the conductivity anisotropy is positive ($\Delta\sigma = \sigma_{\parallel} - \sigma_{\perp} \simeq 6 \times 10^{-10}$ Sm^{-1} at 100 Hz). There is no electroconvection observed in the experimental field and

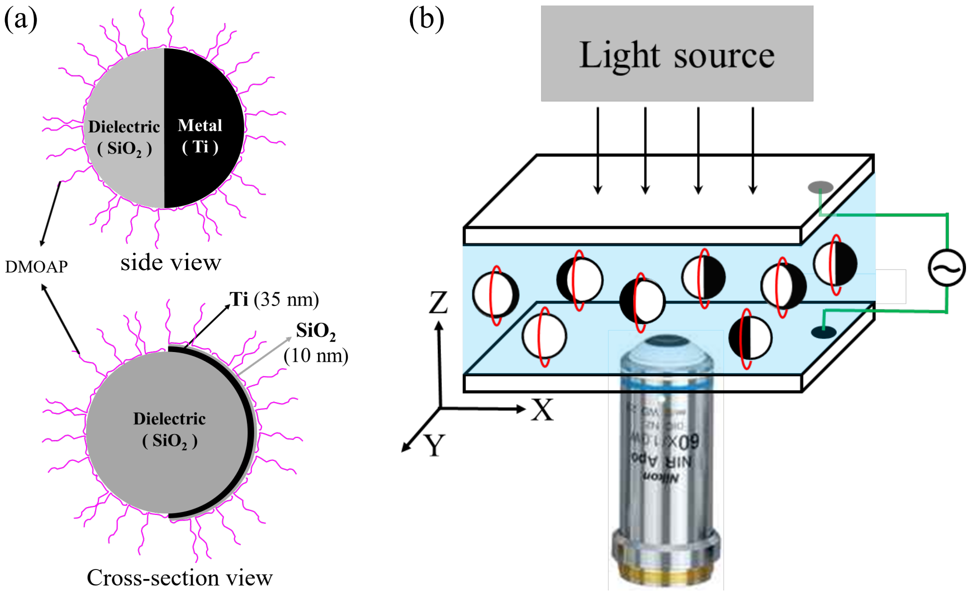

Figure 3.2: (a) Side and cross-section views of a metal-dielectric Janus particle prepared by coating 35 nm Ti layer on SiO_2 microparticle. On top of Ti, 10 nm of SiO_2 is coated. Magenta color strands represent DMOAP molecules, which are anchored to the particle's surface. (b) Diagram of the experimental cell. The electric field is applied along the *z*-direction. Red circles indicate ring defects encircling the Janus particles.

frequency range. An inverted polarising optical microscope (Nikon Ti-U) with water immersion objective (Nikon, NIR Apo 60/1.0) was used for observing the particles as shown schematically in Fig.3.2(b). An infrared laser tweezers setup as described in chapter-2 was used for manipulating particles. A charge-coupled device (CCD) video camera (iDs-UI) at a rate of 50-100 frames per second was used for video recording of the particle trajectory. A particle tracking program was used off-line to track the centers of the particles, with an accuracy of ±20 nm.

3.3 Results and discussion

Macroscopic alignment of the LC director in the x direction is imposed by the treated surfaces of the bounding electrodes parallel to the xy plane (Fig.3.2(b)). Their separation is larger than, but close to, the diameter $2a$ of the suspended particles, which produce a quadrupolar elastic field in the nematic (Fig.3.3(a)). We work in the dilute regime (0.5 wt%) and do not consider cases of higher concentration where aggregation and network formation are important [27, 28]. Due to the elastic distortion of the director, the particles resist sedimentation and levitate in the bulk as discussed in the chapter-1 [29]. This feature, and therefore liquid crystal enabled electrophoresis (LCEEP) as well, is absent in the isotropic phase. As the dielectric anisotropy of the

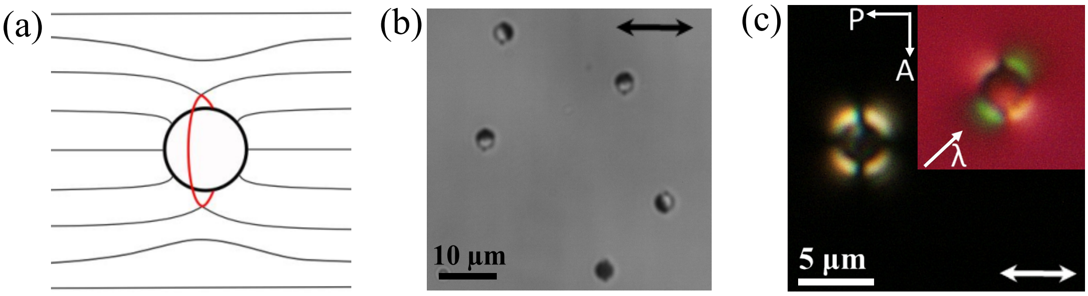

Figure 3.3: (a) Quadrupolar distortion of nematic director around a spherical particle. Red circle represents Saturn-ring defect. (b) Janus quadrupolar particles in a planar cell. The dark hemisphere represents metal. (c) Optical microscope texture of a Janus quadrupolar particle in the NLC between crossed polariser (P) and analyser (A) in the xy plane. (Inset) Texture with a λ-plate (530 nm) with it's slow axis kept at 45° with respect to the director $\hat{\mathbf{n}}$, shown by double headed arrows.

sample is negative, the applied electric field **E** in the z direction does not influence the macroscopic director except near the particles [23]. Figure 3.3(b) shows bright image of a few Janus quadrupolar particles with their metal hemisphere oriented in different directions, always keeping the Saturn rings perpendicular to the macroscopic director. Figure 3.3(c) shows the optical microscope texture of a Janus quadrupolar particle with cross polarisers. The four-lobed intensity pattern of the particle, a characteristic feature of elastic quadrupole, was further substantiated by the texture obtained by inserting a λ-plate (inset of Fig.3.3(c)).

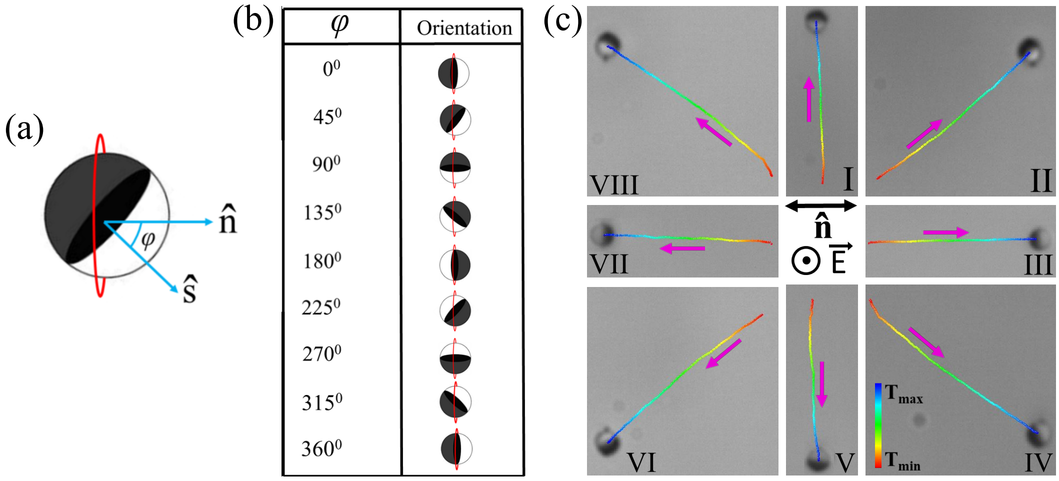

Figure 3.4: (a) φ is the angle between the director $\hat{\mathbf{n}}$ and Janus axis $\hat{\mathbf{s}}$ (normal to the metal-dielectric interface). (b) Selected orientation of a particle in the xy plane at different φ. (c) Time coded trajectories (T_{min} =0s to T_{max}=5s), labelled from I to VIII, under AC electric field (1.54 Vμm^{-1}, 30 Hz). Trajectories of selected particles are grouped. Pink arrows denote the direction of motion. The direction of electric field, **E** and the director ($\hat{\mathbf{n}}$) for all trajectories are shown at the center. Cell thickness: 5.2μm.

Once the AC electric field is switched on, the particles reorient so that the plane of the metal-dielectric interface lies parallel to the field due to the induced dipole moment which will be discussed in details in chapter-6 (Fig.3.2(b)). With increasing field, they start moving in specific directions in the plane of the sample, depending on the orientation of the Janus vector $\hat{\mathbf{s}}$, a unit normal vector to the metal-dielectric interface as shown in Fig.3.4(a). Real-time trajectories of selected particles shown in Fig.3.4(b) are grouped and presented in Fig.3.4(c). The dielectric hemispheres (Fig.3.4(c), III and VII) lead when movement is parallel to, and the metal hemisphere (Fig.3.4(c), I and V) when it is perpendicular to, the macroscopic director. For particles moving at other angles the Janus vector $\hat{\mathbf{s}}$ interpolates smoothly between these two extremes as shown in Fig.3.4(e), II, IV, VI and VIII. This implies that the angle between the Janus vector and far field director decides the direction of transport of particle. Often we used the laser tweezers setup to fine-tune the orientation of Janus vector and achieve the omnidirectioal transport of the particles as shown in Fig.3.5. For all trajectories, the velocity shows a quadratic dependence on the applied field indicating the non-linear behavior of liquid crystal-enabled electrophoresis (LCEEP). For example, Fig.3.6 shows the field dependent velocity of Janus particles in trajectories-III, I and II (Fig.3.4(c)). In all these trajectories $v \propto E^2$, with their respective slopes given by 3.5 ± 0.1 µm^{3}V^{-2}s^{-1}, 2.1 ± 02 µm^{3}V^{-2}s^{-1} and 3.6 ± 0.1 µm^{3}V^{-2}s^{-1}. The slope of v_x is greater than that of v_y as the particles can move easily along the director rather than

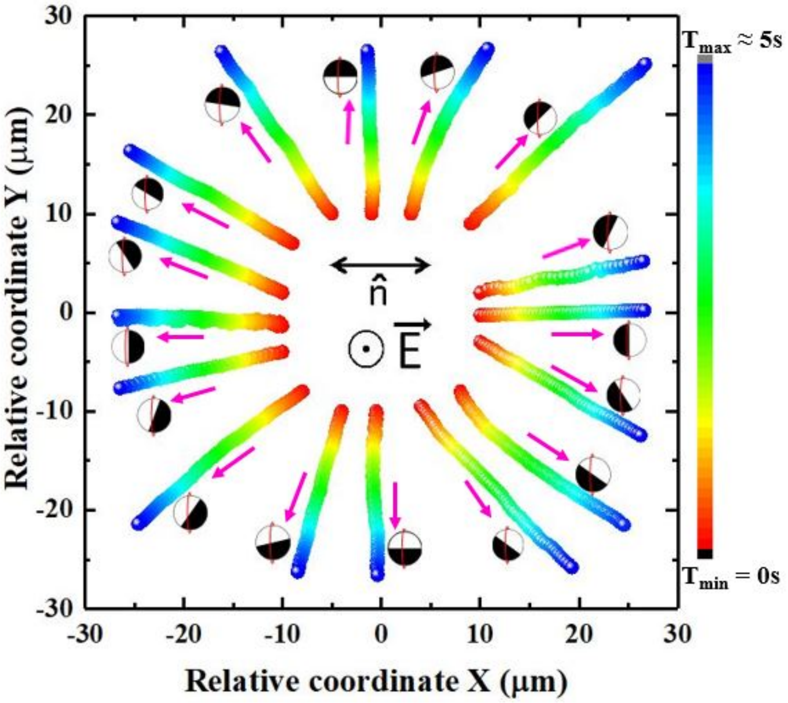

Figure 3.5: Time coded trajectories of particles in many directions. Directions of $\hat{n}$ and E (f = 30 Hz, E = 1.54 Vµm^{-1}) are shown in the central region. Magenta arrows indicate the direction of motion of the particles. By relative coordinate we mean relative to the starting point of each trajectory. Cell thickness: 5.2 µm.

in the perpendicular direction.

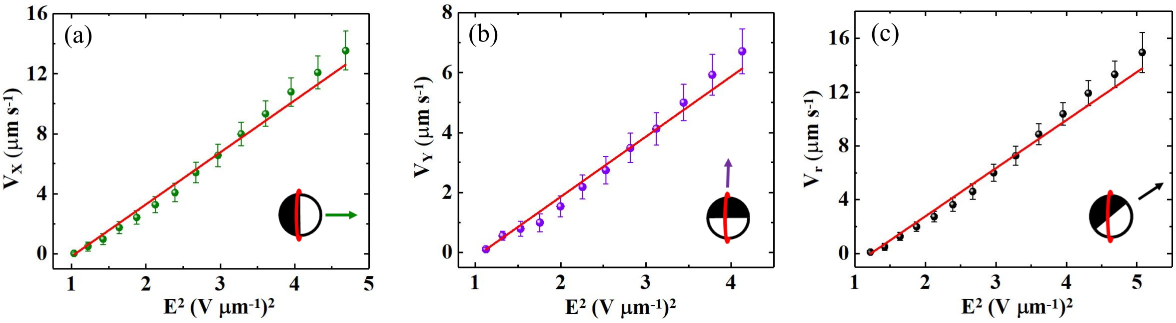

Figure 3.6: Electric field dependent velocity of particles in (a) trajectory-III (v_x), (b) trajectory-I (v_y) and (c) trajectory-II (v_r) (see Fig.3.4(f)). Arrows near the spheres indicate the direction of motion. Solid lines show least squares fit to $v \propto E^2$. Frequency = 30 Hz. Error bars represent the standard deviation of the mean value. Cell thickness: 5.2μm.

To understand the motility of a Janus particle in an AC electric field we calculate the electrostatic force density induced by the field in the region around the particle. This force density drives fluid flow over the surface of the particle in such a way as to turn the particle into a swimmer, as sketched in Fig.3.8.

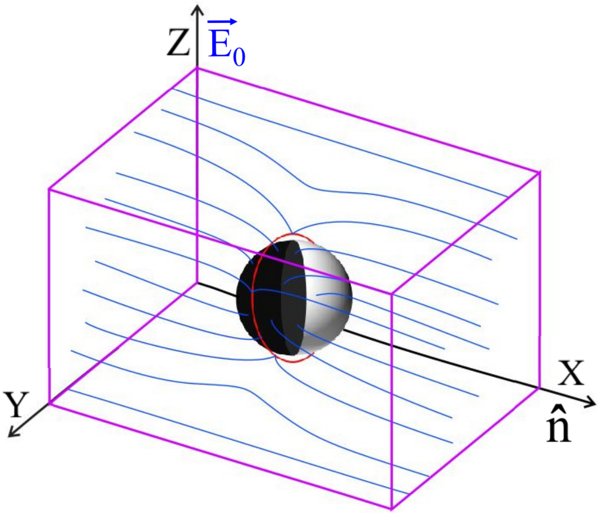

Figure 3.7: Quadrupolar director field surrounding a Janus particle. Applied electric field **E** is transverse to the director. Red circle denotes Saturn ring defect. The dark hemisphere represents metal.

3.3. Results and discussion

We consider a single spherical Janus particle of radius a in a NLC. The particle's surface consists of a conducting and a dielectric hemisphere, both of which are taken to impose identical uniform homeotropic surface anchoring on the ambient nematic, so as to produce an elastic quadrupolar distortion in the director field, that is, a radial hedgehog compensated by a Saturn ring defect. An electric field $\mathbf{E_0}$ along z is externally imposed on the system as shown in Fig.3.7. The mean macroscopic director field lies parallel to the x axis and local deviations from this mean direction are described by an angle θ, positive for counterclockwise rotation. We consider a system with conductivities $\sigma_{||}$, $\sigma_{\perp}$ and dielectric constants $\epsilon_{||}$, $\epsilon_{\perp}$, for electric fields parallel $(||)$ and perpendicular $(\perp)$ to the director $\hat{\mathbf{n}}$, and define the anisotropies $\Delta\sigma = \sigma_{||} - \sigma_{\perp}$ and $\Delta\epsilon = \epsilon_{||} - \epsilon_{\perp}$. Our strategy, generalizing [24], is to use charge conservation and Gauss's law to obtain the total electric field $\mathbf{E}$ and the charge density ρ and thus the electrostatic force density $\mathcal{F}(\mathbf{r}) = \rho(\mathbf{r})\mathbf{E}(\mathbf{r})$, separately for the case of a dielectric and a conducting sphere and to combine these results to infer the character of the induced flow around the Janus sphere.

For our particles of radius $a \simeq 1.5$ µm moving at speed $v \simeq 10$ µm s^{-1} through a liquid crystal of mass density $\rho \simeq 10^3$ kg m^{-3}, shear viscosity $\eta \simeq 0.02$ Pa.s, Frank elastic constants $K \simeq 20$ pN (values quoted by supplier Merck for MLC-6608), Reynolds number $\mathrm{Re} = \rho v a/\eta \simeq 10^{-7}$, and Ericksen number $\mathrm{Er} = \eta v a/K \simeq 10^{-2}$. We can therefore ignore the effect of fluid inertia and we can take the director configuration around the particles to be negligibly influenced by fluid flow. As in [24], we work at zero Peclet number, i.e., take the charge currents to be purely Ohmic and not advected by fluid flow. For simplicity we work at low frequencies so that time dependence can be neglected in the induction equation and thus the electric field $\mathbf{E} = -\nabla\Psi$ where Ψ is a potential. We work to first order in the anisotropies $\Delta\sigma$ and $\Delta\epsilon$. We begin by evaluating the potential for a conducting or dielectric particle in the absence of anisotropy, for which the electrostatic boundary conditions imply

$$\Psi_0 \equiv -E_0 z + \lambda E_0 \Phi \equiv -E_0 z + \lambda \frac{E_0 a^3 z}{r^3}, \tag{3.1}$$

$$\lambda = \begin{cases} 1, & \text{conductor,} \\ \dfrac{\epsilon_r - 1}{\epsilon_r + 2} < 1, & \text{dielectric,} \end{cases}$$

where ϵ_r is the dielectric constant.

To calculate the induced charge density in the nematic due to anchoring, we impose steady-state charge conservation $\nabla \cdot \mathbf{J} = 0$ for a current $\mathbf{J} = \boldsymbol{\sigma} \cdot \mathbf{E} = (\sigma_\perp \mathsf{I} + \Delta\sigma \hat{\mathbf{n}}\hat{\mathbf{n}}) \cdot (-\nabla\Psi)$, where I is the unit tensor. This implies

$$(\sigma_\perp \mathsf{I} + \Delta\sigma \hat{\mathbf{n}}\hat{\mathbf{n}}) : \nabla(\nabla\Psi) = -\Delta\sigma(\hat{\mathbf{n}}\nabla \cdot \hat{\mathbf{n}} + \hat{\mathbf{n}} \cdot \nabla\hat{\mathbf{n}}) \cdot \nabla\Psi, \tag{3.2}$$

where the colon : denotes contraction with both indices of $\nabla(\nabla\Psi)$. For small deviations $\delta\hat{\mathbf{n}}$ about a mean alignment $\hat{\mathbf{n}}_0$, and corresponding deviations $\delta\mathbf{E}$ from a field $\mathbf{E} = -\nabla\Psi_0$ imposed from the boundaries, writing $\delta\mathbf{E} = -\nabla\delta\Psi$ in terms of a potential $\delta\Psi$, (3.2) becomes

$$\begin{aligned}(\sigma_\perp \nabla_\perp^2 + \sigma_{||}\nabla_{||}^2)\Psi = -\Delta\sigma\Big[(\hat{\mathbf{n}}_0\nabla \cdot \delta\hat{\mathbf{n}} + \hat{\mathbf{n}}_0 \cdot \nabla\delta\hat{\mathbf{n}}) \cdot \nabla\Psi_0 + \\ (\hat{\mathbf{n}}_0\delta\hat{\mathbf{n}} + \delta\hat{\mathbf{n}}\hat{\mathbf{n}}_0) : \nabla(\nabla\Psi_0)\Big]\end{aligned} \tag{3.3}$$

where $||$ and $\perp$ denote components along and transverse to $\hat{\mathbf{n}}_0$ and $\Psi = \delta\Psi + \Psi_0$. Next, Gauss's Law $\rho = \nabla \cdot \mathbf{D} = \epsilon_0\nabla \cdot (\boldsymbol{\epsilon}\mathbf{E})$ reads, in the same linearized approximation,

$$\begin{aligned}\rho = -\epsilon_0(\epsilon_\perp\nabla_\perp^2 + \epsilon_{||}\nabla_{||}^2)\Psi - \epsilon_0\Delta\epsilon\Big[(\hat{\mathbf{n}}_0\nabla \cdot \delta\hat{\mathbf{n}} + \\ \hat{\mathbf{n}}_0 \cdot \nabla\delta\hat{\mathbf{n}}) \cdot \nabla\Psi_0 + (\hat{\mathbf{n}}_0\delta\hat{\mathbf{n}} + \delta\hat{\mathbf{n}}\hat{\mathbf{n}}_0) : \nabla(\nabla\Psi_0)]\end{aligned} \tag{3.4}$$

Solving (3.3) for Ψ allows us to write the force density

$$\begin{aligned}\boldsymbol{\mathcal{F}} = \rho\mathbf{E} \simeq \epsilon_0(-\Delta\epsilon + \Delta\sigma G_\epsilon^{-1}G_\sigma)\Big[(\hat{\mathbf{n}}_0\nabla \cdot \delta\hat{\mathbf{n}}\hat{\mathbf{n}}_0 \cdot \nabla\delta\hat{\mathbf{n}})\cdot \\ \nabla\Psi_0 + (\hat{\mathbf{n}}_0\delta\hat{\mathbf{n}} + \delta\hat{\mathbf{n}}\hat{\mathbf{n}}_0) : \nabla(\nabla\Psi_0)\Big]\mathbf{E}_0\end{aligned} \tag{3.5}$$

where we have defined the Green's functions

$$G_\sigma = (\sigma_\perp\nabla_\perp^2 + \sigma_{||}\nabla_{||}^2)^{-1} \tag{3.6}$$

and

$$G_\epsilon = (\epsilon_\perp\nabla_\perp^2 + \epsilon_{||}\nabla_{||}^2)^{-1}. \tag{3.7}$$

At the lowest order in $\delta\hat{\mathbf{n}}$ the charge density is driven by the externally imposed electric field $\mathbf{E}_0$. We show below that the second term (which we call $\boldsymbol{\mathcal{F}_{II}}$) in brackets on the right-hand side of (3.5) contributes only a higher multipole to the force density. The force density thus takes the form

$$\boldsymbol{\mathcal{F}} \simeq \epsilon_0(-\Delta\epsilon + \Delta\sigma G_\epsilon^{-1}G_\sigma)\Big[(\hat{\mathbf{n}}_0\nabla \cdot \delta\hat{\mathbf{n}} + \hat{\mathbf{n}}_0 \cdot \nabla\delta\hat{\mathbf{n}}) \cdot \nabla\Psi_0\Big]\mathbf{E}_0 \tag{3.8}$$

It is useful to decompose the force density as $\boldsymbol{\mathcal{F}} = \boldsymbol{\mathcal{F}}_0 + \boldsymbol{\mathcal{F}}_\lambda$ where $\boldsymbol{\mathcal{F}}_0$ is a contribution independent of whether the sphere is dielectric or conducting, while $\boldsymbol{\mathcal{F}}_\lambda$ depends, through λ, on the electrical nature of the sphere:

$$\boldsymbol{\mathcal{F}}_{\mathbf{0}} \simeq -\epsilon_0(-\Delta\epsilon + \Delta\sigma G_\epsilon^{-1} G_\sigma)(\hat{\mathbf{n}}_0 \nabla \cdot \delta\hat{\mathbf{n}} + \hat{\mathbf{n}}_0 \cdot \nabla\delta\hat{\mathbf{n}}) \cdot \hat{\mathbf{z}} E_0^2 \hat{\mathbf{z}} \tag{3.9}$$

and

$$\boldsymbol{\mathcal{F}}_{\boldsymbol{\lambda}} \simeq \epsilon_0 \lambda(-\Delta\epsilon + \Delta\sigma G_\epsilon^{-1} G_\sigma)(\hat{\mathbf{n}}_0 \nabla \cdot \delta\hat{\mathbf{n}} + \hat{\mathbf{n}}_0 \cdot \nabla\delta\hat{\mathbf{n}}) \cdot \nabla\Phi E_0^2 \hat{\mathbf{z}} \tag{3.10}$$

where Φ is defined in (3.1) above, and $\boldsymbol{\mathcal{F}}_0$ is the same for both dielectric and conducting surfaces, while the symmetry breaking piece is $\boldsymbol{\mathcal{F}}_\lambda$. From (3.9) and (3.10), we see that the effect is proportional to the square of the electric field and thus survives time averaging over a period. Also from (3.10), the force dipole is larger for a conducting sphere than for a dielectric sphere by a factor of $1/\lambda$. Therefore, for a Janus particle, the center of the force dipole shifts from the geometric center towards the conducting side, breaking the symmetry and hence rendering the particle motile in an applied AC electric field.

For Fig.3.7, we consider a local Cartesian coordinate system and small-angle approximation, $\hat{\mathbf{n}}_0 \simeq \hat{\mathbf{x}}$ and $\delta\hat{\mathbf{n}} \sim (0, \theta(x, z))$. The second term in (3.5) reduces to $\boldsymbol{\mathcal{F}}_{\boldsymbol{II}} \simeq 2\epsilon_0(-\Delta\epsilon + \Delta\sigma G_\epsilon^{-1} G_\sigma)\partial_x\theta\partial_z\Psi_0\mathbf{E}_0$, with signs $(- + -+)$ for positive z and $(+ - +-)$ for negative z, as one moves from positive x towards negative x, and hence has only a higher multipole contribution. The force density of (3.8), on the other hand, reads,

$$\boldsymbol{\mathcal{F}} \simeq \epsilon_0(-\Delta\epsilon + \Delta\sigma G_\epsilon^{-1} G_\sigma)\left(\frac{\partial\theta}{\partial z}\frac{\partial\Psi_0}{\partial x} + \frac{\partial\theta}{\partial x}\frac{\partial\Psi_0}{\partial z}\right) E_0 \hat{\mathbf{z}} \tag{3.11}$$

In Fig.3.7 we see that the director curvatures in (3.11) are composed of bend concentrated just outside the Saturn ring ($\partial_x\theta$) coupled to ($\partial_z\Psi_0$) and splay on the particle surface ($\partial_z\theta$) coupled to ($\partial_x\Psi_0$). We see that the signs in the four quadrants are $\partial_x\theta$ $(- - ++)$, $\partial_z\Psi_0$ $(- - - -)$, $\partial_z\theta$ $(+ - -+)$, and $\partial_x\Psi_0$ $(- + -+)$. From (3.6) and (3.7) we see that although $G_\epsilon^{-1} G_\sigma$ has a nonlocal piece decaying as $1/r^3$, it is formally a positive operator if examined in Fourier space. For our system $\Delta\epsilon < 0$ and $\Delta\sigma > 0$. Therefore, the splay contribution produces a force dipole of the contractile or puller type, while the bend produces a force dipole of the extensile or pusher type with respect to the electric-field axis.

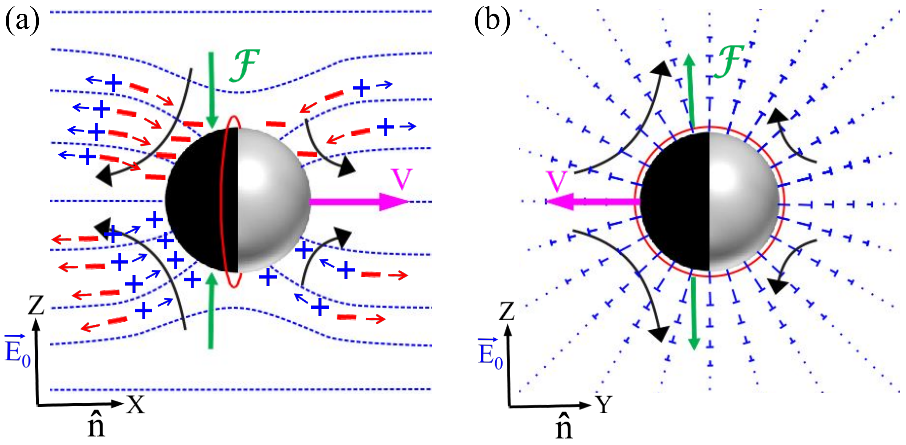

Figure 3.8: Liquid crystal-enabled electroosmotic flows around a quadrupolar Janus particle in two orthogonal planes parallel to the electric field. Red circles represent Saturn-ring defects. The dark hemisphere represents metal. The large curved arrows on the metal hemisphere indicate stronger flows. The off-centered force dipoles $\boldsymbol{\mathcal{F}}$ (shown in green colour) are (a) pullers and (b) pushers. The propulsion direction of the particles is indicated by a pink arrow for (a) Trajectory III/VII (b) Trajectory I/V.

Given that the electric field, via Eq.(3.11), results in a force density along z, we can understand trajectory III and VII (see Fig.3.4(c)) by asking how the Janus character breaks symmetry in the xz plane. In this plane, the splay contribution is greater than the bend as it is present over a larger part of the particle surface. Shifting the force dipole towards the metallic side yields a puller-type force dipole resulting in motility with the dielectric face forward as shown in Fig.3.8(a). To test whether this idea makes sense let us apply it to the case of trajectories I and V in Fig.3.4(c). Here the breaking of symmetry in the yz plane is of relevance. Bend all along the Saturn ring is in play, which gives a pusher force dipole. Shifting this towards the metal face results in motility with the conductor face forward as shown in Fig.3.8(b). The consistency of our explanation for the cases of Janus axis parallel and perpendicular to the macroscopic nematic alignment is reassuring. For other trajectories motility is due to a combination of both the effects stated above and therefore interpolates in direction.

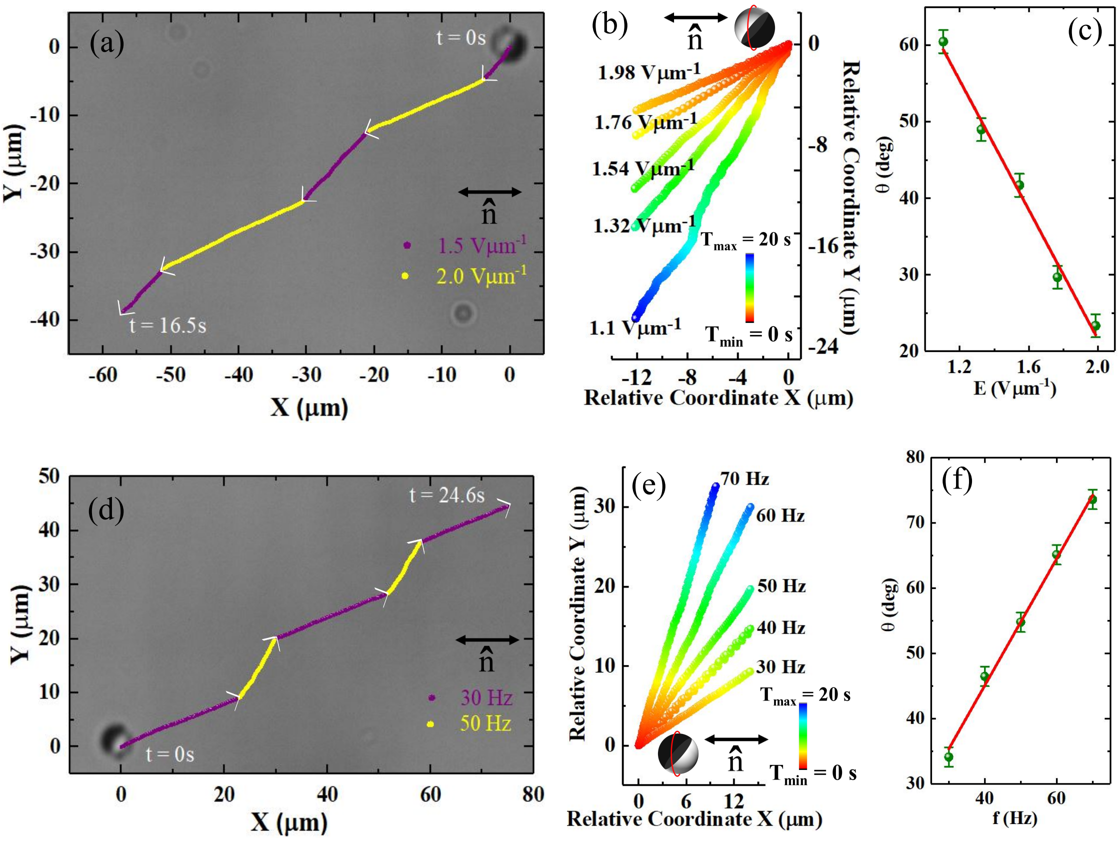

Figure 3.9: (a) Change of direction of motion of a quadrupolar Janus particle by altering the field amplitude recursively between 1.5 Vμm^{-1} (purple) to 2.0 Vμm^{-1} (yellow), keeping the frequency constant at 30 Hz. Arrows indicate the direction of motion. (b) Time-coded trajectories of a particle at different field amplitudes and fixed frequency (30 Hz). (c) Angle between the trajectory and the director (θ) decreases linearly with field at a slope of $-43.2 \pm 2.3°$μmV^{-1}. (d) Change of direction of motion of a particle by altering the frequency recursively between 30 Hz (purple) to 50 Hz (yellow), keeping the field amplitude constant at 1.5 Vμm^{-1}. (e) Time coded trajectories of a particle at different frequencies and fixed amplitude (1.5 Vμm^{-1}). (f) θ increases linearly with f at a slope of $1 \pm 0.05°$ Hz^{-1}. By "relative coordinate" we mean relative to the starting point of each trajectory. Error bars represent the standard deviation of the mean value. Cell thickness: 5.2μm.

When the Janus vector $\hat{\mathbf{s}}$ is oriented neither parallel nor perpendicular to $\hat{\mathbf{n}}$, its direction of motion can be controlled by changing the amplitude and frequency of the field as shown in Figs.3.9(a) and (d), respectively. The moving direction is changed recursively at different points (Fig.3.9(a)) by altering the field amplitude between 1.5 Vμm^{-1} to 2.0 Vμm^{-1} at a fixed frequency. Figure 3.9(b) shows the trajectories of a Janus particle at different fields for a fixed orientation of the metal-dielectric interface. The angle θ their velocity makes with the director $\hat{\mathbf{n}}$ decreases with increasing field (Fig.3.9(c)), with a linear dependence over the range explored. Figure 3.9(d) shows the variation in direction of motion along a trajectory as the frequency is changed from 30 to 50 Hz at a fixed field amplitude. Figure 3.9(e) shows the trajectories of a particle at various frequencies in which θ increases linearly (Fig.3.9(f)).

Particles with appropriately chosen orientation of the Janus vector can be transported to any predetermined place in the plane of the sample by varying the amplitude and frequency of the AC field. Figure 3.10(a) shows the trajectory of a particle whose Janus vector $\hat{\mathbf{s}}$ is oriented at an angle φ = 135° with respect to $\hat{\mathbf{n}}$. The particle is

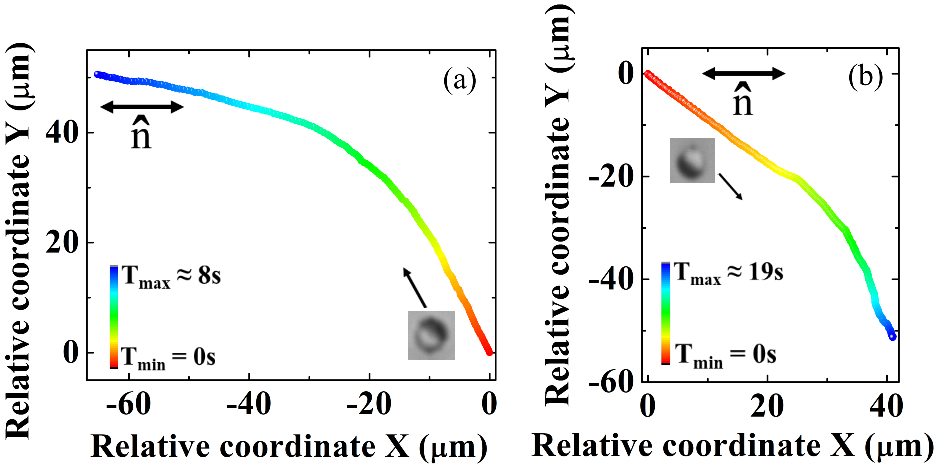

Figure 3.10: (a) A particle with φ = 135° is piloted to a predetermined place by changing the amplitude of the field. The field amplitude is increased in a continuous manner from 1.2 Vμm^{-1} to 2.0 Vμm^{-1}, keeping the frequency fixed at 30 Hz. (b) A particle with φ = 315° is transported to a predetermined place by increasing the frequency in a continuous manner from 20 to 90 Hz, keeping the amplitude fixed at 1.6 Vμm^{-1}. The arrows near the particles show the initial direction of motion. Cell thickness: 5.2μm.

piloted to a predetermined location on the left with respect to the starting point by increasing the amplitude of the field at a fixed frequency. Similarly, a particle with $\varphi = 315°$ is guided to a specified destination by increasing the frequency while keeping the amplitude fixed (see Fig.3.10(b)). In both cases the direction of motion changes continuously while the orientation of the Janus vector $\hat{\mathbf{s}}$ remains unchanged.

To understand the navigation of the Janus quadrupolar particles, we measured the field dependence of the velocity (see Fig.3.6). The motion of the particles shown in Fig.3.9(a) and (d) has two velocity components, namely, V_x and V_y, along the x and y directions, respectively, both of which are proportional to E^2, but the slope of V_x is larger than V_y (see Fig.3.11(a)).

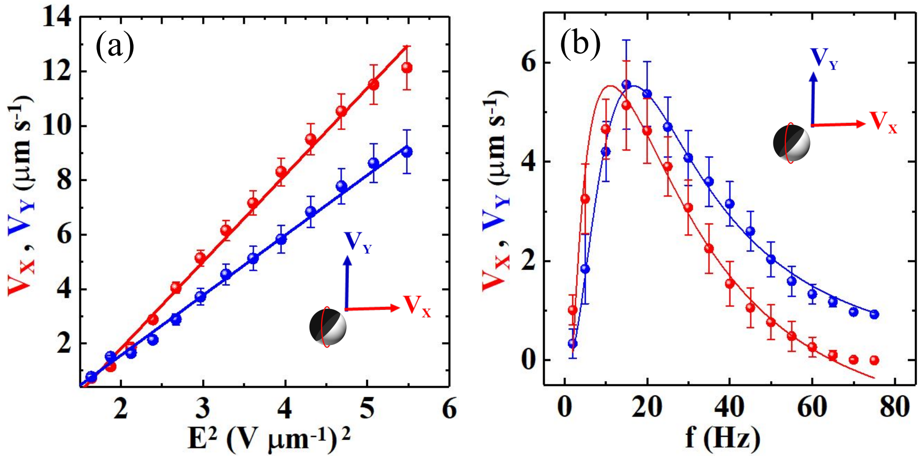

Figure 3.11: (a) Dependence of velocity components V_x and V_y of a Janus particle (trajectory-II, Fig.3.4(f)) on electric-field amplitude E at f=30Hz. Solid lines show least-squares fit to $V \propto E^2$. Slopes of V_x and V_y are 3.2 μm^{3}V^{-2}s^{-1} and 2.2 μm^{3}V^{-2}s^{-1} respectively. (b) Frequency dependent ($E = 1.54$ Vμm^{-1}) velocity components V_x and V_y. Red and blue lines show theoretical fit to Eq.4.12. Fit parameters are: $\tau_e = 0.25$ s, $\tau_p = 0.032$ s for V_x and $\tau_e = 0.08$ s, $\tau_p = 0.04$ s for V_y. Error bars represent the standard deviation of the mean value. Cell thickness: 5.2μm.

When the field is increased, the relative enhancements are unequal, i.e., ΔV_x is larger than ΔV_y, and consequently, $\theta = \tan^{-1}(\Delta V_y/\Delta V_x)$ decreases. The velocity components also depend strongly on the frequency (f) of the field (see Fig.3.11(b)). Both the components show a typical frequency dependence of non-linear electrophoresis as described in the chapter-1 and given by [11, 23]

$$V_i(\omega) = V_{0,i}\frac{\omega^2\tau_e^2}{(1+\omega^2\tau_p^2)(1+\omega^2\tau_e^2)} \tag{3.12}$$

where $i = x, y$; $\omega = 2\pi f$ is the angular frequency of the applied field, τ_e and τ_p are the characteristic electrode and particle charging time, respectively. Both the velocity components increase as f^2 in the low-frequency regime but decrease as f^{-2} at higher frequencies because the ions cannot follow the rapidly changing field. For frequencies above 15 Hz both V_x and V_y are proportional to $1/f^2$ but the coefficient of the decrease in V_x is larger than that for V_y, resulting in an increase in the angle θ when f is increased.

Chiral ordering of the liquid crystals often alters the defect structure induced by the particles, with a possible impact on the liquid crystal-enabled electrophoresis. Further, we studied the effect of twisted nematic on the directional transport of Janus quadrupolar particles. In order to examine, we dispersed quadrupolar Janus particles in a twisted cell, which is prepared by arranging the rubbing directions orthogonal to each other as shown in Fig.3.12(a). This provides a π/2-twisted director configuration between the two plates. The handedness of the twisted structure is determined by

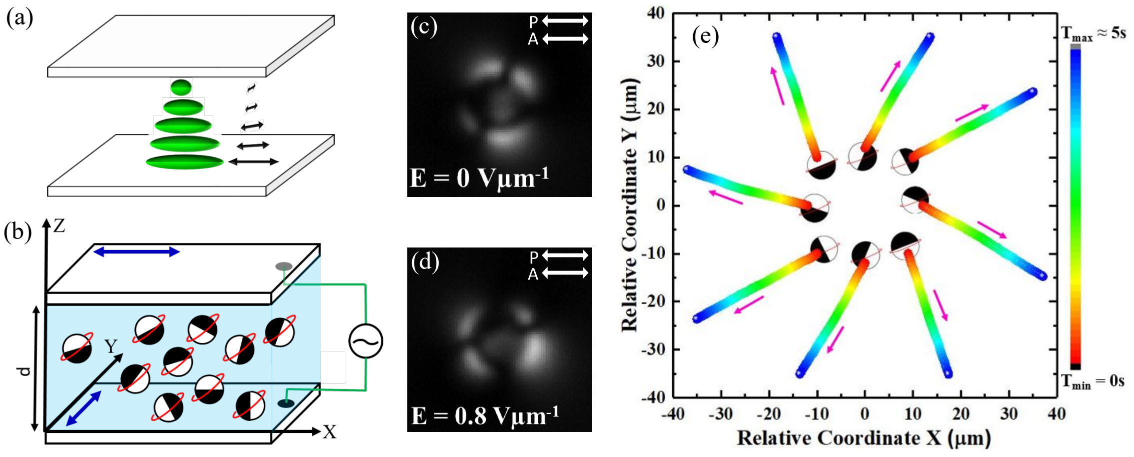

Figure 3.12: (a) Layout of π/2-twisted nematic cell. Blue arrows indicate orthogonal rubbing directions. (b) Light-microscope texture of a quadrupolar particle at $E = 0$ Vμm^{-1}, with polarizer P and analyser A, both being parallel to the bottom plate. (c) Refocused texture in twisted cell after the field is switched on. (d) Time coded trajectories of a few particles are grouped. (T$_{\text{min}}$ = 0 s, T$_{\text{max}}$ = 5 s)

inserting a $\lambda-$plate (530 nm) in the polarising optical microscope. The plane of the Saturn ring is found to be rotated clockwise (Fig.3.12(b)and (c)) in comparison to the orientation in untwisted cell (see Fig.3.3(c)). Once the field is switched on, the particle move slightly to the bottom plate and the Saturn ring is further rotated nearly by 45^0, while going in the downward direction (Fig.3.12(d)). Then, it starts moving along a trajectory which depends on the orientation of the metal-dielectric interface. Trajectories of a few selected particles are grouped and shown in Fig.3.12(e). The trajectories in the twisted cell are found to be rotated clock-wise nearly by 45^0 in the viewing plane in comparison to the untwisted cell. Thus, chirality provides an additional control on the field-induced motility of Janus particles in a liquid crystal.

Two further remarks are in order. First, for induced-charge electro-osmosis in an isotropic medium the flows are always of the puller type with respect to the electric-field axis [32], ruling out directional control of the type we discuss. Second, we expect that hydrodynamic torques arising from the coupling between the squirmer flow field and the anisotropic viscosity of the NLC [33] cannot operate here, as the orientation of the force dipole driving our swimming particles is determined by the direction of the imposed electric field. This rules out spontaneous change of direction of motion of particles due to such torques at a fixed field and frequency.

3.4 Conclusion

We have shown that metal-dielectric Janus particles in a nematic liquid crystal film subjected to a perpendicular AC electric field behave like steerable active particles whose direction of motion can be dictated purely by varying the field amplitude and frequency. The underlying mechanism involves the contrasting electrostatic boundary conditions on the two Janus faces of the particles, the dielectric anisotropy of the nematic, and anchoring on the particle surfaces. We have show that the time-averaged electrostatic force density produced around the Janus particle by the AC field is that of a force dipole whose center is shifted towards the conducting face, causing the particle to swim in the plane transverse to the field, with dielectric (metal) face forward for particle axis parallel (perpendicular) to the nematic director and interpolating smoothly for intermediate orientations. Studies on the motility at higher concentrations, as well as collective dynamics as for diffusiophoretic active colloids [34, 35], are natural experimental and theoretical challenges. Our study has focused only on spherical particles. The abundance of new particles with controlled shapes, surface anchoring [36] and genus [37] now available, and their extraordinary topological [38] and dynamical properties [39, 40] promise a wide range of as yet unexplored physical effects and their applications.

References

[1] A. Ramos, *Electrokinetics and Electrohydrodynamics in Microsystems.* Spinger, 2011.

[2] H. Morgan and N. G. Green, *AC Electrokinetics: Colloids and nanoparticles.* Research Studies Press Ltd, 2003.

[3] S. V. Dorp, U. F. Keyser, N. H. Dekker, C. Dekker, and S. G. Lemay, *Origin of the electrophoretic force on DNA in solid-state nanopores.* Nat. Phys. vol. 5, pp. 347-351, 2009.

[4] J. Yan, M. Han, J. Zhang, C. Xu, E. Luijten, and S. Granick, *Reconfiguring active particles by electrostatic imbalance.* Nat. Mater. vol. 15, pp. 1095-1099, 2016.

[5] A. F. Demirörs, F. Eichenseher, M. J. Loessner, and A. R. Studart, *Colloidal shuttles for programmable cargo transport.* Nat. Commun., vol. 8, no. 1872, 2017.

[6] A. Terray, J. Oakey, and D. W. M. Marr, *Microfluidic control using colloidal devices.* Science, vol. 296, pp. 1841-1844, 2002.

[7] B. Comiskey, J. D. Albert, H. Yoshizawa, and J. Jacobson,*An electrophoretic ink for all-printed reflective electronic displays.* Nature, vol. 394, pp. 253-255, 1998.

[8] R. C. Hayward, D. A. Saville, and I. A. Aksay, *Electrophoretic assembly of colloidal crystals with optically tunable micropatterns.* Nature, vol. 404, pp. 56-59, 2000.

[9] V. A. Murtsovkin, *Nonlinear flows near polarized disperse particles.* Colloid journal of the Russian Academy of Sciences, vol. 58, pp. 341-349, 1996.

[10] T. M. Squires and S. R. Quake, *Microfluidics: Fluid physics at the nanoliter scale.* Rev. Mod. Phys., vol. 77, no. 977-1026, 2005.

[11] M. Z. Bazant, M. S. Kilic, B. D. Storey, and A. Ajdari, *Towards an understanding of induced-charge electrokinetics at large applied voltages in concentrated solutions.* Adv. Colloid Interface Sci., vol. 152, pp. 48-88, 2009.

[12] T. M. Squires and M. Z. Bazant, *Induced-charge electro-osmosis* J. Fluid Mech., vol. 509, pp. 217-252, 2004.

[13] M. Z. Bazant and T. M. Squires, *Induced-charge electrokinetic phenomena: theory and microfluidic applications.* Phys. Rev. Lett., vol. 92, no. 066101, 2004.

[14] S. Gangwal, O. J. Cayre, M. Z. Bazant, and O. D. Velev, *Induced-charge electrophoresis of metallodielectric particles.* Phys. Rev. Lett., vol. 100, no. 058302, 2008.

[15] F. Ma, X. Yang, H. Zhao, and N. Wu, *Inducing propulsion of colloidal dimers by breaking the symmetry in electrohydrodynamic flow.* Phys. Rev. Lett., vol. 115, no. 208302, 2015.

[16] S. Ramaswamy, R. Nityananda, V. A. Raghunathan, and J. Prost, *Power-law forces between particles in a nematic.* Mol. Cryst. Liq. Cryst., vol. 288, pp. 175-180, 1996.

[17] Y. Gu and N. L. Abbott, *Observation of Saturn-ring defects around solid microspheres in nematic liquid crystals.* Phys. Rev. Lett., vol. 85, pp. 4719-4722, 2000.

[18] P. Poulin, H. Stark, T. C. Lubensky, and D. A. Weitz, *Novel colloidal interactions in anisotropic fluids.* Science, vol. 275, pp. 1770-1773, 1997.

[19] H. Stark, *Physics of colloidal dispersions in nematic liquid crystals.* Phys. Rep., vol. 351, pp. 387-474, 2001.

[20] O. D. Lavrentovich, *Active colloids in liquid crystals.* Curr. Opin. Colloid Interface Sci., vol. 21, pp. 97-109, 2016.

[21] O. D. Lavrentovich, *Transport of particles in liquid crystals.* Soft Matter, vol. 10, pp. 1264-1283, 2014.

[22] I. Lazo and O. D. Lavrentovich, *Liquid-crystal-enabled electrophoresis of spheres in a nematic medium with negative dielectric anisotropy.* Phil. Trans. Soc. A, vol. 371, no. 2012255, 2013.

[23] O. D. Lavrentovich, I. Lazo, and O. P. Pishnyak, *Nonlinear electrophoresis of dielectric and metal spheres in a nematic liquid crystal.* Nature, vol. 467, pp. 947-950, 2010.

[24] I. Lazo, C. Peng, J. Xiang, S. V. Shiyanovskii, and O. D. Lavrentovich, *Liquid crystal-enabled electro-osmosis through spatial charge separation in distorted regions as a novel mechanism of electrokinetics.* Nat. Commun., vol. 5, no. 5033, 2014.

[25] R. Golestanian, *Phoretic Active Matter, lectures at the Les Houches Summer School "Active Matter and Non-equilibrium Statistical Physics".* arXiv:1909.03747, 2018.

[26] I. Muševič, M. Škarabot, U. Tkalec, M. Ravnik, and S. Žumer, *Two-dimensional nematic colloidal crystals self-assembled by topological defects.* Science, vol. 313, pp. 954-958, 2006.

[27] J. Cleaver and W. C. K. Poon, *Network formation in colloid–liquid crystal mixtures studied by confocal microscopy.* J. Phys: Condens Matter, vol. 16, pp. S1901-S1909, 2004.

[28] T. A. Wood, J. S. Lintuvuori, A. B. Schofield, D. Marenduzzo, and W. C. K. Poon,*A Self-Quenched Defect Glass in a Colloid-Nematic Liquid Crystal Composite.* Science, vol. 334, pp. 79-83, 2011.

[29] O.P. Pishnyak, S. Tang, J. R. Kelly, S.V. Shiyanovskii, and O.D. Lavrentovich, *Levitation, lift, and bidirectional motion of colloidal particles in an electrically driven nematic liquid crystal.* Phys. Rev. Lett., vol. 99, no. 127802-1-4, 2007.

[30] M. Conradi, M. Ravnik, M. Bele, M. Zorko, S. Žumer, and I. Muševič, *Janus nematic colloids.* Soft Matter, vol. 5, pp. 3905-3912, 2009.

[31] R. Mangal, K. Nayani, Y. K. Kim, E. Bukusoglu, U. M. Córdova-Figueroa, and N. L. Abbott, *Active Janus particles at interfaces of liquid crystals.* Langmuir, vol. 33, pp. 10917-10926, 2017.

[32] T. M. Squires and M. Bazant, *Breaking symmetries in induced-charge electro-osmosis and electrophoresis.* J. Fluid Mech., vol. 560, pp. 65-101, 2006.

[33] J. S. Lintuvuori, A. Würger and K. Stratford, *Hydrodynamics defines the stable swimming direction of spherical squirmers in a nematic liquid crystal.* Phys. Rev. Lett., vol. 119, pp. 068001-1-6, 2017.

[34] S. Saha, S. Ramaswamy, and R. Golestanian, *Pairing, waltzing and scattering of chemotactic active colloids.* New J. Phys., vol. 21, no. 063006, 2019.

[35] S. Saha, R. Golestanian, and S. Ramaswamy, *Clusters, asters, and collective oscillations in chemotactic colloids.* Phys. Rev. E, vol. 89, pp. 062316-1-7, 2014.

[36] B. Senyuk, O. Puls, O. M. Tovkach, S. B. Chernyshuk, and I. I. Smalyukh,*Hexadecapolar colloids.* Nat. Commun., vol. 7, no. 10659, 2016.

[37] B. Senyuk, Q. Liu, S. He, R. D. Kamein, T. C. Lubnesky, and I. I. Smalyukh, *Topological colloids.* Nature, vol. 493, pp. 200-205, 2013.

[38] Y. Yuan, Q. Liu, B. Senyuk, and I. I. Smalyukh, *Elastic colloidal monopoles and reconfigurable self-assembly in liquid crystals.* Nature, vol. 570, pp. 214-218, 2019.

[39] S. Hernàndez-Navarro, P. Tierno, J. A. Farrera, J. Ignés-Mullol, and F. Sagués, *Reconfigurable swarms of nematic colloids controlled by photoactivated surface patterns.* Angew. Chem. Int. Ed., vol. 53, pp. 10696-10700, 2014.

[40] A. V. Straube, J. M. Pagés, P. Tierno, J. Ignés-Mullol, and F. Sagués, *Collective dynamics and conformal ordering in electrophoretically driven nematic colloids.* Phys. Rev. Res., vol. 1, pp. 022008(R)-1-5, 2019.

4

Electrophoresis of metal-dielectric particles with quadrupolar director field: Particles with antipodal surface defects

4.1 Introduction

In the previous chapter we have studied the electrophoretic transport of Janus particles with homeotropic surface anchoring. The particles nucleate equatorial ring defect stabilizing symmetric (quadrupolar) director profile. We showed that the surface asymmetry of the particles breaks the fore-aft symmetry of the surrounding electroosmotic flows and the particles can be transported in all possible direction in a plane perpendicular to the electric field. Moreover, the direction of motion can be navigated at will by changing the amplitude and frequency of the ac electric field. The electrostatic force dipole shows that the particles with ring defects are either puller or pusher type microswimmers depending on the surrounding director curvature.

When the particle's surface is chemically treated for planar or homogeneous alignment of the director on the particle, it nucleates two antipodal surface defects of strength -1/2, known as boojums. These detects appear along the diameter, parallel to the far field director as shown in Fig.1.10 in chapter-1. The particle dressed with these defects are known as boojum colloids. In this case the near field director is symmetric (quadrupolar) and the surrounding electroosmostic flows have fore-aft symmetry as shown in Fig.4.1. As a result of which the particles do not propel [1,2].

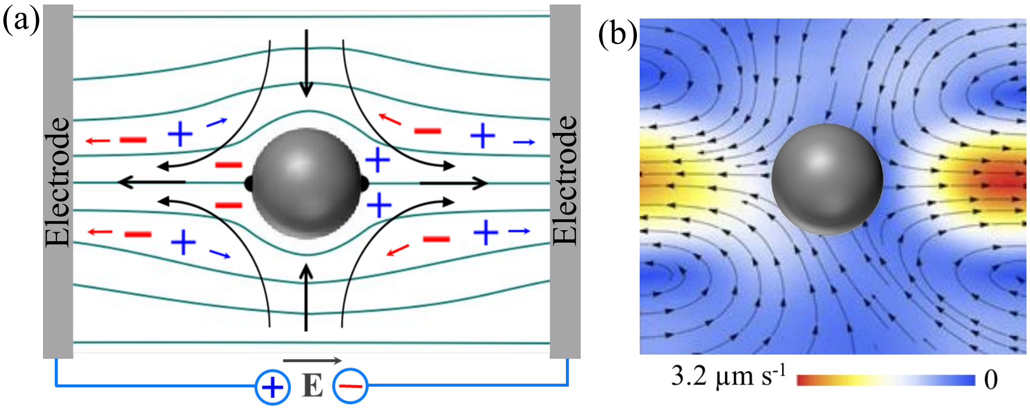

Figure 4.1: (a) A quadrupolar particle (with two antipodal surface defects) under in-plane electric field. (b) Directional streamlines of electroosmotic flows around the same particle (adapted from ref. [2]).

In this chapter we study the effect of ac electric field on metal-dielectric Janus boojum particles. We show that unlike non-Janus boojum-colloids, these Janus boojum colloids can be transported and their direction of motion can be controlled by changing the frequency and amplitude of the ac field. In contrast to the particles with ring defects, we show the boojum particles are pusher type and propel always facing the metal hemisphere.

4.2 Experimental

We synthesized the metal-dielectric Janus particles by following the procedure discussed in the chapter-2 [3, 27]. A schematic view of a Janus particle is shown in Fig.4.2(a). The Janus particles were coated with N-Methyl-3 aminopropyl trimethoxysilane (MAP) to induce planar or homogeneous anchoring of the LC molecules (Fig.4.2(a)). A small quantity of Janus particles was dispersed directly in the nematic liquid crystal (MLC-6608, Merck). It exhibits the following phase transitions: SmA -30°C N 90°C Iso. The dielectric anisotropy is negative ($\Delta\epsilon = \epsilon_{||} - \epsilon_{\perp}$=-4.2), and and the conductivity anisotropy is positive ($\Delta\sigma = \sigma_{||} - \sigma_{\perp} \simeq 6.1 \times 10^{-10}$ S m^{-1}) at room temperature.

The subscripts $\parallel$ and $\perp$ denote the quantities measured with electric field applied parallel and perpendicular to the director $\hat{\mathbf{n}}$, respectively.

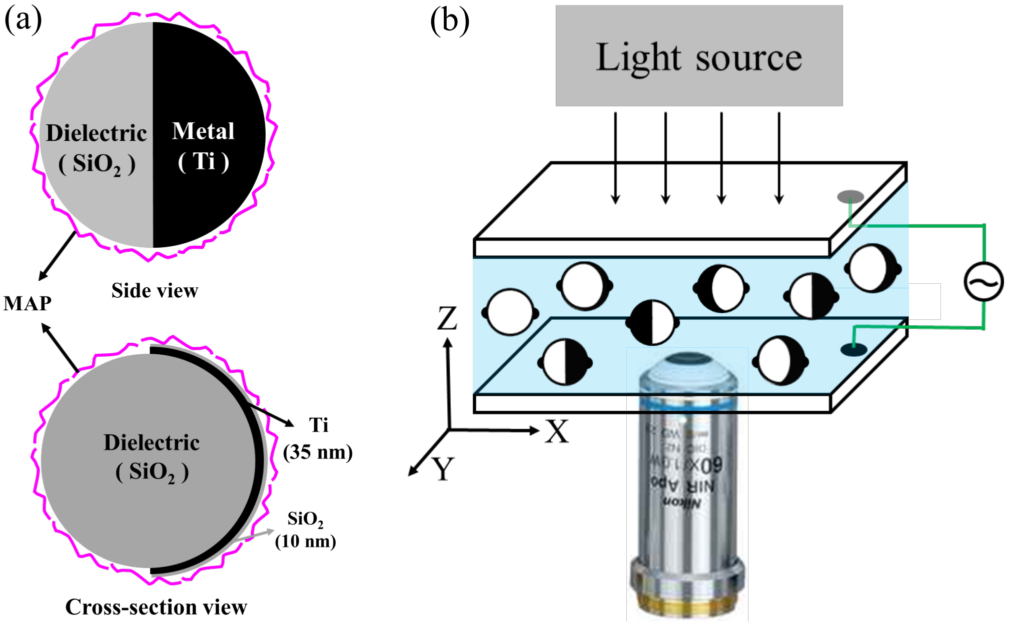

Figure 4.2: (a) Side and cross-section view of a metal-dielectric Janus particle. MAP coating is indicated by magenta strands. (b) Diagram of the experimental cell. Electric field is applied along the z-axis and the observation is made in the xy-plane.

The colloidal mixtures were studied in two different types of cells prepared for out of plane and in-plane field application. For out-of-plane field application, two indium-tin-oxide (ITO) coated glass plates were used (Fig.4.2(b)). For in-plane field application, we used two copper tapes of thickness 35 µm with a gap of 1 mm as shown in Fig.4.5(a). In both cells, the plates are pretreated with a polyimide AL-1254 (JSR Corporation, Japan) and cured at 180°C for 1 h. Then they are rubbed unidirectionally using a benchtop rubbing machine (HO-IAD-BTR-01) for planar alignment of the director. Typical cell thickness used for the out of field application is in the range of 5-7 µm. We used an inverted polarising optical microscope (Nikon Ti-U) with water immersion objective (Nikon, NIR Apo 60/1.0) for the experiments (Fig.4.2(b)). For particle manipulation, a dynamic laser tweezer with a cw solid-state laser operating at 1064 nm (Aresis, Tweez 250si) was used. A charge-coupled device (CCD) camera attached to the microscope is used for recording the particle trajectories at a frame rate of 50-60 per second. The position of the particle is tracked off-line using a computer program with an accuracy of ±20 nm.

4.3 Results and discussion

The MAP coated Janus particles induce boojum defects in NLCs as shown schematically in Fig.4.3(a). Figure 4.3(b) shows the polarising optical micrograph of a Janus boojum-particle in MLC-6608. The anchoring of the LC molecules and the resulting defect structure are confirmed with the help of a λ-plate (530 nm) as shown in Fig.4.3(c). The magenta color corresponds to the parallel orientation of the long axis of the molecules in the rubbing direction (e.g., the far field director $\hat{\mathbf{n}}$), whereas the bluish and yellowish colors surrounding the particle correspond to the anti-clock-wise and clockwise rotation of the director with respect to the rubbing direction, respectively [25].

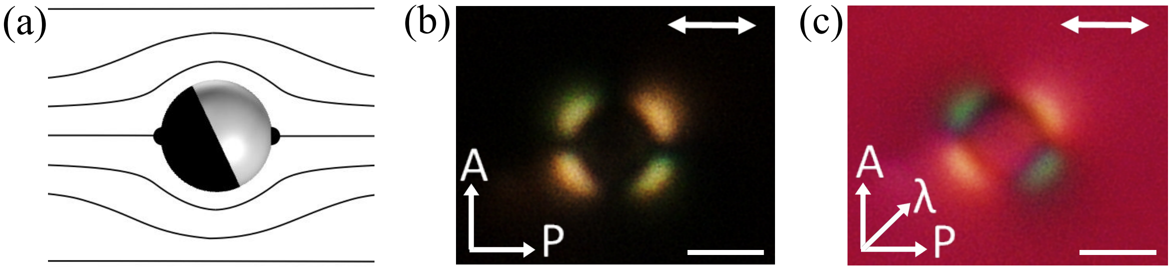

Figure 4.3: (a) Director field around a Janus particle with boojum defects. (b) Polarising optical micrograph of a boojum Janus particle in the NLC. (c) Micrograph with a full-wave plate (530 nm) with it's slow axis oriented at 45° with respect to the director. Blue and yellow color represents the anti-clockwise and clockwise orientation of local director with respect to the far field director, respectively. Double headed arrows represent director $\hat{\mathbf{n}}$. Scale bar: 3 µm.

In what follows, we study the effect of steady ac electric field on the boojum Janus particles. When the field is switched on, the particles reorient such that the metal-dielectric interface becomes parallel to the field direction; consequently, the Janus vector $\hat{\mathbf{s}}$ (a unit normal vector to the metal-dielectric interface to represent the orientation of Janus particles as schematically shown in Fig.4.4(a)) becomes perpendicular to $\mathbf{E}$, to minimise the torque due to the induced dipole moment [26, 28]. Since the dielectric anisotropy is negative, and the field is perpendicular, the macroscopic director remains unaffected except near the particles [1]. Beyond a particular field, the particles start moving along a straight line in some specific directions in the plane of the sample, depending on the orientation of the metal-dielectric interface.

Representative trajectories of some particles with selected orientations (Fig.4.4(b)) at a fixed field are grouped together and shown in Fig.4.4(c). It is noticed that for all trajectories, the particles are moving, facing the metal hemisphere, i.e., the Janus vector $\hat{\mathbf{s}}$ is parallel to the trajectory (Fig.4.4(c)). This is in sharp contrast to the motion of the Saturn-ring Janus particles where the motion is not restricted to the metal facing as discussed in the previous chapter. In particular, the Janus vectors of Saturn-ring particles are not parallel to the trajectory except along the x and y directions (Fig.3.3(c)) [26].

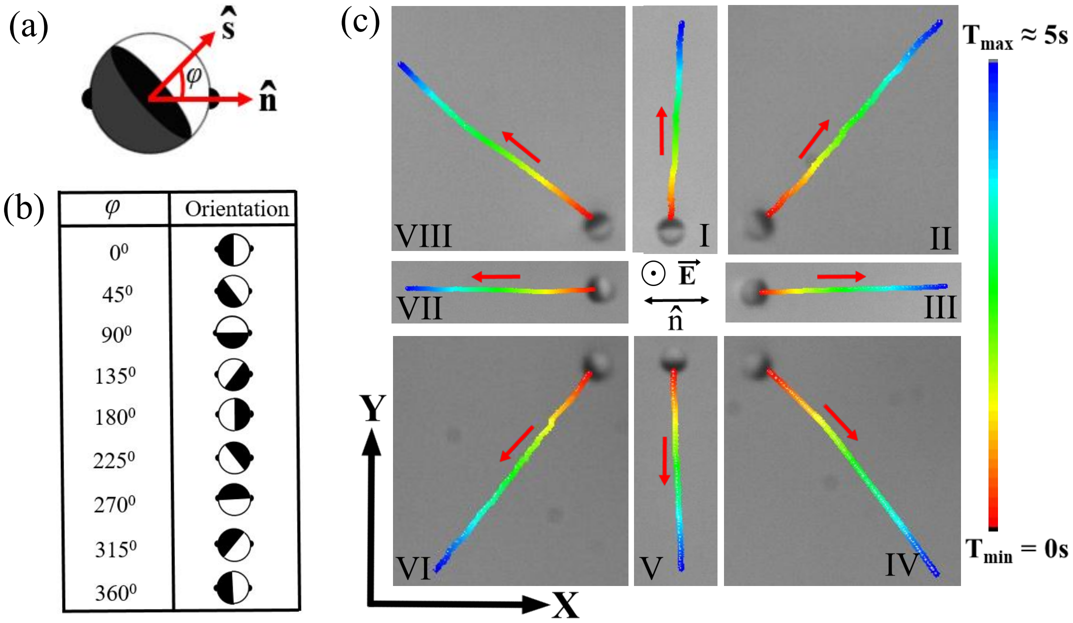

Figure 4.4: (a) Janus vector $\hat{\mathbf{s}}$ is normal to the metal-dielectric interface. φ is the angle between $\hat{\mathbf{s}}$ and the far field director $\hat{\mathbf{n}}$. (b) Particles with selected φ are chosen for the experiments. (c) Trajectories of a few selected particles in the xy-plane, labeled from I to VIII, under the action of an ac electric field (2.38 Vμm^{-1}, 30 Hz). Red arrows denote the direction of motions. The direction of electric field E (along the z-direction, which is out of the plane) and the director $\hat{\mathbf{n}}$ for all the trajectories are shown at the center. T$_{\text{min}}$=0 s and T$_{\text{max}}$=5 s. Cell thickness: 5.2μm.

The motility of the Janus particles with Saturn-ring defect was accounted for theoretically from the electrostatic force density induced by the field, which drags the fluid in the vicinity of the particles as discussed in the previous chapter [26]. The force depends on the field strength, dielectric anisotropy, conductivity anisotropy, and the curvature of the director around the particles. Within a linearised theory and assuming the deviation of director (with respect to the far field director) near the equator is small, it was shown that the resulting force dipole was either a puller or a pusher depending on the orientation of the Janus vector (Fig.3.6). However, for particles with planar anchoring, the director deviation near the defects is not small and the force density equation can not be simplified analytically. A numerical solution of the complete nonlinear theory will be required for getting quantitative values of the force dipoles, which is beyond the scope of the present work. It may be mentioned that the inertial effect is negligibly small for our particles, and the director configuration around the particle remains unaffected because the Reynolds and the Ericksen numbers both are very much less than 1 [26].

To get a qualitative idea about the surrounding flow field, we studied the effect of in-plane ac electric field. The field direction is perpendicular to the director $\hat{\mathbf{n}}$ as shown in Fig.4.5(a). When the electric field is switched on, the particles reorient such that the metal-dielectric interface becomes parallel to $\mathbf{E}$. Figure 4.5(b) shows the trajectory of a boojum Janus particle moving along the x-axis facing the metal hemisphere (Fig.4.5(b)). This is just opposite to the behavior that was observed in case of Janus particles in water by Gangwal *et al.*, wherein the particles move facing the dielectric hemisphere [11]. With respect to the direction of the electric field, two possible types of electroosmotic flows around the particle can be considered, namely, either a pusher or a puller type. In the case of the pusher type, the flows are directed towards the particle and for the puller type, it is directed away from the particle as shown in Fig.4.5(c) and (d), respectively. Since the metal is highly polarised (larger induced charge density), the flow is expected to be stronger on the metal hemisphere relative to the dielectric hemisphere as shown by bigger arrows. Consequently, the fore-aft symmetry of the electroosmotic flows is broken. The puller type flow for boojum particles is ruled out as they should move facing the dielectric hemisphere similar to that was reported in water [11]. Therefore, the LCEO flow around the boojum Janus

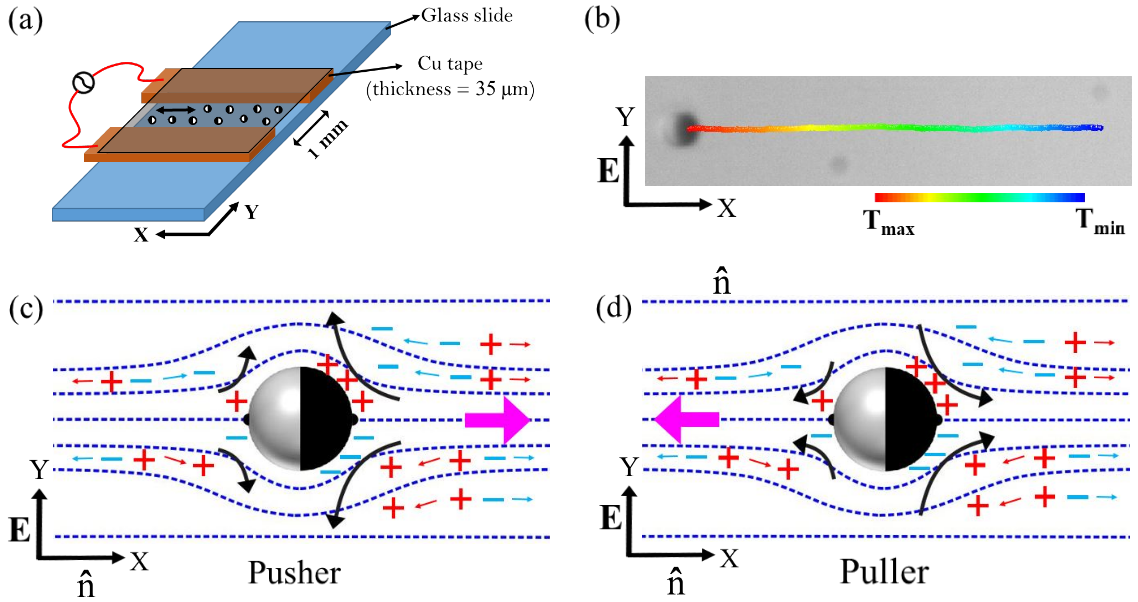

Figure 4.5: (a) Diagram of the cell for the application of the in-plane electric field prepared by copper tapes (orange color). Double headed arrow between the copper electrodes represents director **n̂**. (b) Color coded trajectory of a boojum Janus particle under the action of the ac electric field (E= 1.7 V µm^{-1}, f = 30 Hz). Velocity of the particle, v = 0.7µm s^{-1}. Diagram of (c) pusher and (d) puller LCEO flows around the metal (black) dielectric (white) Janus particle with respect to the field direction (y-axis). Bigger arrows on the metal hemisphere indicate stronger flow. Pink arrows indicate the direction of motion of the particle.

particle is pusher type as shown in Fig.4.5(c). Electrokinetic flows in patterned LCs with topological defects having various configurations such as a pair and triplets of disclinations have been studied by Peng *et al.* [29]. The flow field surrounding a triplet disclinations of strength m=-1/2, 1, -1/2 is pusher type, i.e., similar to the boojum particle. Hence, our result is consistent, and it is also expected as the boojum particle is topologically equivalent to a triplet state.

As a next step, we show the effect of change of the field amplitude in the direction of motion of the particles. The particles, whose Janus vectors are either parallel or perpendicular to the director, direction of motion cannot be changed by varying the field or frequency which was alos observed in the case of Janus particles induced with

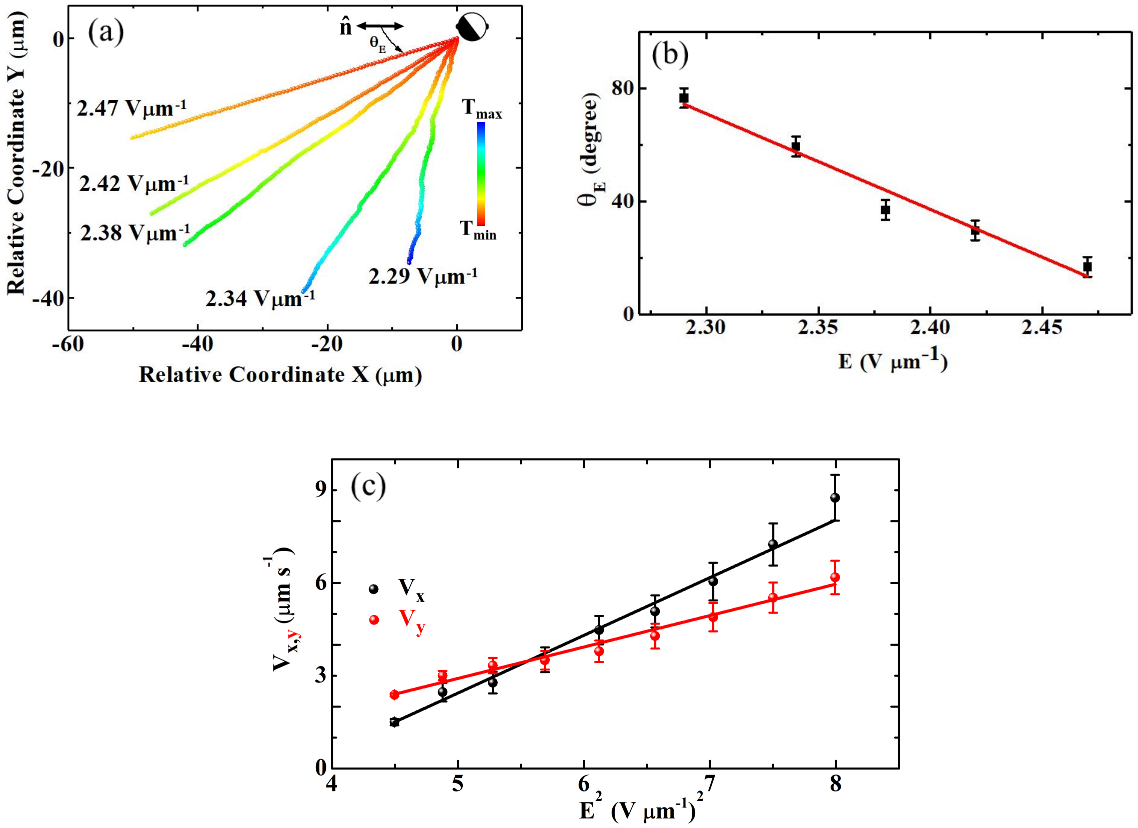

Figure 4.6: (a) A few trajectories of a boojum Janus particle at different field amplitudes and at a fixed frequency (30 Hz) for a fixed orientation ($\varphi = 45°$) of the Janus vector $\hat{\mathbf{s}}$. $\mathrm{T_{max}}$= 14.5 s and $\mathrm{T_{min}}$= 0 s. θ_E is the angle of the trajectories with respect to the director while varying fields. (b) θ_E decreases with the field with a slope $(-340° \pm 35°)$ μm V^{-1}. (c) Velocity components V_x and V_y at different fields obtained from (a). Slopes of V_x and V_y are 1.85 and 1.01 μm^3 s^{-1} V^{-2}, respectively.

Saturn-ring defect in chapter-3. For other particles, it can be changed. For example, we have chosen a particle with a particular orientation of the Janus vector as shown in Fig. 4.6(a). For this particle, the minimum field required for the motion is $E = 2.29$ V μm^{-1}, and the particle moves along a trajectory, making an angle $\theta_E \simeq 76°$ with respect to the director $\hat{\mathbf{n}}$. When the applied field is higher, e.g., $E = 2.34$ V μm^{-1}, it moves along a different trajectory with a smaller angle, $\theta_E \simeq 60°$, and so on. Thus, for a fixed orientation of the Janus vector, the trajectories are different for different starting field amplitudes. It may be mentioned that if the field is increased beyond 2.47

V µm^{-1}, for the chosen particle, θ_E does not reduce further. It means the direction of motion is tunable within a limited range of angle as shown in Fig. 4.6(b). The angle θ_E decreases with increasing field amplitude and can be fitted to a straight line with a slope $(-340° \pm 35°)$ µm V^{-1}. This effect is similar to that was discussed in case of Saturn-ring Janus particles but the slope was $(-43.2° \pm 2.3°)$ µm/V as shown in Fig.3.8(c) [26]. The slope for boojum particles is about 8 times larger than that of the Saturn-ring particles. Hence, the tunability of the trajectories of boojum Janus particles is more sensitive to the field amplitude compared to that of the Saturn-ring Janus particles. The angular sensitivity could be related to the difference in the spatial charge separation in distorted regions of the boojum and Saturn-ring defects [2]. In addition to that the effect of topological-defect-induced surface charge heterogeneities may be important [30]. The field dependent change of direction can be explained following the analysis presented for Saturn-ring Janus particles in the chapter-3 [26]. The amplitude of LCEEP velocity or equivalently the velocity of a spherical particle of radius R in a nematic LC as discussed in the chapter-1, is given by [2, 13]

$$|V| = \alpha \frac{\epsilon_0 \bar{\epsilon} R}{\eta} \left| \frac{\Delta\sigma}{\bar{\sigma}} - \frac{\Delta\epsilon}{\bar{\epsilon}} \right| E^2 \tag{4.1}$$

where $\bar{\sigma} = (\sigma_{||} + \sigma_{\perp})/2$ and $\bar{\epsilon} = (\epsilon_{||} + \epsilon_{\perp})/2$ are the average conductivity and dielectric constant, respectively, η is the average viscosity and α (~ 1) accounts for the director gradients and replacement of anisotropic LC viscosity with η. As expected, both V_x and V_y increases linearly with E^2 (Fig.4.6(c)) but V_x increases at relatively much faster rate than V_y due to the Janus character of the particle. Thus, when the field amplitude is enhanced, ΔV_x is larger than ΔV_y; consequently, the angle between the director $\hat{\mathbf{n}}$ and the trajectory, $\theta_E = \tan^{-1}(\Delta V_y/\Delta V_x)$ decreases.

For a fixed orientation of the Janus vector, the direction of motion of the particles also depends on the frequency of the ac field as shown in Fig.4.7(a). Figure 4.7(b) shows that when the frequency of the field is increased from 30 to 90 Hz, the angle (θ_f) between the trajectory of the particle and the director is increased from 58° to 80°. Similar effect was also observed for Saturn-ring Janus particles in the previous chapter but the rate of change of θ_f with frequency was somewhat larger [26]. The frequency dependence of direction of motion can be explained from the relative variation of the velocity components V_x and V_y with frequency (f) as shown in Fig.4.7(c). The motion

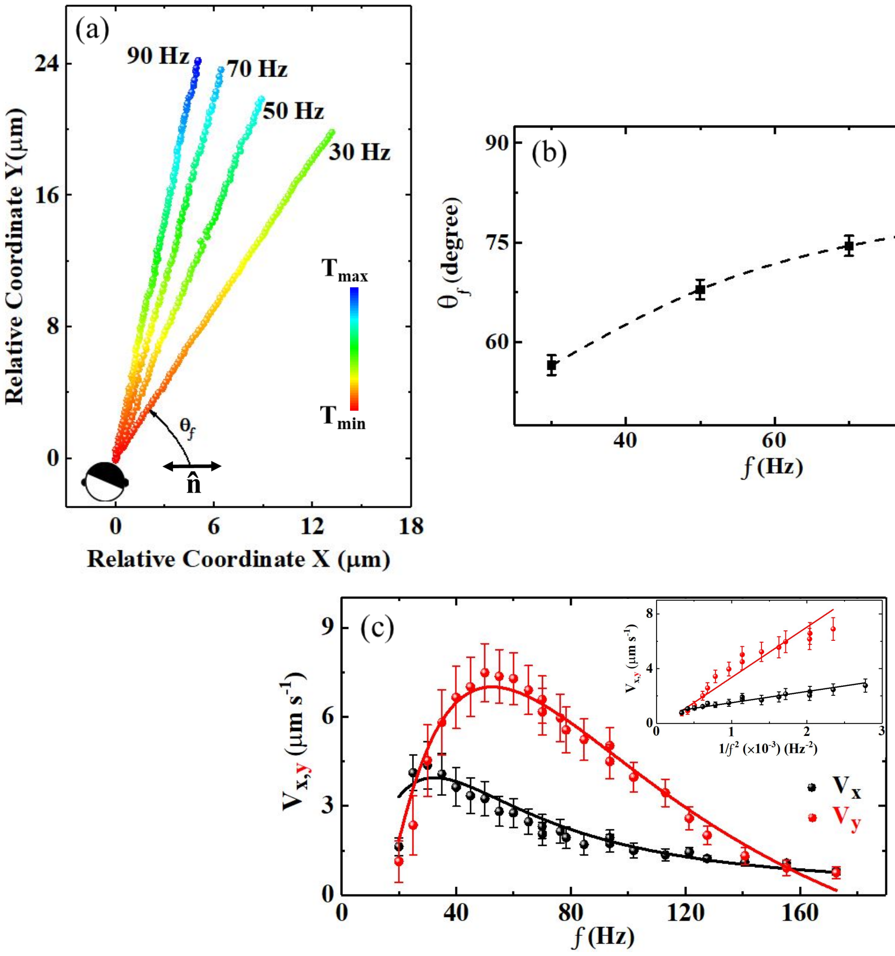

Figure 4.7: (a) A few trajectories of a particle at different frequencies and at a fixed amplitude (2.38 Vµm^{-1}) for a fixed orientation ($\varphi = 250°$) of the Janus vector. T_{max}= 10 s and T_{min}= 0 s. θ_f is the angle between the far field director and the trajectory. (b) Variation of θ_f with f. Dotted curve is a guide to the eye. (c) Velocity components V_x and V_y at different frequencies at E= 2.38 Vµm^{-1}. Red and black curves show theoretical fits to Eq.(4.2). Fit parameters are: $\tau_e = 0.05$ s, $\tau_p = 0.014$ s for V_x and $\tau_e = 0.045$ s, $\tau_p = 0.008$ s for V_y. Inset shows variation of V_x and V_y with $1/f^2$, above the peak frequencies. The slopes of the linear fit for V_y and V_x are $(36.7 \pm 2.7) \times 10^3$ and $(8.2 \pm 0.07) \times 10^3$µm s, respectively. Error bars represent the standard deviation of the mean value.

of the particles is observed within a narrow range of frequency (30-170 Hz). The frequency dependence of both the velocity components shows a typical behavior of

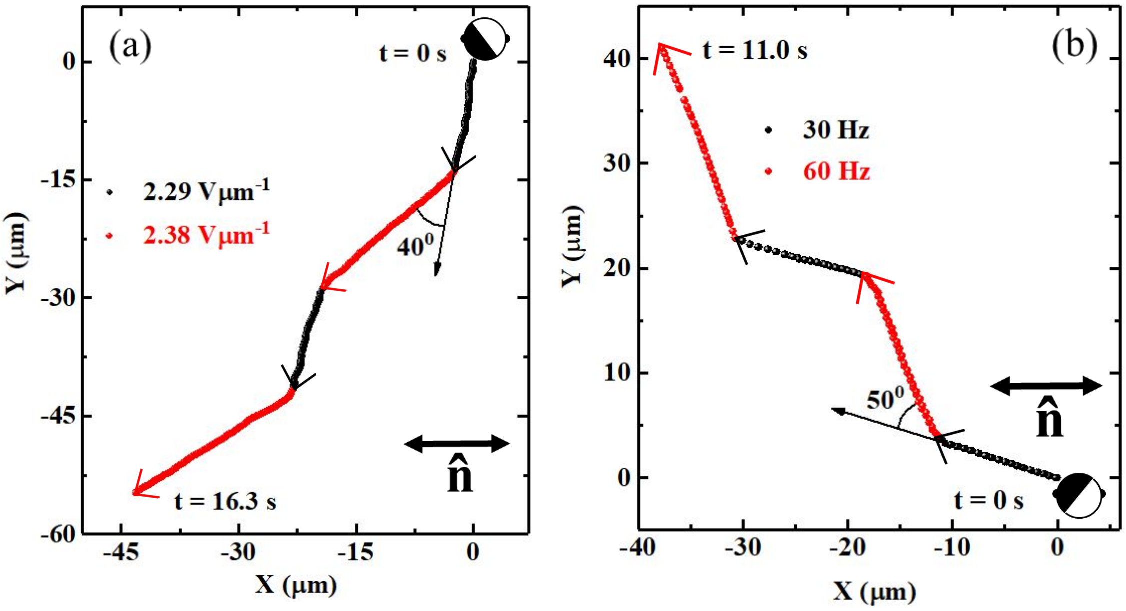

Figure 4.8: (a) Change of direction of motion of a boojum Janus particle with a fixed orientation ($\varphi = 45°$) by altering the field amplitude recursively between 2.29 Vμm^{-1} (black) to 2.38 Vμm^{-1} (red), keeping the frequency constant at 30 Hz. (b) Change of direction of motion of a janus particle ($\varphi = 315°$) by altering the frequency recursively between 30 Hz (Black) to 60 Hz (Red) at a fixed field 2.38 Vμm^{-1}.

the induced charge electrophoresis (ICEP) as disussed in the chapter-1, and can be expressed as

$$V(\omega) = V_o \frac{\omega^2 \tau_e^2}{(1+\omega^2\tau_p^2)(1+\omega^2\tau_e^2)}. \tag{4.2}$$

where the particle charging time is given by $\tau_p = \lambda_D R/D$ (for a conductive sphere) and $\tau_p = \epsilon_m \lambda_D^2/\epsilon_d D$ (for a dielectric sphere), R is the radius of the particle, λ_D is the Debye screening length, D is the diffusion coefficient, ϵ_m and ϵ_d are the permittivities of the medium and the dielectric sphere, respectively. Equation (4.2) can also be used to describe the frequency dependence of the particle's velocity along x and y directions, where V_o contains a quadratic dependence of the electric field amplitude [1, 26, 31]. Figure 4.7(c) shows that both the velocity components, V_x and V_y increase as f^2 when f is low, but decrease as $1/f^2$ when f is high. Above the peak frequencies, the velocity components decrease as $1/f^2$, but the slope of V_y is nearly four times larger than that of V_x (see inset to Fig.4.7(c)), as a result the angle θ_f increases with the increasing frequency.

We have shown that the direction of motion of the particles depends on the field amplitude and frequency. This effect can be exploited for steering the motility of the particles in the plane of the sample. Figure 4.8 presents some representative results for a particle with a fixed orientation of the Janus vector. Figure 4.8(a) shows that the particle changes its direction of motion with respect to the previous direction by nearly 40° when the field amplitude is increased and decreased recursively between 2.29 to 2.38 $\mathrm{V\mu m^{-1}}$. Figure 4.8(b) shows that the direction of motion of the particle is changed by 50° when the frequency is changed alternately between 30 to 60 Hz. Thus, it is possible to guide the transport of the particle to a desired destination. It is noted that while the direction of motion is changed, the orientation of the Janus vector remains unchanged (Fig. 4.8(a) and (b)).

We would like to make a comment here. The studies on the field driven motility of dipolar and Saturn-ring particles are relatively easy than the boojum particles. The dipolar or Saturn-ring particles (homeotropic anchoring) are elastically levitated from the bottom electrode as there is an antagonistic boundary condition on the particle's surface compared to the cell substrates [32]. The boojum particles, with time (more than 24 hours), often get stuck to the bottom electrode, perhaps due to the matching boundary condition i.e., planar anchoring on both the surfaces of the particle and the substrate. Such particles do not show any Brownian motion, and they are not transportable by the electric field.

4.4 Conclusion

We have studied the effect of ac electric field on metal-dielectric Janus particles inducing boojum defects. Non Janus boojum particles have symmetric director configuration and induce quadrupolar LCEO flow. Consequently, they are not motile under applied electric field. The Janus character of the particles breaks the fore-aft symmetry of the flow, making them electrically transportable. In contrast to the Saturn-ring Janus particles, boojum Janus particles are pusher type. The direction of motion of the particles is maneuvrable by changing the amplitude and frequency of the field, similar to that was shown for Saturn-ring Janus particles in the previous chapter. However, the field amplitude and frequency sensitivity of tunability of the boojum particles are quite different than that of the Saturn-ring particles. So far only dipolar particles (non-Janus) [13, 16] and Saturn-ring particles (Janus) [26] are known to be electrically motile in nematic liquid crystals. We have, thus, added a new active particle in the group of active liquid-crystal colloids. From the perspective of active matter, studies on collective dynamics of such active nematic colloids are interesting as well as challenging [33–35]. Our study provides a benchmark for investigating electrically controllable transport of particles in liquid crystals with symmetric director distortion. This idea could be useful for exploring the Janus character of several new shape asymmetric particles in liquid crystals.

References

[1] O. D. Lavrentovich, I. Lazo, and O. P. Pishnyak, *Nonlinear electrophoresis of dielectric and metal spheres in a nematic liquid crystal.* Nature, vol. 467, pp. 947-950, 2010.

[2] I. Lazo, C. Peng, J. Xiang, S. V. Shiyanovskii, and O. D. Lavrentovich, *Liquid crystal-enabled electro-osmosis through spatial charge separation in distorted regions as a novel mechanism of electrokinetics.* Nat. Commun., vol. 5, no. 5033, 2014.

[3] J. Yan, M. Han, J. Zhang, C. Xu, E. Luijten, and S. Granick, Reconfiguring active particles by electrostatic imbalance. Nat. Mater., vol. 15, pp.1095-1099, 2016.

[4] A. F. Demirörs, F. Eichenseher, M. J. Loessner, and A. R. Studart, *Colloidal shuttles for programmable cargo transport.* Nat. Commun., vol. 8, no. 1872, (2017).

[5] A. M. Boymelgreen and T. Miloh, *Alternating current induced-charge electrophoresis of leaky dielectric Janus particles* Phys. Fluids, vol. 24, pp. 082003-1-16, 2012.

[6] A. Nourhani, V. H. Crespi, P. E. Lammert, and A. Borhan, *Self-electrophoresis of spheroidal electrocatalytic swimmers.* Phys. Fluids, vol. 27, pp. 092002-1-12, 2015.

[7] S. Shin, *Diffusiophoretic separation of colloids in microfluidic flows.* Phys. Fluids, vol. 32, pp. 101302-1-15, 2020.

[8] A. Terray, J. Oakey, and D. W. M. Marr, *Microfluidic control using colloidal devices.* Science, VOL. 296, PP. 1841-1844, 2002.

[9] B. Comiskey, J. D. Albert, H. Yoshizawa, and J. Jacobson, *An electrophoretic ink for all-printed reflective electronic displays.* Nature, vol. 394, pp. 253-255, 1998.

[10] R. C. Hayward, D. A. Saville, and I. A. Aksay, *Electrophoretic assembly of colloidal crystals with optically tunable micropatterns.* Nature, vol. 404, pp. 56-59, 2000.

[11] S. Gangwal, O. J. Cayre, M. Z. Bazant, and O. D. Velev, *Induced-charge electrophoresis of metallodielectric particles.* Phys. Rev. Lett., vol. 100, pp. 058302-1-4, 2008.

[12] R. A. Rica and M. Z. Bazant, *Electrodiffusiophoresis: Particle motion in electrolytes under direct current.* Phys. Fluids, vol. 22, pp. 112109-1-14, 2010.

[13] O. D. Lavrentovich, *Active colloids in liquid crystals.* Curr. Opin. Colloid Interface Sci., vol. 21, pp. 97-109, 2016.

[14] O. D. Lavrentovich, *Design of nematic liquid crystals to control microscale dynamics.* Liq. Cryst. Rev., vol. 8, pp. 59-129, 2020.

[15] O. D. Lavrentovich, *Transport of particles in liquid crystal.* Soft Matter, vol. 10, pp. 1264-1283, 2014.

[16] I. Lazo and O. D. Lavrentovich, *Liquid-crystal-enabled electrophoresis of spheres in a nematic medium with negative dielectric anisotropy.* Phil. Trans. Soc. A, vol. 371, no. 20120255, 2013.

[17] I. Dierking, G. Biddulph, and K. Matthews, *Electromigration of microspheres in nematic liquid crystals.* Phys. Rev. E, vol. 73, pp. 011702-1-6, 2006.

[18] P. Poulin, H. Stark, T. C. Lubensky, and D. A. Weitz, *Novel colloidal interactions in anisotropic fluids.* Science, vol. 275, pp. 1770-1773, 1997.

[19] H. Stark, *Physics of colloidal dispersions in nematic liquid crystals.* Phys. Rep., vol. 351, pp. 387-474, 2001.

[20] I. I. Smalyukh, *Liquid crystal colloids.* Annu. Rev. Condens. Matter Phys., vol. 9, pp. 207-226, 2018.

[21] S. Ramaswamy, R. Nityananda, V. A. Raghunathan, and J. Prost, *Power-aw forces between particles in a nematic.* Mol. Cryst. Liq. Cryst., vol. 288, pp. 175-180, 1996.

[22] Y. Gu and N. L. Abbott, *Observation of Saturn-ring defects around solid microspheres in nematic liquid crystals.* Phys. Rev. Lett., vol. 85, pp. 4719-4722, 2000.

[23] G. E. Volovik and O. D. Lavrentovich, *Topological dynamics of defects: boojums in nematic drops.* Sov. Phys. JETP, vol. 58, pp. 1159, 1983.

[24] I. Muševic, *Liquid crystal colloids.* Springer International Publishing AG, Cham, Switzerland, 2017.

[25] K. P. Zuhail and S. Dhara, *Temperature dependence of equilibrium separation and lattice parameters of nematic boojum-colloids.* Appl. Phys. Lett., vol. 106, pp. 211901-1-4, 2015.

[26] D. K. Sahu, S. Kole, S. Ramaswamy, and S. Dhara, *Omnidirectional transport and navigation of Janus particles through a nematic liquid crystal film.* Phys. Rev. Res., vol. 2, pp. 032009(R)-1-6, 2020.

[27] J. Zhang, J. Yan, and S. Granick, *Directed self assembly pathways of active colloidal clusters.* Angew. Chem. Int. Ed., vol. 55, pp. 5166-5169, 2016.

[28] D. K. Sahu and S. Dhara, *Measuring electric-field-induced dipole moments of metal-dielectric Janus particles in a nematic liquid crystal.* Phys. Rev. Applied., vol. 14, pp. 034004-1-8, 2020.

[29] C. Peng, Y. Guo, C. Conklin, J. Viñals, S. V. Shiyanovskii, Qi-H. Wei, and O. D. Lavrentovich,*Liquid crystals with patterned molecular orientation as an electrolytic active medium.* Phys. Rev. E, vol. 92, pp. 052502-1-11, 2015.

[30] M. Ravnik and J. C. Everts, *Topological-defect-induced surface charge heterogeneities in nematic electrolytes.* Phys. Rev. Lett., vol. 125, pp. 037801-1-7, 2020.

[31] S. Herández-Navarro, P. Tierno, J. Ignés-Mullol, and F. Sagués, *AC electrophoresis of microdroplets in anisotropic liquids: transport, assembling and reaction.* Soft Matter, vol. 9, pp. 7999-8004, 2013.

[32] O. P. Pishnyak, S. Tang, J. R. Kelly, S. V. Shiyanovskii, and O. D. Lavrentovich, *Levitation, lift, and bidirectional motion of colloidal particles in an electrically driven nematic liquid crystal.* Phys. Rev. Lett., vol. 99, pp. 127802-1-4, 2007.

[33] A. V. Straube, J. M. Pagés, P. Tierno, J. Ignés-Mullol, and F. Sagués, *Collective dynamics and conformal ordering in electrophoretically driven nematic colloids.* Phys. Rev. Res., vol. 1, pp. 022008(R)-1-5, 2019.

[34] S. Herández-Navarro, P. Tierno, J. A. Farrera, J. Ignés-Mullol, and F. Sagués, *Reconfigurable swarms of nematic colloids controlled by photoactivated surface patterns.* Angew. Chem. Int. Ed., vol. 53, pp. 10696-10700, 2014.

[35] J. M. Pagés, A. V. Straube, P. Tierno, J. Ignés-Mullol, and F. Sagués, *Inhomogeneous assembly of driven nematic colloids.* Soft Matter, vol. 15, pp. 312-320, 2019.

5

Electrophoresis of metal-dielectric Janus particles with dipolar director field: Particles with hyperbolic hedgehog defects

5.1 Introduction

In the previous chapters, we have shown the electrophoretic propulsion of two types of quadrupolar Janus particles, namely, particles with ring defect (chapter-3) and particles with antipodal surface defect (chapter-4). In both cases, the Janus character breaks the fore-aft symmetry of surrounding electroosmotic flows, and consequently the quadrupolar particles become motile. In case of non-Janus dipolar particles (nucleating point defect) the asymmetric director profile around the particles is responsible for breaking the symmetry of electroosmotic flows (Fig.5.1). The dipolar particles propel along the director (see chapter-1) [1, 2].

In this chapter we report experimental studies on the transport of dipolar metal-dielectric Janus particles in two nematic liquid crystals, one with a positive and the other with a negative dielectric anisotropy. We show that the velocity of the Janus particles in both nematic LCs is much higher than that of the non-Janus particles. We map the surrounding flow fields using the micro-particle image velocimetry (μ-PIV) technique and show that not only the left-right symmetry of the flow field is broken

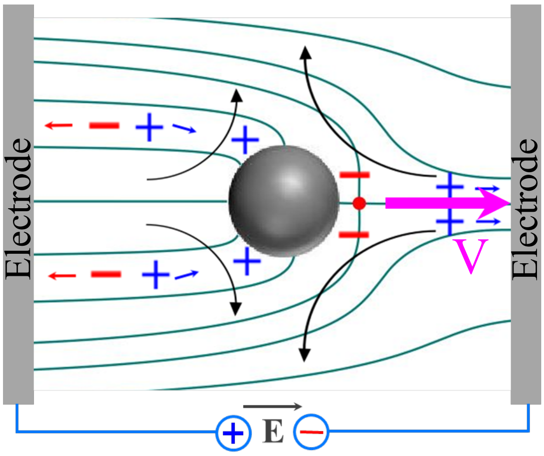

Figure 5.1: Symmetry breaking of the electroosmotic flows around a non-Janus dipolar particle. Bigger curved arrows indicate stronger flows. Magenta arrow presents the direction of propulsion.

but also the flow on the metal hemisphere is stronger than that on the dielectric hemisphere.

5.2 Experimental

We fabricated metal-dielectric Janus particles using normal deposition of Titanium (Ti) onto dry silica particles (SiO_2) of diameter $2a = 3.0\pm0.2$ μm (Bangs Laboratories, USA) as discussed in the 2nd chapter [3]. The surface of the Janus particles is treated with N, N-dimetyl-N-octadecyl-3 aminopropyl-trimethoxysilyl chloride (DMOAP) in order to induce perpendicular (homeotropic) anchoring to the liquid crystal director. A small quantity (∼0.1 wt%) of DMOAP coated Janus particles were dispersed in the nematic liquid crystals. We used two nematic liquid crystals, namely 5CB (pentyl cyanobiphenyl) and MLC-6608 (LC mixture obtained from Merck), which are in nematic phase at room temperature. The dielectric anisotropy $\Delta\epsilon$ of 5CB is positive whereas it is negative for MLC-6608 (Table-5.1). The conductivity anisotropy $\Delta\sigma$ for both LCs is positive. For particle image velocimetry (μ-PIV) experiment, we dispersed CdSe/ZnS quantum dots (∼0.05 wt%) in 5CB using a vortex mixer and an ultrasonicator.

Liquid crystals	$\Delta\epsilon$	$\Delta\epsilon/\overline{\epsilon}$	$\Delta\sigma/\overline{\sigma}$	$\Delta\epsilon/\overline{\epsilon}$ - $\Delta\sigma/\overline{\sigma}$
5CB	13	0.94	0.5	0.44
MLC-6608	-3.8	-0.64	0.9	-1.54

Table 5.1: Dielectric ($\Delta\epsilon = \epsilon_{||} - \epsilon_{\perp}$) and conductivity ($\Delta\sigma = \sigma_{||} - \sigma_{\perp}$) anisotropies of 5CB and MLC-6608 at room temperature. $\overline{\epsilon} = (\epsilon_{||} + \epsilon_{\perp})/2$ and $\overline{\sigma} = (\sigma_{||} + \sigma_{\perp})/2$.

We prepared Hele-Shaw type cells made of two parallel plates as discussed in chapter-2. Both upper and bottom plates were coated with AL-1254, cured at 180°C for 1 h and rubbed antiparallelly for obtaining planar alignment of the director. For applying

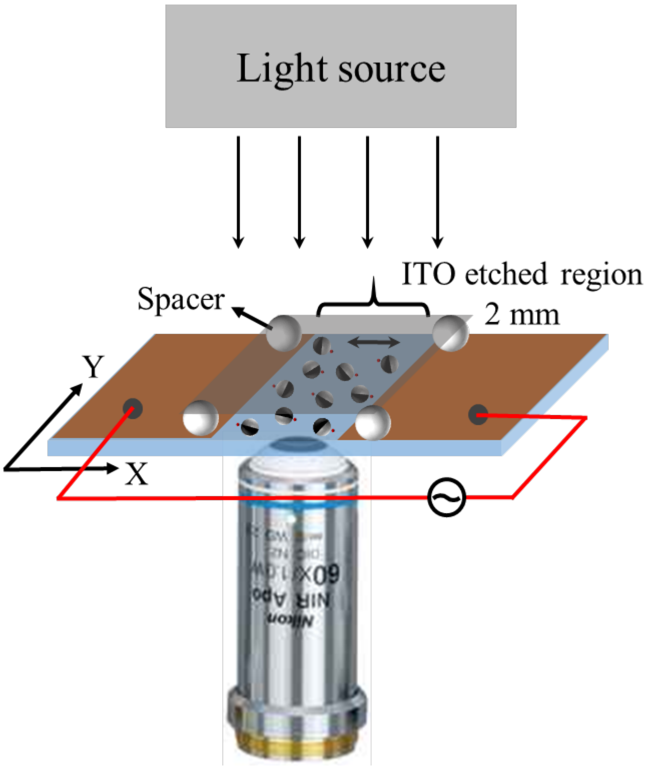

Figure 5.2: Diagram of a cell with in-plane electrodes. xy-plane is the plane of observation. The double headed arrow indicates the director n̂ and the direction of the applied ac electric field.

an in-plane electric field (parallel to n̂ for 5CB), the bottom plate was coated with indium-tin-oxide (ITO) in which a small strip of width 2.0 mm was etched as shown schematically in Fig.5.2. For applying an electric field orthogonal to n̂ (for MLC-6608) two ITO coated glass plates were used as shown in Fig.5.5(a). A function generator (Model: Tektronix AFG31000) and a voltage amplifier (Model: TEGAM 2350) were used for applying ac electric field to the cells. A mixture of Janus particles and LCs was inserted into the cells *via* capillary action. An inverted optical polarizing microscope (Ti-U, Nikon) was used in the experiments. The motion of the particles was recorded using a $60X$ (NA =1.0) water immersion microscope objective (NIR Apo, Nikon) and a charge-coupled device (CCD) camera (iDs-UI) at a rate of 40 frames per second. The position of the particles was tracked from the recorded videos using a particle tracking program.

5.3 Results and discussion

The DMOAP coated Janus particles nucleate a hyperbolic hedgehog defect of strength, $s = -1$, in nematic liquid crystals and the resulting director profile is dipolar as shown in Fig.5.3(a). The elastic dipole $\vec{p}$ points from -1 defect towards the centre of the particle. The bright field image of a dipolar Janus particle in 5CB is shown in Fig.5.3(b). In transmitted light, the metal coated hemisphere appears darker. The corresponding cross polarized image is shown in Fig.5.3(c). When an ac electric field is applied, above a threshold field, the particles start propelling along the director, irrespective of the orientation of the metal-dielectric interface. Here, the electric field is applied parallel to the director n̂, in order to avoid elastic distortion due to the Freedericksz transition. The direction of motion of particles is found to be parallel to

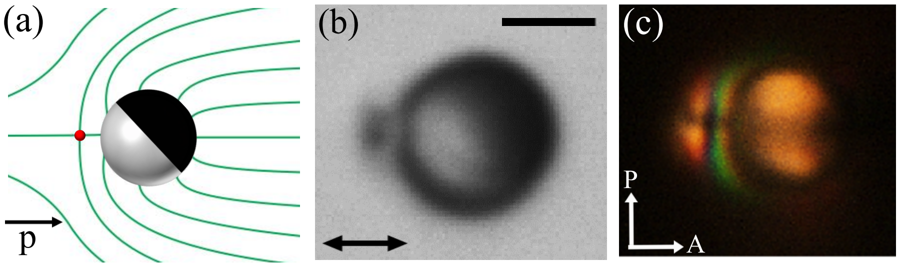

Figure 5.3: (a) Dipolar director profile around a Janus particle. $\vec{p}$ denotes the elastic dipole. (b) Optical micrograph and (c) polarising optical micrograph of a dipolar Janus particle in 5CB. Double headed arrow indicates the director. Scale bar: 2 µm.

the elastic dipole $\vec{p}$ (see Figs. 5.4(a-d)). This observation is very different compared to the multidirectional mobility of quadrupolar Janus particles discussed in the previous chapters where the mobility is not restricted along the director. In particular, the direction of motion of quadrupolar particles depends on the orientation of the metal hemisphere with respect to the director $\hat{n}$.

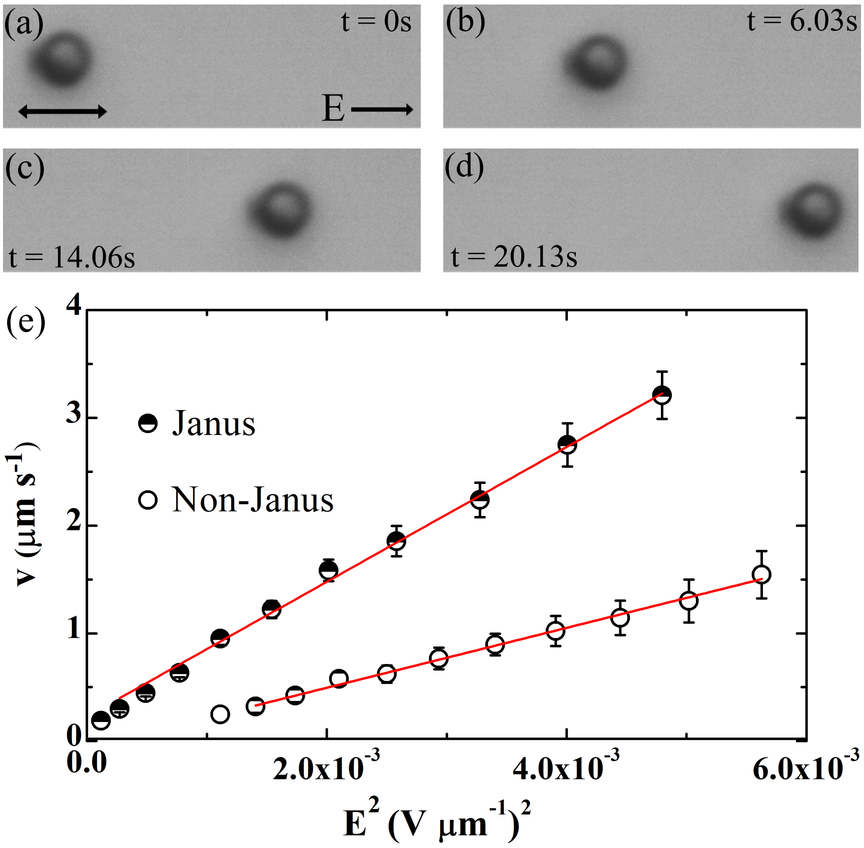

Figure 5.4: (a-d) Sequence of images with elapse time showing the mobility of a dipolar Janus particle along the director in 5CB LC. Note that the direction of motion is parallel to the elastic dipole $\vec{p}$. The double headed black arrow in (a) represents the director, $\hat{n}$. (e) Electric field dependent velocity (v) of a Janus and a non-Janus particle. Red lines represent linear fits to $v \propto E^2$ with slopes 625 and 278 $\mu m^3\ s^{-1}V^{-2}$ for the Janus and non-Janus particles, respectively. Error bars show the standard deviation of the mean value.

Figure 5.4(e) shows that the velocity of Janus particles varies quadratically with the field as expected in liquid crystal enabled electrophoresis (LCEEP) [29]. For comparison, we also present the field dependent velocity of a non-Janus dipolar particle. We observe that Janus particles propel faster than non-Janus particle (Fig. 5.4(e)). For example, at $E^2 = 4 \times 10^{-3}$ (V µm^{-1})^2, the velocities of the Janus and non-Janus particles are v_{J}=2.8 µm s^{-1} and v=1.03 µm s^{-1}, respectively. It is also observed that the threshold field (above which the particles start propelling) for the Janus particles is less compared to non-Janus particles. For example, the threshold fields for the Janus and non-Janus particles were measured as $E_{\mathrm{J}}= 1.1 \times 10^{-4}$ V µm^{-1} and $E = 1.1 \times 10^{-3}$ V µm^{-1}, respectively.

The electroosmotic velocity of the LCs around a particle varies quadratically with the electric field and it can be written as [2, 40]:

$$u = CE^2 \tag{5.1}$$

The constant C is given by

$$C = \alpha \frac{\epsilon_0 \bar{\epsilon} R}{\eta} \left(\frac{\triangle\epsilon}{\bar{\epsilon}} - \frac{\triangle\sigma}{\bar{\sigma}} \right). \tag{5.2}$$

Where R is the radius of the particle, η is the viscosity of LCs [2]. Here the coefficient $\alpha \simeq 1$ is introduced to account for the approximations such as $1/R$ as a measure of director gradients. The sign of the quantity in the parenthesis determines the direction of motion of the particles with respect to the elastic dipole $\vec{\mathrm{p}}$ [40]. If this quantity is positive, the direction of motion is parallel to $\vec{\mathrm{p}}$ and, if it is negative, the direction of motion is antiparallel to $\vec{\mathrm{p}}$. For 5CB, $\Delta\epsilon/\bar{\epsilon} - \Delta\sigma/\bar{\sigma} = 0.44$ (Table 5.1) and, hence, the direction of motion is parallel to $\vec{\mathrm{p}}$ (Fig.5.4(b-d)).

In what follows, we study electrophoresis of Janus dipolar particles in MLC-6608. It exhibits negative dielectric anisotropy (Table 5.1). In this sample, the electric field was applied perpendicular to the director $\hat{\mathrm{n}}$ (Fig. 5.5(a)) in order to avoid elastic distortion due to the Freedericksz transition. Figures 5.5(b-d) show time coded trajectories of three Janus dipolar particles with different orientations of the metal hemisphere under the action of an ac electric field. The particles propel along the director but with point defects leading the way in contrast to the particles in 5CB. This means that the direction of motion is antiparallel to the elastic dipole $\vec{\mathrm{p}}$. This is expected as the quantity in the parenthesis of Eq.(5.2) i.e., $\Delta\epsilon/\bar{\epsilon} - \Delta\sigma/\bar{\sigma}$ (=-1.54) is negative (Table 5.1). Figure 5.5(e) shows that the velocity of both the particles vary quadratically

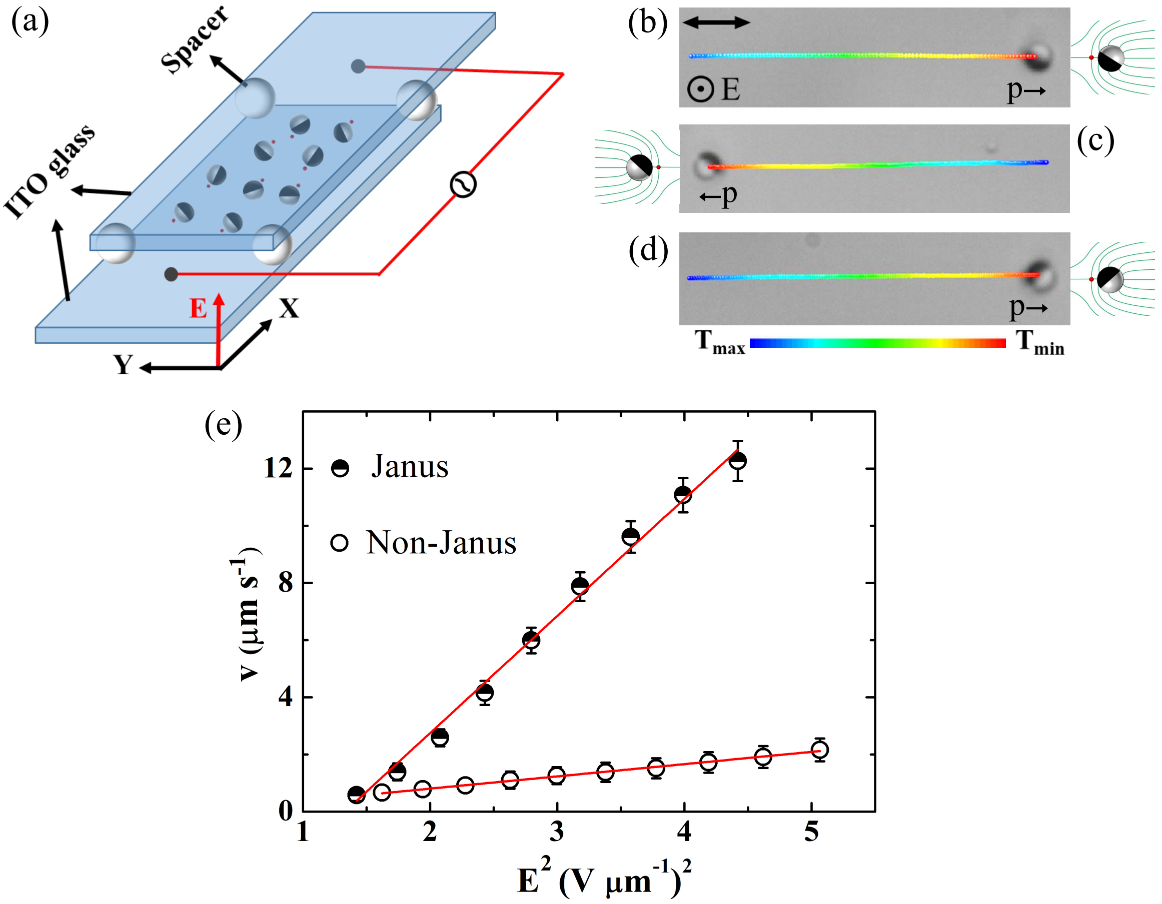

Figure 5.5: (a) Diagram of a cell for applying electric field orthogonal to the director $\hat{\mathbf{n}}$. $\mathbf{E}$ is along the z-axis and the director is along the x-axis. (b-d) Time coded trajectories of a few Janus dipolar particles in MLC-6608 liquid crystal with different orientations of the metal hemisphere under the field amplitude of 2.0 Vμm^{-1} at 30 Hz (see Movie S2). $T_{max} = 5$ s, $T_{min} = 0$ s. Note that the direction of motion is antiparallel to elastic dipole $\vec{\mathrm{p}}$. (e) Electric field dependent velocity (v) of a Janus and non-Janus dipolar particle. Red lines represent linear fits to $v \propto E^2$ with slopes 4.1 and 0.4 μm^3 s^{-1}V^{-2} for the Janus and the non-Janus particles, respectively.

with the field but the slope for Janus particle is about 10 time higher than that for the non-Janus particle. Thus Janus particles propel much faster than the non-Janus particles. It may be noted that in the 5CB LC this factor is about 2.2 times (see Fig.5.4(e)). This difference is expected as the velocity depends on the quantity $\Delta\epsilon/\bar{\epsilon} - \Delta\sigma/\bar{\sigma}$, which is about 3.5 times larger for MLC-6608 than that for 5CB (table

5.1). Moreover, the applied electric field in MLC-6608 is much higher than that in 5CB. In both samples, the velocity of the Janus dipolar particles is much higher than that of the non-Janus particles and this can be quantitatively understood based on the electroosmotic flows surrounding the particles. We have used the μ-PIV technique to observe the electroosmotic flows in 5CB LC.

5.4 Particle Image Velocimetry(μ-PIV)

PIV (Particle Image Velocimetry) is an optical method of visualization of fluid flows. It is used to obtain the instantaneous velocity measurements and related properties in fluids. Generally, the fluid is seeded with tracer particles (sufficiently small in size) which are assumed to faithfully follow the flow dynamics. The fluid with entrained particles is illuminated so that particles are visible. The motion of the seeding particles is used to calculate speed and direction (the velocity field) of the flows. In our experiments, we have chosen a bigger particle of diameter 50 ± 4μm and fixed it with a glue in the middle of the cell as shown in Fig.5.6(a). The gap between the two in-plane electrodes was kept at 4 mm. A small quantity (∼0.01wt%) of CdSe/Zn fluorescent quantum dots (QDs) of size 1-2 nm were dispersed in 5CB and used as tracer particles. The absorption maximum of the QDs was 510-540 nm and the emission wavelength was in the range of 530–550 nm. A bright image and the corresponding fluroscent image of a dipolar Janus particle surrounded by QDs in 5CB is shown in Fig.5.6(b) and (c), respectively. In the presence of an ac field, QDs follow the streamlines of electroosmotic flows. Movies of the flow were recorded using a Ni-S2 (Nikon) colour camera exposed at 300 ms with a rate of one frame per second. The recorded file was saved as an array of images and analysed using μ-PIV software [41]. The final flow pattern was obtained after averaging over nearly 100 images.

Figures 5.7 (b) and (e) show the flow streamlines around a non-Janus and a Janus dipolar particle, respectively. In the case of non-Janus particle, two bigger vortices are formed adjacent to the point defect and smaller vortices are formed on the opposite side; consequently the fore-aft symmetry of the electroosmotic flow is broken. The corresponding directional flow (Fig.5.7(c)) shows that the flow is outward along the

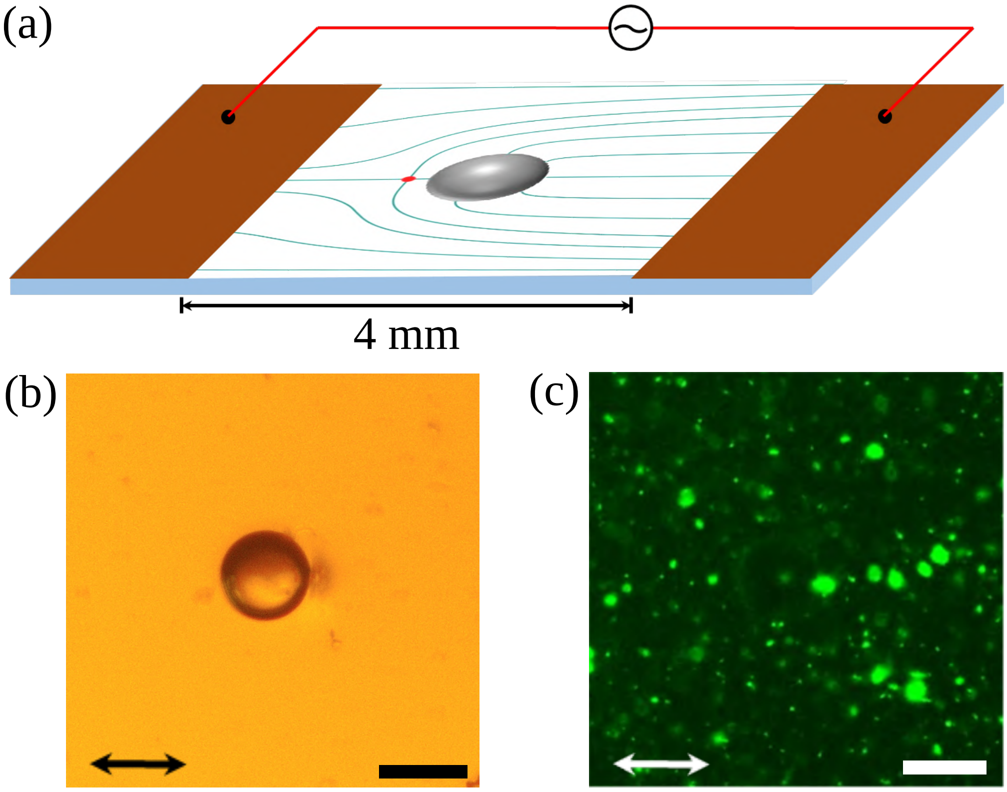

Figure 5.6: (a) Schematic of the experimental cell. (b) Bright image of a Janus dipolar particle in 5CB. (c) Fluorescent image of uniform distribution of QDs around the particle in 5CB excited at 530 nm. Double headed arrow represents the director n̂. Scale bar : 50 μm

director, similar to that of "Pusher" type micro-swimmers [2]. The flow field of the Janus particle is somewhat different. Firstly, two small vortices on the left side of the microsphere disappear. Secondly, the velocity of the fluid near the metal hemisphere is much higher than that on the silica hemisphere (see the colour coded bars). For example, the maximum electroosmotic velocity for the non-Janus particle is 0.07 μm s^{-1}. Using Eq.(5.2) and considering $\overline{\eta}_{LC} \approx 90$ mPas, $E = 9$ mV/μm, R=25 μm and taking $\Delta\epsilon$ and $\Delta\sigma$ from Table 5.1, we estimate the electroosmotic flow velocity for the non-Janus particle $u_{max} \approx 0.05$ μm/s. This is very close to the value measured in the experiments (Fig.5.7(c)). In contrast the maximum velocity for the Janus particle is 0.16 μm s^{-1}, i.e. nearly double that for the non-Janus particle (Fig.**??**(f)). This is expected due to the higher polarisability of the metal hemisphere than that of the

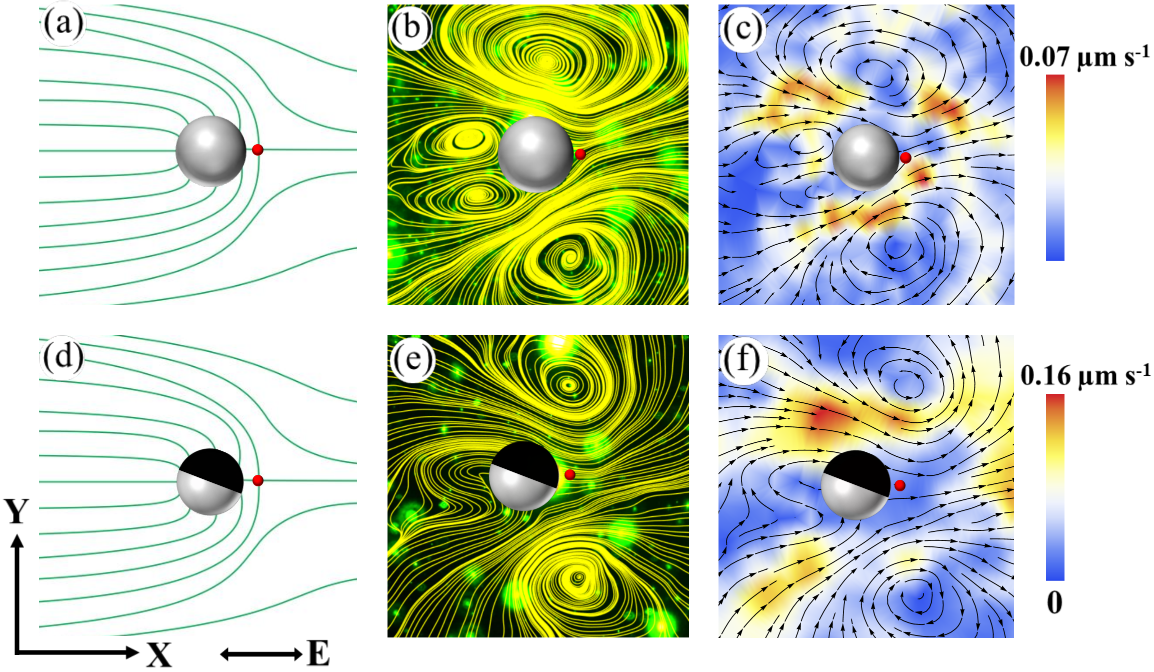

Figure 5.7: (a,d) Director profile around a Janus and non-Janus particles. The applied electric field is parallel to the director i.e., along the x-axis. (b) Streamlines of LC flow around a dipolar non-Janus particle. (c) Directional streamlines i.e., the velocity map of the LCEO flows around the non-Janus dipolar particle. (e) Streamlines of LC flow around a dipolar Janus particle. (f) The velocity map of the LCEO flow around the Janus dipolar particle. Field amplitude: 9.0 mVμm^{-1}, frequency: 30 Hz.

dielectric hemisphere and consequently the higher induced charge density on the metal hemisphere.

We have calculated the volumetric flows $Q_x(x)$ and $Q_y(y)$, defined as the volume of fluid pumping per second around the sphere along x and y directions of the cell, respectively. They can be expressed as [2]:

$$Q_x(x) = \frac{2}{3}h\int_{-y_0}^{y_0} u_x(x,y)dy \tag{5.3}$$

$$Q_y(y) = \frac{2}{3}h\int_{-x_0}^{x_0} u_y(x,y)dx \tag{5.4}$$

where $u_x(x,y)$ and $u_y(x,y)$ are the velocity components known from the experiments, h is thickness of the cell and $x_0 = y_0 = 150$ µm. The calculated $Q_x(x)$ and $Q_y(y)$

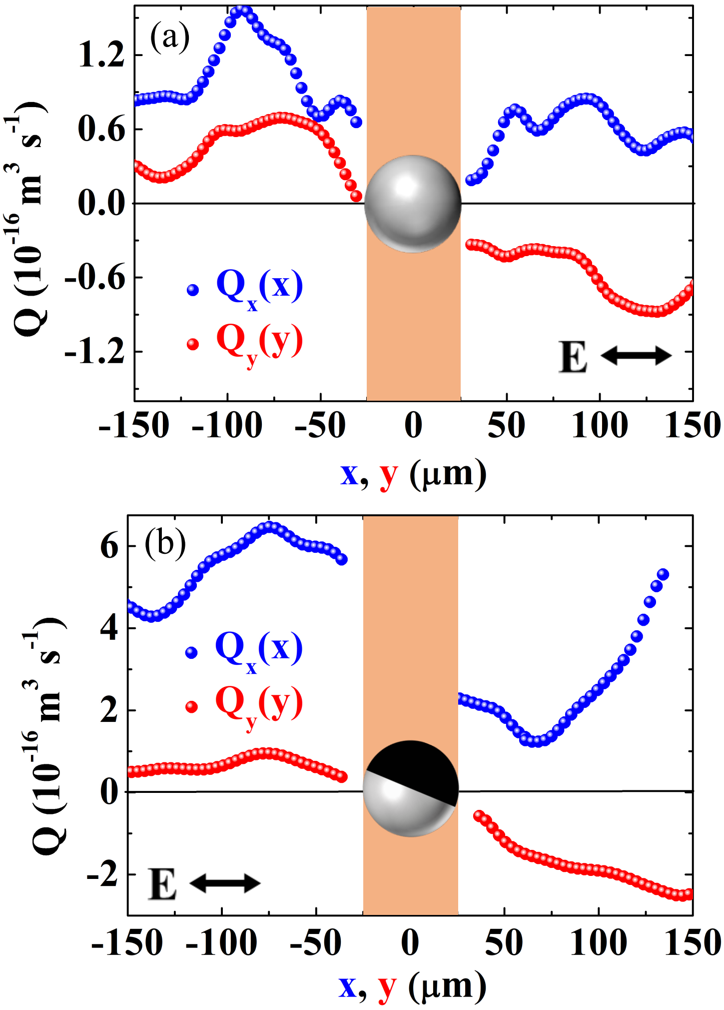

Figure 5.8: Volumetric flow functions $Q_x(x)$ and $Q_y(y)$ for the (a) non-Janus and (b) Janus particles obtained from the directional streamline in Fig.5.7(e,f). Pumping of LC is from the left to the right direction.

for both non-Janus and Janus particles are shown in Fig.5.8(a) and (b), respectively. For the non-Janus particle, Q_x is positive on both left and right sides of the particle, which means that the LC is pumped from left to right. In contrast, Q_y is positive on the left and negative on the right side of the particle, which means no net pumping of the fluid along the y-direction. For the Janus particle, the response is similar but the maximum Q_x value is larger than that of the non-Janus particle. This means that the pumping of the fluid from left to right is more for the Janus particle. It may be mentioned that the magnitudes of Q_x and Q_y depends on the dielectric and conductivity anisotropies of the NLCs and the applied field strength. We obtained an almost one order of magnitude less volumetric flow as our material is different and also our field value is almost 3 times smaller than that used in ref. [2].

Further, we make two observations in comparison to studies on quadrupolar Janus particles discussed in the previous chapters. Firstly, the threshold field required for Janus particles with hyperbolic hedgehog defects (E =1.2 V μm^{-1}) is almost comparable to that of particles with Saturn ring defects (E =1.3 V μm^{-1}). But it is relatively lower compared to particles with boojum defects (E = 2.1 V μm^{-1}). Secondly, the velocity of Janus dipolar particles is much higher compared to both quadrupolar Janus particles (i.e., with boojum and Saturn ring defects). For example, the velocity of a Janus dipolar particle at a frequency of 30 Hz and a field E= 2.12 V μm^{-1} is 12 μm s^{-1}, whereas the velocities of Janus particles with Saturn ring and boojum defects are 6.4 and 1.5 μm s^{-1}, respectively. In particular, for a given field and frequency the velocity of Janus particles can be arranged n decreasing order as: $V_{\text{hyperbolic hedgehog}} > V_{\text{Saturn ring}} > V_{\text{boojum}}$.

5.5 Conclusion

We have studied the electrophoretic locomotion of Janus dipolar particles and shown that the direction of motion of the particles is parallel to the elastic dipoles in 5CB and antiparallel in MCL-6608 LCs. The velocity of the Janus particles is about 10 times higher than that of the non-Janus particles in 5CB and 2 times higher in MLC-6608. We have mapped the electroosmotic flow fields in 5CB using μ-PIV and observed two vortices around the Janus particles as opposed to four vortices around the non-Janus particles. The flows on the metal hemisphere are stronger and the volumetric flow of the fluid along the direction of motion of Janus particles is nearly 2 times higher compared to the dielectric hemisphere. Our experiments demonstrate that the propulsion of Janus dipolar particles in NLCs is the highest compared to both non-Janus and Janus quadrupolar particles. For Janus quadrupolar particles, the surrounding medium (director profile) is symmetric and the asymmetric particle breaks the fore-aft symmetry of electroosmotic flows as discussed in the previous chapters [35, 36]. In case of Janus dipolar particles, both the medium and the particles are asymmetric and they both are responsible for breaking the symmetry of the flow. Overall, the Janus dipolar particles display superior electropphoresis as far as propulsion is concerned, compared to both Janus and non-Janus quadrupolar particles in nematic liquid crystals. Janus particles with an asymmetric shape, a higher order elastic moment and a genus could offer unusual motility and dynamics in liquid crystals.

References

[1] O. D. Lavrentovich, I. Lazo, and O. P. Pishnyak, *Nonlinear electrophoresis of dielectric and metal spheres in a nematic liquid crystal.* Nature, vol. 467, pp. 947-950, 2010.

[2] I. Lazo, C. Peng, J. Xiang, S. V. Shiyanovskii, and O. D. Lavrentovich, *Liquid crystal-enabled electro-osmosis through spatial charge separation in distorted regions as a novel mechanism of electrokinetics.* Nat. Commun., vol. 5, no. 5033, 2014.

[3] J. Yan, M. Han, J. Zhang, C. Xu, E. Luijten, and S. Granick, *Reconfiguring active particles by electrostatic imbalance.* Nat. Mater., vol. 15, pp. 1095-1099, 2016.

[4] C. Bechinger, R. D. Leonardo, H. Löwen, C. Reichhardt, G. Volpe, and G. Volpe, *Active particles in complex and crowded environments.* Rev. Mod. Phys., vol. 88, pp. 045006-1-50, 2016.

[5] J. Wang, and W. Gao, *Nano/Microscale Motors: Biomedical Opportunities and Challenges.* ACS Nano, vol. 6, pp. 5745-5751, 2012.

[6] H. R. Jiang, H. Wada, N. Yoshinaga, and M. Sano, *Manipulation of colloids by a nonequilibrium depletion force in a temperature gradient.* Phys. Rev. Lett., vol. 102, pp. 208301-1-4, 2009.

[7] H. R. Jiang, N. Yoshinaga, and M. Sano, *Active motion of a Janus particle by self-thermophoresis in a defocused laser beam.* Phys. Rev. Lett., vol. 105, pp. 268302-1-4, 2010.

[8] G. Li and J. X. Tang, *Accumulation of microswimmers near a surface mediated by collision and rotational Brownian motion.* Phys. Rev. Lett., vol. 103, pp. 078101-

1-4, 2009.

[9] D. Nishiguchi, and M. Sano, *Mesoscopic turbulence and local order in Janus particles self-propelling under an ac electric field.* Phys. Rev. E, vol. 92, pp. 052309-1-11, 2015.

[10] H. R. Vutukuri, M. Lisicki, E. Lauga and J. Vermant, *Light-switchable propulsion of active particles with reversible interactions.* Nat. Commun., vol. 11, no. 2628, 2020.

[11] S. Thutupalli, R. Seemann, and S. Herminghaus, *Swarming behavior of simple model squirmers.* New J. Phys., vol. 13, no. 073021 (2011).

[12] P. Tierno, R. Golestanian, I. Pagonabarraga, and F. Sagués, *Controlled swimming in confined fluids of magnetically actuated colloidal rotors.* Phys. Rev. Lett., vol. 101, pp. 218304-1-4, 2008.

[13] S. Ramaswamy, *The mechanics and statistics of active matter.* Annu. Rev. Condens. Matter Phy., vol. 1, pp. 323-345, 2010.

[14] M. C. Marchetti, J. F. Joanny, S. Ramaswamy, T. B. Liverpool, J. Prost, M. Rao, and R. A. Simha, *Hydrodynamics of soft active matter.* Rev. Mod. Phy., vol. 85, pp. 1143-1189, 2013.

[15] I. S. Aranson, *Active colloids.* Phys. Usp., vol. 56, pp. 79-92, 2013.

[16] E. Lauga and T. R Powers, *The hydrodynamics of swimming microorganisms.* Rep. Prog. Phys., vol. 72, no. 096601, 2009.

[17] A. Ramos, *Electrokinetics and Electrohydrodynamics in Microsystems.* Spinger, 2011.

[18] H. Morgan and N. G. Green, *AC Electrokinetics: Colloids and nanoparticles.* Research Studies Press Ltd, 2003.

[19] B. Comiskey, J.D. Albert, H. Yoshizawa, and J. Jacobson, *An electrophoretic ink for all-printed reflective electronic displays.* Nature, vol. 394, pp. 253-255, 1998.

[20] R. C. Hayward, D. A. Saville, and I. A. Aksay, *Electrophoretic assembly of colloidal crystals with optically tunable micropatterns.* Nature, vol. 404, pp. 56-59, 2000.

[21] S. Gangwal, O. J. Cayre, M. Z. Bazant, and O. D. Velev, *Induced-charge electrophoresis of metallodielectric particles.* Phys. Rev. Lett., vol. 100, pp. 058302-1-4, 2008.

[22] M. Fuduo, Y. Xingfu, Z. Hui, and N. Wu, *Inducing propulsion of colloidal dimers by breaking the symmetry in electrohydrodynamic flow.* Phys. Rev. Lett., vol. 115, pp. 208302-1-5, 2015.

[23] V.A. Murtsovkin, *Nonlinear flows near polarized disperse particles.* Colloid Jour., vol. 58, pp. 341-349, 1996.

[24] T. M. Squires and S. R. Quake, *Microfluidics: Fluid physics at the nanoliter scale.* Rev. Mod. Phys., vol. 77, pp. 977-1026, 2005.

[25] M. Z. Bazant, M.S. Kilic, B.D. Storey, and A. Ajdari, *Towards an understanding of induced-charge electrokinetics at large applied voltages in concentrated solutions.* Adv. Colloid Interface Sci., vol. 152, 48-88, 2009.

[26] T. M. Squires and M. Z. Bazant, *Induced-charge electro-osmosis.* J. Fluid Mech.,vol. 509, pp. 217-252, 2004.

[27] M.Z. Bazant and T. M. Squires, *Induced-charge electrokinetic phenomena: theory and microfluidic applications.* Phys. Rev. Lett., vol. 92, pp. 066101-1-4, 2004.

[28] T.M. Squires and M. Bazant, *Breaking symmetries in induced-charge electro-osmosis and electrophoresis.* J. Fluid Mech., vol. 560, pp. 65-101, 2006.

[29] I. Lazo and O. D. Lavrentovich, *Liquid-crystal-enabled electrophoresis of spheres in a nematic medium with negative dielectric anisotrop*, Phil. Trans. Soc. A, vol. 371, no. 2012255, 2013.

[30] O. D. Lavrentovich, *Active colloids in liquid crystals.* Curr. Opin. Colloid Interface Sci., vol. 21, pp. 97-109, 2016.

[31] O. D. Lavrentovich, *Transport of particles in liquid crystals.* Soft Matter, vol. 10, pp. 1264-1283, 2014.

[32] O.P. Pishnyak, S. Tang, J. R. Kelly, S.V. Shiyanovskii, and O.D. Lavrentovich, *Levitation, lift, and bidirectional motion of colloidal particles in an electrically driven nematic liquid crystal.* Phys. Rev. Lett., vol. 99, pp. 127802-1-4, 2007.

[33] S. Hernàndez-Navarro, P. Tierno, J. A. Farrera, J. Ignés-Mullol, and F. Sagués, *Reconfigurable swarms of nematic colloids controlled by photoactivated surface patterns.* Angew. Chem. Int. Ed., vol. 53, pp. 10696-10700, 2014.

[34] A. V. Straube, J. M. Pagés, P. Tierno, J. Ignés-Mullol, and F. Sagués, *Collective dynamics and conformal ordering in electrophoretically driven nematic colloids.* Phys. Rev. Res., vol. 1, pp. 022008(R)-1-5, 2019.

[35] D. K. Sahu, S. Kole, S. Ramaswamy and S. Dhara, *Omnidirectional transport and navigation of Janus particles through a nematic liquid crystal film.* Phys. Rev. Res., vol. 2, pp. 032009(R)-1-6, 2020.

[36] D. K. Sahu, and S. Dhara, *Measuring Electric-Field-Induced Dipole Moments of Metal-Dielectric Janus Particles in a Nematic Liquid Crystal.* Phys. Rev. Applied., vol. 14, pp. 034004-1-8, 2020.

[37] D. K. Sahu, and S. Dhara, *Electric field driven controllable motility of metal-dielectric Janus Boojum-particles in a thin film of nematic liquid crystal.* Phys. Fluids, vol. 33, pp. 0187106-1-8, 2021.

[38] I. Muševič, *Liquid crystal colloids.* Springer Inter- national Publishing AG, 2017.

[39] I. I. Smalyukh, *Liquid crystal colloids.* Annu. Rev. Condens. Matter Phys. vol. 9, pp. 207-226, 2018.

[40] S. Paladugu, C. Conklin, J. Viñals, and O. D. Lavrentovich, *Nonlinear electrophoresis of colloids controlled by anisotropic conductivity and permittivity of liquid-crystalline electrolyte.* Phys. Rev. Appl., vol. 7, pp. 034033-1-8, 2017.

[41] W. Thielicke and E. J. Stamhuis, *Time Resolved Digital Particle Image Velocimetry Tool for MATLAB.* http://pivlab.blogspot.com/p/pivlabdocumentation.html, 2010.

6

Measurement of electric field-induced dipole moment of metal-dielectric Janus particles

6.1 Introduction

In recent years, Janus particles have emerged as a new class of colloids that finds potential applications in interdisciplinary areas ranging from physics to biology, medicine and chemistry. Janus particles are used as building blocks for reconfigurable colloidal structures and superstructures on different length scales, which are potential for designing new and functional materials with complex architecture [1]. The imposed electric field induces dipole moment, whose magnitude depends on the electrical properties of the suspending medium and plays a crucial role in determining their equilibrium structures and dynamics. Although several experimental studies have been reported, the magnitude of the induced dipole moments of such particles has not been measured experimentally. In this chapter, we demonstrate a novel method of measuring the effective dipole moments of the Janus particles in a nematic liquid crystal.

Here, we study the effect of small amplitude AC electric fields on a pair of assembled quadrupolar Janus particles. Such pairs are static as they do not move under low electric field. The particles experience dipolar Coulomb as well as elastic forces of the medium which are directed oppositely along the line joining their centres. We demonstrate a competing effect of the two forces, which allows us to measure the effective induced dipole moments of the particles. The applicability of the technique is limited to liquid crystals but relevant to all microscopic particles, irrespective of shapes.

6.2 Theoretical background

Here, we present a theoretical model for calculating polarizability, especially the Clausius-Mossotti factor of metal and dielectric spherical particles dispersed in an aqueous solution.

6.2.1 Polarizability of a conducting spherical particle

Consider a conducting spherical particle of radius 'a' dispersed in an aqueous electrolyte. An external electric field E drives the ions and eventually induce an electric double layer (EDL) on the particle surface of typical thickness ($\lambda_D = \epsilon K_B T / \sum_i n_i^0 z_i^2 e^2$), the so-called Debye length as already discussed in chapter-1. In order to induce voltage less than the threshold voltage required for Faradic reactions at conductor-electrolyte interface, electric field of low strength is considered. At length scale larger than λ_D, the electrolyte remains neutral. The typical charging time for the EDL is $\tau = a\epsilon/\sigma\lambda_D$ which is basically the charging time (RC) of the double-layer capacitance ($C = 4\pi a^2\epsilon/\lambda_D$ for a sphere) on the metal surface through the resistor ($R = 1/4\pi\sigma a$, for a sphere) of the bulk electrolyte. For time scale larger than τ, EDL is fully charged, there is no current normal to the particle surface, and the electric field lines go around the particle. The situation is equivalent to an insulating sphere (Fig.6.1(a)). For time scale smaller than τ, charge accumulated in the EDL is negligible and electric field lines intersect normally to the particle surface which is similar to conducting sphere (Fig.6.1(b)).

As the medium is neutral (at length scales »λ_D), the electric potential in the bulk electrolyte satisfies Laplace's equation ($\nabla^2\Phi = 0$). The solution can be expressed as

$$\Phi = -E_0 r\cos\theta + \frac{A}{r^2}\cos\theta \tag{6.1}$$

where E_0 is the amplitude of the applied electric field, A is a constant, r is distance

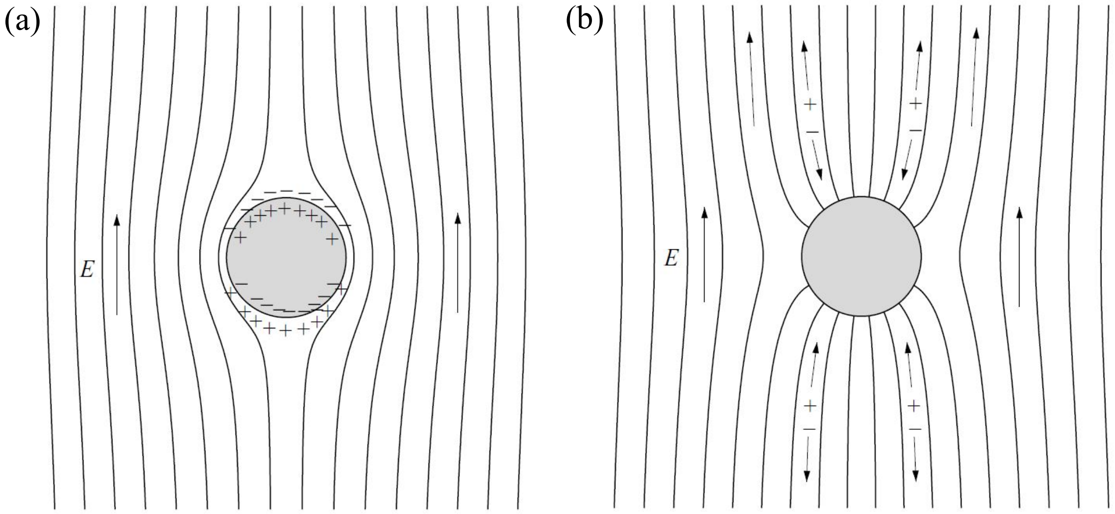

Figure 6.1: (a) For time scale much larger than τ, the EDL is fully charged and electric field lines go around the particle. (b) For time scale much smaller than τ, negligible amount of charge gets accumulated in the EDL and field lines intersect normaly to the particle surface (adapted from ref. [2]).

from the center of particle and θ is the angle between the position vector and the applied field vector. The required boundary condition is provided by the conservation of charge at the particle surface. The dielectric current $\vec{J}.\hat{e} = C_{DL}\left(\partial(V-\Phi)/\partial t\right)$ charges the EDL, where $\hat{e}$ is a unit normal vector to the particle surface, C_{DL} is the specific capacitance of the EDL, V is the electric potential in the metal sphere, and Φ is the potential outside the EDL. Thus, the voltage drop across the EDL is $(V-\Phi)$. If V is taken as zero, the boundary condition for the potential is [3]

$$\sigma\frac{\partial\Phi}{\partial r} = i\omega C_{DL}\Phi, \quad \text{at r = a} \tag{6.2}$$

where ω is the angular frequency of the applied electric field. Solving for A in Eq.(6.1) we obtain,

$$A = E_0 a^3\frac{i\Omega - 1/2}{i\Omega + 1}, \quad \Omega = \omega C_{DL} a/2\sigma \tag{6.3}$$

The term $A\cos\theta/r^2$ in Eq.(6.1) compared to the potential produced by a dipole moment $p = 4\pi\epsilon A$, where ϵ is the dielectric constant of the electrolyte. So the induced dipole moment is given by

$$p = 4\pi\epsilon E_0 a^3\frac{i\Omega - 1/2}{i\Omega + 1} \tag{6.4}$$

In terms of the Clausius-Mossotti factor $K_M(\omega)$, p can be expressed as

$$p(\omega) = 4\pi\epsilon E_0 a^3 K_M(\omega) \tag{6.5}$$

The real and imaginary part of the $K_M(\omega)$ for the conducting sphere can be written as [3]

$$Re[K_M(\omega)] = \frac{\Omega^2 - 1/2}{\Omega^2 + 1} \quad and \quad Im[K_M(\omega)] = \frac{3\Omega/2}{\Omega^2 + 1} \tag{6.6}$$

6.2.2 Polarizability of a dielectric spherical particle

In general, there are mainly two characteristics mechanisms of dielectric dispersion for suspensions in electrolyte solutions working in different frequency scales, which are sensitive to the polarization of the EDL induced on the dispersed particle. In the first case, dielectric dispersion is due to the electrolyte concentration variations on the local currents in the EDL induced by the applied field, known as low-frequency dispersion (α-dispersion). The second type of dispersion happens at higher frequency and is due to the formation of free charge distribution near the surfaces, known as Maxwell-Wagner dielectric dispersion. The reciprocal of the relaxation time of the electrolyte solution τ_m divides the frequency scale and is given by

$$\omega \equiv \frac{1}{\tau_m} \equiv \frac{\sigma_m}{\epsilon_m} \tag{6.7}$$

where ϵ_m and σ_m are the absolute dielectric constant and conductivity of the dispersion medium. Electric field perturbations and screening of charge in the electrolyte solutions are characterized by the time scale τ_m. It's role in the time domain is similar to that played by the Debye screening length

$$\lambda_D \equiv \sqrt{\frac{(D^+ + D^-)\,\epsilon_m}{2\sigma_m}} \tag{6.8}$$

in the space domain, where $D^\pm$ are the ionic diffusion coefficients. The time required for ion diffusion through Debye length is of the order of magnitude of τ_m:

$$\tau_m \approx \frac{\lambda_D^2}{2D} \tag{6.9}$$

where D is the average ion diffusion coefficient.

For frequencies $\omega << \omega_m$, the characteristics value of the conduction current density (*current carried due to the flow of charges*) in the electrolyte solution exceeds the displacement current density (*current caerried due to the varying electric field*), and the space distribution of the local electric fields in the disperse system is determined by the distribution of ionic currents. In the high frequency range $\omega >> \omega_m$, the characteristics value of the displacement current density the conduction current density, and the space distribution of the local electric fields in the disperse system is determined by the polarization of the molecular dipoles, rather than by the distribution of ionic currents. A general formula of the dipole coefficient for the wide-frquency range is given by [4]

$$\begin{aligned}\frac{p^*(\omega)}{a^3} = \frac{\epsilon_d/\epsilon_m - 1}{\epsilon_d/\epsilon_m + 2} - \frac{3}{2}\frac{\epsilon_d/\epsilon_m - 2Du}{(\epsilon_d/\epsilon_m + 2)(Du+1)}\frac{1}{1 + i\omega\tau_{MW}} \\ - \frac{3(R^+ - R^-)H}{2AS}\frac{1 + \sqrt{2/S}\sqrt{i\omega\tau_\alpha}}{1 + \sqrt{2/S}\sqrt{i\omega\tau_\alpha} + i\omega\tau_\alpha} \\ \times\, exp(-\omega)\frac{\epsilon_m}{\sigma_m}\end{aligned} \tag{6.10}$$

where

$$\begin{aligned}
Du(\zeta) &= \frac{\sigma_d}{\sigma_m a}, \\
R^\pm &= \frac{2\sigma_d^\pm}{\sigma_m^\pm a}, \\
A &= 4Du(\zeta) + 4, \\
m^\pm &= \frac{2\epsilon_m}{3\eta D^\pm}\left(\frac{k_B T}{ze}\right)^2, \\
U^\pm &= \frac{48m^\pm\lambda_D}{a} ln\left[cosh\frac{z\zeta}{4}\right], \\
B &= (R^+ + 2)(R^- + 2) - U^+ - U^- - (U^+R^- + U^-R^+)/2, \\
S &= A/B, \\
\tau_\alpha &= \frac{a^2(D^+ + D^-)S}{4D^+D^-}, \\
\Delta &= \frac{D^- - D^+}{z(D^- + D^+)}, \\
H &= \frac{(R^+ - R^-)(1 - z^2\Delta^2) - U^+ + U^- + z\Delta()U^+ + U^-}{A}, \\
\tau_{MW} &= \frac{\epsilon_m}{2\sigma_m}\frac{\epsilon_d/\epsilon_m + 2}{Du + 1},
\end{aligned}$$

ϵ_p is the dielectric constant of the dielectric particle, σ_d is the surface conductivity of the particle, $Du(\zeta)$ is Dukhin's number, ζ is the potential across the EDL, a size of the particle, $D^\pm$ is the diffusion coefficients of ions, η is the viscosity of the electrolyte.,

τ_{MW} is the relaxation time corresponding to Maxwell-Wagner dispersion. The complex dipole coefficient provides both real and imaginary parts which will be used later for calculating induced polarizability of the particles due to external electric field.

6.2.3 Calculation of the effective dipole shift of a dielectric hemisphere

In general, particles dispersed in a medium induce electric dipole moment along the direction of applied electric field. For a dielectric particle with metal coating on one hemisphere, we assume that induced dipole moment on each hemisphere is half of that induced on a full sphere of same material and size. But for a hemispherical particle, there is a shift in the effective induce dipole moment [5]. Let's consider a dielectric hemisphere of radius r in an aqueous solution under an electric field E. Following electrostatics, the surface polarization charge density ρ can be expressed as [5]

$$\rho(\theta) = 3\epsilon_0 E \left(\frac{\epsilon_p/\epsilon_m - 1}{\epsilon_p/\epsilon_m + 2} \right) cos\theta \tag{6.11}$$

where ϵ_m and ϵ_p are the dielectric constant of the medium and the particle, respectively. As schematically shown in the Fig.6.2, the unit dipole moment dp comprising positive and negative surface charge elements each occupying a unit surface area dA, separated by distance l is given by [5]

$$\begin{aligned} dp(\theta,\phi) &= \rho(\theta).dA(\theta,\phi).l(\theta,\phi) \\ &= \left(3\epsilon_0 E \left(\frac{\epsilon_p/\epsilon_m - 1}{\epsilon_p/\epsilon_m + 2} \right) cos\theta \right) . \left(R^2 sin\theta d\theta d\phi \right) . (2Rcos\theta) \\ &= 6\epsilon_0 E \left(\frac{\epsilon_p/\epsilon_m - 1}{\epsilon_p/\epsilon_m + 2} \right) R^3 cos^2\theta sin\theta d\theta d\phi \end{aligned} \tag{6.12}$$

The effective dipole shift $\vec{r}_{shift}$ of the hemisphere, similar to the definition of center of mass is defined as

$$\vec{r}_{shift} = \frac{\oint \vec{r}(\theta,\phi) dp(\theta,\phi)}{\oint dp(\theta,\phi)} \tag{6.13}$$

Symmetry in the Fig.6.2 implies the shift will be along y-axis, so the y component of displacement of dp from the center is $\delta = Rsin\theta sin\phi$ and the shift of dipole along the

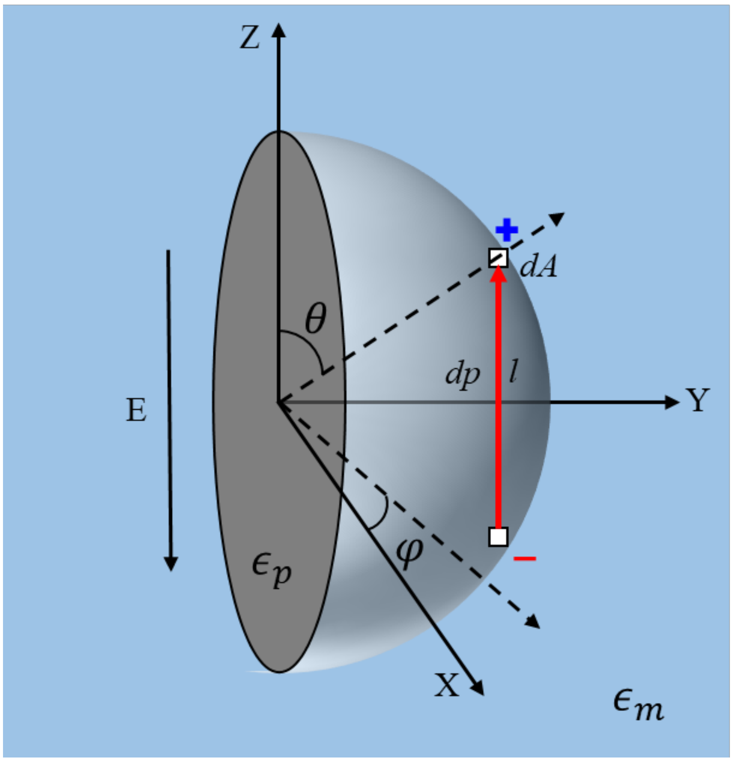

Figure 6.2: Schematic presentation of a dielectric hemisphere in an aqueous solution. The origin of the defined coordinate system matches with center of equatorial plane of the hemisphere.

y-axis is given by [5]

$$\begin{aligned} y_{shift} &= \frac{\oint \delta(\theta,\phi) dp(\theta,\phi)}{\oint dp(\theta,\phi)} \\ &= \frac{\int_0^\pi d\theta \int_0^\pi d\phi 6\epsilon_0 E \left(\frac{\epsilon_p/\epsilon_m - 1}{\epsilon_p/\epsilon_m + 2}\right) R^4 cos^2\theta sin^2\theta sin\phi}{\int_0^\pi d\theta \int_0^\pi d\phi 6\epsilon_0 E \left(\frac{\epsilon_p/\epsilon_m - 1}{\epsilon_p/\epsilon_m + 2}\right) R^3 cos^2\theta sin\theta} \\ &= \frac{3}{8} R \end{aligned} \tag{6.14}$$

For metal hemisphere, the shift in effective dipole is also the same but the magnitude of dipole moment will be higher than the dielectric hemisphere because of higher polarizability. Hence, the effective induce dipole moment of a metal-dielectric Janus particle is given by the sum of the dipole moments induced on both metal and dielectric hemispheres.

6.3 Experimental

We prepared metal-dielectric Janus particles using directional deposition of metal (Ti) onto dry silica particles (SiO_2) of diameter $2a = 3.0 \pm 0.2$ μm (Bangs Laboratories, USA) in vacuum as explained in the 2nd chapter [1]. The surface of the Janus particles is coated with N, N-dimetyl-N-octadecyl-3 aminopropyl-trimethoxysilyl chloride (DMOAP) in order to induce perpendicular (homeotropic) orientation of the liquid crystal director [20–22]. A small quantity (0.01 wt%) of DMOAP coated Janus particles is dispersed in nematic liquid crystal, MLC-6608 (Merck). It exhibits the following phase transitions: SmA −30°C N 90°C Iso. The dielectric anisotropy of MLC-6608 is negative ($\Delta\epsilon = \epsilon_{||} - \epsilon_{\perp} = -3.3$, where $\epsilon_{||}$ and $\epsilon_{\perp}$ are the dielectric permittivities for electric field $\mathbf{E}$, parallel and perpendicular to $\hat{\mathbf{n}}$) whereas the conductivity anisotropy is positive ($\Delta\sigma = \sigma_{||} - \sigma_{\perp} \simeq 6 \times 10^{-10}$ Sm^{-1} at 100 Hz) (see Appendix). No electroconvection was observed in the experimental field and frequency range.

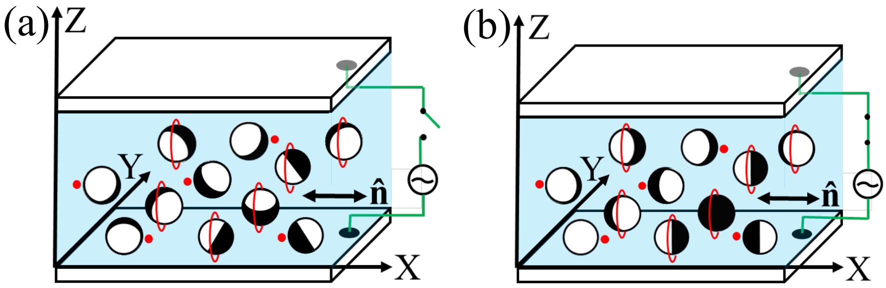

Figure 6.3: Janus quadrupolar particles (a) without and (b) with electric field. Note that the metal-dielectric interface becomes parallel to the field direction.

The experimental cells are prepared with use of two indium-tin-oxide (ITO) coated glass plates. The plates were spin coated with polyimide AL-1254 (JSR Corporation, Japan) and cured at 180^{0}C for 1 h. They were then rubbed unidirectionally with a benchtop rubbing machine (HO-IAD-BTR-01) for homogeneous or planar alignment of the nematic director $\hat{\mathbf{n}}$. The ITO plates were separated by spherical spacers of diameter 5.0 μm, making the rubbing directions antiparallel, and then sealed with UV-curing optical adhesive (NOA-81, Norland). A schematic diagram of a cell is shown in Fig.6.3(a). The output of a function generator (AFG 3102, Tektronix) is connected to a voltage amplifier for application of sinusoidal voltage to the cell (Fig.6.3(b)). An inverted polarising optical microscope (Nikon Ti-U) with water-immersion objective (NIR Apo 60/1.0, Nikon) was used for observing the particles. A laser tweezer is built on the microscope using a cw solid-state laser operating at 1064 nm (Tweez 250si, Aresis) for manipulating the particles. A charge-coupled device (CCD) video camera (iDs-UI, CMOSIS) at a rate of 50-100 frames per second was used for video recording of the particle trajectory. A particle-tracking program is used off-line to track the particles with an accuracy of ±20 nm.

6.4 Results and discussion

We worked in the dilute regime of the concentration (0.001wt%) and disperse the particles in a cell whose gap is larger than but close to the diameter of the particles. In this case the particles mostly stabilize quadrupolar director field as shown in Fig.6.4(a). Figure 6.4(b) shows the light-microscope texture of a few Janus particles placed between crossed polarizers. The four-lobed intensity pattern of the particles, a characteristic feature of elastic quadrupoles, is further substantiated from the texture obtained by inserting a λ-plate (inset to Fig.6.4(b)). The texture of the particles (without polarizers) shows that the metal hemisphere (dark half) of particles is oriented in different directions, always keeping the Saturn-rings perpendicular to the macroscopic director (Fig.6.4(c)). Once the ac electric field is switched on along the z-axis, the particles reorient [24] such that the plane of the metal-dielectric interface lies parallel to the field as shown in Fig.6.3(b). Since the dielectric anisotropy of MLC-6608 is negative, the applied electric field does not influence the far field director except very close to the particles [17]. We focused on a pair of Janus particles that are assembled by elastic forces of the nematic liquid crystal and study the effect of field. At zero field, the line joining the centers of the particles makes an angle of 57° with respect to the director $\hat{\mathbf{n}}$. [6]. At this angle the particles experience an attractive elastic force. Once the electric field is switched on, the particles rotate such that the metal-dielectric interface becomes parallel to the field due to the effective induced electric dipole moment (p_{eff}), keeping the mutual separation unchanged as shown in Figs.6.5(a) and (b). With increasing field amplitude, the particles are displaced in the opposite directions along the joining line of their centers as shown in Figs.6.5(c) to (e). Above a certain

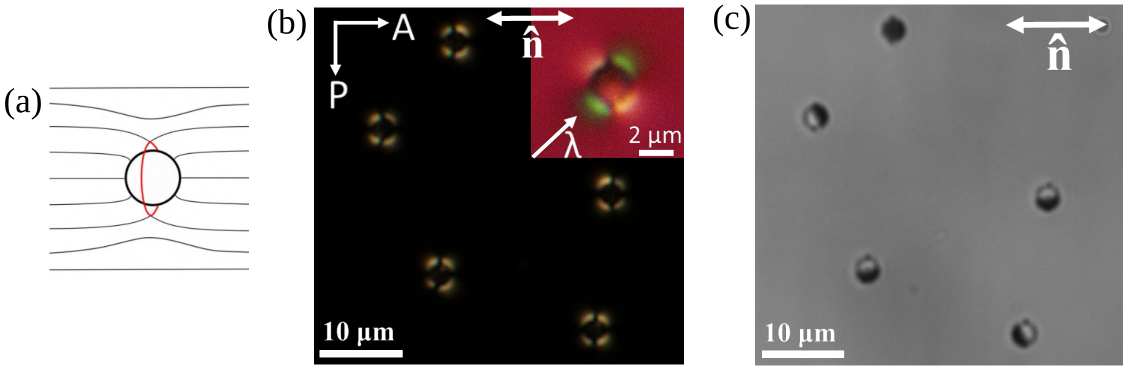

Figure 6.4: (a) Quadrupolar elastic distortion of nematic director $\hat{\mathbf{n}}$ around a spherical dielectric particle. Red circle represents Saturn-ring defect. (b) Cross-polarised micrograph of a few quadrupolar particles without electric field. Inset shows the micrograph of a particle with a λ-plate (530 nm) inserted in between the polariser and sample with it's slow axis at 45° to the director. (c) Image captured by CCD camera. Dark (bright) hemisphere represents the metal (dielectric).

field, the particles become free from each other's influence and swim independently as described in the chapter-3.

The centre-to-centre separation r as a function of the field at different frequencies is shown in Fig.6.5(f). For a given frequency f, it is apparent that there is a threshold field E_2, beyond which r increases rapidly. Careful observation reveals that in the low field region ($E < E_2$) there is another threshold E_1, beyond which the separation begins to increase. For clarity, the low field region of Fig.6.5(f) is expanded and shown in Fig.6.5(g). For example at 20 Hz, the threshold fields are $E_1 \simeq 0.2$ Vμm^{-1} and $E_2 \simeq 0.7$ Vμm^{-1}. With increasing field the magnitude of p_{eff}, and consequently the repulsive dipolar force F_d increases, which pushes the particles apart. At E_1, the magnitude of F_d just exceeds the elastic binding force F_{el}, and beyond E_2 the particle's state is controlled by the surrounding electroosmotic flows. In the field range $E_1 \leq E \leq E_2$, the dipolar Coulomb (repulsive) and elastic (attractive) forces are balanced as shown schematically in Fig.6.6(a), resulting in a stable system in which the equilibrium separation (r_{eq}) is measured. Within this range the effect of the field is reversible (i.e., r_{eq} reduces to zero when the field is decreased to zero). Below E_2,

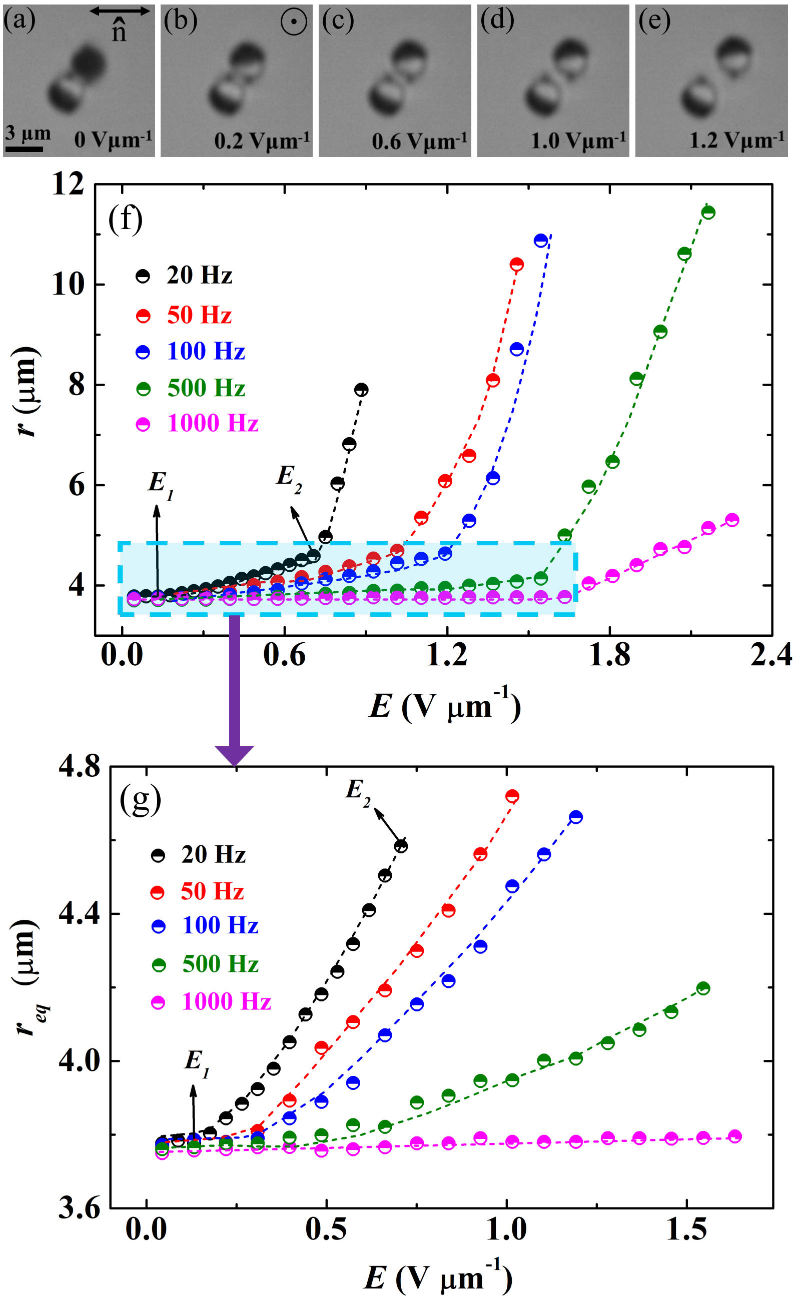

Figure 6.5: (a-e) Effect of AC field on a pair of assembled quadrupolar Janus particles (f = 100 Hz). (f) Centre-to-centre separation r with field at different frequencies. (g) Expanded rectangular region in (f) enclosed by dashed line. E_1 and E_2 are the first and second threshold fields, respectively and r_{eq} is the equilibrium separation in the field range: $E_1 \leq E \leq E_2$. Dotted lines are drawn as a guide to the eye. Cell thickness: 5.5 µm.

the separation occurs along the line joining their centers, which makes an angle 57° with respect to the far-field director $\hat{\mathbf{n}}$, irrespective of the orientation of the Janus vector $\hat{\mathbf{s}}$ (normal to the metal-dielectric interface). This indicates that the induced electroosmotic flows surrounding the particles are weak and does not affect to their equilibrium separation. Above E_2, the surrounding electroosmotic flows are stronger and the particles start swimming in different directions in the plane of the sample, depending on the orientation of $\hat{\mathbf{s}}$ as discussed in the chapter-3 [19].

The electric field also induces a dipole moment in silica particles (non-Janus) and hence a similar effect is expected to be seen in a pair of silica quadrupolar particles. To see such an effect, we applied an electric field and compared the results with those for the Janus particles. Figure 6.6(b) shows that the equilibrium separation between two silica particles does not change upto the applied field ($E \leq E_2$). Even at much higher fields the separation remains unchanged until electrohydrodynamic instability was observed. This indicates that the magnitude of induced dipole moment in silica particles is much smaller than that of the Janus particles. This is expected as the polarizability of silica is lower than that of Titanium metal. As a result, the dipolar Coulomb repulsion between the two silica particles is not sufficiently strong in the applied-field range to overcome the attractive elastic forces.

The Coulomb force F_d between two identical induced electric dipoles (p_{eff}) of the Janus particles is expressed as:

$$F_d(r) = 3p_{eff}^2(E)/4\pi\epsilon_0\epsilon_m r_{eq}^4(E) \tag{6.15}$$

where ϵ_m is the relative permittivity of the medium and $r_{eq}(E)$ is the equilibrium separation. In the field range: $E_1 \leq E \leq E_2$, the Coulomb force $F_d(r)$ is obtained by balancing it against the elastic force $F_{el}(r)$, which is obtained by videomicroscopy in the absence of an electric field. To measure F_{el}, initially two particles are held at a distance with the help of the laser tweezers and then allowed to interact freely, by switching off the laser. The centre-to-centre separation $r(t)$ between two particles obtained from the recorded movie is shown in Fig.6.7(b). The motion of the particles in the NLC is overdamped due to high viscosity. Consequently, the Stokes drag force (F_S) in a uniformly aligned NLC is in equilibrium with the elastic force $F_{el}(r)$, resulting in no acceleration. The elastic force between two particles is calculated from the

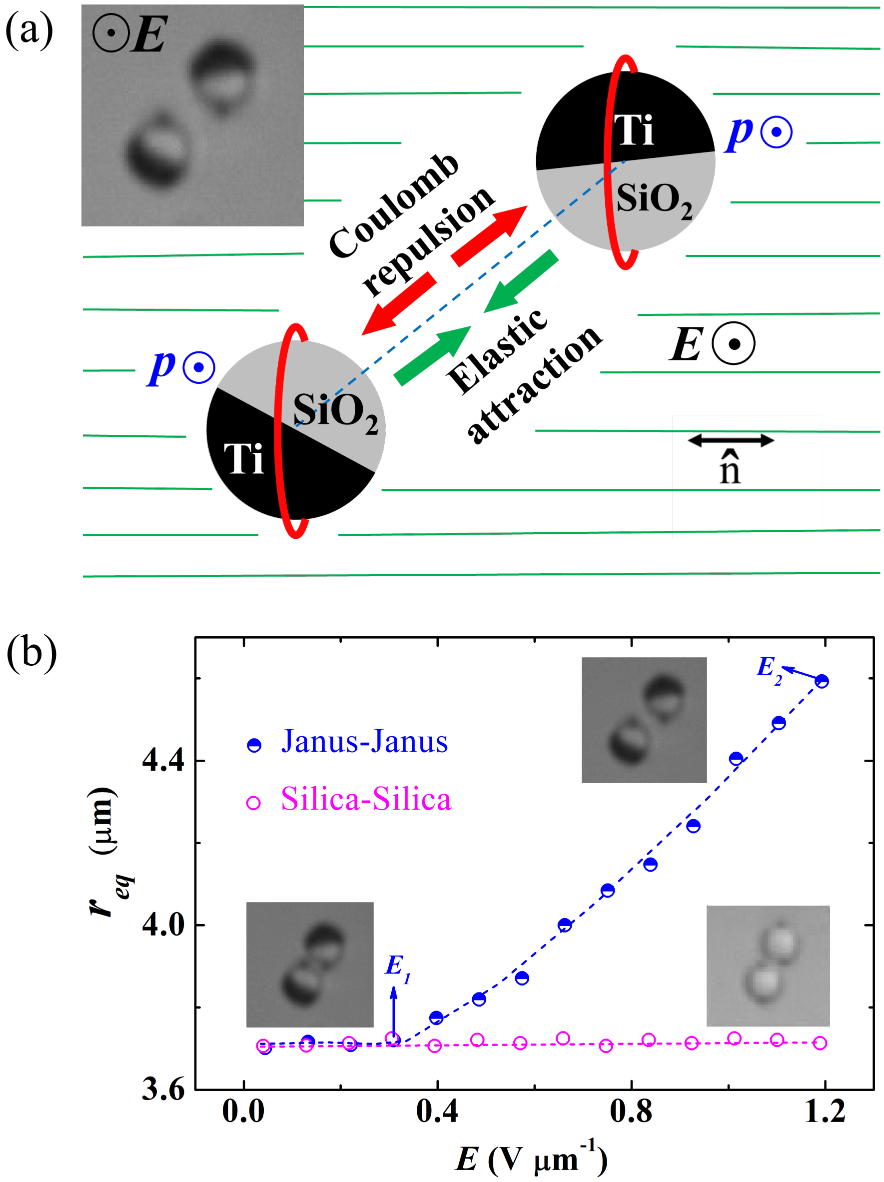

Figure 6.6: (a) Schematic diagram demonstrating the balance of elastic and dipolar Coulomb forces. Induced dipole moments ($\vec{p}$) are parallel to **E** (out of plane). Green lines indicate far field director **n̂**. (Inset) CCD image of Janus particles under AC field. (b) Equilibrium separation r_{eq} between a pair of Janus (blue half-filled circles) and silica (pink open circles) particles with field (f=100 Hz).

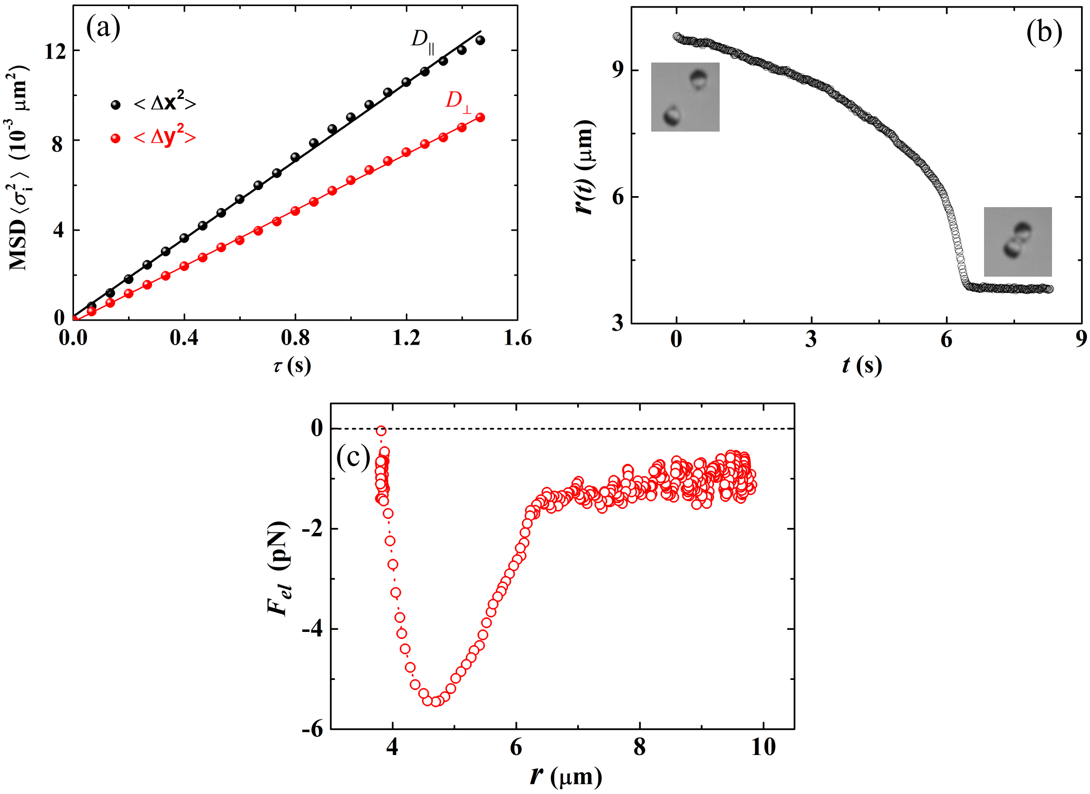

Figure 6.7: (a) Mean squared displacements of a quadrupolar Janus particle in two orthogonal directions (parallel and perpendicular to the director) in MLC-6608. (b) Centre-to-centre distance $r(t)$ between two Janus quadrupolar particles approaching due to elastic interaction in the absence of electric field. Inset shows the snapshots at initial ($t = 0$ s) and final time ($t \simeq 9$ s). (c) Variation of elastic force F_{el} between two Janus particles as a function of r measured from the videomicroscopy.

numerical differentiation of the trajectory, which is given by $F_{el}(r) = -F_S = \zeta_i \frac{dr(t)}{dt}$, where ζ_i is the drag coefficient and the subscript, i refers to the motion either parallel to $\hat{\mathbf{n}}$ ($i =\parallel$) or perpendicular to $\hat{\mathbf{n}}$ ($i =\perp$) [25, 26]. Using methods similar to those reported in references [21,22], we have determined $\zeta_\parallel$ and $\zeta_\perp$ of a Janus particle in MLC-6608 by measuring its anisotropic diffusive motion. Particle displacements ($\triangle x$ and $\triangle y$) along parallel and perpendicular to the director $\hat{\mathbf{n}}$ were measured using videomicroscopy as a function of delay time τ. The mean squared displacements along x and y directions shown in Fig.6.7(a) are linear in τ with different slopes corresponding to two diffusivities, $D_\parallel$ and $D_\perp$ as $\sigma^2_{\parallel,\perp} = 2D_{\parallel,\perp}\tau$. The diffusion constants obtained from from the least-squares fits are given by $D_{\parallel} = 4.1 \pm 0.1 \times 10^{-3}$µ m^{2}s^{-1} and $D_{\perp} = 2.9 \pm 0.2 \times 10^{-3}$µm^{2}s^{-1}. The corresponding drag coefficients obtained by using the Stokes-Einstein relation $\zeta_{\parallel,\perp} = K_B T / D_{\parallel,\perp}$ are $\zeta_{\parallel} \simeq 1.0 \times 10^{-6}$ kg s^{-1} and $\zeta_{\perp} \simeq 1.4 \times 10^{-6}$ kg s^{-1}. In estimating $F_{el}(r)$, the average drag coefficient $\zeta = (\zeta_{\parallel} + \zeta_{\perp})/2 \approx 1.2 \times 10^{-6}$ kg s^{-1} is used. The variation of $F_{el}(r)$ between two Janus particles as a function of separation is shown in Fig.6.7(c). If we substitute $F_d(r) = F_{el}(r)$ in Eq.(6.16), the magnitude of the effective induced dipole moment of the Janus particles can be expressed as:

$$p_{eff}(E) = \sqrt{(4/3)\pi\epsilon_0\epsilon_m r_{eq}^4(E) F_{el}(r)} \tag{6.16}$$

where ϵ_m is the average relative permittivity of the sample and can be written as $\epsilon_m = (\epsilon_{\parallel} + 2\epsilon_{\perp})/3 = 6.4$ (see Appendix). The variation of p_{eff} calculated with Eq.(6.17) as a function of the field amplitude ($E_1 \leq E \leq E_2$) at different frequencies is shown in Fig.6.8(a). We observe a linear variation with field, that is, $p_{eff} = \alpha_{eff} E$, where α_{eff} is the effective electric polarizability of the Janus particles. The best-fit lines nearly pass through the origin. This means that the dipole moment is induced only by the electric field and eventually it asserts that the separation (r_{eq}) between the two particles (below E_2) occurs primarily due to the dipolar Coulomb repulsion. Figure 6.8(b) shows α_{eff} obtained as a fit parameter at different frequencies. It decreases with increasing frequency as expected.

In what follows, we theoretically calculate the polarizability of the Janus particles. For a spherical particle polarizability can be expressed as [5]

$$\alpha_{M,D}(\omega) = 4\pi\epsilon_0\epsilon_m K_{M,D}(\omega) a^3 \tag{6.17}$$

where ϵ_m is the relative permittivity of the dispersing medium, $K(\omega)$ is the complex Clausius-Mossotti factor, a is the radius of the sphere and M and D stand for metal and dielectric, respectively. The Clausius-Mossotti (CM) factors of the metallic and dielectric spheres are calculated by using the analytical solutions provided above, given by Ramos *et al.* [29] and Shilov *et al.* [**?**], respectively. The real and imaginary components of the Claussius-Mossotti factors for both metal and dielectric spheres are presented in Fig.6.9. The average relative permittivity of the sample obtained from the experiments is given by $\epsilon_m = 6.4$ (see Appendix). We use superposition principle

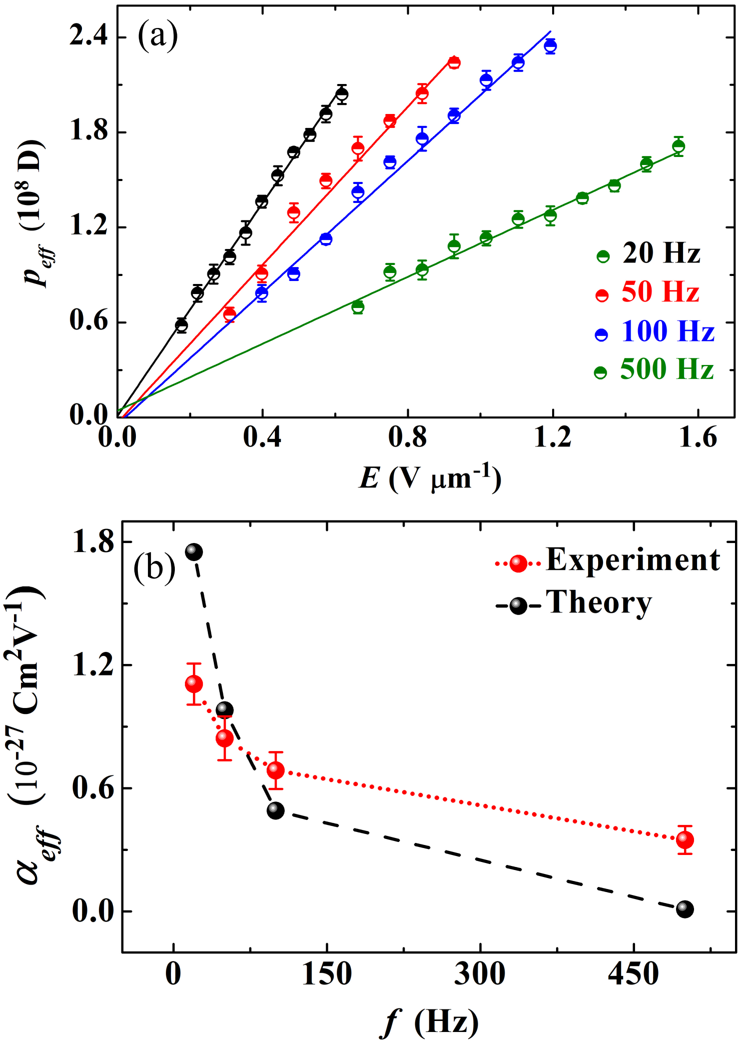

Figure 6.8: (a) Effective induced dipole moment p_{eff} with field at different frequencies. Solid lines show the least squares fit to equation: $p_{eff} = \alpha_{eff}E$. (b) Polarisability α_{eff} at different frequencies obtained from the experiments (filled red circles) and theory (filled black circles). Dotted and dashed lines are drawn as a guide to the eye. Error bars represent the standard deviation of the mean value.

in which it is assumed that the induced dipole moment of a Janus particle is equal to the sum of half the contribution from a metal sphere and half the contribution form a dielectric sphere, so the effective theoretical polarizability of the Janus particles can be written as $\alpha_{eff} = \frac{1}{2}(\alpha_M + \alpha_D)$. The polarizability calculated using Eq.(6.18) at different frequencies is shown in Fig.6.8(b), and is in reasonably good agreement with

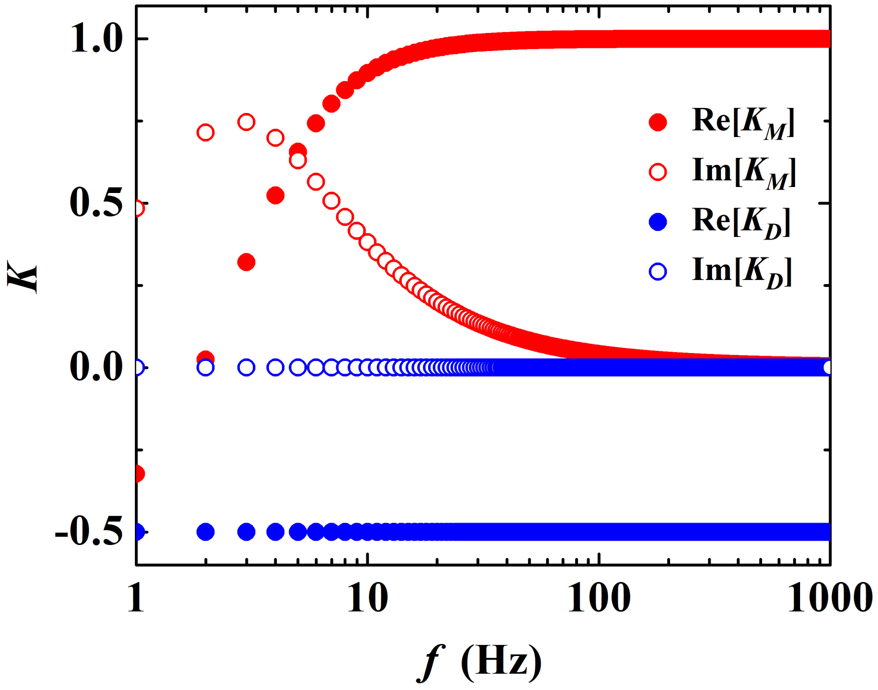

Figure 6.9: Frequency dependence of the Clausius-Mossotti factors. Filled and empty circles represent the real and imaginary parts of the K_M for metal (red circles) and K_D for dielectric spheres (blue circles) respectively at different frequencies.

the experiments.

Two further remarks are in order. First, apart from dipolar repulsion, the hydrodynamic repulsion due to the overlap of electroosmotic flows may also contribute to the interparticle separation [30]. We present an approximate estimation of the magnitudes of the two forces. The swimming force of the particles can be written as $F_{swim} = 6\pi\eta av$, which approximately sets the upper limit of effective hydrodynamic force. Taking radius $a = 1.5$ μm, flow viscosity $\eta = 20$ mPas and swimming velocity $v = 1$ μm s^{-1} (below E_2), we find the estimated hydrodynamic force $F_{swim} \simeq 0.6$ pN. Using eq.(6.16) and taking separation $r = 4$μm, $\epsilon_m = 6.4$, and $p_{eff} = 2 \times 10^8$ D we find the estimated dipolar force between two particles is given by $F_d \simeq 7$ pN, which is one order of magnitude higher than the upper limit of the hydrodynamic force. Therefore, the effect of hydrodynamic repulsion is much smaller compared with that of the dipolar repulsion between the two particles. Further, reasonably good agreement between the experimentally measured and theoretically calculated polarizabilities based on an approximate model affirms that the effect of hydrodynamic repulsion on the equilibrium separation between two Janus particles below E_2 is negligibly small compared with the effect of the dipolar Coulomb repulsion. Second, conceptually this method could also be employed to measure the induced dipole moments of silica particles but a much higher electric field is required. Hence, an appropriate liquid crystal must be chosen such that no electroconvection is observed at the desired fields.

6.5 Conclusion

We have studied the effect of an ac electric field on a pair of quadrupolar Janus particles that are assembled in a nematic liquid crystal by the elastic forces of the director field. The imposed electric field induces an effective dipole moment in each particle that is parallel to the field direction. The dipolar Coulomb repulsion between two assembled Janus particles increases with field, and beyond a particular field the repulsive force exceeds the elastic binding force of the particles, as a result of which the mutual separation increases. The competing effects of these two oppositely directed forces within a certain field range allows us to measure the effective induced dipole moments of the Janus particles, which vary linearly with the field. We measured the effective polarizability at different frequencies. The theoretically calculated polarizability of the particles based on the superposition principle agrees well with the experimental findings. Our study focussed on spherical particles in nematic liquid crystals; however, this method is applicable to all microscopic Janus particles irrespective of their shape in a variety of liquid crystals.

Appendix: Measurements of relative permittivity and conductivity anisotropy

The relative permittivity and conductivity of MLC-6608 at room temperature (30°C) in the experimental frequency range (20-500 Hz) are measured using an LCR-meter. The frequency dependence of the parallel and perpendicular components of the relative permittivity ($\epsilon_{||}$ and $\epsilon_{\perp}$) and conductivity ($\sigma_{||}$ and $\sigma_{\perp}$) are shown in Fig.6.10. Both the permittivities remain constant (Fig.6.10(a)) whereas both conductivities are increasing with frequency and $\sigma_{\|}$ increases at much faster rate than $\sigma_{\perp}$ (Fig.6.10(b)). The relative permittivity anisotropy of the sample (MLC-6608) is negative ($\Delta\epsilon = \epsilon_{\|} - \epsilon_{\perp} < 0$), whereas the conductivity anisotropy is positive ($\Delta\sigma = \sigma_{\|} - \sigma_{\perp} > 0$).

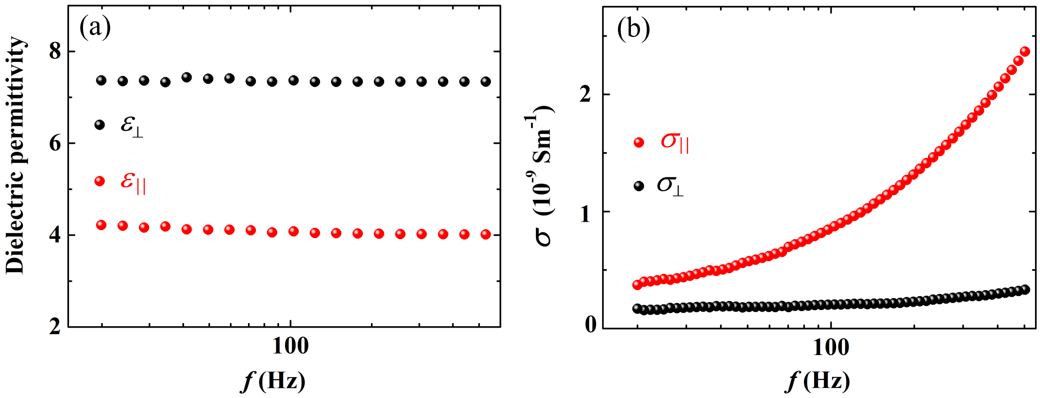

Figure 6.10: Parallel and perpendicular components of (a) the relative permittivities ($\epsilon_{\|}$ and $\epsilon_{\perp}$) and (b) the conductivities ($\sigma_{\|}$ and $\sigma_{\perp}$) as a function of frequency at room temperature at an applied field of 0.1 V μm^{-1}.

References

[1] J. Yan, M. Han, J. Zhang, C. Xu, E. Luijten, and S. Granick, *Reconfiguring active particles by electrostatic imbalance.* Nat. Mater., vol. 5, pp. 1095-1099, 2016.

[2] T. M. Squires and M. Z. Bazant, *Induced-charge electro-osmosis* J. Fluid Mech., vol. 509, pp. 217-252, 2004.

[3] P. García-Sánchez, Y. Ren, J. J. Arcenegui, H. Morgan, and A. Ramos, *Alternating current electrokinetic properties of gold-coated microspheres*, vol. 28, pp. 13861-13870, 2012.

[4] V. N. Shilov, A. V. Delgado, F. Gonzalez-Caballero, and C. Grosse, *Thin double layer theory of the widefrequency range dielectric dispersion of suspensions of non-conducting spherical particles including surface conductivity of the stagnant layer*, Colloid Surface A, vol. 192, pp. 253-265, 2001.

[5] J. Zhang, J. Yan, and S. Granick, *Directed Self Assembly Pathways of Active Colloidal Clusters.* Angew. Chem. Int. Ed., vol. 55, pp. 5166-5169, 2016.

[6] S. Ramaswamy, R. Nityananda, V. A. Raghunathan, and J. Prost, *Power-law forces between particles in a nematic.* Mol. Cryst. Liq. Cryst., vol. 288, pp. 175-180, 1996.

[7] Y. Gu and N. L. Abbott, *Observation of Saturn-Ring Defects around Solid Microspheres in Nematic Liquid Crystals.* Phys. Rev. Lett., vol. 85, pp. 4719-4722, 2000.

[8] P. Poulin, H. Stark, T. C. Lubensky, and D. A. Weitz, *Novel Colloidal Interactions in Anisotropic Fluids.* Science, vol. 275, pp. 1770-1773, 1997.

[9] H. Stark, *Physics of colloidal dispersions in nematic liquid crystals.* Phys. Rep., vol. 351, pp. 387-474, 2001.

[10] I. Muševič, *Liquid crystal colloids.* Springer International Publishing AG, 2017.

[11] I. Muševič, *Optical manipulation and self-assembly of nematic colloids: colloidal crystals and superstructures.* Liq. Cryst. Today, vol. 19, pp. 2-12, 2010.

[12] I. I. Smalyukh, *Liquid Crystal Colloids.* Ann. Rev. Cond. Mat. Phy., vol. 9, pp. 207-226, 2018.

[13] I. Muševič, M. Škarabot, U. Tkalec, M. Ravnik, and S. Žumer, *Two-Dimensional Nematic Colloidal Crystals Self-Assembled by Topological Defects.* Science, vol. 313, pp. 954-958, 2006.

[14] Y. Yuan, Q. Liu, B. Senyuk, and I. I. Smalyukh, *Elastic colloidal monopoles and reconfigurable self-assembly in liquid crystals.* Nature, vol. 570, pp. 214-218, 2019.

[15] H. Mundoor, S. Park, B. Senyuk, H. H. Wensink, I. I. Smalyukh, *Hybrid molecular-colloidal liquid crystals.* Science, vol. 360, pp. 768-771, 2018.

[16] O. D. Lavrentovich, *Active colloids in liquid crystals.* Curr. Opin. Colloid Interface Sci., vol. 21, pp. 97-109, 2016.

[17] O. D. Lavrentovich, I. Lazo, and O. P. Pishnyak, *Nonlinear electrophoresis of dielectric and metal spheres in a nematic liquid crystal.* Nature, vol. 467, pp. 947-955, 2010.

[18] I. Lazo, C. Peng, J. Xiang, S. V. Shiyanovskii, and O. D. Lavrentovich, *Liquid crystal-enabled electro-osmosis through spatial charge separation in distorted regions as a novel mechanism of electrokinetics.* Nat. Commun., vol. 5, no. 5033, 2014.

[19] D. K. Sahu, S. Kole, S. Ramaswamy, and S. Dhara, *Omnidirectional transport and navigation of Janus particles through a nematic liquid crystal film.* Phys. Rev. Res., vol. 2, pp. 032009(R)-1-6, 2020.

[20] K. P. Zuhail, P. Sathyanarayana, D. Seč, S. Čopar, M. Škarabot, I. Muševič, and S. Dhara, *Topological defect transformation and structural transition of two-dimensional colloidal crystals across the nematic to smectic- A phase transition.* Phys. Rev. E, vol. 91, pp. 030501(R)-1-4, 2015.

[21] U. Tkalec, M. Ravnik, S. Žumer, and I. Muševič, *Vortexlike topological defects in nematic colloids: chiral colloidal dimers and 2D crystals.* Phys. Rev. Lett., vol. 103, pp. 127801-1-4, 2009.

[22] M. Škarabot, M. Ravnik, D. Babič, N. Osterman, I. Poberaj, S. Žumer, I. Muševič, A. Nych, U. Ognysta, and V. Nazarenko, *Laser trapping of low refractive index colloids in a nematic liquid crystal.* Phys. Rev. E, vol. 73, pp. 021705-1-10, 2006.

[23] K. P. Zuhail, S. Čopar, I. Muševič, and S. Dhara, *Spherical microparticles with Saturn ring defects and their self-assembly across the nematic to smectic- A phase transition.* Phys. Rev. E, vol. 92, pp. 052501-1-5, 2015.

[24] S. Gangwal, O. J. Cayre, M. Z. Bazant, and O. D. Velev, *Induced-Charge Electrophoresis of Metallodielectric Particles.* Phys. Rev. Lett., vol. 100, pp. 058302-1-4, 2008.

[25] M. Rasi M, R. K. Pujala, and S. Dhara, *Colloidal analogues of polymer chains, ribbons and 2D crystals employing orientations and interactions of nano-rods dispersed in a nematic liquid crystal.* Sci. Rep., vol. 9, no. 4652, 2019.

[26] D. V. Sudhakaran, R. K. Pujala, and S. Dhara, *Orientation Dependent Interaction and Self-Assembly of Cubic Magnetic Colloids in a Nematic Liquid Crystal.* Adv. Opt. Mater., vol. 8, pp. 1901585(1-9), 2020.

[27] C. P. Lapointe, T. G. Mason, and I. I. Smalyukh, *Shape-Controlled Colloidal Interactions in Nematic Liquid Crystals.* Science, vol. 326, pp. 1083-1086, 2009.

[28] U. Tkalec and I. Muševič, *Topology of nematic liquid crystal colloids confined to two dimensions.* Soft Matter, vol. 9, pp. 8140-8150, 2013.

[29] A. Ramos, H. Morgan, N. G. Green, and A. Castellanos, *AC Electric-Field-Induced Fluid Flow in Microelectrodes.* J. Colloid Interface Sci., vol. 217, pp. 420-422, 1999.

[30] A. V. Straube, J. M. Pagés, P. Tierno, J. Ignés-Mullol, and F. Sagués, *Collective dynamics and conformal ordering in electrophoretically driven nematic colloids.* Phys. Rev. Res., vol. 1, pp. 022008(R)-1-5, 2019.

[31] S. Dhara, and N. V. Madhusudana, *Ionic contribution to the dielectric properties of a nematic liquid crystal in thin cells.* J. Appl. Phys., vol. 90, pp. 3483-3488, 2001.

7

Defects, elastic interactions and magnetic response of peanut-shaped hematite particles in a nematic liquid crystal

7.1 Introduction

In the previous chapters, we worked on shape symmetric (sphere) particles with asymmetric surface and studied their electrophoretic motion. In this chapter, we focus on shape asymmetric particles. It has been shown that the symmetry of the elastic interaction and the resulting colloidal assembly can be markedly different due to the shape of the colloids. In fact there are several reports on the induced defects and complex interaction of nonspherical microparticles such as rod-shaped [1, 2], star-shaped [3], rectangular [4, 5], triangular [6], square, bullet [7] and doughnut-shaped [8] etc in nematic LCs.

Most of the studies reported on LC colloids are so far based on non-magnetic particles. However, recent advances in colloidal synthesis has made it possible to fabricate magnetic particles with different shapes. These particles induce topological defects and self-assemble due to long range elastic interactions. The self-assembly of such particles can be manipulated by external magnetic fields which are very promising for advanced tunable materials. Brochard and de Gennes first theoretically studied the magnetic particles in nematics and proposed the idea of a ferronematic [10]. Lately there are several experimental studies on magnetic nanowires [9,13] and nanoparticles in nematic liquid crystals [14–16]. However, after the discovery of true ferronematic by Mertelj *et al.* [17], it has created immense interests [18–20]. In this chapter, we introduce a new nematic colloid – peanut-shaped hematite colloids in nematic liquid crystals. The assembly and interactions of these particles have been studied in aqueous medium. They interact via dipolar magnetic interaction and also experience a magnetic torque under the influence of external magnetic field. In isotropic solvents like water they exhibit complex self-assembled and ordered structures [21]. In anisotropic solvent such as in nematic liquid crystals, we can expect the diversity of the interaction, orientation and hence the self-assembly of the magnetic colloids by exploiting the combined effect of magnetic and elastic interactions. With this aim we study spontaneous orientation, induced defects, anisotropic elastic interactions, directed self-assembly and magnetically driven rearrangement of peanut-shaped magnetic colloids. By balancing the liquid crystal imposed forces with applied magnetic field we determine the elastic torque which leads to the quantitative measurement of the magnetic dipole moment of the peanut-shaped magnetic particles.

7.2 Experimental

The peanut-shaped hematite(α-Fe_2O_3) particles were synthesized based on gel-sol method by our collaborators at IIT Madras [23, 24]. In a typical synthesis, 90 ml of 5.4 M NaOH solution is added to 100 ml of 2 M $FeCl_3$ solution for 5 minutes under magnetic stirring, followed by an addition of 10 ml of 0.6 M Na_2SO_4 solution. Thus, the obtained condensed $FeHO_2$ gel is aged for 8 days at 100°C.

The hematite particles in the resulting suspension were separated by repeated washing with Milli-Q water and centrifugation, and finally stored in Milli-Q water. The particles were characterized using high resolution scanning electron microscope (HR-SEM, Hitachi S-4800, Japan) and transmission electron microscope (TEM, Tecnai 12) as shown in Fig.7.1(a) and (b), respectively. The particle size analysis is performed using ImageJ [25]. The average length and the lobe diameter of these particles are about 3.2 µm and 1.54 µm, respectively (Fig.7.1(c)).

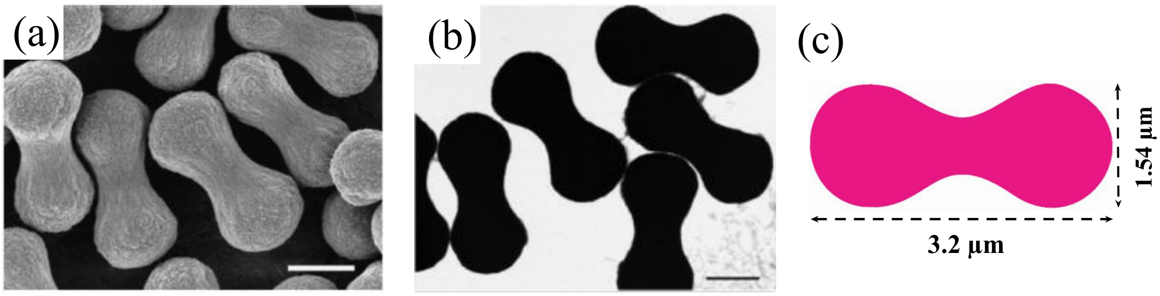

Figure 7.1: (a) SEM and (b) TEM micrograph of peanut-shaped particles spreaded on a clean glass plate. (c) Diagram of a peanut-shaped particle. The length and lobe diameter of the particles are 3.2 µm and 1.54 µm, respectively.

The particles were dispersed in 4-cyano-4' pentylbiphenyl (5CB) liquid crystal without any surface treatment for the anchoring of liquid crystal molecules. Cells with spacing in the range of 8-10 µm were fabricated using glass plates, spin coated with polyimide, AL-1254 and cured at 180 °C. The glass plates were rubbed along a particular direction and then fixed using a UV curable optical adhesive mixed with the desired spacer as discussed in the chapter-2. Prepared cells provide planar orientation of liquid crystal director along the rubbing direction. The LC-colloid mixture was introduced into the cells by capillary action and the textures were observed using an inverted polarising optical microscope. A laser tweezer operating at 1064 nm, is built on the same inverted microscope (Nikon eclipse Ti-U) and was used for optical trap and hence particle-defect manipulation. The motion of the particle was video recorded using a CCD camera (Pixelink PLB 741F) and an appropriate software was used to track the time dependent positions of the particles. All the experiments were performed at a temperature of 25°C.

7.3 Numerical simulation

Numerical simulations were done in collaberation with Dr. Simon Čopar, Jožef Stefan Instutute, Slovenia. It was done with a finite difference scheme based on a Landau-de

Gennes Q-tensor free energy density model with equal elastic constants in the form [22]:

$$f = \frac{L}{2} Q_{ij,k} Q_{ij,k} + \frac{A}{2} Q_{ij} Q_{ij} + \frac{B}{3} Q_{ij} Q_{jk} Q_{ki} + \frac{C}{4} (Q_{ij} Q_{ij})^2 \tag{7.1}$$

and surface free energy term $f_S = \frac{1}{2} W (Q_{ij} - Q^0_{ij})^2$ with Q^0_{ij} being the preferred Q-tensor consistent with the director pointing along the particle surface normal. The elastic constants are set to the well-tested set for simulating 5CB liquid crystals: $L = 8 \times 10^{-12}$J, $A = -0.172$ MJ m^{-3}, $B = -2.12$ MJ m^{-3}, $C = 1.73$ MJ m^{-3}, and relatively weak anchoring $W = 1.0 \times 10^{-3}$ J m^{-2}. The simulations were done for particle dimensions 1.0 µm×0.5 µm×0.5 µm with computational grid resolution of 10nm in a 300×300×300 simulation box. The particle size is smaller than in experimental setting, to make the computation feasible. However, as long as the defects are in the same positions as in the experiments, the director field is scale-independent, making the simulations suitable for reproducing the optical micrographs. The simulations of the crossed polarizer micrograph with an inserted retarder plate were performed using the Jones matrix formalism.

7.4 Results and discussion

The mixture of peanut-shaped colloids and 5CB was introduced in planar cells. Figure 7.2(a) and (b) show bright and polarized optical micrograph of few dispersed peanut-shaped hematite particles. It was observed that the colloids orient themselves with their long axis at all possible angles with respect to the nematic director, $\hat{\mathbf{n}}$. The statistical analysis of orientation of about 250 particles is shown in Fig.7.2(c). About 35% colloids are oriented perpendicular to the director and 13% are oriented parallel to the director. The remaining colloids are oriented at all other angles ($0° < \theta < 90°$). This possibly indicates a slight differences in anchoring strength of the particles.

The elastic distortion of a few isolated colloids which are either parallel or perpendicular to the director are investigated with a 60× objective and numerical aperture (NA) of 1.0. To get qualitative information about the anchoring and the induced defects, a retarder wave plate (530 nm) was introduced into the optical path between the polarizer and the sample stage making the fast axis 45° with respect to the director and the corresponding image is shown in Fig.7.3(b). The molecules, parallel

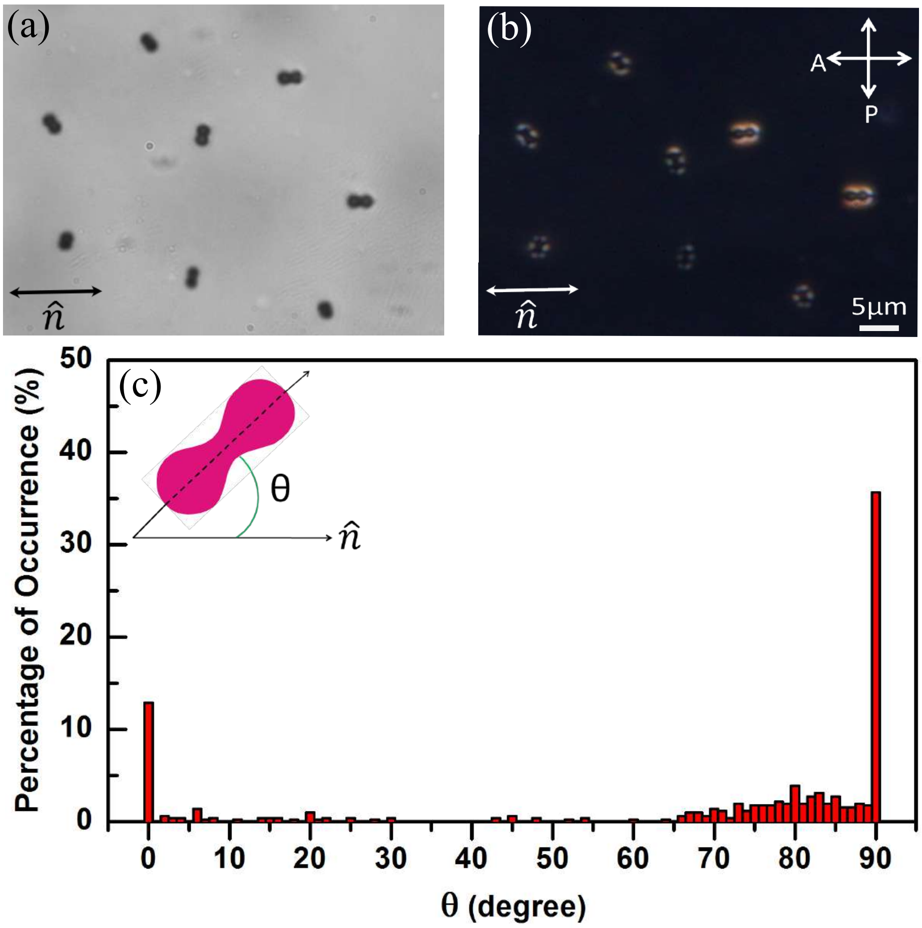

Figure 7.2: (a) Bright field micrograph of peanut-shaped particles spreaded on a clean glass plate. (b) POM texture of dispersed particles in 5CB, where double headed arrow above $\hat{n}$ indicates the nematic director and crossed double headed arrows indicate orientation of polariser and analyser. (c) The percentage of number of colloids orientated at different angles with respect to the director ($\hat{n}$). Orientation of about 250 particles are analysed. Cell thickness $d = 9.5\,\mu\text{m}$.

or perpendicular to the slow axis of the wave plate, transmit blue or yellow colour representing the clockwise or anticlockwise orientation with respect to the director, respectively. Figure 7.3(a) shows the POM micrograph of a particle oriented parallel to the director. It induces a hyperbolic hedgehog point defect and elastic distortion similar to that of spherical micro-particles, excepting the presence of another point defect between them (see Fig.7.3(d)). The point defect is slightly extended, possibly

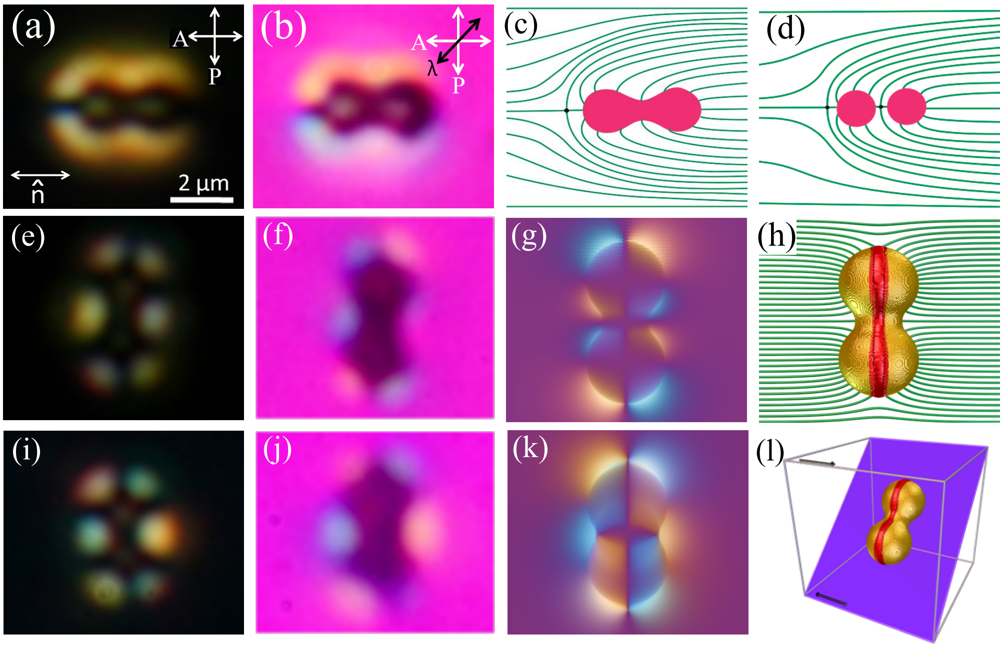

Figure 7.3: (a,e,i) POM images of particles orientated parallel and perpendicular to the director. (b,f,j) Corresponding images obtained by keeping the fast axis of the λ-plate (530 nm) at 45° with respect to the polariser. (c) Schematic diagram of elastic dipolar-type deformation around a colloid with parallel orientation (d) Schematic diagram of elastic deformation around a pair of spherical dipolar colloids for comparison. Perpendicular colloids with (e) nontilted and (i) tilted orientations. Simulated POM images with λ-plate of perpendicular colloids with (g) nontilted and (k) tilted orientations. (h) Director image from the simulation showing elastic distortion and ring defect around the nontilted colloid (thick-red band along the length). (l) Schematic diagram of a tilted colloid in 3D perspective. In this configuration, the particle is positioned near the bottom of the cell. The black arrows near the edges of the box indicate the rubbing direction.

due to the shape or the aspect ratio of the particle. A schematic diagram of the director field around the particle is shown in Fig.7.3(c). POM micrographs of two particles oriented perpendicular to the director are shown in Fig.7.3(e,i). Unlike the colloids that are oriented parallel to the director, the defects in this case are not easily identifiable. They exhibit two different retardation profiles when observed under λ-plate.

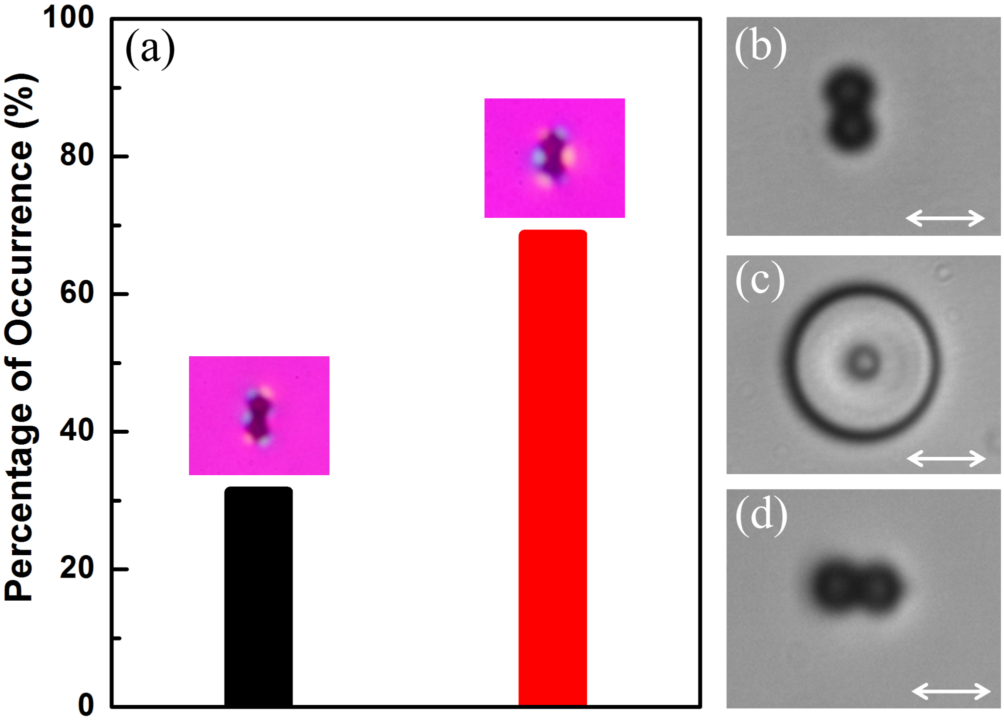

Figure 7.4: (a) Statistical analysis of perpendicular colloids on the basis of λ-plate images. Black and red bars represent percentage of nontilted and tilted colloids. (b-d) Sequence of CCD images showing that the orientation of a particle is changed by using a laser tweezer from horizontal to vertical.

In type-I, a typical sequence of blue and yellow colors that surrounds the particles (similar to that is observed in case of spherical colloids) suggests homeotropic anchoring of the liquid crystal molecules (Fig.7.3(f)). Figure 7.3(g) shows the corresponding simulated image, where the particle is surrounded by a $-1/2$ disclination ring (Saturn ring) around its larger perimeter. The surrounding elastic distortion resembles to that of a pair of quadrupolar colloids except the concave surface around the neck. The λ-plate image of a type-II colloid shown in Fig.7.3(j) is noticeably different than that of type-I (Fig.7.3(f)) though their POM images look similar (Fig.7.3(e) and (i)). Careful observation shows that not all the particles that are oriented perpendicular to the director appear to have same length while dispersed in liquid crystals (Fig.7.2(b)). The type-II colloids appear somewhat smaller than that of type-I, suggesting that the type-II colloids are tilted with respect to the plane of the cell. Based on this idea we carried out computer simulation for different tilt angles and vertical particle positions. Figure 7.3(k) shows the corresponding simulated λ-plate image of the tilted particle associated with the Saturn ring defect where the upper part of the particle is tilted 45° out of the plane of paper and the lower part is set close to the bottom glass plate. In this configuration, the blue and yellow colour coincides best with that of the experiment (Fig.7.3(f)). This suggests that the type-II relies on the interaction with the cell walls for stability, while the type-I is floating in the bulk. We have also done a statistical analysis of the two types of particle configurations. Figure 7.4(a) shows that among the particles that are oriented perpendicular to the director nearly 70% are type-II i.e., tilted and remaining 30% are parallel to the glass plate. However, the orientation of the particles can be changed from parallel to perpendicular or from type-I to type-II or vice versa by using the optical tweezer as shown in Fig.7.4(b-d).

The elastic interaction between two particles is studied using a video microscopy technique. Two dipolar colloids are brought a few micrometers apart with the help of the optical tweezer and left free to evolve. Figure 7.5(a) shows the variation of separation $R(t)$ between two colloids with time. In this case, the attractive elastic force (F_e) is balanced by the viscous drag force acting opposite to F_e, hence $F_e + F_{drag} = 0$, where $F_{drag} = -\zeta dR(t)/dt$. The interaction force between two dipolar colloids is given by $F_e = -k/R^4$, where k is a constant and depends on the mean elastic constant of the medium, size and shape of the particles. The time dependent inter-particle separation is given by $R(t) = (R(0)^5 - 5\alpha t)^{1/5}$, where $\alpha = K/\zeta$ and $R(0)$ is the initial separation at $t = 0\,\mathrm{s}$ [29]. The red line in Fig.7.5(a) shows the best fit to the experimental data. Figure 7.5(b) shows time coded trajectories of a particle when it approaches another particle from different angles with parallel orientation of their dipolar axes. They have attractive interaction within about ±30° angle along the joining line and repulsive at other angles. When the dipolar particles approach along the broad-side on position with opposite orientations (Fig.7.5(c)), they exhibit repulsive interaction within ±45° with respect to the joining line and attractive at other angles (Fig.7.5(d)). The overall anisotropic interaction of two peanut-shaped colloids are almost similar to that of spherical colloids except the numerical values of the interaction time and the range.

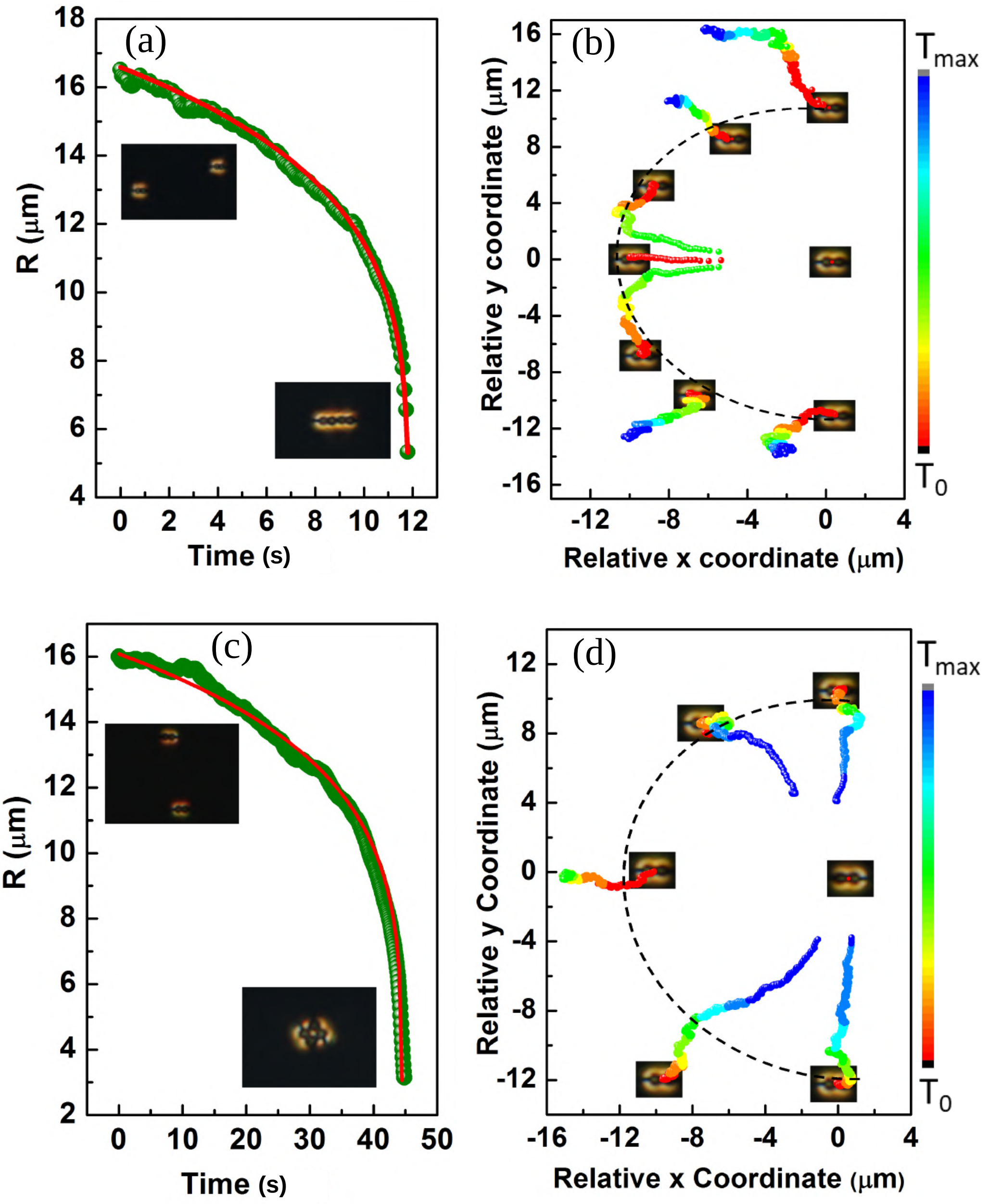

Figure 7.5: The variation of center-to-center separation distance between two peanut-shaped particles with (a) parallel and (c) antiparallel dipolar configuration as a function of time. Red lines are the best fit to the equation: $R(t) = (R(0)^5 - 5\alpha t)^{1/5}$. Time coded trajectories of a dipolar particle from different angles with respect to another (b) parallel and (d) antiparallel dipole at the center. Each trajectory is recorded for time interval from T$_0$= 0 s to (b) T$_{max}$= 144 s and (d) T$_{max}$= 120 s .

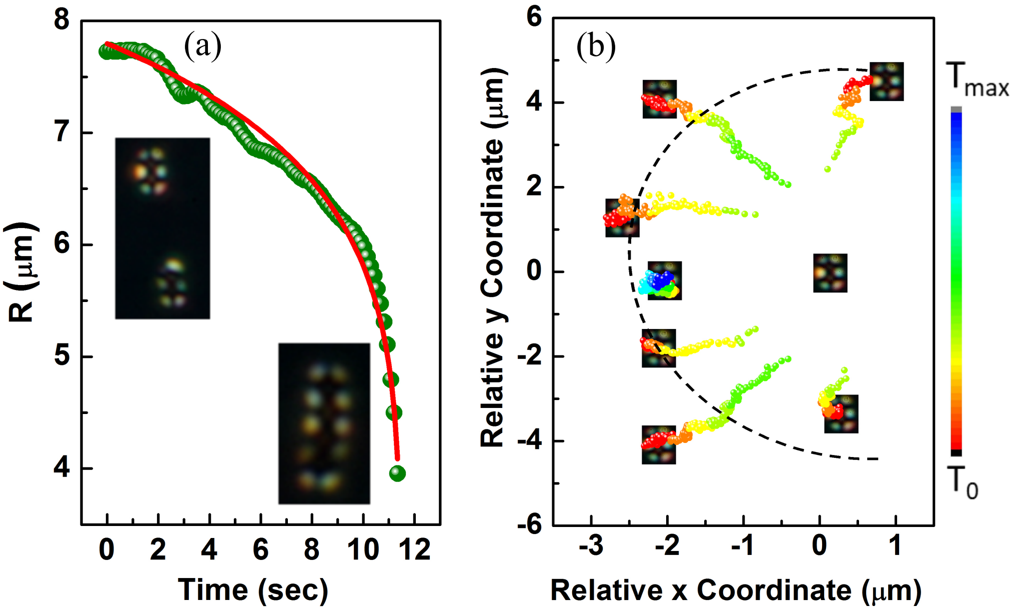

Figure 7.6: (a) Variation of equilibrium separation between two peanut-shaped particles with tilted elastic quadrupolar configurations. Red line is the best fit to the equation: $R(t) = (R(0)^7 - 7\alpha t)^{1/7}$. (b) Time coded trajectories of a tilted quadrupolar particle from different angles with respect to another at the centre. Each trajectory is recorded for time interval from T_0= 0 s to T_{max}= 30 s.

Pairs of perpendicular colloids (both types) show quadrupolar interaction (i.e $F_e = -k/R^6$). Figure 7.6(a) shows the variation of inter-particle separation with the best fit to the corresponding equation, $R(t) = (R(0)^7 - 7\alpha t)^{1/7}$. Figure 7.6(b) shows that except along the joining line of two colloids, they have attractive but short-range interaction. We prepared linear chains with a few colloids using the optical tweezer. Figure 7.7(a) and (b) shows self-assembled chains of peanut-shaped colloids with dipolar and quadrupolar defect configurations. The dipolar chain is oriented parallel to the director and the quadrupolar chain is oriented perpendicular to the director. Two orthogonal chains are guided by the laser tweezer to combine and form a L-shaped structure (Fig.7.7(c)). This can be used as a building block for making complex colloidal self-assembled structures, which are responsive to external magnetic field. It may be mentioned that the orthogonal orientation of colloidal chains of spherical particles are not stable in nematic liquid crystals.

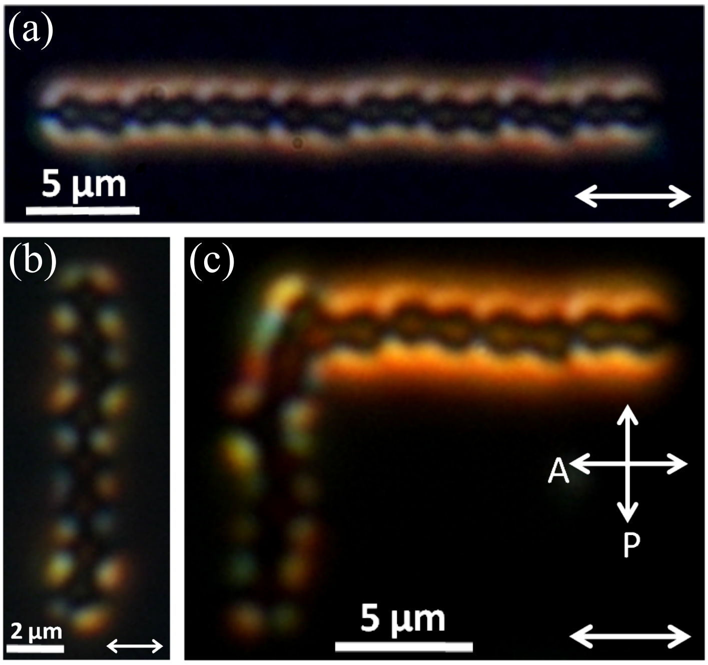

Figure 7.7: (a) Laser tweezer assisted self-assembly of dipolar and quadrupolar peanut-shaped colloids. (b) A linear chain of dipolar colloids parallel to the director. (b) A linear chain of tilted quadrupolar colloids normal to director. (c) L-shaped structure obtained by combining the two chains..

We studied the effect of external magnetic field on the orientation and defects of dipolar colloids and estimated the magnetic dipole moment from the competing effects of elastic and magnetic torques. Two thick, disc-shaped magnets of diameter 20 mm were placed diametrically opposite in a circular track around the microscope objective, keeping the cell at the centre as shown schematically in Fig.7.8(a). This arrangement produces a uniform magnetic field with a fixed amplitude at the sample, which depends on the diameter of the circular track (Fig.7.8(b)). The direction of magnetic field is changed by rotating the two magnets simultaneously in the track. The magnetic field at the centre is calibrated by a magnetometer. Figure 7.9(a-e) shows the effect of rotating magnetic field of strength 300 gauss on a dipolar colloid. Since the diamagnetic anisotropy of 5CB liquid crystal is very small the applied magnetic field does not have any effect on the orientation of the director. The orientation of the particle remains unaffected when the magnetic field is perpendicular to the long axis. As the magnetic field is rotated from 90° to 0°, the colloid rotates, keeping the point defect facing toward the rubbing direction. This suggests that the direction of magnetic moment is perpendicular to the length of the colloids. Figure 7.9(f) shows the response of the colloid when the magnetic field is rotated from +90° to −90° (right to left). Below ±30° the colloid tilts out of the observation plane. At $\phi = 0°$, the tilt angle reaches maximum and the particle flips its direction from anti-clockwise to clock-wise.

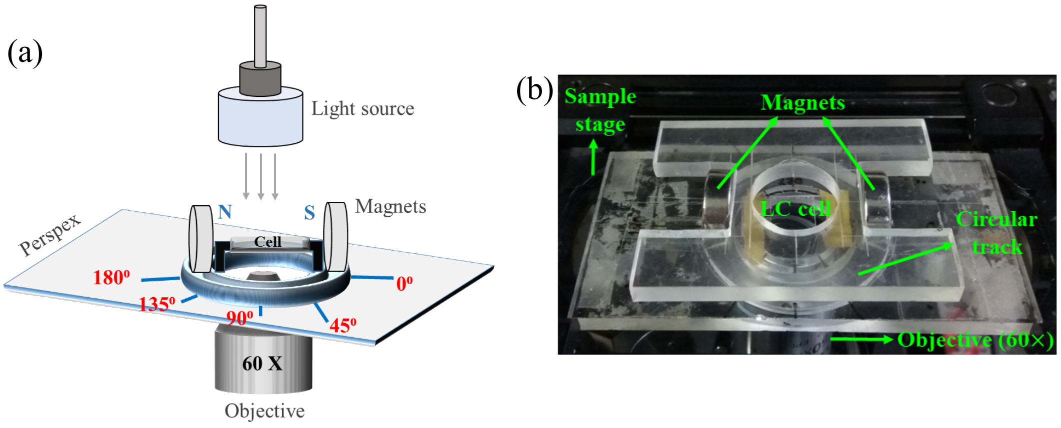

Figure 7.8: (a) Schematic diagram of experimental setup for applying horizontal magnetic field from two disc shaped magnets on a circular track. (b) Real experimental setup.

To calculate the magnetic torque on the colloid we present a simple diagram in Fig.7.10(a). It shows an equilibrium orientation of the colloid when the magnetic field is applied at an angle ϕ with respect to the director. The long axis of the colloid makes an angle α with respect to the director. The angle of the magnetic moment with respect to the director is θ. At equilibrium the magnetic toque $\mu B \sin(\phi - \theta)$ is balanced with the gradient of elastic energy $-\partial U/\partial\theta$ and the torque balance equation is written as [30]:

$$-\partial U/\partial\theta + \mu B \sin(\phi - \theta) = 0 \tag{7.2}$$

Considering usual one constant approximation for the nematic, the distortion free energy is given by

$$U = \frac{1}{2}K \int dv |\nabla \mathbf{n}|^2 \tag{7.3}$$

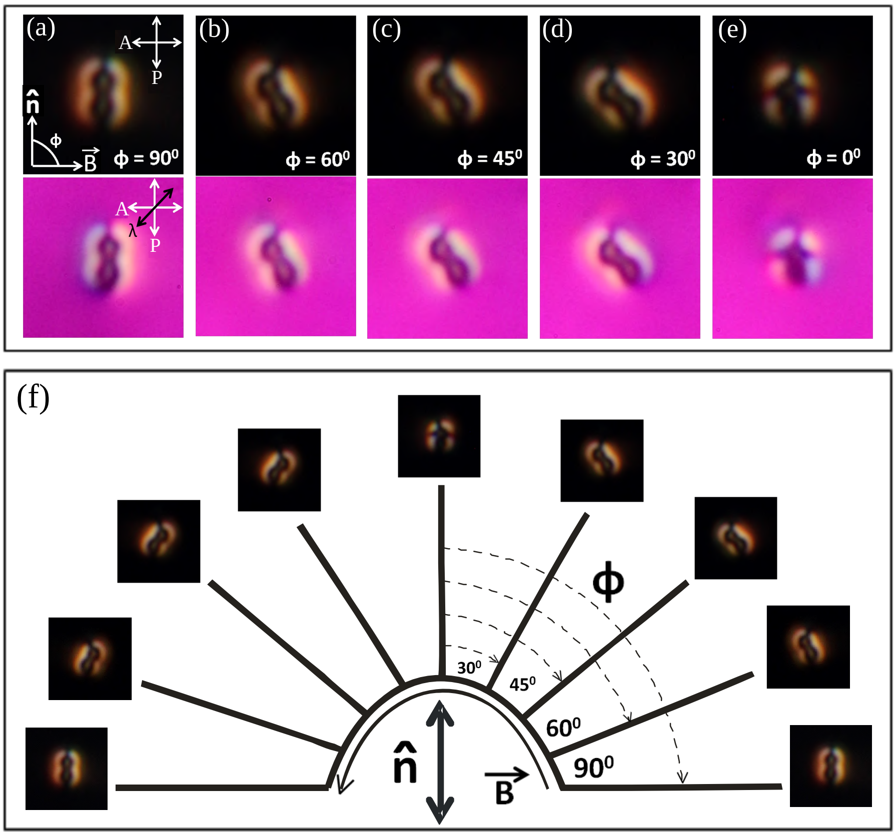

Figure 7.9: (a-e) Effect of magnetic field of strength 300 gauss on a peanut-shaped dipolar nematic colloid at different directions from 90° to 0° with respect to the director, $\hat{\mathbf{n}}$. ϕ is the angle between the director and the magnetic field ($\vec{B}$). Corresponding λ-plate images are shown underneath. (f) POM images when the magnetic field direction is changed from $+90°$ to $-90°$. Double headed arrow at the centre represents the director $\hat{\mathbf{n}}$.

where $K = K_{11} = K_{22} = K_{33}$ is the elastic constant. Considering the rotation of the particle only in the xy-plane, the director components can be written as $n_x = sin\alpha(r)$, $n_y = cos\alpha(r)$ and $n_z = 0$. This gives:

$$U = \frac{1}{2}K\int dv|\nabla\alpha|^2 \tag{7.4}$$

and the optimum corresponds to $\nabla^2\alpha = 0$. Brochard and de Gennes showed that this equation is equivalent to the field energy of $(4\pi K)^{1/2}\alpha(r)$ with a spatially varying voltage in electrostatics. Within this analogy, the boundary condition at the surface of the elongated particle is equivalent to that of a surface at fixed voltage V. Now,

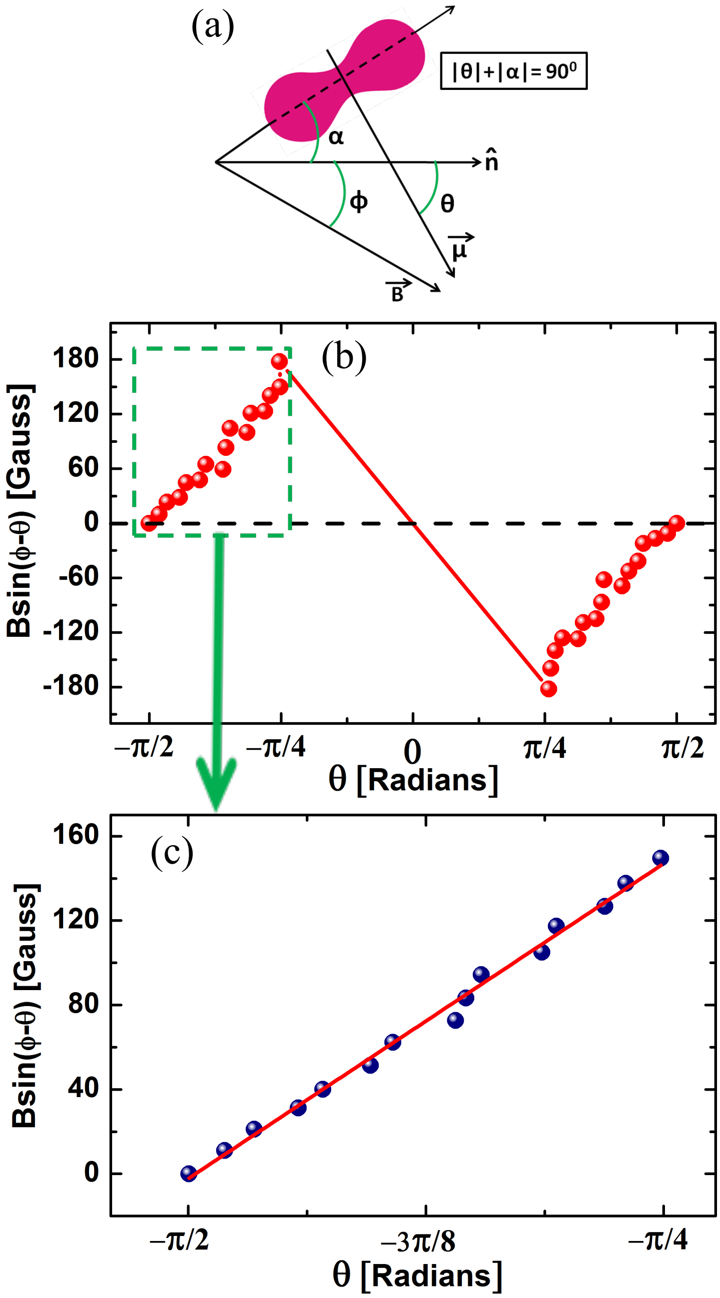

Figure 7.10: (a) Schematic diagram showing the direction of magnetic field and the magnetic moment with respect to the director. (b) Variation of magnetic torque $B\sin(\phi - \theta)$ with θ. Measurement is restricted within $\pm\pi/2$ to $\pm\pi/4$ as the colloid tilts out of the plane preventing the exact measurement of θ. (c) Red line represent best linear fit to the selected experimental data as highlighted by dotted green box.

associating the elastic energy of rotated particle with the field energy $\frac{1}{2}CV^2$, stored in a capacitor, we get [10, 11]

$$\int \frac{(\nabla\alpha)^2}{8\pi}dv = \frac{1}{2}C\theta^2 \tag{7.5}$$

where C is the capacitance of the particle of length L and diameter d [10]. From the work of Maxwell [12], the charge density per unit length of such elongated object is approximately constant $\lambda = Q/L$ along the axis of the body (let's say, x-axis). The potential can be estimated at the center and consequently the capacitance is given by

$$V = 2\int_0^{L/2} \frac{Q}{L}\frac{dx}{\sqrt{x^2+d^2}} = \frac{Q}{L}2\log\left[\frac{L/2+\sqrt{d^2+L^2/4}}{d}\right] \sim \frac{Q}{L}2\log\frac{L}{d} \tag{7.6}$$

Hence, the corresponding capacitance is given by

$$C \sim \frac{L}{2\log\frac{L}{d}} \tag{7.7}$$

Using Eq.(7.7) in (7.5), we arrive at

$$U = 2\pi CK\theta^2 \tag{7.8}$$

Thus, from Eq.(7.2) we get,

$$\mu B\sin(\phi-\theta) = 4\pi CK\theta \tag{7.9}$$

The variation of $B\sin(\phi-\theta)$ with θ is shown in Fig.7.10(b). The magnetic torque varies linearly but in a periodic manner and at $\theta = 0°$, it changes direction. The slope of the best fit is given by $4\pi CK/\mu = 190$ gauss/radians (Fig.7.10(c)). Taking $K \simeq 5\times10^{-7}$ dyn and $C \simeq 5\times10^{-4}$ cm, the estimated magnetic dipole moment $\mu \simeq 1.7\times10^{-11}$ emu. This is very close to the value reported by Lee *et al.* from an independent measurement of bulk sample [31].

We also studied the effect of magnetic field on a self-assembled dipolar chain structure. Figure 7.11(a–h) shows a few textures of a dipolar chain, when the magnetic field is rotated around the director. The angle between the director $\hat{n}$, and magnetic field, $\overrightarrow{B}$ is ϕ. The chain remains straight when the magnetic field $\overrightarrow{B}$ is perpendicular to the length of the chain, i.e., $\phi = 90^0$. The chain as a whole, tends to reorient and the

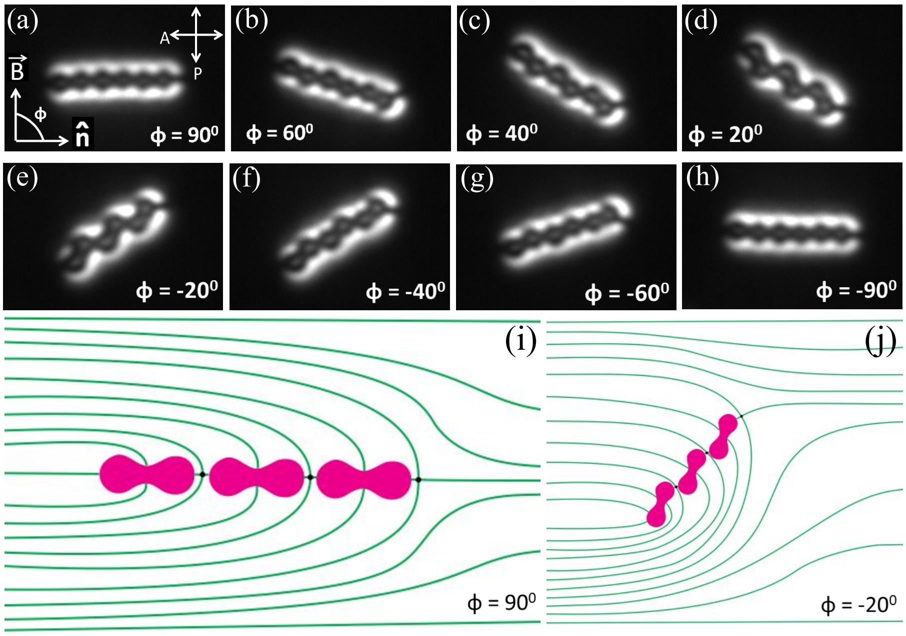

Figure 7.11: (a–h) Polarising optical microscope images showing the effect of rotating magnetic field on a dipolar chain of peanut-shaped particles. (i) Schematic diagram of the director structure when the magnetic field is perpendicular to the chain as shown in texture (a). (j) Schematic diagram of the director structure when the magnetic field is rotated at the angle.

colloids slide over each other as ϕ is decreased from 90^0. The sliding is associated with a slight displacement of the point defects from their initial positions. Consequently the length becomes shorter and finally the chain flips its direction at $\phi = 0^0$. Director structures for two orientations are schematically shown in Fig.7.11(i,j) respectively.

7.5 Conclusion

In summary, peanut-shaped hematite microparticles spontaneously orientate at various angles with respect to the nematic director exhibiting both dipolar and quadrupolar symmetry of elastic distortion. Among the quadrupolar colloids majority of them are tilted with respect to the plane of the cell, which has been corroborated by the computer simulation results obtained from Landau de Gennes Q-tensor modelling. The elastic interactions are highly anisotropic and short-ranged compared to that of a pair of spherical colloids. The dipolar and quadrupolar linear chains are combined with the help of a laser tweezer to form a stable structure retaining their orthogonal orientations. The colloids have transverse magnetic dipole moments and hence their reorientations are manipulated in the liquid crystal by the applied external magnetic field. The estimated magnetic moment obtained from the competing effects of elastic and magnetic torques is about 1.7×10^{-11} emu. Magnetic colloids with anisotropic shape have a potential use for making magnetic field responsive complex self-assembling colloids, as demonstrated on magnetically rearranging linear chain of particles. Peanut shape is structurally very similar to a pair of spherical particles, bound at a fixed distance, so the particles could also be used in a mixture of spherical and peanut-shaped particles to functionalize the particle assembly with magnetic response.

References

[1] U. Tkalec, M. Škarabot, and I. Muševič, *Interactions of micro-rods in a thin layer of a nematic liquid crystal*. Soft Matter, vol. 4, pp. 2402-2409, 2008.

[2] D. Andrienko, M. P. Allen, G. Skačej, and S. Žumer, *Defect structures and torque on an elongated colloidal particle immersed in a liquid crystal host*. Phys. Rev. E, vol. 65, pp. 041702-1-7, 2002.

[3] C. P. Lapointe, K. Mayoral, and T. G. Mason, *Star colloids in nematic liquid crystals*. Soft Matter, vol. 9, pp. 7843-7854, 2013.

[4] M. V. Rasna, K. P. Zuhail, U. V. Ramudu, R. Chandrasekar, ans S. Dhara, *Dynamics of electro-orientation of birefringent microsheets in isotropic and nematic liquid crystals*. Phy. Rev. E, vol. 94,pp. 032701-1-5, 2016.

[5] M. V. Rasna, K. P. Zuhail, U. V. Ramudu, R. Chandrasekar, J. Dontabhaktuni, and S. Dhara, *Orientation, interaction and laser assisted self-assembly of organic single-crystal micro-sheets in a nematic liquid crystal*. Soft Matter, vol. 11, pp. 7674-7679, 2015.

[6] C. P. Lapointe, T. G. Mason, and I. I. Smalyukh, *Shape-controlled colloidal interactions in nematic liquid crystals*. Science, vol. 326, pp. 1083-1086, 2009.

[7] M. A. Gharbi, M. Cavallaro, G. Wu, D. A. Beller, R. D. Kamien, S. Yang, and K. J. Stebe, *Microbullet assembly: interactions of oriented dipoles in confined nematic liquid crystal*. Liq. Cryst., vol. 40, pp. 1619-1627, 2013.

[8] B. Senyuk, Q. Liu, S. He, R. D. Kamien, R. B. Kusner, T. C. Lubensky, and I. I. Smalyukh, *Topological colloids*. Nature, vol. 493, pp. 200-205, 2013.

[9] G. Lapointe, A. Hultgren, D. M. Silevitch, E. J. Felton, D. H. Reich, and R. L. Leheny, *Elastic torque and the levitation of metal wires by a nematic liquid crystal.* Science, vol. 303, 652-655, 2004.

[10] F. Brochard, and P. G. de Gennes, *Theory of magnetic suspensions in liquid crystals.* Journal de Physique, vol. 31, pp. 691-708, 1970.

[11] C. Lapointe, N. Cappallo, D. H. Reich, and R. L. Leheny, *Static and dynamic properties of magnetic nanowires in nematic fluids* , Jour. Appl. Phy., vol. 97, pp. 10Q304(1-6), 2005.

[12] J. C. Maxwell, The Scientific Papers of James Clerk Maxwell, edited by W. D. Nivens, New York, Vol. 2, pp.672-680, 1878.

[13] G. Lapointe, N. Cappallo, D. H. Reich, and R. L. J. Leheny, *Static and dynamic properties of magnetic nanowires in nematic fluids.* J. Appl. Phys., vol. 97, 10Q304-1-6, 2005.

[14] S. H. Chen, and N. Amer, *Observation of Macroscopic Collective Behavior and New Texture in Magnetically Doped Liquid Crystals.* Phys. Rev. Lett., vol. 51, pp. 2298-2301, 1983.

[15] C. D. Cruz, O. Sandre, and V. Cabuil, *Phase Behavior of Nanoparticles in a Thermotropic Liquid Crystal.* J. Phys. Chem. B, vol. 109, pp. 14292-14299, 2005.

[16] J. P. F. Lagerwall, and G. Scalia, *Liquid crystals with nano and microparticles*, World Scientific Publishing Co., Singapore, 2016.

[17] A. Mertelj, D. Lisjak, M. Drofenik, and M. Čopič, *Ferromagnetism in suspensions of magnetic platelets in liquid crystal.* Nature, vol. 504, pp. 237-241, 2013.

[18] R. Sahoo, M. V. Rasna, D. Lisjak, A. Mertelj, and S. Dhara, *Magnetodielectric and magnetoviscosity response of a ferromagnetic liquid crystal at low magnetic fields.* Appl. Phys. Lett., vol. 106, pp. 161905-1-4, 2015.

[19] M. Mur, J. Ahmad, I. Kvasić, A. Mertelj, D. Lisjak, V. Niranjan, I. Musevic, and S. Dhara, *Magnetic-field tuning of whispering gallery mode lasing from ferromag-*

netic nematic liquid crystal microdroplets. Opt. Express, vol. 25, pp. 1073-1083, 2017.

[20] Q. Liu, P. J. Ackerman, T. C. Lubensky, and I. I. Smalyukh, *Biaxial ferromagnetic liquid crystal colloids.* Proc. Natl. Acad. Sci., vol. 113, pp.10479-10484, 2016.

[21] S. H. Lee, S. J. Gerbode, B. S. John, A. K. Wolfgang, F. A. Escobedo, I. Cohenb, and C. M. Liddell, *Synthesis and assembly of nonspherical hollow silica colloids under confinement.* J. Mater. Chem., vol. 18, pp. 4912-4916, 2008.

[22] M. Ravnik and S. Zumar, *Landau–de Gennes modelling of nematic liquid crystal colloids.* Liq. Cryst., vol. 36, pp. 1201-1214, 2009.

[23] T. G. Anjali, and M. G. Basavaraj, *Contact angle and detachment energy of shape anisotropic particles at fluid-fluid interfaces.* J. Coll. Inter. Sci., vol. 478, pp. 63-71, 2016.

[24] T. Sugimoto, M. M. Khan, and A. Muramatsu, *Preparation of monodisperse peanut-type* α*-*Fe_2O_3 *particles from condensed ferric hydroxide gel*, Colloids and Surfaces A: Physicochemical and Engineering Aspects, vol. 70, pp. 167-169, 1993.

[25] C. A. Schneider, W. S. Rasband, and K. W. Eliceiri, *NIH Image to ImageJ: 25 years of image analysis*, Nat. methods, vol. 9, pp. 671-675, 2012.

[26] K. P. Zuhail, P. Sathyanarayana, D. Seč, S. Čopar, M. Škarabot, I. Muševič, and S. Dhara, *Topological defect transformation and structural transition of two-dimensional colloidal crystals across the nematic to smectic-A phase transition.* Phys. Rev. E, vol. 91, pp. 030501(R)-1-4, 2015.

[27] K. P. Zuhail, S. Čopar, I. Muševič, and S. Dhara, *Spherical microparticles with Saturn ring defects and their self-assembly across the nematic to smectic-A phase transition.* Phys. Rev. E, vol. 92, pp. 052501-1-5, 2015.

[28] M. Rasi, K. P. Zuhail, A. Roy, and S. Dhara, *N-SmA-SmC phase transitions probed by a pair of elastically bound colloids.* Phys. Rev E, vol. 97, pp. 032702-1-6, 2018.

[29] P. Poulin, V. Cabuil, and D. A. Weitz, *Direct Measurement of Colloidal Forces in an Anisotropic Solvent*. Phys. Rev. Lett., vol. 79, pp. 4862-4865, 1997.

[30] C. Lapointe, A. Hultgren, D. M. Silevitch, E. J. Felton, D. H. Reich, and R. L. Leheny, *Elastic Torque and the Levitation of Metal Wires by a Nematic Liquid Crystal*. Science, vol. 303, pp. 652-655, 2004.

[31] S. H. Lee and C. M. Liddell, *Anisotropic Magnetic Colloids: A Strategy to Form Complex Structures Using Nonspherical Building Blocks*. Small vol. 5, pp. 1957-962, 2009.

Future work

Although the goal of the thesis has been accomplished, there are plenty of scopes for improvements to achieve better results. The results reported in this thesis provide a strong foundation for future work and create many opportunities in the field of active particles in liquid crystals. Some of the future perspectives are mentioned below.

1. In order to achieve more precise and greater control over the directional transport, magneto-dielectric Janus particles can be prepared. In such systems, the orientation of the particles could be controlled by external magnetic field.

2. Shape asymmetric Janus particles could show interesting dynamics and offer higher degree of freedom in commanding their transport.

3. The spatially varying LC director can act as an additional parameter for piloting particles. In such case, patterned LC and chiral LCs can be used as the host.

4. This thesis focused on the dynamics of individual particles, but the collective behaviour of such particles could create a new class of active matter, which could be termed as "topological active matter".

Publications

Publications related to thesis

1. Omnidirectional transport and navigation of Janus particles through a nematic liquid crystal film.

   Dinesh Kumar Sahu, Swapnil Kole, Sriram Ramaswamy, and Surajit Dhara.

   Phys. Rev. Res. **2**, 032009(R) (2020).

2. Electric field driven controllable motility of metal-dielectric Janus particles with boojum defects in thin films of a nematic liquid crystal.

   Dinesh Kumar Sahu and Surajit Dhara.

   Phys. Fluids **33**, 087106 (2021).

3. Enhanced electrophoretic mobility of nematic dipolar Janus colloids.

   Dinesh Kumar Sahu and Surajit Dhara.

   Soft Matter **18**, 1819 (2022).

4. Measuring electric-field-induced dipole moments of metal-dielectric Janus particles in a nematic liquid crystal.

   Dinesh Kumar Sahu and Surajit Dhara.

   Phys. Rev. Appl. **14**, 034004 (2020).

5. Orientation, elastic interaction and magnetic response of asymmetric colloids in a nematic liquid crystal.

   Dinesh Kumar Sahu, Thriveni G. Anjali, Madivala G. Basavaraj, Jure Aplinc, Simon Čopar and Surajit Dhara.

   Sci. Rep. **9**, 81 (2019).

Other Publications

1. Defect-polymorphism controlled electrophoretic propulsion of anisometric microparticles in a nematic liquid crystal.
   Devika V S, **Dinesh Kumar Sahu**, Ravi Kumar Pujala and Surajit Dhara.
   Accepted in *Phys. Rev. Appl.*

Contact:

Dinesh Kumar Sahu
Soft Matter Lab
School of Physics
University of Hyderabad
Gachibowli, Hyderabad, India - 500046
Email: dinesh@uohyd.ac.in

Non-linear electrophoresis of metal-dielectric Janus particles in nematic liquid crystals

by Dinesh Kumar Sahu

Submission date: 21-Jun-2022 03:17PM (UTC+0530)
Submission ID: 1860686405
File name: Dinesh_Kumar_Sahu.pdf (9.98M)
Word count: 35515
Character count: 176753

Sdhara

Dr. Surajit Dhara
Professor
School of Physics
University of Hyderabad
Hyderabad-500 046. INDIA.

Non-linear electrophoresis of metal-dielectric Janus particles in nematic liquid crystals

ORIGINALITY REPORT

53%	36%	49%	4%
SIMILARITY INDEX	INTERNET SOURCES	PUBLICATIONS	STUDENT PAPERS

PRIMARY SOURCES

1	arxiv.org Internet Source	12%
2	Dinesh Kumar Sahu, Thriveni G. Anjali, Madivala G. Basavaraj, Jure Aplinc, Simon Čopar, Surajit Dhara. "Orientation, elastic interaction and magnetic response of asymmetric colloids in a nematic liquid crystal", Scientific Reports, 2019 Publication	8%
3	Dinesh Kumar Sahu, Surajit Dhara. "Electrophoresis of metal-dielectric Janus particles with dipolar director symmetry in nematic liquid crystals", Soft Matter, 2022 Publication	8%
4	Dinesh Kumar Sahu, Surajit Dhara. "Electric field driven controllable motility of metal-dielectric Janus particles with boojum defects in thin films of a nematic liquid crystal", Physics of Fluids, 2021 Publication	7%

Sdhara

Dr. Surajit Dhara
Professor
School of Physics
University of Hyderabad
Hyderabad-500 046. INDIA.

Sdhara

Dr. Surajit Dhara
Professor
School of Physics
University of Hyderabad
Hyderabad-500 046. INDIA.

Sdhara

Dr. Surajit Dhara
Professor
School of Physics
University of Hyderabad
Hyderabad-500 046. INDIA.

Sdhara

Dr. Surajit Dhara
Professor
School of Physics
University of Hyderabad
Hyderabad-500 046. INDIA.

Sdhara

5 Dinesh Kumar Sahu, Swapnil Kole, Sriram Ramaswamy, Surajit Dhara. "Omnidirectional transport and navigation of Janus particles through a nematic liquid crystal film", Physical Review Research, 2020 — 4%

Publication

Dr. Surajit Dhara
Professor
School of Physics
University of Hyderabad
Hyderabad-500 046. INDIA.

---

6 Dinesh Kumar Sahu, Surajit Dhara. "Measuring Electric-Field-Induced Dipole Moments of Metal-Dielectric Janus Particles in a Nematic Liquid Crystal", Physical Review Applied, 2020 — 3%

Publication

Sdhara

Dr. Surajit Dhara
Professor
School of Physics
University of Hyderabad
Hyderabad-500 046. INDIA.

---

7 Submitted to University of Hyderabad, Hyderabad — 2%

Student Paper

---

8 export.arxiv.org — 2%

Internet Source

Sdhara

Dr. Surajit Dhara
Professor
School of Physics
University of Hyderabad
Hyderabad-500 046. INDIA.

---

9 www.nature.com — 1%

Internet Source

Sdhara

Dr. Surajit Dhara
Professor
School of Physics
University of Hyderabad
Hyderabad-500 046. INDIA.

---

10 coek.info — 1%

Internet Source

---

11 Pablo García-Sánchez, Yukun Ren, Juan J. Arcenegui, Hywel Morgan, Antonio Ramos. "Alternating Current Electrokinetic Properties of Gold-Coated Microspheres", Langmuir, 2012 — <1%

Publication

12	Shilov, V.N.. "Thin double layer theory of the wide-frequency range dielectric dispersion of suspensions of non-conducting spherical particles including surface conductivity of the stagnant layer", Colloids and Surfaces A: Physicochemical and Engineering Aspects, 20011130 Publication	<1 %
13	www.ncbi.nlm.nih.gov Internet Source	<1 %
14	Oleg D. Lavrentovich. "Active colloids in liquid crystals", Current Opinion in Colloid & Interface Science, 2016 Publication	<1 %
15	Igor Muševič. "Liquid Crystal Colloids", Springer Nature, 2017 Publication	<1 %
16	"Springer Handbook of Electronic and Photonic Materials", Springer Science and Business Media LLC, 2007 Publication	<1 %
17	Natan Osterman. "TweezPal – Optical tweezers analysis and calibration software", Computer Physics Communications, 2010 Publication	<1 %
18	journals.aps.org Internet Source	<1 %

19	Fedor V. Podgornov, Anna V. Ryzhkova, Wolfgang Haase. "Dynamics of nonlinear electrophoretic motion of dielectric microparticles in nematic liquid crystal", Journal of Molecular Liquids, 2018 Publication	<1 %
20	Submitted to University of Leeds Student Paper	<1 %
21	Deng - Ke Yang, Shin - Tson Wu. "Fundamentals of Liquid Crystal Devices", Wiley, 2014 Publication	<1 %
22	Submitted to Indian Institute of Technology, Kharagpure Student Paper	<1 %
23	theblogbyjavier.com Internet Source	<1 %
24	D. Demus, J. Goodby, G. W. Gray, H. - W. Spiess, V. Vill. "Handbook of Liquid Crystals Set", Wiley, 1998 Publication	<1 %
25	scholar.colorado.edu Internet Source	<1 %
26	Israel Lazo, Oleg D. Lavrentovich. "Liquid-crystal-enabled electrophoresis of spheres in a nematic medium with negative dielectric	<1 %

	anisotropy", Philosophical Transactions of the Royal Society A: Mathematical, Physical and Engineering Sciences, 2013 Publication	
27	García-Sánchez, Pablo, Yukun Ren, Juan J. Arcenegui, Hywel Morgan, and Antonio Ramos. "Alternating Current Electrokinetic Properties of Gold-Coated Microspheres", Langmuir, 2012. Publication	<1 %
28	hdl.handle.net Internet Source	<1 %
29	Submitted to UC, Boulder Student Paper	<1 %
30	"A Short Review on the Rheology of Twist Grain Boundary-A and Blue Phase Liquid Crystals", Fluids, 2018 Publication	<1 %
31	Thriveni G. Anjali, Madivala G. Basavaraj. "Influence of pH and Salt Concentration on Pickering Emulsions Stabilized by Colloidal Peanuts", Langmuir, 2018 Publication	<1 %
32	www.olympus-lifescience.com Internet Source	<1 %
33	Ravnik, Miha, and Slobodan Žumer. "Landau–de Gennes modelling of nematic liquid crystal	<1 %

colloids", Liquid Crystals, 2009.
Publication

34	"Liquid Crystal Polymers: From Structures to Applications", Springer Science and Business Media LLC, 1993 Publication	<1 %
35	etd.ohiolink.edu Internet Source	<1 %
36	Submitted to Indian Institute of Technology, Madras Student Paper	<1 %
37	dspace.rri.res.in Internet Source	<1 %
38	"Liquid Crystals", Wiley, 2021 Publication	<1 %
39	Muhammed Rasi M., Ravi Kumar Pujala, Sathyanarayana Paladugu, Surajit Dhara. "Interactions of charged microrods in chiral nematic liquid crystals", Physical Review E, 2021 Publication	<1 %
40	epdf.pub Internet Source	<1 %
41	Mohamed Amine Gharbi, Marcello Cavallaro, Gaoxiang Wu, Daniel A. Beller, Randall D. Kamien, Shu Yang, Kathleen J. Stebe.	<1 %

"Microbullet assembly: interactions of oriented dipoles in confined nematic liquid crystal", Liquid Crystals, 2013
Publication

42	V.N. Shilov, A.V. Delgado, F. Gonzalez-Caballero, C. Grosse. "Thin double layer theory of the wide-frequency range dielectric dispersion of suspensions of non-conducting spherical particles including surface conductivity of the stagnant layer", Colloids and Surfaces A: Physicochemical and Engineering Aspects, 2001 Publication	<1 %
43	C. Lapointe. "Static and dynamic properties of magnetic nanowires in nematic fluids (invited)", Journal of Applied Physics, 2005 Publication	<1 %
44	aip.scitation.org Internet Source	<1 %
45	vdoc.pub Internet Source	<1 %
46	H. Stark. "Director field configurations around a spherical particle in a nematic liquid crystal", The European Physical Journal B, 1999 Publication	<1 %
47	Submitted to Indian Institute of Science Education and Research Student Paper	<1 %

48	Sumit Gangwal, Olivier J. Cayre, Martin Z. Bazant, Orlin D. Velev. "Induced-Charge Electrophoresis of Metallodielectric Particles", Physical Review Letters, 2008 Publication	<1 %
49	J. Fukuda, H. Yokoyama. "Stability of the director profile of a nematic liquid crystal around a spherical particle under an external field", The European Physical Journal E, 2007 Publication	<1 %
50	Ahmad Ali Manzoor, Lauren Romita, Dae Kun Hwang. "A review on microwell and microfluidic geometric array fabrication techniques and its potential applications in cellular studies", The Canadian Journal of Chemical Engineering, 2020 Publication	<1 %
51	Submitted to University of Hull Student Paper	<1 %
52	C. Lapointe, N. Cappallo, D. H. Reich, R. L. Leheny. "Static and dynamic properties of magnetic nanowires in nematic fluids (invited)", Journal of Applied Physics, 2005 Publication	<1 %
53	Submitted to University of Limerick Student Paper	<1 %

54	"Introduction to Liquid Crystals", Springer Science and Business Media LLC, 1976 Publication	<1%
55	Lin Ling, Yong-qing Li. "Measurement of Raman spectra of single airborne absorbing particles trapped by a single laser beam", Optics Letters, 2013 Publication	<1%
56	Submitted to University of Bolton Student Paper	<1%
57	Hari Krishna Bisoyi, Timothy J. Bunning, Quan Li. "Stimuli-Driven Control of the Helical Axis of Self-Organized Soft Helical Superstructures", Advanced Materials, 2018 Publication	<1%
58	Romualdas Rimeika, Paulius Každailis, Daumantas Čiplys, Saulius Balakauskas. "Control of light polarization by acousto-optic diffraction from leaky acoustic wave in LiNbO_3", Optics Letters, 2011 Publication	<1%
59	Sarma, Kalluri. "Liquid Crystal Displays", The Measurement Instrumentation and Sensors Handbook on CD-ROM, 1999. Publication	<1%
60	hal.archives-ouvertes.fr Internet Source	<1%

61	Partially Ordered Systems, 1992. Publication	<1 %
62	Wang Yu-Sheng. "Stability of Disclinations in Nematic Liquid Crystals", Communications in Theoretical Physics, 06/2006 Publication	<1 %
63	drsr.daiict.ac.in Internet Source	<1 %
64	epdf.tips Internet Source	<1 %
65	A. V. Delgado, F. González-Caballero, R. J. Hunter, L. K. Koopal, J. Lyklema. "Measurement and Interpretation of Electrokinetic Phenomena (IUPAC Technical Report)", Pure and Applied Chemistry, 2005 Publication	<1 %
66	Arnold A. Fontaine, Steven Deutsch, Keefe B. Manning. "Flow Measurement", Wiley, 2006 Publication	<1 %
67	Submitted to Dr. B R Ambedkar National Institute of Technology, Jalandhar Student Paper	<1 %
68	Singh, S.. "Phase transitions in liquid crystals", Physics Reports, 200002 Publication	<1 %

69	G. Foffano, J.S. Lintuvuori, A. Tiribocchi, D. Marenduzzo. "The dynamics of colloidal intrusions in liquid crystals: a simulation perspective", Liquid Crystals Reviews, 2014 Publication	<1 %
70	Lavrentovich, Oleg D.. "Transport of particles in liquid crystals", Soft Matter, 2014. Publication	<1 %
71	R. Manda, V. Dasari, P. Sathyanarayana, M. V. Rasna, P. Paik, Surajit Dhara. "Possible enhancement of physical properties of nematic liquid crystals by doping of conducting polymer nanofibres", Applied Physics Letters, 2013 Publication	<1 %
72	www.hkdivedi.com Internet Source	<1 %

Exclude quotes	On	Exclude matches	< 14 words
Exclude bibliography	On		

Plagiarism-free statement

This is to certify that the thesis titled "Non-linear electrophoresis of metal-dielectric Janus particles in nematic liquid crystals" has been screened by the Turnitin software at the Indira Gandhi Memorial Library of University of Hyderabad. The software shows a 53% similarity index, out of which 45% came from candidate's own five research articles related to this thesis, which are already published and available online. Thus, the effective similarity index excluding his research articles is 53% -45% = 8%, which is lower than the 10% stipulated by the University guidelines. Therefore, the thesis is free from plagiarism.

Sdhara

Prof. Surajit Dhara
Thesis Supervisor
School of physics
University of Hyderabad

Date: 24/06/2022

Dr. Surajit Dhara
Professor
School of Physics
University of Hyderabad
Hyderabad-500 046. INDIA.